

Forschungsbericht 2023-22

Sources of tropospheric ozone over Europe and East Asia

Markus Kilian

Deutsches Zentrum für Luft- und Raumfahrt
Institut für Physik der Atmosphäre
Oberpfaffenhofen

Dissertation an der Fakultät für Physik
der Ludwig-Maximilians-Universität München



DLR

**Deutsches Zentrum
für Luft- und Raumfahrt**

Forschungsbericht 2023-22

Sources of tropospheric ozone over Europe and East Asia

Markus Kilian

Deutsches Zentrum für Luft- und Raumfahrt
Institut für Physik der Atmosphäre
Oberpfaffenhofen

Dissertation an der Fakultät für Physik
der Ludwig-Maximilians-Universität
München

245 Seiten
147 Bilder
23 Tabellen
181 Literaturstellen



Deutsches Zentrum
DLR für Luft- und Raumfahrt



Herausgeber:

Deutsches Zentrum
für Luft- und Raumfahrt e. V.
Wissenschaftliche Information
Linder Höhe
D-51147 Köln

ISSN 1434-8454
ISRN DLR-FB-2023-22
Erscheinungsjahr 2023

DOI: [10.57676/w96b-3r32](https://doi.org/10.57676/w96b-3r32)

Erklärung des Herausgebers

Dieses Werk wird unter den Bedingungen der Creative Commons Lizenz vom Typ Namensnennung 4.0 International, abrufbar über <https://creativecommons.org/licenses/by/4.0/legalcode>, zur Nutzung überlassen.

Lizenz



Creative Commons Attribution 4.0 International

Ozon, Attributionstechnik, Europa, Ostasien, Luftverschmutzung, Stickstoffoxid, VOC, Sentinel-5P, MESSy, MECO(n), COSMO, EMAC

Markus Kilian
DLR, Institut für Physik der Atmosphäre, Oberpfaffenhofen

Quellen von troposphärischem Ozon in Europa und Ostasien

Ludwig-Maximilians-Universität, Fakultät für Physik

Troposphärisches Ozon ist ein wichtiges Treibhausgas und Luftschadstoff, der die menschliche Gesundheit und Ökosysteme gefährdet. Emissionen des Landverkehrs und anderer anthropogener Quellen wie Industrie sind wichtige Quellen für Stickoxide (NO_x), Kohlenmonoxid und flüchtige organische Verbindungen (VOC). Diese sind wichtige Vorläufersubstanzen für troposphärisches Ozon und beeinflussen die Luftqualität. Da die Ozonchemie nichtlinear ist, ist eine direkte Berechnung des Beitrags von Emissionssektoren zum Ozon nicht möglich. Dies funktioniert nur unter Verwendung detaillierter Klima- Chemie-Modelle. In meiner Dissertation untersuche ich die Beiträge verschiedener Emissionssektoren zum bodennahen Ozon in Europa und Ostasien. Hierfür verwende ich das MECO(n)-Modellsystem, welches aus einem globalen und regionalen Modell besteht. Letzteres ermöglicht es bestimmte Regionen besonders hoch aufzulösen. Das Modell verwendet eine Attributions-Technik, die den Beitrag von verschiedenen Emissionsquellen zu Ozon berechnet. Es wurden zwei Simulationen mit je zwei regionalen Verfeinerungen für Europa und Ostasien über 2 Jahre durchgeführt, mit Auflösungen von 50 und 12 km. Die Modellergebnisse wurden mithilfe von Satellitendaten, Daten von Luftqualitätsstationen und Flugkampagnen in Europa und Asien sowie schiffsbasierten MAX-DOAS-Messungen über dem chinesischen Meer evaluiert. Mehrere Gebiete in Europa und Ostasien mit hohen anthropogenen Emissionen wurden untereinander, sowie mit ländlichen Gebieten verglichen. Die absoluten Beiträge regionaler anthropogener Emissionen zum bodennahen Ozon in der Po-Ebene mit 20 nmol mol^{-1} (31 %) sind größer als im Benelux-Gebiet mit 9 nmol mol^{-1} (22 %) für Sommer 2017–2018. Ähnliche Ergebnisse wurden für Ostasien gefunden, wo das Perlfuss- und Jangtse-Delta, sowie das Sichuan-Becken die größten Beiträge regionaler anthropogener Emissionen zum bodennahen Ozon mit $25\text{--}40 \text{ nmol mol}^{-1}$ (46– 49 %) aufweisen. In einigen küsten- und ländlich geprägten Gebieten von Europa und Ostasien spielen Ferntransportbeiträge zum Ozon eine wichtigere Rolle als regionale anthropogene Emissionen. In stark verschmutzten Regionen in Europa und Ostasien ist die Ozon-Titration wichtig. Hier ist die Ozonproduktion ineffizient und wird durch VOCs limitiert. In den betrachteten Becken und ländlichen Lagen, ist die Ozonproduktion effizienter und NO_x -limitiert. Die Po-Ebene in Europa und das Perlfussdelta in Ostasien haben das größte Potenzial zur Minderung von bodennahem Ozon durch Reduktion lokaler anthropogener NO_x beziehungsweise VOC Quellen. Der Effekt unterschiedlicher Repräsentationen von Emissionen mit großen Unsicherheiten, wie Biomassenbrände und biogene VOCs, auf die Ozonbeiträge aus anthropogenen Emissionsquellen ist nahezu vernachlässigbar.

ozone, source apportionment method, Europe, East Asia, pollution, nitrogen oxide, VOC, Sentinel-5P, MESSy, MECO(n), COSMO, EMAC

(Published in English)

Markus Kilian
German Aerospace Center (DLR),
Institute of Atmospheric Physics, Oberpfaffenhofen

Sources of tropospheric ozone over Europe and East Asia

Ludwig-Maximilians-University, Faculty of Physics

Tropospheric ozone is an important greenhouse gas and air pollutant that is harmful to human health and ecosystems. Emissions from land transport and other anthropogenic sources, such as industry, are significant contributors of nitrogen oxides (NO_x), carbon monoxide, and volatile organic compounds (VOC). These serve as important precursor substances for tropospheric ozone and influence air quality. Due to the nonlinear ozone chemistry, directly calculating the contribution of emission sectors to ozone is not possible. For this purpose, detailed chemistry-climate models are required. In my dissertation, I examine the contributions of different emission sectors to ground-level ozone in Europe and East Asia. I utilise the MECO(n) model system, which comprises a global and regional model. The latter allows for high-resolution analysis of specific regions. The model employs a tagging method to calculate the contributions of various emission sources to ozone. Two simulations, each with two regional refinements for Europe and East Asia, are conducted over a span of 2 years, at resolutions of 50 and 12 km. The model results are evaluated using satellite data, air quality station data, data from two flight campaigns in Europe and Asia, and ship-based MAX-DOAS measurements over the Chinese Sea. Several regions in Europe and East Asia with large anthropogenic emissions are compared with one another, as well as with rural areas. The absolute contributions of regional anthropogenic emissions to ground-level ozone in the Po Valley, with 20 nmol mol^{-1} (31 %), are larger than in the Benelux region, with 9 nmol mol^{-1} (22 %), for the summer of 2017–2018. Similar results are found for East Asia, where the Pearl River Delta, Yangtze River Delta, and Sichuan Basin exhibit the largest contributions of regional anthropogenic emissions to ground-level ozone, ranging from $25\text{--}40 \text{ nmol mol}^{-1}$ (46–49 %). In some coastal and rural areas of Europe and East Asia, long-range transport contributions to ozone are more important than regional anthropogenic emissions. In heavily polluted regions of Europe and East Asia, ozone titration is large and ozone production is inefficient. In these areas, ozone production is limited by VOCs. In most basins and rural locations, ozone production is rather efficient and NO_x -limited. The Po Valley in Europe and the Pearl River Delta in East Asia have the largest mitigation potential for ground-level ozone by reducing local anthropogenic NO_x and VOC sources, respectively. The effect of different representations of emissions with large uncertainties, such as from biomass burning and biogenic VOCs, on the ozone contributions from anthropogenic emission sources is almost negligible.

Sources of tropospheric ozone over Europe and East Asia

Markus Kilian



München 2023

Sources of tropospheric ozone over Europe and East Asia

Markus Kilian

Dissertation
an der Fakultät für Physik
der Ludwig-Maximilians-Universität
München

vorgelegt von
Markus Kilian
aus Arnsberg-Neheim

München, den 21. August 2023

Erstgutachter: Prof. Dr. Robert Sausen

Zweitgutachter: Prof. Dr. Mark Wenig

Tag der mündlichen Prüfung: 31. Oktober 2023

Contents

Zusammenfassung	xxiii
1 Introduction	1
1.1 Motivation	1
1.2 Scientific Questions	4
1.3 Investigation Strategy	4
2 Background	7
2.1 Tropospheric and stratospheric ozone	7
2.2 Chemical production and destruction of tropospheric ozone	9
2.2.1 Non-Linearity of ozone production	13
2.2.2 Chemistry of O ₃ during daytime and nighttime	15
2.3 Sources of NO _x , CO and VOCs	16
2.4 Ozone budget of the troposphere	18
2.5 Perturbation and Source Attribution Methods	20
3 Methods	23
3.1 MESSy infrastructure	25
3.2 MESSy Basemodels	26
3.2.1 EMAC	26
3.2.2 COSMO	26
3.2.3 MECO(n) model system	26
3.3 MESSy Submodels	27
3.3.1 The MECCA submodel: calculates tropospheric and stratospheric chemistry	27
3.3.2 The Lightning NO _x submodel: parameterisation of lightning NO _x .	27
3.3.3 The BIOBURN submodel: calculates biomass burning fluxes	28
3.3.4 The MEGAN submodel: estimates net emission of gases and aerosols from terrestrial ecosystems	29
3.3.5 The OFFEMIS submodel: represents emission fluxes in 2D and 3D	32
3.3.6 The S4D submodel: sampling in 4 Dimensions	32
3.3.7 The SORBIT submodel: sampling model data along sun-synchronous satellite orbits	33

3.3.8	The TAGGING submodel: contribution of different emission categories	33
3.3.9	Emission inventories used	36
3.4	Description of the model setup	38
4	Evaluation of the MECO(n) system	43
4.1	Meteorological Evaluation East Asia	43
4.2	Intercomparison of simulation results of tropospheric columns with satellite observations	45
4.2.1	Model results compared to satellite observations: NO ₂	45
4.2.2	Model results compared to satellite observations: Ozone	53
4.3	Ground-Level Observations	60
4.3.1	D21 Ozone Dataset	60
4.3.2	Air Quality Stations	63
4.4	Observations from campaigns	65
4.4.1	HALO in situ measurements during EMERGE measurement campaigns	65
4.4.2	MAX-DOAS measurements over the East China Sea	75
4.5	Discussion and Summary of the Model Evaluation	79
4.5.1	Europe	79
4.5.2	East Asia	80
5	Comparison of the ozone chemistry in Europe and East Asia	83
5.1	Contribution of different emission sectors to ground-level O ₃ in Europe	83
5.1.1	Contributions during summer 2017–2018 in Europe	83
5.1.2	Contributions during periods of large ozone values in Europe	92
5.2	Contribution of different emission sectors to ground-level ozone in East Asia	96
5.2.1	Contributions during summer 2017–2018 in East Asia	96
5.2.2	Contributions during periods of large ozone values in East Asia	103
5.3	Comparison of the study areas in Europe and East Asia	107
5.4	Summary and Discussion	117
6	Sensitivity Simulations	119
6.1	Sensitivity Study with BIOBURN: EUBB and ASIABB	119
6.2	Sensitivity Study with MEGAN: EUMEGAN	123
7	Conclusions and Outlook	133
	Appendices	137
A.1	Appendix Tables and Descriptions	137
A.1.1	Definition of NO _y in the TAGGING submodel	137
A.1.2	Definition of NO _y in the Evaluation Chapter	137
A.1.3	Tagging regions and the submodel SCALC	141
A.1.4	Detailed description of BIOBURN	141

A.1.5	Mechanism of the gas phase chemistry	144
A.1.6	Extensions of the MEGAN namelist	167
B.2	Appendix Additional Results and Figures Chapter 4	168
B.2.1	Further detailed evaluation of EMeRGe Europe	168
B.2.2	Further detailed evaluation of EMeRGe Asia	168
C.3	Appendix Tables and Figures Chapter 5 and 6	187
Danksagung		243

Parts of my thesis have been submitted to the Atmospheric Chemistry and Physics (ACP) journal with multiple co-authors [Kilian et al., 2023] with the title “Ozone source attribution in polluted European areas during summer as simulated with MECO(n)”. The manuscript is currently under review.

List of Figures

2.1	Isopleths show the net rate of O_3 production (P_{O_3}) as a function of mixing ratios of VOCs as amount of carbon and NO_x for mean summer daytime meteorology and clear sky.	14
2.2	Illustration of the tropospheric O_3 budget (adopted after Mertens 2017). .	19
2.3	Illustration of the sensitivity method (pair of simulations) to derive contributions with the tagging method adopted from Grewe et al. [2010].	22
3.2	Sketch of the MESSy concept.	25
3.3	Sketch of the tagging method in the TAGGING submodel.	34
3.4	Domains of both MECO(2) setups with the global EMAC and regional COSMO instances.	37
4.1	Monthly averaged differences between CM50 and ERA5 in East Asia for March and April 2018.	44
4.2	Tropospheric NO_2 column over Central Europe for JJA 2018 resulting from COSMO in comparison with Sentinel-5P.	49
4.3	Histogram of the probability density of the tropospheric vertical NO_2 column for Central Europe during JJA 2018 simulated by CM50 and CM12.	50
4.4	Tropospheric NO_2 column over East Asia for JJA 2018 resulting from COSMO in comparison with Sentinel-5P.	51
4.5	Histogram of the probability density of the tropospheric vertical NO_2 column for East Asia during JJA 2018 simulated by CM50 and CM12.	52
4.6	Tropospheric O_3 column over Central Europe for JJA 2018 resulting from COSMO in comparison with Sentinel-5P.	54
4.7	Probability density function (PDF) of the tropospheric vertical O_3 column for Europe during JJA 2018 simulated by CM50 and CM12 in comparison with the Sentinel-5P observations.	55
4.8	Tropospheric O_3 column over East Asia for JJA 2018 resulting from COSMO in comparison with Sentinel-5P.	57
4.9	Probability density function (PDF) of the tropospheric vertical O_3 column over East Asia during JJA 2018 simulated by CM50 and CM12 in comparison with the Sentinel-5P observations.	58

4.10	Tropospheric O ₃ column over Central Europe for JJA 2018, simulated by CM50 and CM12 calculated based on different tropopause pressures. . . .	59
4.11	Comparison of the seasonal daily maximum 8-hour ground-level O ₃ mixing ratio for Central Europe in 2017 with the D21 dataset.	61
4.12	Comparison of the seasonal daily maximum 8-hour ground-level O ₃ mixing ratio for East Asia in 2017 with the D21 dataset.	62
4.13	PDF of the NO _x concentrations of the model output of CM12 and the rural AIRBASE station data for July 2017 in Europe.	63
4.14	PDF of the O ₃ concentrations of the model output of CM12 and the rural AIRBASE station data for July 2017 in Europe.	63
4.15	Observed (EPA) and simulated (CM12) diurnal cycle of the hourly ground-level NO ₂ mixing ratios during JJA 2018 in East Asia.	65
4.16	Observed (EPA) and simulated (CM12) diurnal cycle of the hourly ground-level O ₃ mixing ratios during JJA 2018 in East Asia.	65
4.17	CM12 simulated NO _y mixing ratios in horizontal comparison with HALO in situ measurements for the flight date 11.07.2017.	67
4.18	CM12 simulated O ₃ mixing ratios in horizontal comparison with HALO in situ measurements for the flight date 11.07.2017.	68
4.19	Part 1: CM12 simulated NO _y mixing ratios in vertical comparison with HALO in situ measurements for the flight date 11.07.2017.	69
4.20	Part 1: CM12 simulated O ₃ mixing ratios in vertical comparison with HALO in situ measurements for the flight date 11.07.2017.	69
4.21	Part 2: CM12 simulated NO _y mixing ratios in vertical comparison with HALO in situ measurements for the flight date 11.07.2017.	69
4.22	Part 2: CM12 simulated O ₃ mixing ratios in vertical comparison with HALO in situ measurements for the flight date 11.07.2017.	69
4.23	Part 1: CM12 simulated NO _y mixing ratios in horizontal comparison with HALO in situ measurements for the flight date 22.03.2018.	72
4.24	Part 1: CM12 simulated O ₃ mixing ratios in horizontal comparison with HALO in situ measurements for the flight date 22.03.2018.	72
4.25	Part 2: CM12 simulated NO _y mixing ratios in horizontal comparison with HALO in situ measurements for the flight date 22.03.2018.	73
4.26	Part 2: CM12 simulated O ₃ mixing ratios in horizontal comparison with HALO in situ measurements for the flight date 22.03.2018.	73
4.27	CM12 simulated NO _y mixing ratios in vertical comparison with HALO in situ measurements for the flight date 22.03.2018.	74
4.28	CM12 simulated O ₃ mixing ratios in vertical comparison with HALO in situ measurements for the flight date 22.03.2018.	74
4.29	Comparison between mean model results of NO ₂ vertical column densities with MAX-DOAS measurements.	76
4.30	Timeseries of the simulated (CM12) NO ₂ vertical column densities with the MAX-DOAS ship-based measurements in June 2017.	77

4.31	Comparison between model results of the NO ₂ vertical column densities with the MAX-DOAS ship-based measurements for June 2017.	78
4.32	PDFs of the NO ₂ vertical column densities of CM12 model results and MAX-DOAS observations for different integration heights.	78
5.1	Seasonal mean (JJA 2017–2018) absolute contributions of NO _y as mixing ratios in Europe.	85
5.2	Seasonal mean (JJA 2017–2018) absolute contributions of O ₃ as mixing ratios in Europe.	86
5.3	Seasonal mean (JJA 2017–2018) of the ozone net production rate in Europe.	87
5.4	Seasonal mean (JJA 2017–2018) of the absolute contribution of different emissions sectors and regions to ground-level ozone in four European study areas.	90
5.5	Seasonal mean (JJA 2017–2018) of the relative contribution of different emissions sectors and regions to ground-level ozone in four European study areas.	91
5.6	Box-whisker plot showing the contributions of the most important emission sources for the 95th, 90th, and 75th percentiles of ozone as simulated by CM12 for JJA 2017–2018 in Europe.	94
5.7	Box-whisker plot showing the contributions of the most important emission sources of ozone as simulated by CM12 for JJA 2017–2018 in Europe.	95
5.8	Seasonal mean absolute contributions of NO _y from long-range transported and East Asian NO _y emissions as simulated with CM12 in East Asia.	97
5.9	Seasonal mean absolute contribution from long-range transported and East Asian emissions as mixing ratios of O ₃ for JJA 2017–2018 in East Asia.	98
5.10	Seasonal mean (JJA 2017–2018) of the ozone net production rate in East Asia.	99
5.11	Seasonal mean (JJA 2017–2018) of the absolute contribution of different emissions sectors and regions to ground-level ozone in five East Asian study areas.	100
5.12	Seasonal mean (JJA 2017–2018) of the relative contribution of different emissions sectors and regions to ground-level ozone in five East Asian study areas.	101
5.13	Box-whisker plot showing the seasonal mean (JJA 2017–2018) contributions of the most important emission sources at the 95th, 90th, and 75th percentiles of ozone as simulated by CM12 in East Asia.	105
5.14	Box-whisker plot showing the contributions of the most important emission sources of ozone as simulated by CM12 for JJA 2017–2018 in East Asia.	106
5.15	OPE in JJA 2017–2018 for Europe and East Asia in CM12.	108
5.16	Seasonal mean (JJA 2017–2018) of the monthly production of NO ₂ + OH and HNO ₃ for CM12 in JJA 2017–2018 for Europe and East Asia.	109
5.17	Relation of OPE with the NO _x and NMHC mixing ratio as simulated by CM12 in JJA 2017–2018 for the European and East Asian study areas.	110
5.18	SR of CM12 in JJA 2017–2018 for Europe and East Asia.	111
5.19	Chemical regimes classified after their Sillman ratio for Europe and East Asia.	111

5.20	Relation of SR with the NO_x and NMHC mixing ratio as simulated by CM12 in JJA 2017–2018 for the European and East Asian study areas as scatter plots.	112
5.21	Illustration of the Leighton Ratio (ϕ) for CM12 during JJA 2017–2018 for Europe and East Asia.	114
5.22	Relation of Leighton Ratio with the NO_x and NMHC mixing ratio as simulated by CM12 in JJA 2017–2018 for the European and East Asian study areas as scatter plots.	115
6.1	Annual mean (2017–2018) of the vertically summed NO_x biomass burning fluxes of the model results from EUBB and its differences with EUREF. . .	121
6.2	Annual mean (2017–2018) of the vertically summed NO_x biomass burning fluxes of the model results from ASIABB and its differences with ASIAREF. . .	127
6.3	Vertical zonal mean of the NO_x biomass burning flux as simulated by EMAC in both BB simulations and its differences with REF for 2017–2018.	128
6.4	Seasonal mean (JJA 2017–2018) of the differences between EUBB minus EUREF of total ozone and the absolute contribution of different emissions sectors and regions to ground-level ozone in four European study areas. . .	129
6.5	Seasonal mean (JJA 2017–2018) of the differences between ASIABB minus ASIAREF of total ozone and the absolute contribution of different emissions sectors and regions to ground-level ozone in five East Asian study areas. . .	129
6.6	Annual mean (2017) of the simulated biogenic CO flux from EUMEGAN and its differences with EUREF for the instances EMAC and CM50 for Europe.	130
6.7	Seasonal mean (JJA 2017) of the differences between EUMEGAN minus EUREF of total ozone and the absolute contribution of different emissions sectors and regions to ground-level ozone in four European study areas. . .	131
A.1	Land cover class map based on dominant fire type in GFAS and organic soil and peat maps after Kaiser et al. [2012].	144
A.2	Source regions for tagging in the MECO(2) model setup.	167
B.3	CM12 simulated NO_y mixing ratios as horizontal comparison with HALO in situ measurements for the flight date 20.07.2017.	170
B.4	CM12 simulated O_3 mixing ratios as horizontal comparison with HALO in situ measurements for the flight date 20.07.2017.	170
B.5	CM12 simulated NO_y mixing ratios as vertical comparison with HALO in situ measurements for the flight date 20.07.2017.	171
B.6	CM12 simulated O_3 mixing ratios as vertical comparison with HALO in situ measurements for the flight date 20.07.2017.	171
B.7	CM12 simulated NO_y mixing ratios as horizontal comparison with HALO in situ measurements for the flight date 26.07.2017.	172
B.8	CM12 simulated O_3 mixing ratios as horizontal comparison with HALO in situ measurements for the flight date 26.07.2017.	172

B.9	CM12 simulated NO_y mixing ratios as vertical comparison with HALO in situ measurements for the flight date 26.07.2017.	173
B.10	CM12 simulated O_3 mixing ratios as vertical comparison with HALO in situ measurements for the flight date 26.07.2017.	173
B.11	Part 1: CM12 simulated NO_y mixing ratios as horizontal comparison with HALO in situ measurements for the flight date 24.03.2018.	173
B.12	Part 1: CM12 simulated O_3 mixing ratios as horizontal comparison with HALO in situ measurements for the flight date 24.03.2018.	173
B.13	Windspeed of the model output of CM12 and the wind direction for the HALO flight at the 24th of March 2018.	174
B.14	Part 1: CM12 simulated NO_y mixing ratios as vertical comparison with HALO in situ measurements for the flight date 24.03.2018.	175
B.15	Part 1: CM12 simulated O_3 mixing ratios as vertical comparison with HALO in situ measurements for the flight date 24.03.2018.	175
B.16	Part 2: CM12 simulated NO_y mixing ratios as horizontal comparison with HALO in situ measurements for the flight date 24.03.2018.	176
B.17	Part 2: CM12 simulated O_3 mixing ratios as horizontal comparison with HALO in situ measurements for the flight date 24.03.2018.	176
B.18	Part 2: CM12 simulated NO_y mixing ratios as vertical comparison with HALO in situ measurements for the flight date 24.03.2018.	177
B.19	Part 2: CM12 simulated O_3 mixing ratios as vertical comparison with HALO in situ measurements for the flight date 24.03.2018.	177
B.20	Part 1: CM12 simulated NO_y mixing ratios as horizontal comparison with HALO in situ measurements for the flight date 28.03.2018.	178
B.21	Part 1: CM12 simulated O_3 mixing ratios as horizontal comparison with HALO in situ measurements for the flight date 28.03.2018.	178
B.22	Part 2: CM12 simulated NO_y mixing ratios as horizontal comparison with HALO in situ measurements for the flight date 28.03.2018.	179
B.23	Part 2: CM12 simulated O_3 mixing ratios as horizontal comparison with HALO in situ measurements for the flight date 28.03.2018.	179
B.24	CM12 simulated NO_y mixing ratios as vertical comparison with HALO in situ measurements for the flight date 28.03.2018.	180
B.25	CM12 simulated O_3 mixing ratios as vertical comparison with HALO in situ measurements for the flight date 28.03.2018.	180
B.26	Comparison of ground-level ozone between CM50 and CM12.	181
B.27	Observed (EPA) and simulated (CM12) NO_2 versus O_3 mixing ratios. . . .	182
B.28	Observed (EPA) and simulated (CM12) NO_2 versus MDA8 O_3 mixing ratios. . . .	182
B.29	Overview of all flights conducted by the EMeRGe Europe campaign.	182
B.30	Part 1: NO_y mixing ratios (CM12) versus HALO in situ measurements for four flight dates of the EMeRGe Europe campaign.	183
B.31	Part 1: O_3 mixing ratios (CM12) versus HALO in situ measurements for four flight dates of the EMeRGe Europe campaign.	183

B.32	Part 2: NO _y mixing ratios (CM12) versus HALO in situ measurements for three flight dates of the EMeRGe Europe campaign.	183
B.33	Part 2: O ₃ mixing ratios (CM12) versus HALO in situ measurements for three flight dates of the EMeRGe Europe campaign.	183
B.34	Overview of all flights conducted by the EMeRGe Asia campaign.	184
B.35	Part 1: NO _y mixing ratios (CM12) versus HALO in situ measurements for four flight dates of the EMeRGe Europe campaign.	184
B.36	Part 1: O ₃ mixing ratios (CM12) versus HALO in situ measurements for four flight dates of the EMeRGe Europe campaign.	184
B.37	Part 2: NO _y mixing ratios (CM12) versus HALO in situ measurements for four flight dates of the EMeRGe Europe campaign.	185
B.38	Part 2: O ₃ mixing ratios (CM12) versus HALO in situ measurements for four flight dates of the EMeRGe Europe campaign.	185
B.39	Part 3: NO _y mixing ratios (CM12) versus HALO in situ measurements for three flight dates of the EMeRGe Europe campaign.	185
B.40	Part 3: O ₃ mixing ratios (CM12) versus HALO in situ measurements for four flight dates of the EMeRGe Europe campaign.	185
B.41	Topography and mean planetary boundary layer height for East Asia for JJA 2017–2018.	186
C.42	Seasonal mean (JJA 2017–2018) of the ground-level NO _x mixing ratios in CM12 for Europe and East Asia.	188
C.43	Seasonal mean (JJA 2017–2018) mean absolute contributions of NMHC as mixing ratios simulated by CM12.	188
C.44	Seasonal mean (JJA 2017–2018) absolute contribution as mixing ratios of O ₃ from long-range transported and European emissions as simulated with CM50.	189
C.45	Absolute and relative contribution as mixing ratios of all sectors to ground-level O ₃ for JJA 2017–2018 in the Po Valley.	189
C.46	Absolute and relative contribution as mixing ratios of all sectors to ground-level O ₃ for JJA 2017–2018 in the Benelux region.	190
C.47	Absolute and relative contribution as mixing ratios of all sectors to ground-level O ₃ for JJA 2017–2018 in Ireland.	190
C.48	Absolute and relative contribution as mixing ratios of all sectors to ground-level O ₃ for JJA 2017–2018 over the Iberian Peninsula.	191
C.49	Mean of the ground-level isoprene emission flux for JJA 2017–2018 in CM12 for Europe.	191
C.50	Mean of the ground-level soil NO _x emission flux for JJA 2017–2018 in CM12 for Europe.	192
C.51	Box-whisker plot showing the seasonal mean (JJA 2017–2018) contributions of the most important emission sectors at the 95th, 90th, and 75th percentiles of ozone by CM12 for JJA 2017–2018 for Europe.	193
C.52	Shown is ozone during the seasonal maximum, mean and minimum (JJA 2017–2018) of MDA8 ozone in Europe as simulated by CM12.	194

C.53	Box-whisker plot showing the contributions of the most important European emission sectors (separated by LRT and EU) of ozone for JJA 2017–2018 as simulated by CM12.	195
C.54	Seasonal mean (JJA 2017–2018) absolute contributions of NMHC for East Asia as simulated by CM12.	196
C.55	Seasonal mean (JJA 2017–2018) absolute contribution to O ₃ as simulated by CM50.	197
C.56	Seasonal mean (JJA 2017–2018) absolute contributions of PAN as simulated with CM12.	198
C.57	Absolute and relative contribution as mixing ratios of all sectors to ground-level O ₃ for JJA 2017–2018 in the Pearl Delta.	198
C.58	Absolute and relative contribution as mixing ratios of all sectors to ground-level O ₃ for JJA 2017–2018 in the Yangtze Delta.	199
C.59	Absolute and relative contribution as mixing ratios of all sectors to ground-level O ₃ for JJA 2017–2018 in Taiwan.	199
C.60	Absolute and relative contribution as mixing ratios of all sectors to ground-level O ₃ for JJA 2017–2018 in the Sichuan Basin.	200
C.61	Absolute and relative contribution as mixing ratios of all sectors to ground-level O ₃ for JJA 2017–2018 in Ningxia.	200
C.62	Mean of the ground-level isoprene emission flux for JJA 2017–2018 in CM12 for East Asia.	201
C.63	Mean of the ground-level soil NO _x emission flux for JJA 2017–2018 in CM12 for East Asia.	201
C.64	Box-whisker plot showing the seasonal mean (JJA 2017–2018) contributions of the most important emission sectors at the 95th, 90th, and 75th percentiles of ozone by CM12 for East Asia.	202
C.65	Shown is ozone in JJA 2017–2018 during the seasonal maximum, mean and minimum of MDA8 ozone in East Asia for JJA 2017–2018 as simulated by CM12.	203
C.66	Box-whisker plot showing the contributions of the most important East Asian emission sectors of ozone as simulated by CM12 for JJA 2017–2018.	204
C.67	Box-whisker plot showing the contributions of the most important East Asian emission sectors (separated by LRT and EA) of ozone for JJA 2017–2018 as simulated by CM12.	205
C.68	Seasonal mean (JJA 2017–2018) of the OH mixing ratio for CM12 in JJA 2017–2018 for Europe and East Asia.	206
C.69	Seasonal mean (JJA 2017–2018) of the specific humidity for CM12 for Europe and East Asia.	206
C.70	Seasonal mean (JJA 2017–2018) of the NO ₂ -NO ratio for CM12 for Europe and East Asia.	207
C.71	Annual mean (2017–2018) of the dry particulate matter (DM) flux, and the fraction of the firetype (land and water) of the model results from EUBB.	208

C.72	Annual mean (2017–2018) of the dry particulate matter (DM) flux, and the fraction of the firetype (land and water) of the model results from ASIABB.	209
C.73	Seasonal mean (2017–2018) of the ground-level O ₃ contributions from long-range transported (LRT: ROW + NA + EU) and European emissions as simulated by CM50.	210
C.74	Seasonal mean (2017–2018) of the ground-level O ₃ contributions from long-range transported (LRT: ROW + NA + EA) and East Asian emissions as simulated by CM50.	211
C.75	Seasonal mean (JJA 2017–2018) of the ground-level O ₃ contributions from biomass burning emissions as simulated by CM50.	212
C.76	Seasonal mean (JJA 2017–2018) of the relative differences between EUBB minus EUREF of the absolute contribution of different emissions sectors and regions to ground-level ozone in four European study areas.	213
C.77	Seasonal mean (JJA 2017–2018) of the relative differences between ASIABB minus ASIAREF of the absolute contribution of different emissions sectors and regions to ground-level ozone in five East Asian study areas.	213
C.78	Annual mean (2017–2018) of the biogenic CO flux of the model results from EUREF minus EUMEGAN for the instances EMAC and CM50 for Europe.	214
C.79	Seasonal mean (2017) of the ground-level O ₃ contributions from long-range transported (LRT: ROW + NA + EU) and European emissions for JJA 2017 as simulated by CM50.	215
C.80	Seasonal mean (JJA 2017) of the relative differences between EUMEGAN and EUREF of the absolute contribution of different emissions sectors and regions to ground-level ozone in four European study areas.	216

List of Tables

2.1	Global totals of the ozone precursors NO_x , CO and VOCs in Tg a^{-1} from the literature.	17
3.1	Global and regional scaling factors used in MEGAN.	30
3.2	Annual totals in EMAC and CM50 in comparison with the desired annual totals from 2000.	31
3.3	Description of the different tagging categories applied in this study following Grewe et al. [2017].	40
3.4	Totals of the ozone precursors NO_x , CO and VOCs in Tg a^{-1} of the global EMAC simulation.	41
3.5	Overview of the simulations analysed in the present thesis.	41
4.1	Statistical comparison of CM12 simulation results with observations from EMeRGe Europe.	68
4.2	Statistical comparison of CM12 simulation results with observations from EMeRGe Asia.	71
4.3	RMSE and MB for NO_2/NO_x , NO_y and O_3 as simulated by CM50 and CM12 in comparison with different data sets in Europe.	80
4.4	RMSE and MB for NO_2/NO_x , NO_y and O_3 as simulated by CM50 and CM12 in comparison with different data sets in East Asia.	82
5.1	Definition of the regions in Europe, which are analysed in this study in detail.	84
5.2	Definition of the regions in East Asia, which are analysed in this study in detail.	96
5.3	Seasonal means (JJA 2017–2018) of the absolute and relative O_3 contributions from regional anthropogenic emissions, and medians of the measures OPE, SR and Leighton Ratio.	116
6.1	Global totals of the GFASv1.2 data set and the calculated totals by OFF-FEMIS and BIOBURN in EMAC in 2017.	120
6.2	Global annual totals of biogenic emissions in EUMEGAN and EUREF for 2017.	124
A.1	Part 1: List of all submodels used in the model setup.	138

A.2	Part 2: List of all submodels used in the model setup.	139
A.3	Fractional distribution (in %) of emission heights for different emission sectors (EDGAR, v5.0).	139
A.4	Fractional distribution of emission heights for biomass burning.	140
A.5	Part 1: Emission factors for the species in BIOBURN based on Kaiser et al. [2012].	142
A.6	Part 2: Emission factors for the species in BIOBURN based on Kaiser et al. [2012].	143
C.7	Annual totals of EDGAR v5.0 emissions in the European study areas for the year 2015.	187
C.8	Annual totals of EDGAR v5.0 emissions in the East Asian study areas for the year 2015.	187

Zusammenfassung

Troposphärisches Ozon ist ein wichtiges Treibhausgas und Luftschadstoff, der die menschliche Gesundheit und Ökosysteme gefährdet. Emissionen des Landverkehrs und anderer anthropogener Quellen wie Industrie sind wichtige Quellen für Stickoxide (NO_x), Kohlenmonoxid und flüchtige organische Verbindungen (VOC). Diese sind wichtige Vorläufersubstanzen für troposphärisches Ozon und beeinflussen die Luftqualität. Da die Ozonchemie nichtlinear ist, ist eine direkte Berechnung des Beitrags von Emissionssektoren zum Ozon nicht möglich. Dies funktioniert nur unter Verwendung detaillierter Klima-Chemie-Modelle. In meiner Dissertation untersuche ich die Beiträge verschiedener Emissionssektoren zum bodennahen Ozon in Europa und Ostasien. Hierfür verwende ich das MECO(n)-Modellsystem, welches aus einem globalen und regionalen Modell besteht. Letzteres ermöglicht es bestimmte Regionen besonders hoch aufzulösen. Das Modell verwendet eine Attributions-Technik, die den Beitrag von verschiedenen Emissionsquellen zu Ozon berechnet. Es wurden zwei Simulationen mit je zwei regionalen Verfeinerungen für Europa und Ostasien über 2 Jahre durchgeführt, mit Auflösungen von 50 und 12 km. Die Modellergebnisse wurden mithilfe von Satellitendaten, Daten von Luftqualitätsstationen und Flugkampagnen in Europa und Asien sowie schiffsbasierten MAX-DOAS-Messungen über dem chinesischen Meer evaluiert. Mehrere Gebiete in Europa und Ostasien mit hohen anthropogenen Emissionen wurden untereinander, sowie mit ländlichen Gebieten verglichen. Die absoluten Beiträge regionaler anthropogener Emissionen zum bodennahen Ozon in der Po-Ebene mit 20 nmol mol^{-1} (31 %) sind größer als im Benelux-Gebiet mit 9 nmol mol^{-1} (22 %) für Sommer 2017–2018. Ähnliche Ergebnisse wurden für Ostasien gefunden, wo das Perlfluss- und Jangtse-Delta, sowie das Sichuan-Becken die größten Beiträge regionaler anthropogener Emissionen zum bodennahen Ozon mit $25\text{--}40 \text{ nmol mol}^{-1}$ (46–49 %) aufweisen. In einigen küsten- und ländlich geprägten Gebieten von Europa und Ostasien spielen Ferntransportbeiträge zum Ozon eine wichtigere Rolle als regionale anthropogene Emissionen. In stark verschmutzten Regionen in Europa und Ostasien ist die Ozon-Titration wichtig. Hier ist die Ozonproduktion ineffizient und wird durch VOCs limitiert. In den betrachteten Becken und ländlichen Lagen, ist die Ozonproduktion effizienter und NO_x -limitiert. Die Po-Ebene in Europa und das Perlflussdelta in Ostasien haben das größte Potenzial zur Minderung von bodennahem Ozon durch Reduktion lokaler anthropogener NO_x beziehungsweise VOC Quellen. Der Effekt unterschiedlicher Repräsentationen von Emissionen mit großen Unsicherheiten, wie Biomassenbrände und biogene VOCs, auf die Ozonbeiträge aus anthropogenen Emissionsquellen ist nahezu vernachlässigbar.

Abstract

Tropospheric ozone is an important greenhouse gas and air pollutant that is harmful to human health and ecosystems. Emissions from land transport and other anthropogenic sources, such as industry, are significant contributors of nitrogen oxides (NO_x), carbon monoxide, and volatile organic compounds (VOC). These serve as important precursor substances for tropospheric ozone and influence air quality. Due to the nonlinear ozone chemistry, directly calculating the contribution of emission sectors to ozone is not possible. For this purpose, detailed chemistry-climate models are required. In my dissertation, I examine the contributions of different emission sectors to ground-level ozone in Europe and East Asia. I utilise the MECO(n) model system, which comprises a global and regional model. The latter allows for high-resolution analysis of specific regions. The model employs a tagging method to calculate the contributions of various emission sources to ozone. Two simulations, each with two regional refinements for Europe and East Asia, are conducted over a span of 2 years, at resolutions of 50 and 12 km. The model results are evaluated using satellite data, air quality station data, data from two flight campaigns in Europe and Asia, and ship-based MAX-DOAS measurements over the Chinese Sea. Several regions in Europe and East Asia with large anthropogenic emissions are compared with one another, as well as with rural areas. The absolute contributions of regional anthropogenic emissions to ground-level ozone in the Po Valley, with 20 nmol mol^{-1} (31 %), are larger than in the Benelux region, with 9 nmol mol^{-1} (22 %), for the summer of 2017–2018. Similar results are found for East Asia, where the Pearl River Delta, Yangtze River Delta, and Sichuan Basin exhibit the largest contributions of regional anthropogenic emissions to ground-level ozone, ranging from $25\text{--}40 \text{ nmol mol}^{-1}$ (46–49 %). In some coastal and rural areas of Europe and East Asia, long-range transport contributions to ozone are more important than regional anthropogenic emissions. In heavily polluted regions of Europe and East Asia, ozone titration is large and ozone production is inefficient. In these areas, ozone production is limited by VOCs. In most basins and rural locations, ozone production is rather efficient and NO_x -limited. The Po Valley in Europe and the Pearl River Delta in East Asia have the largest mitigation potential for ground-level ozone by reducing local anthropogenic NO_x and VOC sources, respectively. The effect of different representations of emissions with large uncertainties, such as from biomass burning and biogenic VOCs, on the ozone contributions from anthropogenic emission sources is almost negligible.

Chapter 1

Introduction

1.1 Motivation

Tropospheric ozone (O_3) is a strong greenhouse gas [Myhre et al., 2013] and an air pollutant, with a potentially significant risk to human health, explicitly on the respiratory system. Additionally, it has the potential to cause damage to plants and ecosystems [WHO, 2006, Jimenez-Montenegro et al., 2021]. The subsequent pollution-related illness and chronic diseases contribute to around 365,000 premature deaths every year globally [Global Burden of Disease Collaborative Network, 2021]. It is able to reduce annual yields of soy, wheat, and rice up to 15% [Wang et al., 2022, Pei et al., 2023]. Furthermore, as about 30% of carbon dioxide (CO_2) emissions are stored in the world's ecosystems [IPCC, 2022], tropospheric O_3 doubles its climate impact by harming plants and reducing their capacity to absorb CO_2 [Tai et al., 2021]. Tropospheric O_3 is radiatively active in the shortwave and longwave spectra and contributes to global warming, making it the third most powerful anthropogenically influenced greenhouse gas [Skeie et al., 2020, IPCC, 2014]. On the other hand, stratospheric O_3 functions differently and plays a vital role in safeguarding ecosystems and human health against harmful ultraviolet radiation.

Since tropospheric O_3 does not have direct emission sources, it forms when sunlight interacts with various air pollutants, known as ozone precursors. As a result, extreme tropospheric ozone events are most likely to occur during heat waves in highly polluted areas. A reduction in the pollutants contributing to the formation of tropospheric O_3 would be advantageous for both, the climate and human health. Tropospheric O_3 originates from anthropogenic and natural sources. The primary sources of tropospheric O_3 are the downward transport from the stratosphere and the in situ production that occurs when precursor gases, including carbon monoxide (CO), methane (CH_4), nitrogen oxides ($NO_x = NO_2 + NO$), and volatile organic compounds (VOCs) react with each other [Monks, 2005, Haagen-Smith, 1952]. The major anthropogenic precursor sources of tropospheric O_3 are land transport [Mertens et al., 2020a], industry [Ou et al., 2020], and shipping [Jonson et al., 2020]. Typical natural sources of tropospheric O_3 precursors include agriculture [Hui et al., 2023], lightning [Hauglustaine et al., 2001, Schumann and Huntrieser, 2007],

wildfires [Di Carlo et al., 2015], and soil bacteria [Yienger and Levy, 1995, Vinken et al., 2014].

The chemistry of tropospheric O_3 is non-linear, which means that an increase of ozone precursors does not necessarily result in an increase of O_3 formation [Seinfeld and Pandis, 2006]. Larger concentrations of NO_x initially enhance O_3 formation, but beyond a certain threshold, the production decreases and can only be intensified by increasing concentrations of VOCs. These two chemical regimes are called NO_x -limited and VOC-limited, respectively. Since nitrogen oxides are even more harmful to human health and are significant precursors of tropospheric ozone, their presence can greatly impair air quality. Therefore, it is crucial to accurately measure the levels of NO_x , VOCs, and other precursors, however the estimation of anthropogenic emissions, including NO_x and VOCs, and consequently the emission inventories, is subject to significant uncertainties [Logan, 1983, Gschwandtner, 1993, Crippa et al., 2020]. To obtain accurate quantification, it is crucial to gain a better understanding of the underlying processes of both anthropogenic and natural emissions of NO_x and VOCs, as direct measurements are not feasible.

Due to significant global variations in these emissions and incomplete understanding of the processes, particularly related to natural NO_x and VOCs emissions, quantifying them accurately remains challenging. Instead, emission fluxes must be parameterised, which is challenging, as there is often insufficient data to accurately represent these processes in models. Consequently, this approach leads to significant uncertainties [Yienger and Levy, 1995, Tost et al., 2007, Mebust et al., 2011, Vinken et al., 2014]. For example, biomass burning emissions in chemistry-climate models come with large uncertainties due to inadequate representation of pyro-convection and small-scale patterns [e.g., Pan et al., 2020]. The same applies to biogenic VOC emissions, which depend on ambient meteorological conditions and introduce significant uncertainties in chemistry-climate models [e.g., Guenther et al., 1995, Simpson et al., 1995, Li et al., 2020a]. To reduce these uncertainties, new representations of biomass burning emissions and biogenic VOC emissions are necessary and are applied within this study.

This is also important for accurately estimating the effect of these emissions on tropospheric ozone. The non-linear chemistry of tropospheric O_3 makes it challenging to directly estimate the contribution of various ozone precursors. To achieve this, a numerical model based source apportionment method can be employed, where two distinct approaches are available: the perturbation method and the attribution method, depending on the specific scientific question to be addressed (Grewe [2004], Mertens et al. [2020b]; see their Table 1). The perturbation method estimates changes in ozone resulting from either a reduction or an increase in emissions from a particular sector. This is done by comparing the results of an unperturbed simulation with those of a simulation in which emissions have been altered (sensitivity analysis). The difference between the two simulations is referred to as the impact. The source attribution method, on the other hand, breaks down the budgets of ozone and ozone precursors from various emission sources to determine their share to overall ozone (referred to as contribution).

The present study aims to identify the primary precursors responsible for ozone formation and assess their mitigation potential in order to develop effective ozone mitigation

strategies. Europe and Asia are among the most polluted regions in the world, particularly during summer, providing ideal conditions for the formation of tropospheric O_3 . Consequently, both continents are well-suited for a comprehensive analysis of the contributions of various emission sectors to O_3 in order to assess their potential for mitigation. Several investigations have utilised the perturbation method to assess the impact of land transport emissions on tropospheric ozone. Granier and Brasseur [2003] employed a Chemical Transport Model (CTM) to assess the impact of land transport emissions with the perturbation approach. They discovered that road traffic emissions in Europe have a significant influence on surface-level ozone during summer months. Likewise, Han et al. [2019] utilised the perturbation method and differentiated between impacts from long-range transported and regional emissions on tropospheric O_3 in East Asia. They showed that three-quarters of the foreign ozone of anthropogenic origin comes from North-America, Europe and South Asia, and has a substantial impact on surface ozone in East Asia. Wang et al. [2019] conducted a sensitivity analysis for China and investigated the source contributions of surface ozone. They revealed that the transport sector dominates relative contributions to O_3 in South China, North China, and the Yangtze River Delta, while local sources contribute to O_3 pollution in the Pearl River Delta and the Beijing-Tianjin-Hebei region. Dahlmann et al. [2011] utilised a source attribution approach to compute the contribution of NO_x emission sources from different sectors to ozone levels. Their findings indicate that anthropogenic sources, such as road traffic, ships, and industries, are the primary contributors to tropospheric ozone in the northern mid-latitudes. Mertens et al. [2020b] investigated ozone contributions from land transport precursors in Europe and Germany and discovered that land transport emissions play a critical role in periods with high ozone values, particularly in the Po Valley and western Germany. Li et al. [2012] employed an ozone source attribution technique to distinguish between regional and long-range transported emissions' contributions in the Pearl River Delta in China. They emphasised the necessity of utilising regional models in conjunction with source attribution approaches to accurately represent emission gradients in urban areas. Liu et al. [2020] summarised the current state of research on ozone apportionment methods for China and reported that land transport and industrial emissions are the primary sources contributing to O_3 in China's hotspot regions (as shown in their Table 4).

In general, numerous studies have employed the source attribution method in global and regional chemistry-climate models to investigate the contributions of various emission sectors to tropospheric ozone in Europe and East Asia. However, the present study stands out as the first to use a consistent attribution method by concurrently tagging NO_x and VOCs to investigate ozone contributions in both regions simultaneously. Moreover, it addresses the research gap in separating the contributions of regional and long-range transported emissions, which is essential for evaluating regional mitigation potential.

Thus, my thesis seeks to examine the contributions of regional and long-range transported anthropogenic and biogenic emissions on tropospheric ozone in Europe (EU) and East Asia (EA). Given the high levels of anthropogenic emissions in these two regions, particularly in the polluted areas, I have employed the source attribution method in a global-regional chemistry-climate model to assess ozone contributions from different sources and

regions.

The thesis is organised as follows: Section 2 provides an overview of the theoretical background of the tropospheric ozone chemistry. Section 3 describes the model system and explains the model setup that was used for simulations. In Section 4, simulation results are presented and compared with other model data, air quality station measurements, measurements from the High Altitude and Long Range Aircraft (HALO) research aircraft, as well as satellite data. The results and new findings are discussed in Section 5, with a focus on the major differences between Europe and East Asia. Section 6 includes a sensitivity study, which investigates the effect of different representations of biomass burning and biogenic VOC emissions on the anthropogenic O_3 contributions. Section 7 answers the scientific questions and gives an outlook on further investigation strategies.

1.2 Scientific Questions

The scientific questions that motivated this thesis are specified as follows:

- Q1: How do various emission sectors contribute to ground-level NO_y and O_3 in Europe and how does this differ in comparison to East Asia?*
- Q2: How large are the contributions from regional emissions compared to the contributions from long-range transported emissions to ground-level O_3 in Europe and how does this differ in East Asia?*
- Q3: How does the O_3 chemistry differs between Europe and East Asia?*
- Q4: How robust are the simulated anthropogenic O_3 contributions in the MECO(n) model when the previous implementations of emissions from biomass burning and biogenic VOC emissions are replaced with improved representations of these processes?*

1.3 Investigation Strategy

To address the research questions of the current thesis, I utilised the MECO(n) (“MESSy-fied ECHAM and COSMO models nested n-times”) model system, which involves an online nesting of the regional chemistry-climate model COSMO-CLM/MESSy (“Consortium for Small-scale Modeling-Climate Limited-area Modelling/Modular Earth Submodel System”) into the global chemistry-climate model EMAC (ECHAM5/MESSy Atmospheric Chemistry). This model system, which incorporates a detailed chemistry setup, was previously introduced by Kerkweg and Jöckel [2012].

Two different model setups, each with three instances were used, including one global EMAC instance and two COSMO-CLM/MESSy instances that cover Europe and East Asia with resolutions of 50 km (CM50) and 12 km (CM12), respectively. The model system is equipped with a source attribution method (tagging) for calculating the contributions

of different precursor emission sectors and regions to ozone Grewe et al. [2017]. Before application of the model to answer the scientific questions, the model is first evaluated using various observational data. Next, the NO_y and O_3 contributions from various emission sectors are compared within Europe and East Asia by defining different study areas. These study areas are selected based on their geographical location, climate zone (maritime, continental, or topography), and level of pollution. The evaluation is followed by a comparison between Europe and East Asia, with a focus on comparing the contributions of long-range transported and regional emissions to O_3 . In a subsequent step, a sensitivity study investigates the effect of different representations of biomass burning and biogenic VOC emissions in the MECO(n) model on the anthropogenic O_3 contributions.

Chapter 2

Background

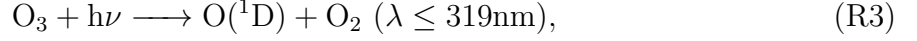
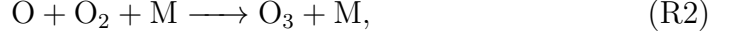
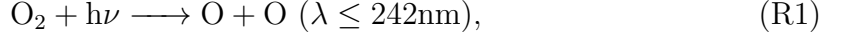
The primary focus of this chapter is to provide an overview of the key background information, specifically regarding the chemistry of tropospheric O_3 . The content is mostly based on Monks [2005], Seinfeld and Pandis [2006], and Fowler et al. [2008], the reactions are taken from Seinfeld and Pandis [2006].

2.1 Tropospheric and stratospheric ozone

The majority (90 %) of atmospheric ozone is located in the stratosphere, typically between 15 and 30 km altitude, where it forms the so-called ozone layer [Seinfeld and Pandis, 2006]. The ozone layer, found in the stratosphere, contains high concentrations of ozone, which absorb most of the ultraviolet radiation. The remaining 10 % of ozone is located in the troposphere [Crutzen, 1973, 1974].

Ozone is radiatively active in both, the shortwave and longwave spectra, making it an important greenhouse gas. Radiative forcing (RF) is a measure to evaluate the impact of different forcing agents on the climate. It quantifies how much a forcing agent alters the energy balance within the Earth-atmosphere system [IPCC, 2007]. According to the Intergovernmental Panel on Climate Change (IPCC) sixth assessment report (AR6) [IPCC, 2022], ozone is the third strongest anthropogenic (secondary) greenhouse gas with a total RF of 0.47 W m^{-2} in 2019 relative to the pre-industrial atmosphere in 1750 [Skeie et al., 2020].

In 1930, British scientist S. Chapman proposed that ozone is continually produced in the atmosphere by a cycle initiated by the photolysis of oxygen (O_2), which partially explains the ozone layer [Seinfeld and Pandis, 2006]. It describes the equilibrium between ozone production and dissociation in the upper stratosphere. The equilibrium is sustained by the following reactions, where M denotes a molecule (N_2 or O_2) acting as a third collision partner to remove the decomposition energy generated during the reaction and keeping the momentum balance [Seinfeld and Pandis, 2006]:



where h denotes the Planck's constant, which gives the relationship between the energy of a photon and its frequency ν . Hence, the product $h\nu$ represents the energy of a photon at a specific frequency. An O_2 molecule will dissociate into two oxygen atoms (R1) when it absorbs the energy of a photon ($h\nu$) with a wavelength of 242 nm or shorter. These atoms can react with another oxygen molecule to form ozone (R2). However, ozone is also prone to destruction by photochemical processes. The bond energy of one ozone molecule corresponds to a 319 nm photon, which can break apart the molecule into an excited oxygen atom and a molecule of oxygen (O_2) (R3). Alternatively, atomic oxygen can react with ozone to form two molecules of oxygen (R4), which also leads to depletion of ozone in the atmosphere. Chapman's theory assumed an excessive amount of O_3 in the stratosphere because he suggested that only sunlight was responsible for ozone breakdown.

In reality, other chemical reactions and processes also contribute to ozone depletion. In 1970, Crutzen [1972] and Molina and Rowland [1974], investigated the depletion of stratospheric ozone by nitrogen oxide and chlorine, due to a catalytic effect. These catalytic cycles contribute to the depletion of stratospheric ozone, which is mostly dominated by the catalysts OH, NO, Cl and Br [McElroy et al., 1992, Seinfeld and Pandis, 2006] as follows:



where X denotes the catalysts (OH, NO, Cl or Br), which deplete stratospheric O_3 .

The chemistry of ozone in the troposphere differs from that in the stratosphere. Ozone is not directly emitted by human activities, but it is primarily produced by anthropogenic and natural precursors, such as NO_x , CO and VOCs, which are gases that can react with sunlight and other compounds in the atmosphere to form ozone. VOCs encompass a broader range of compounds, such as methane (CH_4), ethane (C_2H_6), propane (C_3H_8), isoprene (C_5H_8), formaldehyde (CH_2O) and many more [Seinfeld and Pandis, 2006]. More details on these processes are provided in the next section.

Unlike in the stratosphere, tropospheric ozone poses a risk to human health and damages plants [Thurston, 2017]. According to guidelines published by the World Health Organization (WHO), adverse health effects occur at ozone concentrations above $70 \mu\text{g m}^{-3}$

[World Health Organization, 2021]. High ozone concentrations are typically found in major polluted areas during hot and sunny days. In the European Union, the alert threshold for ground-level O_3 over an 8-hour mean is $120 \mu\text{g m}^{-3}$. This measure is called maximum daily 8-hour average ozone (MDA8) and is calculated as the daily maximum of the 8-hour rolling mean of the O_3 concentration. It is a widely used standard because it captures the average exposure of people to ozone over a significant portion of the day. When this threshold is exceeded, heavy outdoor exertion should be restricted to prevent damage to the respiratory system [Fowler et al., 2008, World Health Organization, 2021]. In section 2.2, an explanation of the chemical production and destruction of tropospheric ozone is provided, along with an explanation of why high ozone concentrations occur during hot and sunny days in major polluted areas.

2.2 Chemical production and destruction of tropospheric ozone

The dominant contributors to in situ tropospheric O_3 production are NO_x , CO and VOCs. The ozone formation starts with the presence of NO_2 in sunlight, where photolysis of NO_2 occurs at wavelengths $\leq 424 \text{ nm}$ with a rate j_{NO_2} :



followed by Reaction R2. Following the production of O_3 , it reacts with NO with the rate coefficient k_{R9} in order to regenerate NO_2 [Seinfeld and Pandis, 2006]:



As long as no other reactions than the photochemical NO_x cycle (R8, R2 and R9) take place, the chemical system will reach a point where NO_2 is continuously formed and destroyed until a steady state is reached [Seinfeld and Pandis, 2006]. In this state the concentrations of O_3 , NO and NO_2 depend on the efficiency of the NO_2 photolysis, which is represented by j_{NO_2} and by the rate coefficient k_{R9} :

$$[O_3]^1 = \frac{j_{NO_2}[NO_2]}{k_{R9}[NO]}, \quad (2.1)$$

This cycle will maintain a steady-state concentration of O_3 , which is directly proportional to the ratio of NO_2/NO [Seinfeld and Pandis, 2006]. Leighton [1961] rearranged equation

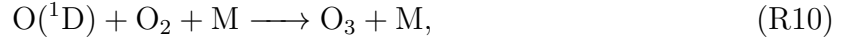
¹In this thesis, the concentration of a species is represented by brackets, otherwise it is a mixing ratio.

2.1 and introduced the Leighton ratio (ϕ), which is the ratio between the primary ozone production and destruction and thus a measure for the deviation from the steady state. It is defined as

$$\phi = \frac{j_{\text{NO}_2}[\text{NO}_2]}{k_{\text{R9}}[\text{NO}][\text{O}_3]}. \quad (2.2)$$

The Leighton ratio is around 1, when the concentration of O_3 is in a photostationary state. Leighton ratios greater than 1 result from additional pathways, such as the conversion of NO to NO_2 in the presence of peroxy radicals (e.g. RO_2) or other reactions that deplete O_3 besides reaction R9 [Leighton, 1961, Chate et al., 2014]. Small Leighton ratios (< 1) may indicate significant local emissions of NO , because here O_3 can be titrated by NO , which perturbs the steady-state of O_3 .

Tropospheric O_3 is not only destroyed by chemical reactions but also by direct photolysis (as shown in reaction R3), which forms one oxygen molecule and one excited singlet ($\text{O}(^1\text{D})$) oxygen atom [Seinfeld and Pandis, 2006]. The excited oxygen atom has two reaction pathways, firstly it can rapidly react with O_2 to reform O_3



or secondly it collides with a water molecule and forms two OH radicals:



OH is a radical and is the primary oxidizing agent due to its high reactivity towards other molecules [Seinfeld and Pandis, 2006]. The formation of OH by reaction R11 is enhanced with increasing humidity as more water vapour becomes available to react with the singlet oxygen atom. Radicals are highly reactive and short-lived molecules or atoms that contain at least one unpaired valence electron. They typically last for only a few seconds [Hayyan et al., 2016]. The photolysis of ozone, as described above, is the primary source of OH in the troposphere. The global mean concentration of OH is about 10^6 molecules cm^{-3} during daylight hours [Seinfeld and Pandis, 2006].

Next to the photolysis of O_3 , it is depleted chemically by the reactions with OH , the hydroperoxyl radical (HO_2), and by other peroxy radicals (RO_2) as follows:



Peroxy radicals, including HO_2 , RO_2 and the alkoxy radical (RO), where R is any organic group, are important tropospheric photochemical species having a critical role in tropospheric ozone formation [Hornbrook et al., 2011].

Next to the importance of NO_x in forming ozone, CO is a significant air pollutant that plays also a crucial role in the formation of ozone. The atmospheric oxidation of CO shows many key-features of much more complex organic molecules, but belongs to one of the simplest compound in the tropospheric chemistry [Seinfeld and Pandis, 2006]. Since, CO is representative for other molecules, an overview about its role in the troposphere is given. CO undergoes a reaction with the hydroxyl radical OH, leading to the formation of carbon dioxide (CO_2):



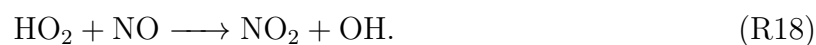
The atomic hydrogen reacts further to form a hydroperoxyl radical HO_2 :



Thus, reactions R15 and R16 can be combined to:

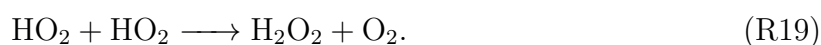


The presence of an additional H atom weakens the O-O bond in O_2 , making the HO_2 radical more reactive than O_2 [Seinfeld and Pandis, 2006]. In the presence of NO, the most important reaction of HO_2 is:

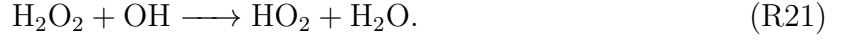


Now the product of reaction R18 NO_2 participates in the photochemical NO_x cycle, represented by reactions R8, R2 and R9.

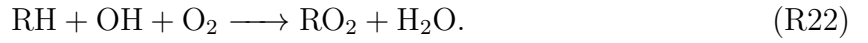
Additionally the HO_2 radical reacts with itself to produce hydrogen peroxide (H_2O_2), which is an important sink for HO_x [Monks, 2005]:



H_2O_2 acts as a temporary reservoir for HO_x and is photolysed and reacts with OH:



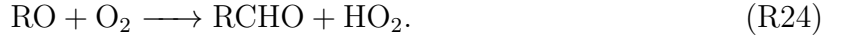
Next to CO, the troposphere contains a variety of VOCs, which are predominantly oxidised by OH and are important for O_3 formation. Similar to CH_4 , the reaction of OH with hydrocarbons (RH) produces the alkyl peroxy radical (RO_2):



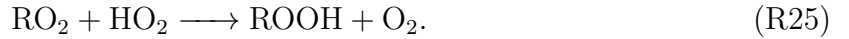
The alkyl peroxy radical RO_2 reacts with NO:



Again, NO_2 participates in the photochemical NO_x cycle as explained above. Then the alkyl radical (RO) reacts with O_2 :



The HO_2 radical reacts with NO to regenerate OH (see reaction R18). Reaction R18 is terminated by R19 because it removes HO_2 from the system. The reaction of RO_2 with NO (R23) is terminated by the following reaction:



The reaction chain is terminated, when OH and NO_2 form the meta-stable reservoir gas nitric acid (HNO_3):



which removes NO_x and HO_x (OH and HO_2) from the system. The reservoir species HNO_3 is taken up by cloud droplets and precipitation, and subsequently washed out from

the troposphere and transported to the surface.

The rapid cycling of OH and HO₂ results in a steady-state of OH/HO₂, which relies on the NO_x level [Seinfeld and Pandis, 2006]. The photolysis process drives the NO_x cycle, and the partitioning between NO and NO₂ is mainly controlled by the photostationary state relation (Equation 2.2; Seinfeld and Pandis 2006). The atmospheric chemistry of NO_x and CO has shown that the formation of ozone in the atmosphere involves a competition of HO_x around NO_x (R18) and VOCs (R22), which is crucial for the chemical reactions that lead to ozone formation.

2.2.1 Non-Linearity of ozone production

Sillman [1999] stated that ozone formation through NO_x follows a nearly linear process at first, but at a certain point, it transitions to a non-linear process that depends on the mixing ratio of VOCs. Figure 2.1 presents the rate of ozone production (nmol mol⁻¹ h⁻¹) as a function of NO_x and VOC mixing ratios, shown by the isopleths. When the ratio of VOCs to NO_x mixing ratios is high, OH primarily reacts with VOCs. Conversely, when the ratio is low, NO_x dominates the reaction with OH [Seinfeld and Pandis, 2006]. In the so-called NO_x limited regime, the rate of O₃ formation increases with an increasing NO_x mixing ratio, but is independent of the VOC mixing ratio [Seinfeld and Pandis, 2006]. In this regime, the O₃ formation is only limited by NO_x.

When the ratio of NO_x:VOC reaches a certain value, OH reacts with VOCs at an equal rate. At a specific mixing ratio of VOC, there is a NO_x mixing ratio along this “ridge line” where the maximum amount of O₃ is produced. This threshold represents the optimal VOC:NO_x ratio for efficient O₃ formation, and the white line in Figure 2.1 shows this threshold between the NO_x-limited and the VOC-limited chemical regimes.

In a VOC-limited regime, the abundance of NO_x is large, and OH mostly reacts with NO₂. This reduces the production of O₃ by decreasing the amount of NO₂ available for photolysis. Every additional VOC increases the probability of a reaction of OH with VOC. In the case where OH-VOC reactions are dominant, new radicals are generated through photolysis from intermediate products, which results in an increase in the production of O₃. In the VOC limited regime, increasing the mixing ratio of VOC leads to an increase in O₃ formation, but increasing the NO_x mixing ratio has the opposite effect and decreases O₃ formation.

Since, reactions R2, R8 and R9 are catalytic and do not consume any NO_x molecules, one NO_x can undergo multiple oxidation cycles and produce several O₃ molecules before it is removed from the troposphere by reaction R26 or deposition as explained above [Seinfeld and Pandis, 2006]. To evaluate this oxidation cycles, which are responsible for atmospheric ozone formation, a useful metric is the ozone production efficiency (OPE) [Seinfeld and Pandis, 2006]. Assuming HO_x is in a steady-state (R18), the balance OPE can be defined as the number of cycles in which a NO_x molecule participates in the production of O₃ before it is eliminated through chemical loss. The production rate of O₃ can be written as (see R18)

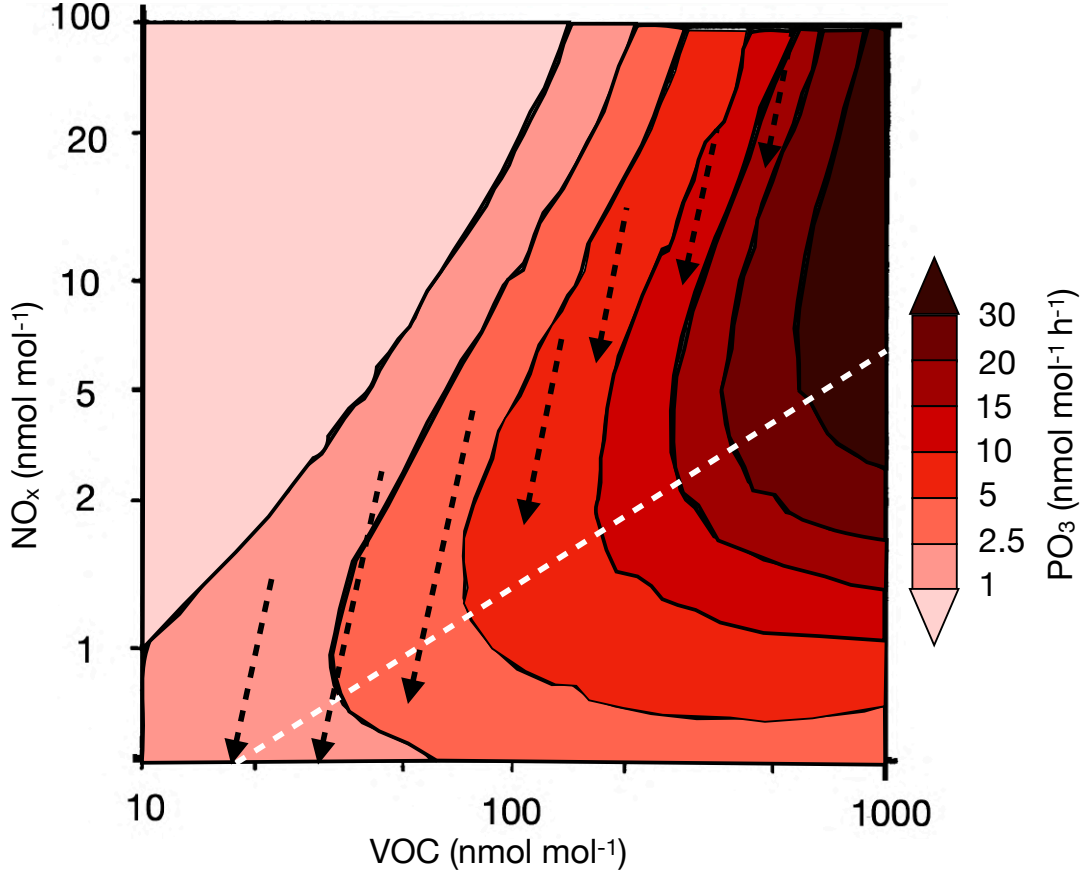


Figure 2.1: Isopleths show the net rate of O_3 production (P_{O_3} in $\text{nmol mol}^{-1} \text{h}^{-1}$, solid lines) as a function of mixing ratios of VOCs as amount of carbon (nmol mol^{-1} , carbon) and NO_x (nmol mol^{-1}) for mean summer daytime meteorology and clear sky. The white dashed line shows the threshold between 'NO $_x$ ' (below) - and 'VOC-limited' (above) ozone production. The black dashed lines and arrows show the calculated evolution of VOC and NO_x mixing ratios in a series of air parcels over an 8 h period (during daytime, adopted after Sillman [1999]).

$$P_{O_3} = 2 \cdot k_{R18}[\text{HO}_2][\text{NO}]. \quad (2.3)$$

The loss rate of NO_x (see R26) is defined as

$$L_{\text{NO}_x} = k_{R26}[\text{OH}][\text{NO}_2]. \quad (2.4)$$

Thus, the OPE can be calculated as follows

$$\text{OPE} = \frac{P_{O_3}}{L_{\text{NO}_x}} = \frac{2 \cdot k_{R18}[\text{HO}_2][\text{NO}]}{k_{R26}[\text{OH}][\text{NO}_2]}, \quad (2.5)$$

which means, that OPE is largest for large NO and small NO₂ concentrations and vice versa. At sufficiently high NO_x concentrations (and low VOC concentrations) the chain is terminated by reaction R26 and this condition is called VOC-limited. If the abundance of HO₂ exceeds that of NO_x, reaction R19 terminates the reaction chain, as it perturbs the assumed OH/HO₂ ratio which assumes that all HO₂ reacts with NO [Seinfeld and Pandis, 2006]. So far, the focus has been on daytime, thus the following section highlights the most significant differences of the O₃ chemistry between day- and nighttime.

2.2.2 Chemistry of O₃ during daytime and nighttime

During daytime, NO and NO₂ interconvert by the photochemical NO_x cycle (reactions R8, R2 and R9) [Seinfeld and Pandis, 2006]. The steady state of the [NO]/[NO₂] ratio is then defined as shown in Equation 2.2. The removal path of NO_x during daytime is reaction R26. Seinfeld and Pandis [2006] assumed surface conditions of 300 K and 1 atm, a rate coefficient k_{R26} of 1×10^{-11} cm³ molecules⁻¹ s⁻¹ and an [OH] concentration of $\approx 10^6$ molecules cm⁻³ in the troposphere with vertical uniform O₃ mixing ratio. Based on this they calculated a lifetime of ground-level NO_x during daytime of 1 day, assuming a constant vertical photolysis of NO₂. At the surface the [NO]/[NO₂] ratio is smaller 1, at 10 km it increases up to 12. This increase is caused by two factors. Firstly, the rate coefficient k_{R9} is temperature-dependent, and a decrease in temperature leads to a decrease of k_{R9} and slows down the return of NO to NO₂. Since the concentration of O₃ decreases with height because the number concentration of air decreases [Seinfeld and Pandis, 2006], it slows down the rate of reaction R9. As explained above, the lifetime of ground-level NO_x is around 1 day and increases with altitude up to 2 weeks in the upper troposphere because most of the NO_x family exists as NO, and the net removal of NO₂ by OH is slowed down [Seinfeld and Pandis, 2006].

During nighttime, the chemistry of the NO_x family is completely different as there is no photolysis of NO₂. The balance between reaction R9 and the photolysis of NO₂ during the day is disrupted after sunset. As a result, all NO reacts rapidly with O₃, leading to the conversion of almost all NO_x to NO₂. This chemical loss of O₃ is called ozone titration, and also takes place during daytime in the vicinity of strong emission sources of NO. NO₂ further reacts with O₃ to form the NO₃ radical as:



This reaction is the only direct source of the nitrate radical (NO₃). In urban plumes at night, NO₃ mixing ratios reach a few hundred parts per trillion (ppt), values up to 40 ppt are common in remote areas [Seinfeld and Pandis, 2006]. During daytime NO₃ is photolysed back to NO or reacts to:



Again, the photolysis of NO_2 (R8) forms NO , which in turn reacts to produce O_3 (R9). During night NO_3 reacts with NO_2 to form N_2O_5



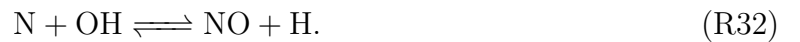
where afterwards N_2O_5 can thermally decompose back to NO_2 and NO_3 .

2.3 Sources of NO_x , CO and VOCs

“Primary source” typically refers to a physical or chemical process or type of activity, which causes emissions of a substance into the atmosphere. Since there is no primary source of O_3 , it is only chemically produced in the atmosphere. Only its precursors do have primary emissions. In order to keep it simple, in this thesis sources are defined as primary sources. For example, a source of ozone precursors could be a coal-fired power plant, a vehicle, or an industrial process. “Sector”, on the other hand, generally refers to a broader category of activities that generate emissions. Land transport, anthropogenic non-traffic (e.g. industry, households and energy sector) and shipping are important emission sectors of anthropogenic ozone precursors. Natural O_3 precursors, arise from lightning and soil processes. Biomass burning can be attributed to either man-made fires or natural events that trigger them.

Table 2.1 presents an overview of the annual global totals for the most significant emission sectors of NO_x , CO, and VOCs in Tg a^{-1} .

The data in Table 2.1 arise primarily from the Community Emissions Data System (CEDS) for the year 2017, as reported by McDuffie et al. [2020]. While the estimates have some uncertainty, the purpose here is to provide an approximation of global annual totals. The results show that land transport emissions are the most significant anthropogenic source of global NO_x , accounting for 10.4 Tg a^{-1} . The energy sector (8.2 Tg a^{-1}) and shipping sector (7.6 Tg a^{-1}) are the next most significant anthropogenic sources of NO_x . NO_x is primarily formed thermally, which occurs through various pathways. Here, the extended Zeldovich mechanism is explained, which describes the production of NO_x via thermal means [Zeldovich and Semenov, 1946, Lavoie et al., 1970]:



Reactions R30 and R31 convert N and N_2 into NO, respectively, a process that is highly dependent on temperature. This is because breaking the strong triple bond in N_2 and the

Table 2.1: Global totals of the ozone precursors NO_x, CO and VOCs in Tg a⁻¹ from the literature. The NO_x emissions are given in amount of nitrogen, CO in amount of CO, and the VOC emissions are given in amount of carbon. Industry includes all economic activities related to the extraction, production, and manufacturing of goods and services, such as mining, manufacturing, and construction. Commercial includes all activities related to the sale and provision of goods and services, such as retail stores, office buildings, and restaurants.

Sector	NO _x (Tg N a ⁻¹)	CO (Tg CO a ⁻¹)	VOCs (Tg C a ⁻¹)	Reference
Aviation	0.7		0.5	Terrenoire et al. [2022]
Land Transport	10.4	175	33	McDuffie et al. [2020]
Energy	8.2	53	63	McDuffie et al. [2020]
Solvents			28	McDuffie et al. [2020]
Waste	0.6		3	McDuffie et al. [2020]
Industry	5.8	75	12	McDuffie et al. [2020]
Residential	1.2	185	31	McDuffie et al. [2020]
Commercial	1.2	20		McDuffie et al. [2020]
Agricultural waste burning	0.2	19	2.0	Lamarque et al. [2010]
Agriculture	1.5			McDuffie et al. [2020]
Shipping	7.6	30	4	McDuffie et al. [2020]
Biogenic			440–660	Guenther et al. [2006]
Biomass burning	5.1–7.5	438–568	29–40	Jain et al. [2006]
Soil	4.0–15.0			Vinken et al. [2014]
Lightning	2.0–8.0			Schumann and Huntrieser [2007]

double bond in O₂ requires a significant amount of energy, which is only available at high temperatures.

Combustion processes run in various applications, including gasoline and diesel engines, industrial boilers and furnaces that burn fossil fuels like coal or natural gas, and gas turbines [Elliott, 1958]. These processes involve high temperatures (and pressures), which promote the formation of NO_x. In nature, biomass burning during wildfires forms NO_x as well (5.1–7.5 Tg a⁻¹). These emissions are transported upwards, and the produced heat enhances pyro-convection, enhancing the upward transport. Wildfire plumes can reach heights of up to 4.5 km or higher, depending on the location, such as in North America [Dentener et al., 2006]. This can intensify the formation of O₃ towards the middle troposphere.

Lightning strikes are another significant source of NO_x (2–8 Tg a⁻¹), in addition to combustion processes. Lightning-induced NO_x (LNO_x) emissions result from the dissociation of O₂ and N₂ in the extremely hot lightning channel [Schumann and Huntrieser, 2007, Grewe, 2008]. Following a lightning return stroke, which can generate temperatures of up to 30000 K, the channel cools down to 3000–4000 K due to expansion, radiation, and conduction, and LNO_x is formed [Zeldovich and Raizer, 2002, Schumann and Huntrieser, 2007]. LNO_x is mostly produced during convective thunderstorms in the upper troposphere.

Soil bacteria are one of the major natural sources of NO_x (4–15 Tg a⁻¹). Soil NO_x is primarily generated by microbial activity in a complex set of interactions involving soil nitrogen content and anthropogenic fertiliser rates [Hudman et al., 2012]. The bacteria

in the soil absorb energy during the nitrification of ammonium (NH_4^+) to nitrite (NH_2^-) and nitrate (NH_3^-) [Norton and Ouyang, 2019]. The emissions of soil NO_x are determined by the soil temperature, biome type, and soil moisture [Yienger and Levy, 1995]. High temperatures and wet conditions increase microbial activity, affecting soil NO_x emissions. Pulsing, which occurs when a very dry soil becomes wet, results in a sudden reactivation of water-stressed bacteria and enhances the emission of soil NO_x . Many bacteria and plants emit also VOCs, what makes the biosphere the dominant source of global VOC emissions (440–660 Tg a^{-1}). Isoprene (C_5H_8) is the major contributor to biogenic VOC emissions, as reported by Pacifico et al. [2010]. At the cellular level, the emissions of C_5H_8 are predominantly regulated by factors such as light [Loreto and Sharkey, 1993], temperature [Guenther et al., 1993], and the concentration of CO_2 [Monson et al., 2007]. Light and high temperatures increase isoprene emissions up to an optimum at around 40 °C [Niinemets et al., 1999]. Pacifico et al. [2009] investigated that high CO_2 concentrations inhibit isoprene emissions, while low CO_2 concentrations enhance the emission of C_5H_8 [Pacifico et al., 2010]. In addition to biogenic VOC emissions, VOCs are also emitted by anthropogenic sectors, such as energy (63 Tg a^{-1}), land transport (33 Tg a^{-1}), and solvents (28 Tg a^{-1}). These emissions are mostly caused by incomplete combustion processes and are one order of magnitude lower than the biogenic VOC emissions, which make up 90% of global emissions.

The most significant contributors to anthropogenic CO emissions are the residential (185 Tg a^{-1}), including homes and buildings with all household activities, land transport (175 Tg a^{-1}), industry (75 Tg a^{-1}), and shipping (30 Tg a^{-1}) sectors. However, biomass burning is responsible for the largest amount of CO emissions, with a global annual total of 438–568 Tg a^{-1} . In the following section the global abundance of tropospheric O_3 caused by these precursors is described.

2.4 Ozone budget of the troposphere

Next to the in situ production of tropospheric O_3 by its natural and anthropogenic precursors, it originates from the downward transport from the stratosphere. Dry deposition serves as significant sink for tropospheric ozone, whereas wet deposition is less important. Hu et al. [2017, their Table 3] compared the global ozone burden across various studies and they reported 300–351 Tg. The most recent study by Archibald et al. [2021] estimated a global tropospheric ozone burden of (315 ± 27) Tg.

An overview of the tropospheric O_3 budget with data from Young et al. [2013] is presented in Figure 2.2. According to Young et al. [2013], the chemical production of tropospheric O_3 is (4880 ± 850) Tg a^{-1} , with a relatively high uncertainty of ± 17 %. The stratosphere-to-troposphere exchange contributes 10 % to tropospheric O_3 , with (480 ± 100) Tg a^{-1} . However, the uncertainty in this case is even larger with ± 21 %, as the stratosphere-to-troposphere exchange is a complex process [Meloan et al., 2003]. The complexity of stratosphere-to-troposphere transport of ozone arises from the interaction between chemical processes and dynamic factors, including large-scale transport such as

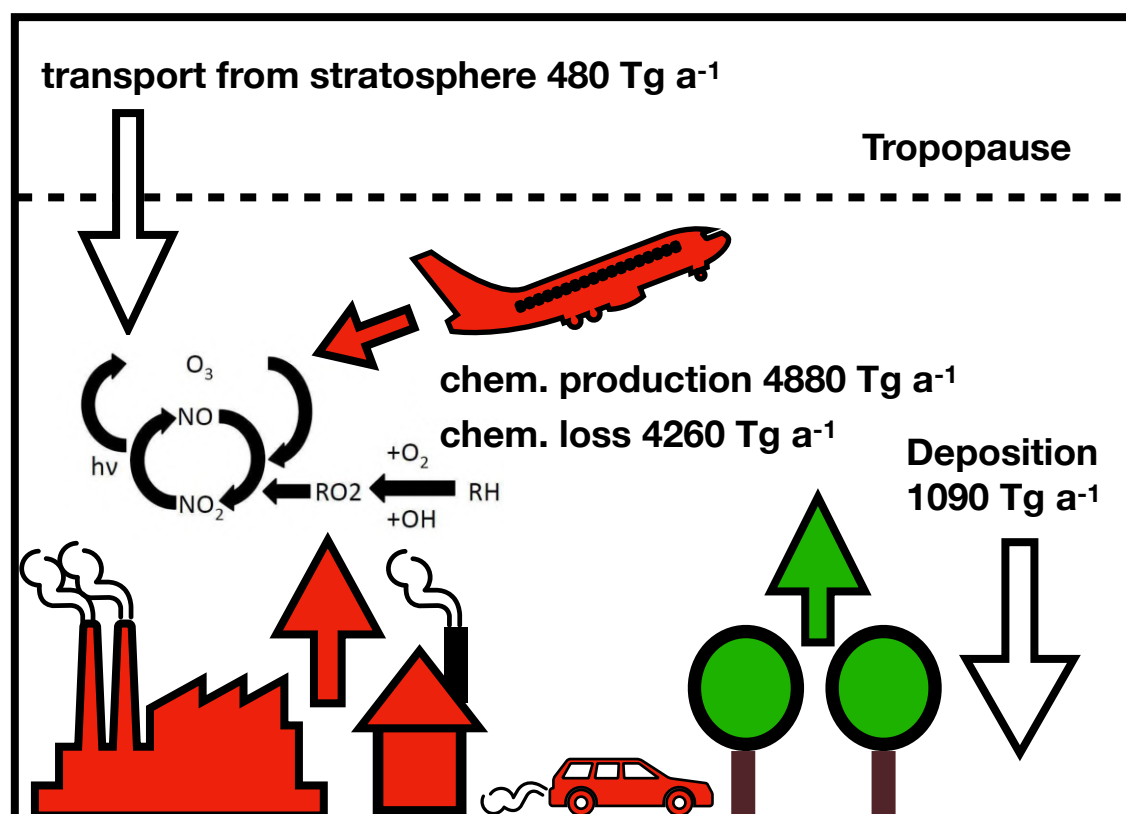


Figure 2.2: Illustration of the tropospheric O_3 budget (adopted after Mertens 2017). The coloured arrows indicate emissions of precursors from which O_3 is formed from anthropogenic (red) or natural (green) sources. Numbers are according to Young et al. [2013]. Details about the uncertainties are given in the text.

the Brewer-Dobson circulation, as well as small-scale atmospheric waves and turbulence. Additionally, the large O_3 gradient between the troposphere and stratosphere means that even small amounts of transport can lead to significant changes in tropospheric ozone concentrations.

The sink of tropospheric O_3 by chemical loss is estimated to be $(4260 \pm 650) \text{ Tg a}^{-1}$. Chemical production and destruction are the largest sources and sinks of tropospheric O_3 . Both processes are mostly driven by natural and anthropogenic pollutants such as NO_x and VOCs, as well as photolysis caused by sunlight (explained in previous section 2.1).

About $(1090 \pm 260) \text{ Tg a}^{-1}$ of tropospheric O_3 is lost through dry deposition, which occurs via turbulence and downward transport to the surface. Ozone is deposited by stomatal uptake [Rich et al., 1970], leaf cuticles uptake [Rondón et al., 1993], and by contact with soil [Garland and Penkett, 1976], snow [Helmig et al., 2007], and man-made surfaces [Shen and Gao, 2018]. Surfaces with high roughness, such as vegetation, cause high deposition rates, while plain surfaces like snow and water cause lower rates but are still important in the tropospheric ozone budget [Clifton et al., 2020].

Wet deposition, on the other hand, occurs when a species is taken up by cloud water

or precipitation and transported downwards. However, since O_3 is not very soluble, dry deposition is the dominant deposition process for tropospheric O_3 [Seinfeld and Pandis, 2006].

2.5 Perturbation and Source Attribution Methods

Due to the non-linear nature of ozone chemistry (see section 2.2.1), direct estimation of the contribution of precursors from different sectors or regions to ozone is not possible. The use of numerical models is essential for this purpose. To estimate the impact of various emission sectors on tropospheric ozone, two methods can be employed: the perturbation method and the source attribution method, as elucidated by [Wang et al., 2009].

The perturbation method is employed to evaluate emission control scenarios aiming to achieve air quality or climate change objectives, requiring knowledge of the atmospheric concentration sensitivity to emissions [Grewe et al., 2010]. This method estimates changes in ozone levels resulting from either a reduction or an increase in emissions from a specific sector. It involves comparing the results of an unperturbed simulation with those of a simulation in which emissions have been altered (sensitivity analysis). The difference between these two simulations is referred to as the impact.

On the other hand, the source attribution method can attribute climate change to specific sectoral emissions, indicating the extent to which these emissions contribute to climate change. This contribution depends on their absolute contributions. The source attribution method breaks down the ozone and ozone precursor budgets from various emission sources to determine their respective shares of the overall ozone concentration.

The difference between both concepts is illustrated in Figure 2.3, where the O_3 concentration in arbitrary units is plotted against NO_x emissions [Grewe et al., 2010]. Please note that, for the sake of simplicity, the basic sketch applies only to a well-mixed, zero-dimensional box model chemistry. The perturbation method involves two simulations, where an emission category (e.g., road traffic) with a base emission of e_0 is perturbed by a factor α , as denoted by the turquoise and pink stars. In this sketch (Fig. 2.3a), the NO_x emissions of a base case (turquoise star) of an emission category are reduced by a factor α to a smaller emission level (pink star). In typical emission scenarios, the base case is perturbed by an α of 5 or 10 %. The line through both simulation points (green) is an approximation of the tangent (dashed line) [Grewe et al., 2010], hence it represents the estimated derivative between the base case and the perturbed simulation. In order to do so, the perturbation method uses the tangent approximation. Out of this, the horizontal red line indicates the arbitrary NO_x emissions change, while the vertical red line represents the ozone contributions caused by the NO_x source, as estimated by the perturbation method.

Conversely, the source attribution method, here called tagging, uses a different approach. The change in the O_3 contribution caused by reduced NO_x emissions is not calculated out of a derivative of two simulations, but the tagging method is based on the origin line to determine the ratio between the change in ozone mass and the emission of NO_x . The tagging method operates under the assumption that all emissions possess the

same ozone formation potential, as evident from the origin line [Grewe et al., 2010]. In simpler terms, molecules with the potential to undergo a specific reaction have an equal probability of undergoing this reaction, regardless of the emission category. This indicates that the breakdown into categories follows a linear relationship (as shown by the dotted origin line) even in situations involving non-linear chemistry (as represented by the dark blue curve) [Grewe et al., 2010]. Overall it breaks down the budget of ozone and ozone precursors into contributions from various emission sectors.

According to Grewe et al. [2010], in the case of a system that is either non-linear or close to linear, the difference between both approaches is minimal if the approximation tangent (green line) and the origin line (dotted line) also only slightly differ (Fig. 2.3a). That means, the horizontal brown line showing an arbitrary NO_x emission and the vertical brown line representing the ozone contributions caused by the NO_x source, estimated by the tagging method, is comparable with the results found by the perturbation method for linear or close-to-linear systems.

However, for non-linear systems, both approaches can lead to larger differences between the estimated derivative (green line) and the origin line (dotted line), as shown in Figure 2.3b.

Therefore, it is crucial to accurately determine the tangent (green line) and evaluate its deviation from the origin line [Grewe et al., 2010]. As demonstrated earlier, it is essential to distinguish between two different questions related to attribution and emission control scenarios, acknowledging that addressing these questions necessitates the use of different methodologies. In a numerical simulation framework, the attribution of atmospheric concentrations to emissions (and sources in general) can be achieved using a source attribution (commonly referred to as tagging) methodology, whereas the effect of emission control scenarios can be assessed through perturbation methods [Grewe et al., 2010].

In summary, the perturbation method investigates the change in ozone due to an emission reduction (or increase) by comparing the results of an unperturbed simulation with those of a sensitivity simulation. This difference describes the impact of a specific emission sector on ozone. Mertens et al. [2020b] clarify in their Table 1 which scientific questions can be answered by impacts (using a perturbation method) and contributions (calculated by a source attribution method such as tagging).

Several studies, including Wang et al. [2009], Grewe et al. [2010], Clappier et al. [2017], have compared the perturbation and tagging methods and have demonstrated that the perturbation method is not suitable for source attribution. Therefore, the perturbation method is better suited for evaluating future emission policies. For my thesis, which aims to differentiate between various emission sectors and determine the spatial origin of emissions and their products, the source attribution method is indispensable.

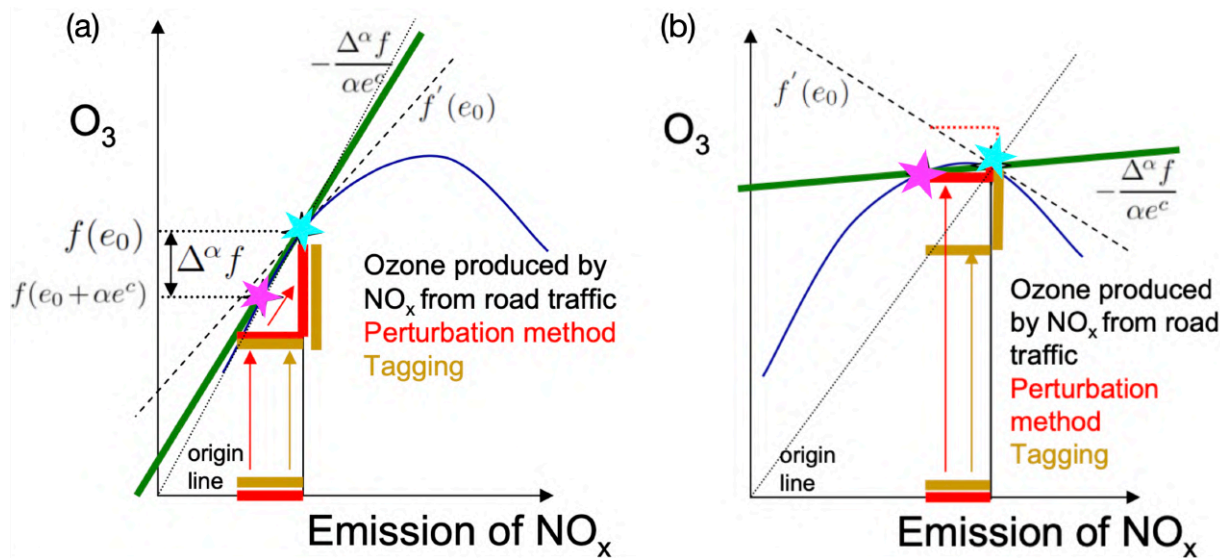


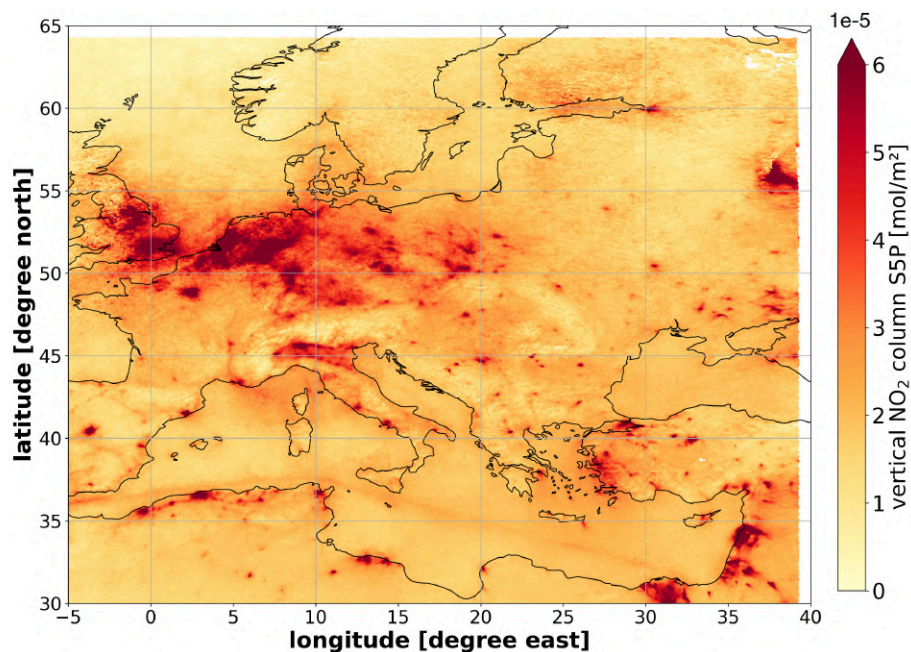
Figure 2.3: Figure adopted from Grewe et al. [2010]. The respective caption is explained in the text of section 2.5, which is based on Grewe et al. [2010].

Chapter 3

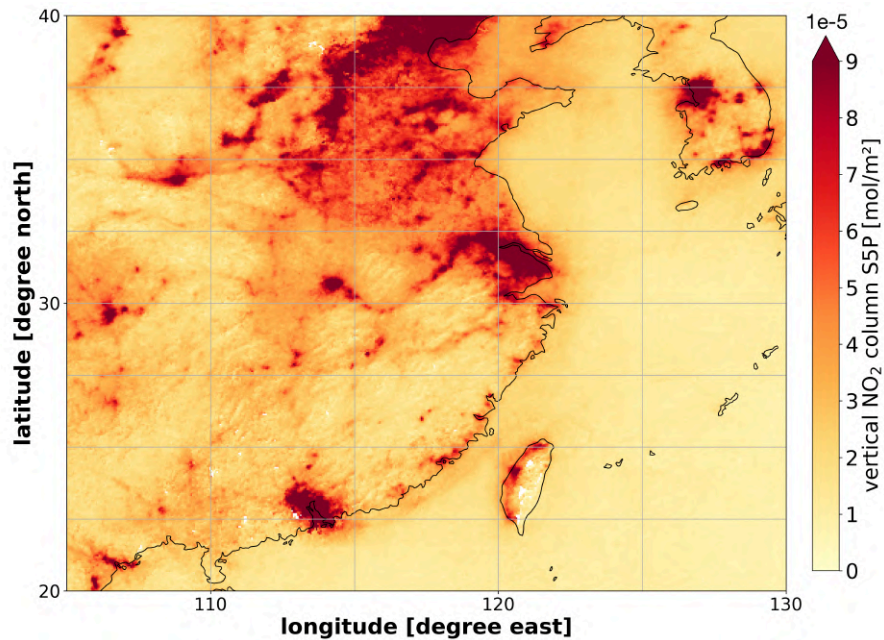
Methods

As demonstrated in Chapters 1 and 2, air pollution represents a major environmental problem, and numerical models are indispensable for calculating the contributions of emissions sources to O_3 due to the non-linearity of its chemistry. Furthermore, emission gradients of ozone precursors between urban and rural areas are frequently substantial, as shown by ground-level NO_2 for August 2018 in Europe and East Asia (Figs. 3.1a and 3.1b). Therefore, regional models with fine resolutions are more useful in simulating the dilution of large mixing ratios downwind of localised sources than coarser models. In this context, an online-coupled global-regional model system is established, with two regional refinements for Europe and East Asia, to address the research questions outlined in Section 1.2.

Chapter 3 is structured as follows: Section 3.1–3.2 gives an overview of the model infrastructure and the applied global and regional atmospheric circulation models. In Section 3.3 an overview about the submodels and the most important applied emissions inventories is given. In Section 3.4, the actual model setup is described.



(a) Monthly mean tropospheric NO_2 column in units of $10^{-5} \text{ mol m}^{-2}$ over Europe for August 2018, measured by Sentinel 5P (S5P) with a resolution (latitude, longitude) of $5.5 \text{ km} \times 3.5 \text{ km}$. The data quality is verified by a quality flag that excludes “cloudy pixels”, and any missing values are represented by white pixels.



(b) The same as Figure 3.1a, but over East Asia.

3.1 MESSy infrastructure

The Modular Earth Submodel System (MESSy), developed by a consortium of institutions [Jöckel et al., 2005, 2010], serves as an infrastructure for enhancing current geoscientific models, including atmospheric models, into more comprehensive Earth System Models (ESMs) [Kerkweg and Jöckel, 2012]. Figure 3.2 provides an overview of the MESSy concept, which is composed of four software layers: the submodel core layer (SMCL), the submodel interface layer (SMIL), the base model interface layer (BMIL) and the base model layer (BML; Jöckel et al. 2005). The SMCL contains the implementation of a specific process in the earth system, or of a diagnostic tool of the model system independent of the basemodel [Jöckel et al., 2010]. The SMCL functions as an operator, utilising data from its SMIL and returning data to other submodels and basemodels through the same SMIL. The SMIL serves as the interface between a particular process and the infrastructure, and is plugged into the BMIL. The BMIL is a basemodel-specific implementation of the MESSy infrastructure, acting as a multi-socket outlet for communication between the submodels and the base model. The BML serves as the power supply for the BMIL, but ultimately it only includes a central clock and run-time control. BML typically consists of a general circulation model (GCM), or a box model [Jöckel et al., 2010]. The MESSy infrastructure offers a great deal of flexibility and efficiency due to its ability to switch submodels on and off, as illustrated in Figure 3.2. MESSy comes with a large set of submodels for a variety of processes, which can be found on the MESSy website² or in various articles [Jöckel et al., 2006, 2010, 2016].

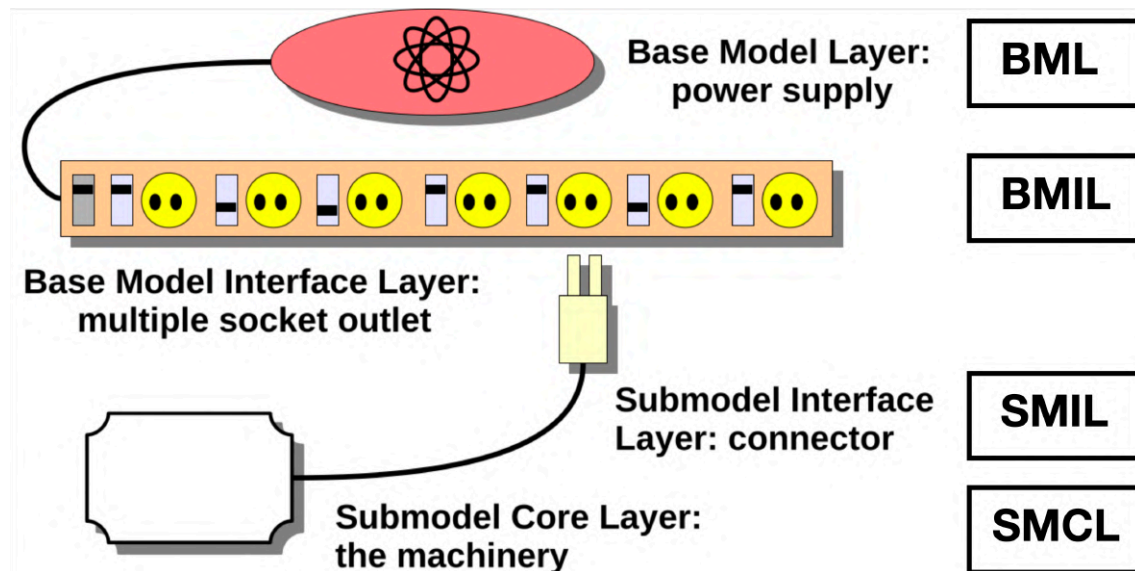


Figure 3.2: Sketch of the MESSy concept. A detailed explanation is given in section 3.1. Adopted from the original sketch of Kerkweg and Jöckel [2012].

²<https://messy-interface.org/messy/submodels/>

3.2 MESSy Basemodels

3.2.1 EMAC

As described by Jöckel et al. [2010] the ECHAM5/MESSy Atmospheric Chemistry (EMAC) model is a numerical chemistry and climate simulation system that includes submodels describing tropospheric and middle atmosphere processes and their interaction with oceans as well as the influence on land and humans [Jöckel et al., 2010]. The model uses the second version of the Modular Earth Submodel System (MESSy2) to link multi-institutional computer codes. The core atmospheric model is the 5th generation European Centre Hamburg general circulation model (ECHAM5; Roeckner et al. 2006a). “The physics subroutines of the original ECHAM code have been modularised and reimplemented as MESSy submodels and have continuously been further developed. Only the spectral transform core, the flux-form semi-Lagrangian large scale advection scheme, and the nudging routines for Newtonian relaxation are remaining from ECHAM” (see <https://messy-interface.org>).

3.2.2 COSMO

The COSMO model, developed by the Consortium for Small-scale Modeling (COSMO) (Rockel, Burkhard and Will, Andreas and Hense, Andrea 2008), is a non-hydrostatic limited-area numerical weather prediction model (NWP) [Doms and Schättler, 1999, Steppler et al., 2003, Kerkweg and Jöckel, 2012]. The Climate Limited-area Modelling-community (CLM Community) has made further developments to enhance its use case for regional climate studies. This involves considering various physical processes through parameterisations such as grid-scale and subgrid-scale clouds, precipitation, moist and shallow convection, radiation, and a soil model [Kerkweg and Jöckel, 2012]. In the COSMO model, temperature and pressure are computed at the center of each grid box, while velocities are defined at the boundaries of each grid box [Arakawa and Lamb, 1977]. The COSMO model relaxes towards the driving model by replacing the values of the outermost grid boxes with values from the driving model (e.g., EMAC) in a relaxation area at the lateral boundaries. This feature can be adjusted by the user. Additional details of the COSMO setup used in this study are explained in section 3.4 (p. 38).

3.2.3 MECO(n) model system

This section provides a description of the model system used in this thesis. The model system used is MECO(n), which stands for “MESSy-fied ECHAM and COSMO models nested n-times” and is described in previous studies [Kerkweg and Jöckel, 2012, Mertens et al., 2020b]. The model system MECO(n) combines two models: the global atmospheric chemistry model ECHAM for Atmospheric Chemistry (EMAC), and the regional COSMO-CLM/MESSy model. The online coupling of these two models is established by the Multi-Model-Driver submodel (MMD), a component of the MESSy infrastructure [Kerkweg and Jöckel, 2012, Mertens et al., 2016a]. MMD consists of a library, which performs the data ex-

change between the concurrently running models and the MMD2WAY submodel performs the coupling and the data exchange between the MECO(n) model instances [Kerkweg et al., 2018]. The MECO(n) system is unique, because of its online coupling of the ECHAM and COSMO models. This means that the two models are coupled together, and the output of one model is used as input for the other model at run-time. The on-line coupling is crucial for my study as it ensures consistent meteorological and chemical boundary conditions with high frequency at the boundaries of the regional refinements.

3.3 MESSy Submodels

In this section, I describe only a subset of the various submodels, focusing on the most important ones (see Tables A.1 and A.2, pp. 138–139), that have been employed in the present study.

3.3.1 The MECCA submodel: calculates tropospheric and stratospheric chemistry

The chemical mechanism used by the submodel MECCA (Module Efficiently Calculating the Chemistry of the Atmosphere) considers the basic gas-phase chemistry of ozone, methane, and odd nitrogen as described by Sander et al. [2011] and Jöckel et al. [2016]. The oxidation of certain NMHCs and C_5H_8 follows the Mainz Isoprene Mechanism (MIM) in version 1, as proposed by Pöschl et al. [2000]. I use the CCMI-2 (Chemistry-Climate Model Initiative phase 2) mechanism, which is based on Jöckel et al. [2016]. The halogen chemistry includes bromine and chlorine species. The mechanisms of MECCA is part of the Appendix (see section A.1.5, p. 144). The scavenging of trace gases by clouds and precipitation is represented by the submodel SCAV (Scavenging), which is explained in detail by Tost et al. [2006a] and Tost et al. [2010].

3.3.2 The Lightning NO_x submodel: parameterisation of lightning NO_x

The LNOX submodel contains 8 different parameterisations, all based on different convective parameters. This thesis utilises the parameterisation described by Price and Rind [1992], which is briefly summarised here. It is widely employed and has been investigated by Tost et al. [2007]. The parameterisation is based on the relationship between the height of convective cloud tops and the frequency of lightning flashes obtained from local measurements. The overall lightning frequency consists of a continental and oceanic flash frequency, which depends on the convective cloud top height above the ground. Therefore, for each grid cell the fractional land-sea mask is computed. The amount of NO discharged by lightning is computed by employing a value of 6.7×10^{26} molecules/flash (equivalent to approximately 15.6 kg N/flash) for cloud-to-ground flashes [Tost et al., 2007]. Schumann and Huntrieser [2007] estimated an amount of $15 (2-40) \times 10^{25}$ NO molecules per flash.

3.3.3 The BIOBURN submodel: calculates biomass burning fluxes

Biomass burning is relevant in all vegetated terrestrial ecosystems. As in Table 2.1 (section 2.3) shown, biomass burning emits large amounts of NO_x , CO and VOC. Biomass burning emissions have large horizontal and vertical spatial variabilities on a small scale; thus, it is a challenge to represent them as precisely as possible in the MECO(n) model system. The BIOBURN submodel calculates biomass burning fluxes based on arbitrary wildfire datasets containing the required data. In this study, data from the Global Fire Assimilation System (GFAS) is used. The flux of biomass burning emissions ($\text{molecules m}^{-2} \text{s}^{-1}$) is defined as follows:

$$\text{BB}_{flux} = \text{DM}(x, y) \cdot \text{EF}(s) \cdot \text{FT}(x, y) \cdot \text{VF}(z(x, y)), \quad (3.1)$$

where DM is the burnt dry particulate matter (kg), EF the emission factor (g kg^{-1}), which is specific for each emitted species (s), FT the firetype and VF the vertical fraction. The horizontal dimensions are denoted by x and y, the vertical dimension by z. In order to understand the theoretical background of DM, a short introduction into the GFAS algorithm is given. DM is calculated out of the daily average Fire Radiative Power (FRP) density [mW m^{-2}] arising from Moderate Resolution Imaging Spectroradiometer (MODIS) satellite data and has a large spatial and temporal variability [Kaiser et al., 2012]. MODIS observes the emitted thermal radiation from biomass burning between $3.9 \mu\text{m}$ and $11 \mu\text{m}$ wavelength [Kaiser et al., 2012]. FRP was quantitatively linked to the combustion rate of a wildfire by Wooster et al. [2005]. The spatial resolution of the GFAS data is 0.5° in latitude and longitude. The FRP data undergo different correction processes and observation quality procedures (details in section 2.1 of Kaiser et al. 2012). Other studies (e.g. Wooster et al. 2005) linked the FRP to the dry matter combustion rate by a universal factor. Heil et al. [2010] and Kaiser et al. [2012] argued, that the conversion of the FRP to the DM is not universally linked, but rather depends on the land cover type. This could limit the comparability of the DM between different datasets. The calculation of the dry particulate matter DM for each grid cell is explained in detail in the Appendix in section A.1.4 (p. 141).

The land cover classes used in this study are taken from Kaiser et al. [2012] as a global map for each grid cell (Fig. A.1, p. 144). Tables A.5 and A.6 (pp. 142–143) list the emission factors used in BIOBURN, which are based on literature values from Kaiser et al. [2012].

As pyro-convection and small-scale patterns of biomass burning emissions play a crucial role, it is essential to address them in a chemistry-climate model to improve the representation of biomass burning emissions in future studies.

To achieve this, I further developed the BIOBURN submodel within this study by implementing an online vertical distribution with prescribed static injection heights. As a side effect, this extension makes the pre-processing of biomass burning emission data obsolete. In a future study, a further enhancement of the vertical representation could be achieved by incorporating local satellite instrument-derived injection heights. This would

enable a more accurate vertical representation of small-scale patterns. However, for now, the focus is on the initial step, which involves integrating a vertical representation based on static injection heights into the BIOBURN code. For this the code of the BIOBURN submodel interface layer (SMIL) is expanded (*messy-bioburn-si.f90*) accordingly:

1. To achieve the online calculation of the vertical distribution of the biomass burning flux, a third dimension is added.
2. Equation 3.1 shows the implemented adjustments: The emission flux is additionally multiplied by a vertical fraction (VF) for each level.
3. The number of levels (3rd dimension) can be selected flexibly and depends on a vertical fraction file obtained from an external dataset.

The vertical fraction VF in my study is based on the distribution shown in Table A.4 (p. 140) by Dentener et al. [2006]. Sensitivity simulations described in section 3.4 are performed to test the new code implementation. The results are discussed in section 6.1.

3.3.4 The MEGAN submodel: estimates net emission of gases and aerosols from terrestrial ecosystems

Biogenic VOC emissions are mostly emitted by complex processes in plants and are one of the most important sources of CO and VOC emissions (see Table 2.1). Since, its precursors directly affect ozone chemistry, an appropriate representation in the MECO(n) model system is crucial. Previously, biogenic emissions are based on a climatology provided by the Global Emissions Initiative (GEIA) dataset. The Model of Emissions of Gases and Aerosols from Nature (MEGAN) quantifies the net terrestrial biosphere emission of various biogenic species into the above-canopy atmosphere [Guenther et al., 2006] and replaces offline datasets. The submodel MEGAN is used for the first time in the MECO(n) model system. The net emission rate ($\text{mg m}^{-2} \text{h}^{-1}$) of biogenic VOC emissions at a specific location and time is calculated as follows:

$$\text{Emission} = \epsilon \gamma \rho, \quad (3.2)$$

where ϵ ($\text{mg m}^{-2} \text{h}^{-1}$) represents the emission factor of a trace gas into the canopy at standard conditions, γ is an activity factor describing the emission changes due to deviations from standard conditions, and ρ includes the production and loss processes within the plant canopies [Guenther et al., 2006]. Guenther et al. [2006] describe the standard conditions for the MEGAN canopy-scale emission factors in detail, with a leaf area index (LAI) of 5 and a canopy with 80 % mature, 10 % growing and 10 % old foliage. The environmental standard conditions comprise a solar angle of 60° , an air temperature of 303 K, a humidity of 14 g kg^{-1} and a windspeed of 3 m s^{-1} (in detail described by Guenther et al. [2006]). MEGAN divides each grid cell into plant functional types (PFT) and a non-vegetated part.

This approach enables to consider different light and temperature distributions for various canopy types (e.g., broadleef-trees and needle trees) [Guenther et al., 2006]. Out of this, Guenther et al. [2006] calculated global averages of the emission factor ϵ for different vegetation types and climate conditions (see Table 3 in Guenther et al. 2006). The emission activity factor γ depends on the ambient conditions and is calculated as follows:

$$\gamma = \gamma_{\text{CE}} \gamma_{\text{age}} \gamma_{\text{SM}}, \quad (3.3)$$

where γ_{CE} includes the variation due to the LAI, light, temperature, humidity, and wind conditions within the canopy environment [Guenther et al., 2006]. γ_{age} describes the effect of leaf age, and γ_{SM} considers the direct changes of γ due to changes in soil moisture. The processes behind the biogenic VOC emissions are quite complex, which makes the estimates of annual biogenic emissions rather uncertain. Since MEGAN is used for the first time in MECO(n), a detailed description of the preparatory technical work is given in the following. Furthermore this makes it interesting to perform a sensitivity simulation with MEGAN in MECO(n), which setup is described in section 3.4 and analysed in section 6.2.

Table 3.1: Global and regional scaling factors used in MEGAN and the desired³ annual biogenic NMHC⁴ totals in Tg a⁻¹ (species) for all species which are explicitly considered in the applied chemical mechanism of the simulated gas phase photochemistry.

Species	Desired 2000	GS EMAC	GS*RS CM50 (EU)	GS*RS CM50 (EA)
CO	97.36	1.02	0.79	0.78
C₂H₄	21.10	1.02	0.79	0.78
C₂H₆	0.32	1.01	0.78	0.77
C₃H₆	12.98	1.06	0.82	0.81
C₃H₈	0.16	1.01	0.78	0.77
NC₄H₁₀	0.24	1.01	0.78	0.77
CH₃COCH₃	31.62	1.03	0.76	0.73
CH₃COOH	3.15	1.02	0.79	0.78
CH₃OH	96.91	0.92	0.74	0.74
HCOOH	3.15	1.02	0.78	0.78
C₅H₈	598.00	0.63	0.49	0.56

³ This climatology data was obtained through personal communication with A. Pozzer from the Max Planck Institute for Chemistry.

⁴ Non-methane hydrocarbons (NMHCs) are a subgroup of VOCs, consisting of organic compounds that contain carbon and hydrogen atoms, but do not include methane.

Before MEGAN can be used in the MECO(n) model system, some preparatory work has to be done in order to make sure, that the emission fluxes (and totals) are consistent with the climatology:

Table 3.2: Annual totals in EMAC and CM50 in comparison with the desired annual totals from 2000 in Tg a^{-1} (species) for all species which are explicitly considered in the applied chemical mechanism of the simulated gas phase photochemistry.

Species	Desired 2000	EMAC 2000 (2017)	CM50 (EU) 2000	CM50 (EA) 2000
CO	97.36	96.64 (101.25)	3.65	18.60
C₂H₄	21.10	20.94 (21.94)	0.79	4.03
C₂H₆	0.32	0.32 (0.33)	0.01	0.06
C₃H₆	12.98	13.30 (14.10)	0.50	2.58
C₃H₈	0.16	0.16 (0.17)	0.01	0.03
NC₄H₁₀	0.24	0.24 (0.25)	0.01	0.05
CH₃COCH₃	31.62	31.48 (33.44)	0.90	5.66
CH₃COOH	3.15	3.12 (3.27)	0.12	0.60
CH₃OH	96.91	96.46 (100.66)	3.62	18.61
HCOOH	3.15	3.12 (3.27)	0.12	0.60
C₅H₈	598.00	389.09 (416.46)	5.73	58.22

- First, a reference simulation without full chemistry is performed with EMAC for the year 2000 to determine the biogenic emission fluxes of MEGAN for a global scaling factor (GS) of 1.
- Out of this results, the totals of the biogenic emissions, which are referred to as original emissions, are calculated.
- Biogenic emissions have large uncertainties, so as a third step, the emission fluxes from MEGAN in EMAC are scaled to the desired emissions, which correspond to a typical T42 ($2.8^\circ \times 2.8^\circ$ resolution) climatology for the year 2000, as explained above.
- Afterwards, the desired totals in Tg a^{-1} (see Table 3.1) are divided by the original totals in Tg a^{-1} (see Table 3.2).
- This results in a new GS for EMAC, which scales the biogenic emissions towards the climatology of 2000 (i.e., the desired emissions).
- The GS for EMAC can now be applied to scale the biogenic emission fluxes for the year 2017 based on the year 2000.
- Usually, the fluxes could be scaled with an interannual factor based on the totals for 2017. In order to allow a comparison with the GEIA dataset (Chapter 6.2), the scaling in this study remains based on the year 2000.
- Table 3.1 provides an overview of the desired totals and the scaled totals for 2000 and 2017 for different species in MEGAN.

After scaling the emissions in EMAC, scaling factors must be calculated for COSMO to ensure that the emission fluxes and totals, and therefore the emissions of each COSMO instance, are comparable to those in the global EMAC model:

- First, one simulation without chemistry using the MECO(n) setup with the COSMO instance CM50 is performed for Europe and East Asia, respectively.
- Based on these results, the annual totals for each species in CM50 are calculated.
- Afterwards, the total for the same geographical section from CM50 in EMAC is calculated.
- To ensure that the totals of the biogenic emissions in CM50 are similar to those in EMAC, the totals for EMAC are divided by the totals for CM50.
- This results in an additional regional scaling factor (RS) for each species, which is multiplied with the global scaling factor (GS) from EMAC for CM50 (Table 3.1).

Finally, all scaling factors are inserted into the MEGAN namelists for EMAC and CM50, which ensures consistent biogenic emission fluxes in all instances.

3.3.5 The OFFEMIS submodel: represents emission fluxes in 2D and 3D

The OFFline EMISsions (OFFEMIS) submodel retrieves emission fluxes from IMPORT_GRID, which reads netCDF files of emission inventories and transforms them via remapping onto the model grid [Kerkweg and Jöckel, 2015]. In this way OFFEMIS makes the imported data available to other MESSy submodels. OFFEMIS uses the emission fluxes to modify the tracer tendencies [Kerkweg et al., 2006b]. According to Kerkweg et al. [2006b], OFFEMIS is specifically designed to handle emissions that are not strongly influenced by the current state of the atmosphere, biosphere, or hydrological cycle. OFFEMIS automatically detects the dimension of the emissions, respectively [Kerkweg et al., 2006b]. In this study, OFFEMIS computes the change in mixing ratio, or tracer tendency, of a prescribed emission flux over a single model time step. This computed change is then applied to the corresponding tracer [Kerkweg et al., 2006b].

3.3.6 The S4D submodel: sampling in 4 Dimensions

Since measurement data from moving platforms such as planes, ships and trains are well suited for model evaluation, the “sampling in 4 dimensions” (S4D) submodel was developed by Jöckel et al. [2010]. This submodel facilitates the direct comparison of observations from campaigns with model results, which is typically a challenging task. During model simulation (i.e., on-line), S4D interpolates the model data to the moving platform track, with the platform type and additional track information specified in the namelist [Jöckel et al., 2010]. S4D produces an additional output channel for each defined track with the same temporal resolution as the model time step. In my study, I focus on the evaluation of the EMeRGe Europe and Asia flight measurement campaigns against the MECO(n) model output, and therefore, I apply the S4D submodel in all simulations.

3.3.7 The SORBIT submodel: sampling model data along sun-synchronous satellite orbits

The SORBIT submodel enables the sampling of data along sun-synchronous satellite orbits. A particular type of satellite, known as a sun-synchronous orbiter, has an almost polar orbit with a specific altitude and inclination that causes the orbital plane to precess one full circle per year due to the Earth's oblateness [Jöckel et al., 2010]. As a result, these satellites pass over any given point on the Earth's surface at the same local solar time, and therefore always under the same light conditions. The local time $T_{L,O}$ (hour of day) of the orbiter's flyover (index O) at a given latitude Θ is defined as:

$$T_{L,O}(\Theta) = (T_{L,O}(0) \pm \arcsin(\frac{\tan\theta}{\tan\delta})\frac{12}{\pi} + 48), \quad (3.4)$$

where $T_{L,O}(0)$ is the local time when a satellite crosses the equator and δ is the inclination of the orbital plane. A positive sign indicates an ascending orbit, while a negative sign indicates a descending orbit. This relationship allows for online data sampling from a model, which facilitates a direct comparison with satellite observations without requiring precise knowledge of the satellite's position at any given time. Jöckel et al. [2010] defined a second variable X_O for a given scalar variable X in grid-point representation as follows:

$$X_O(i, j, k, l) = \begin{cases} X(i, j, k, l), & \text{if } |T_L(i, j, l) - T_{L,O}(0(j))| \leq \Delta T \\ X_U, & \text{else } otherwise, \end{cases} \quad (3.5)$$

where variables i , j , and k denote the grid-box indices in the longitudinal, latitudinal, and vertical direction, respectively, while l is the time step of the model [Jöckel et al., 2010]. At model time step l , the local solar time (hours of day) in the corresponding grid-box (with indices i and j) is denoted by T_L , as described by Jöckel et al. [2010] (see Equation (5)). If the condition in Equation 3.5 is not fulfilled for a grid-box due to the discrete grid, SORBIT sets the value to an undefined value X_U . The required time interval ΔT is typically defined as half the model time step length [Jöckel et al., 2010]. Understanding this relation is essential to comprehend the model output generated by SORBIT, which is used to evaluate satellite data in sections 4.2.1 and 4.2.2.

3.3.8 The TAGGING submodel: contribution of different emission categories

In this study the TAGGING submodel is applied, which is developed by [Grewe et al., 2017]. The TAGGING submodel implements a source attribution method, which allows a separation of the precursor emissions and their products by their source sectors and geographical origin (tagging category). Figure 3.3 gives an overview of the tagging concept. Two tagged tracers A and B from the emissions sources land transport (blue flag) and industry (red flag) react and form the tracer C. All tracers from landtransport and industry,

⁵An ascending orbit is the path a satellite takes while heading towards Earth's north pole.

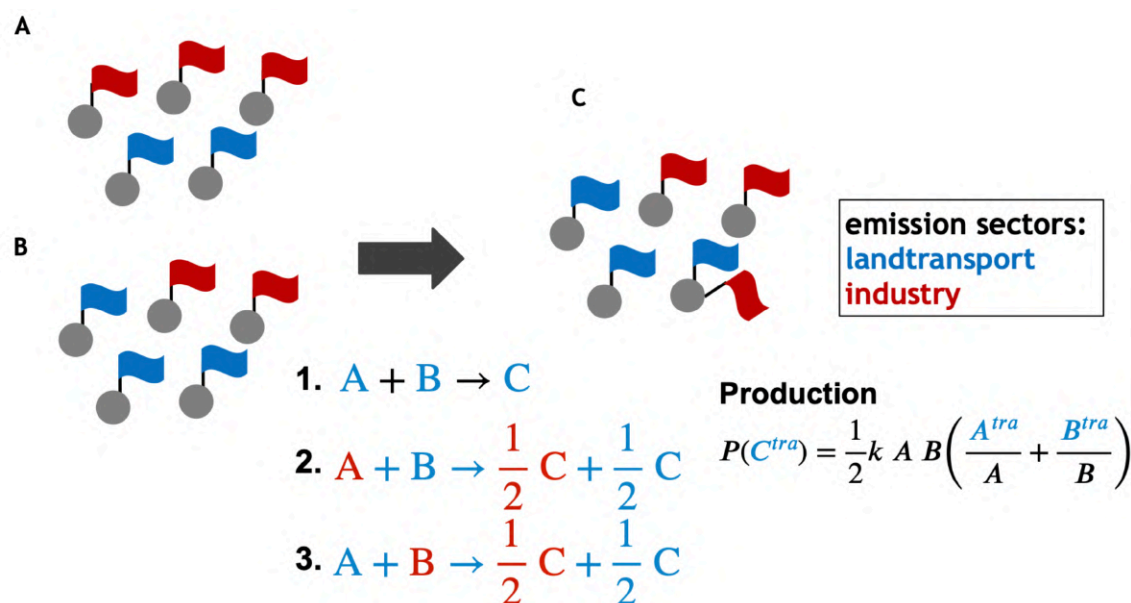


Figure 3.3: Sketch of the tagging method in the TAGGING submodel. Adopted from Tsati [2014], Grewe et al. [2017] and personal communication with M. Mertens, V. Rieger and V. Grewe.

which react with tracers from the same tagging category are still assigned to the respective source [Tsati, 2014, Grewe et al., 2010, 2017]. If tracer A from landtransport reacts with tracer B from industry (and vice versa), one half of tracer C is assigned to land transport and the other half to industry (Reactions 2 and 3 in Figure 3.3). The production of C^{tra} (blue) is then

$$P(C^{tra}) = \frac{1}{2} k A B \frac{A^{tra}}{A} + \frac{B^{tra}}{B}, \quad (3.6)$$

where k is the reaction rate of reaction 1 in Figure 3.3.

The TAGGING submodel enables the quantification of the share of different source categories on the mixing ratios of the species NO_y , NMHC, CO, HO_2 , O_3 , OH and peroxyacetyl nitrate (PAN) [Grewe et al., 2017]. Due to memory limit, Grewe et al. [2017] mapped the complex chemistry scheme to a family concept, which clearly reduces the number of additional tracers. NO_y ⁶ and NMHCs are therefore defined as two families that include all chemically active nitrogen compounds (15) (see Appendix section A.1.1, p. 137) and hydrocarbons (42) [see for details in Supplement, Table 1, Grewe et al., 2017], respectively. Table 3.3 gives an overview of the defined 16 tagging categories within this study, which are applied for 7 species (and families), what means the tagging model introduces 112 new tracers.

For each tracer initialisation, the TAGGING submodel receives information on the chemical reaction rates, tracer transport (except for OH and HO_2), online emissions, such

⁶The definition of the NO_y family in the TAGGING submodel slightly differs from the definition used in the next Chapter 4 (see for details section A.1.2 in the Appendix, p. 137).

as lightning, and scavenging rates from other submodels of EMAC (e.g. MECCA) [Grewé et al., 2017]. Since OH and HO₂ have a very short lifetime, here a steady-state is assumed for their contributions. During the simulation, online emissions are added to the respective tagged tracer at each time step. The processes of dry and wet deposition are considered as a bulk process. To calculate changes in the concentration of all relevant chemical species, the difference between the respective concentrations before and after dry and wet deposition is calculated [Grewé et al., 2017]. Based on these chemical tendencies a set of differential equations is solved and then distributed among the tagged species rely on their relative contribution to the total concentration [Grewé et al., 2017].

In order to obtain these concentration changes, it is necessary to accurately determine the individual production and loss terms. Grewé et al. [2017] examined the effective production and loss terms for ozone as proposed by Crutzen and Schmailzl [1983]. For example, the ozone family takes into account all rapid interactions between ozone and other chemical species [see Table 1 in Supplement of Grewé et al., 2017]. In order to identify ozone production and loss reactions, Grewé et al. [2017] used the *ProdLoss* tool. *ProdLoss* is used to instrument the chemical mechanism of the submodel MECCA for additional diagnostics. This tool identifies the effective production and loss reactions for a given family within the chosen chemical mechanism [see supplement of Grewé et al., 2017]. The tool differentiates between two O₃ production channels and five O₃ destruction channels. Consequently, seven diagnostic production and loss rates are calculated by the chemical mechanism. The production of the tagged ozone tracers can be obtained out of four terms with:

$$\begin{aligned} \tau_{\text{PO}_3}^{\text{tag}} = & \frac{1}{2} P_{\text{R18}} \frac{\text{NO}_y^{\text{tag}}}{\text{NO}_y} + \frac{\text{HO}_2^{\text{tag}}}{\text{HO}_2} \\ & + \frac{1}{2} P_{\text{R23}} \frac{\text{NO}_y^{\text{tag}}}{\text{NO}_y} + \frac{\text{NMHC}^{\text{tag}}}{\text{NMHC}}, \end{aligned} \quad (3.7)$$

and the depletion of tagged ozone is defined as

⁷R* is the reference number of the respective chemical reaction defined in Chapter 2.

$$\begin{aligned}
\text{DO}_3^{tag} = & \frac{1}{2}L_{R12} \frac{\text{OH}^{tag}}{\text{OH}} + \frac{\text{O}_3^{tag}}{\text{O}_3} \\
& + \frac{1}{2}L_{R13} \frac{\text{HO}_2^{tag}}{\text{HO}_2} + \frac{\text{O}_3^{tag}}{\text{O}_3} \\
& + \frac{1}{2}L_{R26} \frac{\text{NO}_y^{tag}}{\text{NO}_y} + \frac{\text{O}_3^{tag}}{\text{O}_3} \\
& + \frac{1}{2}L_{R14} \frac{\text{NMHC}^{tag}}{\text{NMHC}} + \frac{\text{O}_3^{tag}}{\text{O}_3} \\
& + \frac{1}{2}L_{R12} \frac{\text{O}_3\text{C}^{tag}}{\text{O}_3},
\end{aligned} \tag{3.8}$$

where “tag” denotes an emission sector or a geographical region or a combination of both. P_{R18} and P_{R23} are reaction rates of the respective production reactions shown in chapter 2. L_{R12} , L_{R13} , L_{R14} and L_{R26} are the respective loss reactions of ozone. L_{R26} is the loss reaction rate for ozone depletion by NO_y . This shows, that the TAGGING submodel considers also chemically competing effects, during ozone production and depletion between NO_x , CO, and NMHCs, which are rather complex processes. In a similar manner, Rieger et al. [2018] determined the individual production and loss terms for OH and HO_2 , but a detailed description is not provided here.

3.3.9 Emission inventories used

In the framework of this thesis various gridded global emission inventories are used, in order to represent emissions of anthropogenic and natural air pollutants. Table 3.4 lists the global totals of the most important ozone precursors in EMAC for anthropogenic and natural sectors.

- The “Emissions Database For Global Atmospheric Research” (EDGAR, v5.0), which consists of anthropogenic emissions arising from land transport, shipping, households and industrial processes, is used (Table A.3, p. 139). It is available as monthly averages from 1970 up to 2015, whereupon in this work just the monthly means of 2015 are taken for the whole simulation period. The horizontal resolution is $0.1^\circ \times 0.1^\circ$. The data is vertically distributed after Mailler et al. [2013] onto 7 levels, available for each emission sector after the Selected Nomenclature for sources of Air Pollution (SNAP; see supplement A.3, 139). Table A.3 lists the vertical fractions for each emission height depending on the SNAP sector.
- The “Global Fire Assimilation System” (GFASv1.2) data (monthly averages), available from 2003 onward, are taken to represent global biomass burning emissions with a horizontal resolution of $0.1^\circ \times 0.1^\circ$. The injection height is prescribed, and the emissions data is vertically distributed onto six levels, depending on the geographical location (Table A.4, p. 140; Dentener et al. 2006).

- Aircraft traffic emissions are represented by a dataset based on the Representative Concentration Pathway scenario RCP8.5 from the Intergovernmental Panel on Climate Change's (IPCC) Fifth Assessment Report (AR5).
- CCMI (Chemistry-Climate Model Initiative) is a research project that aims to improve the understanding of the Earth's climate system by using chemistry-climate models. The initiative contributes to the assessment reports mentioned above by representing greenhouse gases such as N_2O , CH_4 , and CO_2 , as well as halocarbons and other compounds. The monthly means from their datasets for the years 2017–2019 are used in this study with a horizontal resolution of $0.5^\circ \times 0.5^\circ$.
- The agricultural waste burning emissions (AWB) are also based on the data base from CCMI with a horizontal resolution of $0.5^\circ \times 0.5^\circ$.
- The GEIA database, as documented by Sindelarova et al. [2014], represents biogenic emissions as monthly means with a horizontal resolution of $1^\circ \times 1^\circ$.
- Volcanic SO_2 is included in the model based on research conducted by Diehl et al. [2012], represented as monthly means at a coarser horizontal resolution of $2^\circ \times 2^\circ$.

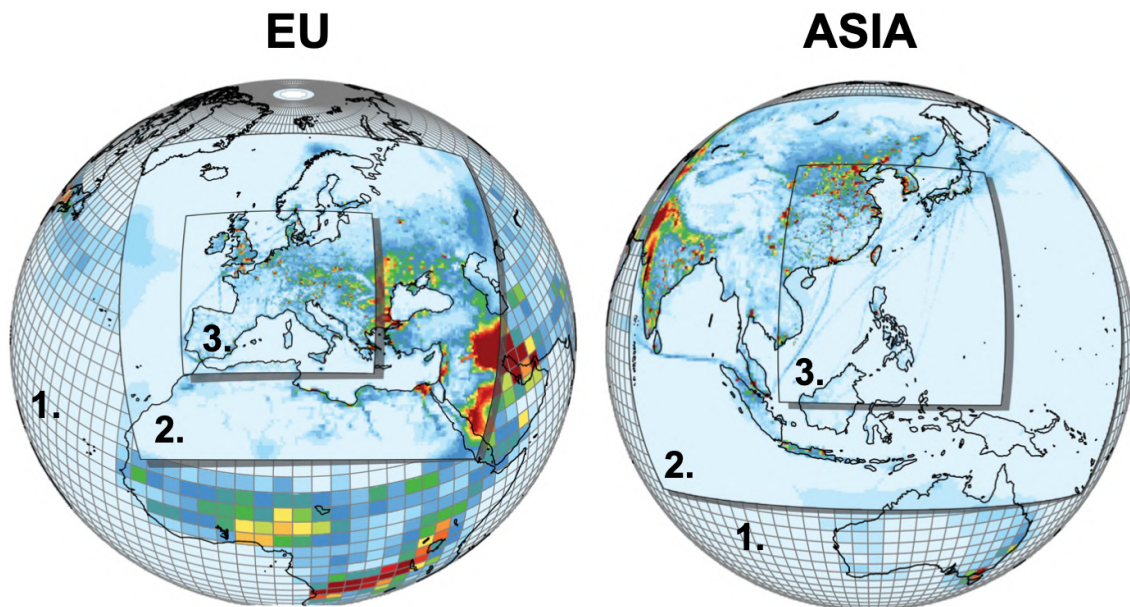


Figure 3.4: Domains of both MECO(2) setups with the global EMAC, and both European COSMO instances CM50 and CM12, as well as both East Asian COSMO instances for CM50 and CM12 (personal communication, Mariano Mertens).

3.4 Description of the model setup

In the following a description of the standard model set up with all versions and technical details is given. In this study, EMAC (ECHAM5 version 5.3.01, MESSy version 2.55.2-1912) in the T42L90MA-resolution, i.e. with a spherical truncation of T42 (corresponding to a quadratic Gaussian grid of approximately $2.8^\circ \times 2.8^\circ$, degrees in latitude and longitude) with 90 vertical hybrid pressure levels up to 0.01 hPa is applied [Jöckel et al., 2010]. EMAC is operated with a timestep length of 720 s.

Comparable to the study by Mertens et al. [2020b] a MECO(2) setup with one COSMO-CLM/MESSy instance CM50 (further denoted as CM50) over Europe with a horizontal grid resolution of $0.44^\circ \times 0.44^\circ$ (≈ 50 km), and a further nested instance CM12 (further denoted as CM12) covering Central Europe with a horizontal grid resolution of $0.11^\circ \times 0.11^\circ$ (≈ 12 km) is applied (see Fig. 3.4, left panel). The timestep length for Europe in CM50 is 240 s and in CM12 120 s. Similarly, two COSMO-CLM/MESSy instances with the same resolutions (CM50 and CM12), have been applied for East Asia (see Fig. 3.4, right panel). Here, the timestep length in CM50 is 240 s and in CM12 60 s. The COSMO-CLM/MESSy instances for Europe use 40 vertical model levels (terrain following) with geometric height as the vertical coordinate. The height of the uppermost model level is at ≈ 22 km; the damping zone starts at 11 km.

For East Asia 45 vertical model levels are applied and the uppermost model level is at ≈ 30 km; here the damping zone starts at 18 km. The thickness of the lowest model layer is ≈ 20 m. The lateral boundary conditions for CM50 are provided by EMAC, the boundary conditions for CM12 are provided by CM50 [Mertens et al., 2020b]. In order to facilitate a one-to-one comparison with observations, EMAC is operated in a “specified dynamics” (SD) mode, i.e., the temperature, the divergence, the vorticity, and the logarithm of the surface pressure are “nudged” by a Newtonian relaxation towards the ERA5 reanalysis data [Hersbach et al., 2020]. ERA5 is the fifth generation ECMWF (European Centre for Medium-Range Weather Forecasts) reanalysis for the global climate and weather. The boundary conditions of the sea surface temperature and sea ice coverage within this simulation setup are prescribed from the same dataset.

The spin-up simulation with EMAC is initialised at the 1st September 2015 with a simulation time of 15 months for the spin-up of the chemical tracers. The MECO(n) simulations start with the initial conditions on December 1st, 2016, allowing for a one-month spin-up time. The soil climatology in COSMO is initialised by climatological conditions based on previous simulations. The actual simulation period is 12/2016–12/2018, and was chosen because during this time the two important flight campaigns “Effect of Megacities on the Transport and Transformation of Pollutants on the Regional to Global Scales” (EMERGE) took place in Europe and East Asia (see sections 4.4.1.1 and 4.4.1.2).

Due to the MESSy infrastructure, the same diagnostics and chemical process descriptions are applied in all model instances. LNOX is only applied in the global EMAC instance as in previous studies [Mertens et al., 2020a,b].

The MECO(2) and MECO(1) simulations are performed in the QCTM (quasi chemistry-transport model) mode also for the nested regions, what means that the chemistry does

not affect the meteorology [Deckert et al., 2011]. In the QCTM mode all radiatively active substances are prescribed for the radiation calculation based on data from a preparatory simulation. This is essential to make sure that sensitivity simulations with modified chemical conditions can be compared with each other on a point-by-point basis, since the time series of meteorological quantities are identical Mertens et al. [2016b].

Next to the reference simulations for Europe and East Asia using the MECO(2) setup, respectively, sensitivity simulations are performed with the BIOBURN and MEGAN submodels in order to determine their effect on the O_3 chemistry and thus the O_3 contributions. Tables A.1 and A.2 (pp. 138–139) list all of the submodels used in the reference simulations described below. The following list and Table 3.5 explain the adjustments made in the sensitivity simulations and provides the names of all five simulations:

EUREF: Reference simulation targeting on Europe, performed with the standard model setup as described above.

ASIAREF: Reference simulation targeting on East Asia, performed with the standard model setup as described above.

EUBB: The code implementation in BIOBURN described in Section 3.3.3 has been tested within EUBB based on the MECO(1) setup of EUREF but with adjustments shown in Table 3.5. The results of the sensitivity simulation EUBB are analysed in section 6.1.

ASIABB: The same setup as for EUBB, but for East Asia. The results of ASIABB are analysed in section 6.1.

EUMEGAN: EUMEGAN is a sensitivity simulation based on the model setup of EUREF but with adjustments shown in Table 3.5. Additionally some adjustments are made in the MEGAN namelist concerning the tagging tracers, further details can be found in section A.1.6 in the Appendix (p. 167). Section 6.2 provides a comprehensive outline of the MEGAN sensitivity simulations and their comparison with EUREF.

Table 3.3: Description of the different tagging categories applied in this study following Grewe et al. [2017]. Please note that some tagging categories combine different emission sectors (see description). The last row shows the nomenclature of the tagged tracers for ozone as used in this study. Nomenclature of other species is accordingly.

Tagging category	Description	Notation for tagged ozone
Land transport ROW	emissions of road traffic, inland navigation, railways (IPCC codes 1A3b_c_e) from Rest of the world	O_3^{tra}
Land transport EU	emissions of road traffic, inland navigation, railways (IPCC codes 1A3b_c_e) from Europe	O_3^{teu}
Land transport NA	emissions of road traffic, inland navigation, railways (IPCC codes 1A3b_c_e) from North America	O_3^{tna}
Land transport EA	emissions of road traffic, inland navigation, railways (IPCC codes 1A3b_c_e) from East Asia	O_3^{tea}
Anthropogenic non-traffic ROW	sectors energy, solvents, waste, industries, residential, agriculture from Rest of the world	O_3^{ind}
Anthropogenic non-traffic EU	sectors energy, solvents, waste, industries, residential, agriculture from Europe	O_3^{ieu}
Anthropogenic non-traffic NA	sectors energy, solvents, waste, industries, residential, agriculture from North America	O_3^{ina}
Anthropogenic non-traffic EA	sectors energy, solvents, waste, industries, residential, agriculture from East Asia	O_3^{iea}
Shipping	emissions from ships (IPCC code 1A3d)	O_3^{shp}
Aviation	emissions from aircraft	O_3^{air}
Lightning	lightning- NO_x emissions	O_3^{lig}
Biogenic	online calculated isoprene and soil- NO_x emissions, offline emissions from biogenic sources and agricultural waste burning (IPCC code 4F)	O_3^{soi}
Biomass burning	biomass burning emissions	O_3^{bio}
CH_4	degradation of CH_4	$O_3^{\text{CH}_4}$
N_2O	degradation of N_2O	$O_3^{\text{N}_2\text{O}}$
Stratosphere	downward transport from the stratosphere	O_3^{str}

Table 3.4: Totals of the ozone precursors NO_x , CO and VOCs in Tg a^{-1} of the global EMAC simulation. The NO_x emissions are given in amount of nitrogen, CO in amount of CO, and the VOC emissions are given in amount of carbon. AWB is the abbreviation for agricultural waste burning.

Sector	NO_x (Tg a^{-1})	CO (Tg a^{-1})	VOCs (Tg a^{-1})
Aviation	2.6	11.0	
Land Transport	10.2	202.0	30.9
Anthropogenic Non-traffic	20.4	334.4	114.0
Shipping	5.9	6.0	1.5
Lightning	5.6		
Biogenic	8.1		
Biomass Burning + AWB	3.8	18.3	

Table 3.5: Overview of the simulations analysed in the present thesis.

Simulation	MECO(1) period	MECO(2) period	biomass burning emissions	biogenic emissions	VOC
EUREF	2017–2018	JJA 2017– 2018; MA ⁸ 2018	OFFEMIS (BB flux ⁹)	OFFEMIS (GEIA)	
ASIAREF	2017–2018	JJA 2017– 2018; MA 2018	OFFEMIS (BB flux)	OFFEMIS (GEIA)	
EUBB	2017–2018	–	BIOBURN (DM flux ¹⁰)	OFFEMIS (GEIA)	
ASIABB	2017–2018	–	BIOBURN (DM flux)	OFFEMIS (GEIA)	
EUMEGAN 2017		–	OFFEMIS (BB flux)	MEGAN parametrisation	

⁸ MA 2018 stands for March and April 2018.

⁹ Biomass burning emissions are prescribed by the biomass burning flux (BB flux) provided by GFASv1.2 via OFFEMIS.

¹⁰ Biomass burning emissions within BIOBURN are calculated based on the dry particulate matter (DM) flux (and other parameters, see section 3.3.3), which originates from the GFASv1.2 dataset.

Chapter 4

Evaluation of the MECO(n) system

In this Chapter, the capability of the MECO(n) model to reproduce dynamic processes and the meteorology, including the distribution of temperature, pressure, and winds, in East Asia, is evaluated. Here, only a MECO(1) simulation for East Asia is analysed, since for this region no MECO(n) simulation was conducted so far. The MECO(1) simulation results, examined here, are achieved with a slightly different model setup than ASIAREF (see section 3.4), i.e. with a different domain and without interactive chemistry. A meteorological evaluation of the model system for Europe was already conducted by Hofmann et al. [2012], and is therefore not demonstrated explicitly here. After the meteorological evaluation, the models ability with respect to reproducing the chemical composition of the atmosphere above Europe and East Asia, in the MECO(2) simulation results of EUREF and ASIAREF, is assessed (both described in section 3.4).

This is accomplished by utilising, observational data from air quality stations, aircraft based observations, and satellite data on both, global and regional scales, to determine whether the model represents the atmospheric chemical composition sufficiently realistic to be usable for addressing my scientific questions. Thus, the primary focus is on key ozone precursors such as NO_y and O_3 itself.

4.1 Meteorological Evaluation East Asia

In this section, the 925 hPa temperature, sea level pressure, and wind speed are assessed to ensure that the model represents the meteorology in a realistic way. In the subsequent analysis, several monthly averaged meteorological parameters simulated by CM50 are compared to ERA5 (resolution of $0.25^\circ \times 0.25^\circ$) reanalysis data. The data of CM50 (resolution of $0.44^\circ \times 0.44^\circ$) was transformed to the rectilinear grid of the ERA5 reanalysis data to enable a comparison between the two.

The model simulation and analysis was conducted for the period during the EMeRGe Asia flights in March and April 2018. Figure 4.1 depicts the differences of monthly averages between CM50 and ERA5 for temperature at 925 hPa (upper panels), sea level pressure (SLP, central panels), and 10 m wind speed (bottom panels). The synoptic situation in

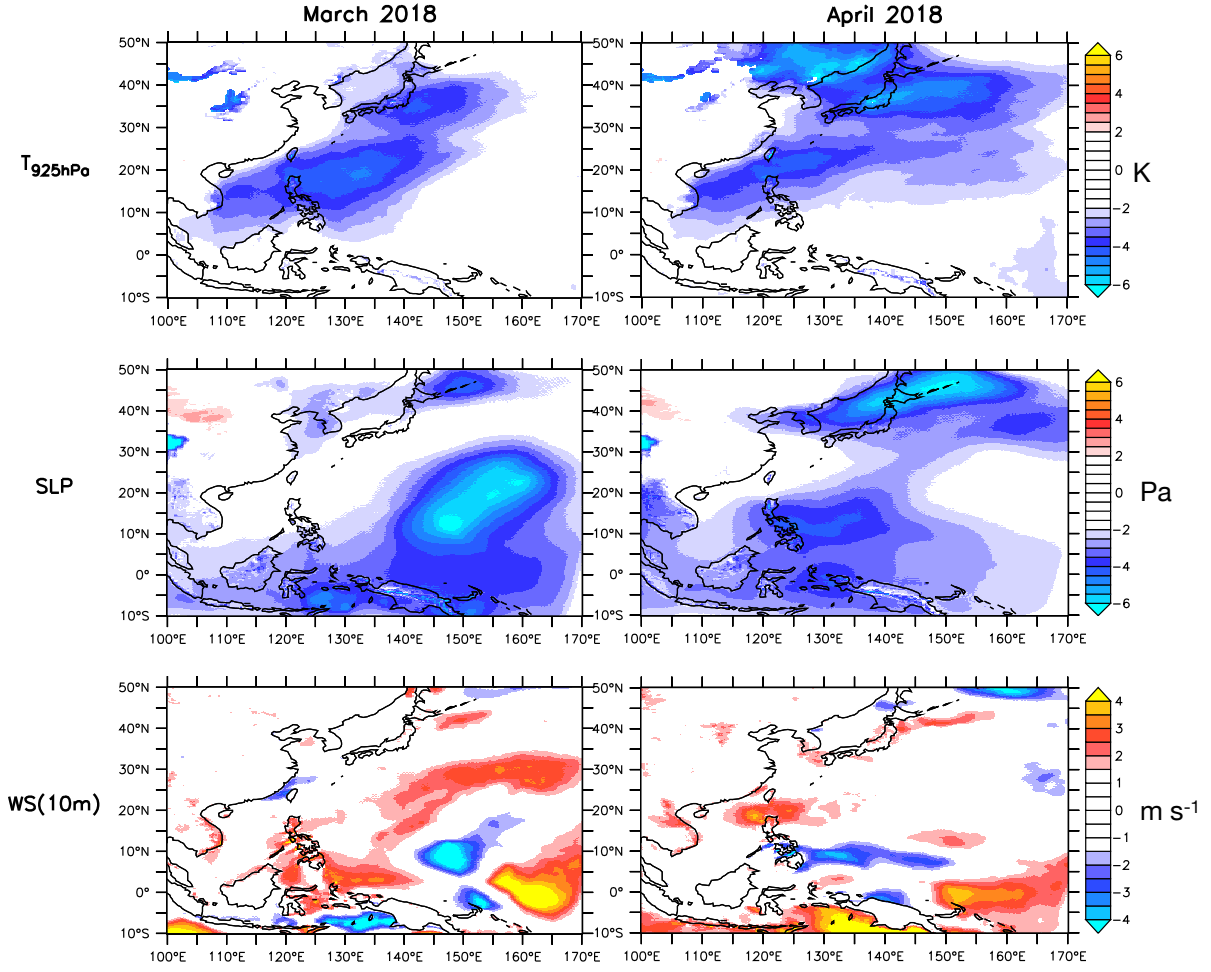


Figure 4.1: Monthly averaged differences between CM50 minus ERA5 for March 2018 (left) and April 2018 (right). Shown are the differences of the temperature at 925 hPa (T_{925} , in K), the sea level pressure (SLP, in hPa) and the wind speed (WS(10 m)), in m s^{-1} .

East Asia during March 2018 was dominated by typhoon “Jelawat”, which influenced the pressure pattern for several weeks [Duran, 2018]. For March 2018, CM50 exhibits negative temperature biases of up to -4 K at 925 hPa, especially over the Chinese Sea. The negative bias of CM50 over the ocean ranges from Japan to Vietnam (Fig. 4.1, upper left). A similar negative temperature bias, with values as low as -6 K, is simulated for April 2018, with a stronger extent towards Japan and further north. In March 2018, CM50 underestimates the SLP by up to -5 to -6 hPa over the Pacific Ocean. The simulated wind speed (10 m, lower left panel) shows an overestimation of up to 3–4 m s^{-1} on the South- and North-West sides of the section, where SLP is underestimated. During March 2018, CM50 seems to slightly overestimate the activity of low pressure systems over the Pacific Ocean. This overestimation would require further evaluations, but they are beyond the scope of this study. A similar wind speed bias is simulated around and south of the Philippines. Along the Taiwan Strait, CM50 underestimates the wind speed by up to -3 m s^{-1} in comparison

to ERA5. In April 2018, the SLP bias decreases, particularly around the Philippines and North of Japan. Overall, despite the analysed biases, CM50 (nested into EMAC in SD mode) is capable of reproducing the reanalysed (ERA5) synoptic situation sufficiently well. This means that COSMO-CLM/MESSy can be applied with chemistry, which is important for my further analyses.

4.2 Intercomparison of simulation results of tropospheric columns with satellite observations

The following section evaluates CM50 and CM12 simulated O_3 and NO_2 tropospheric columns in comparison to satellite measurements of the TROPOMI (Tropospheric Monitoring Instrument) instrument on board the Sentinel-5P (Sentinel-5 Precursor) satellite, a satellite launched by the European Space Agency (ESA) under the European Earth Observation program Copernicus [Copernicus, 2019]. The TROPOMI is the satellite's single payload instrument, a push broom imaging spectrometer with a wide field-of-view, providing routine observations of atmospheric trace gases and aerosols for air quality, climate, and stratospheric ozone research, through continuous high-resolution spectral measurements in ultraviolet (UV), visible (VIS), near-infrared (NIR), and shortwave-infrared (SWIR) bands [Copernicus, 2019].

For this study, Sentinel-5 Precursor Level-2 (NO_2) and Level-3 (O_3) products¹¹ are used [Copernicus, 2019]. The O_3 data was provided by the Earth Observation Center (EOC, personal communication K.P. Heue). Sentinel-5 Precursor operates according to a pre-defined, fully repetitive observation scenario, maximizing the measurement time on the day-side of the orbit at an equatorial crossing (mean local solar) time of 13:30. The model results of SORBIT for CM50 and CM12 enable the direct comparison with the Sentinel-5P data (see section 3.3.7). To demonstrate the consistency of the MECO(2) refinements CM50 and CM12, I compared ground-level O_3 simulated by the two model instances for the summer months (JJA) 2017. I interpolated the data from CM12 onto the grid of CM50 and found that both model instances show the same order of magnitude and geographical distribution of ground-level O_3 (see Fig. B.26, p. 181). This comparison further shows that the refinement CM12 is essential, as it allows for the visualisation of fine structures such as city plumes that are not represented in CM50.

4.2.1 Model results compared to satellite observations: NO_2

This section evaluates the results of the MECO(n) model by comparing them with retrieved tropospheric NO_2 columns from S5P. In order to evaluate the model data with the satellite measurements, the following section briefly describes the satellite dataset and points out the most important pre-processing steps for the model data.

¹¹The NO_2 data can be accessed through the Sentinel data access website <https://sentinel.esa.int/web/sentinel/sentinel-data-access>; last accessed on 19.10.2022.

Sentinel-5P completes approximately 14.4 orbits per day around the Earth, with a swath width of approximately 2600 km [Copernicus, 2019]. The instrument takes continuous measurements as it orbits, covering a new swath on each orbit. Due to the overlap of the swaths between consecutive orbits, a particular point on the Earth's surface is typically observed by TROPOMI every 24 hours, or once per day, on average.

Therefore, the TROPOMI Level-2 dataset includes at least one measurement per day for each geographical location. The data is organised on a 2D grid (scanline and groundpixel) with equally sized grid boxes of 3.5 km x 5.5 km (latitude and longitude) [Copernicus, 2019]. Vertically, the retrieval data is aggregated into pressure layers, the number of which varies depending on the measured species. For NO₂, there are 34 layers.

To compare the model data with the TROPOMI data, the required COSMO-CLM/MESSy model data such as NO₂ mixing ratio (SORBIT), dry grid mass, pressure, and grid box area are first horizontally interpolated using the nearest neighbor method onto the equirectangular retrieval grid. This method assigns pixels with the same model data on the retrieval grid. Once the model data is on the retrieval grid, the simulated NO₂ mixing ratio at the corresponding geographical location is linearly interpolated based on the model pressure onto the vertical pressure layers of the retrieval grid. Then, the NO₂ mixing ratio is divided by the product of the dry grid mass and the molar mass¹² of dry air, which yields the amount of mol of NO₂ per grid box.

Next, on the same grid, the amount of mol of NO₂ on each level is multiplied by the tropospheric averaging kernel of the retrieval. This means equally great NO₂ mixing ratios might have different tropospheric averaging kernels, but this step is important to make the model data comparable to the satellite data, as the averaging kernel describes the sensitivity of the satellite instrument for each layer. An ideal instrument would have an averaging kernel exactly equal to 1. However, as no instrument is perfect and sensitivity varies between layers, the averaging kernel is mostly either below or above 1. The tropospheric averaging kernel A^{trop} is calculated from the averaging kernel A as follows:

$$A^{\text{trop}} = \begin{cases} \frac{M}{M_{\text{trop}}} \cdot A, & \text{if } l \leq l_p^{\text{TM5}} \\ 0, & \text{if } l > l_p^{\text{TM5}} \end{cases} \quad (4.1)$$

where M is the total, M_{trop} the tropospheric air mass factor, and l the respective layer. Above the tropopause, which is based on the global chemistry transport model (TM5) (l_{pTM5}) A^{trop} is zero [Huijnen et al., 2010]. When clouds are present, the value of A^{trop} is nearly zero below the clouds and can exceed 1 above the clouds. After this step, the results are summed up vertically to the tropopause pressure and divided by the grid box area, resulting in the tropospheric vertical column in units of mol m⁻² for each point on the retrieval grid. Finally, the tropospheric vertical NO₂ column of the prepared model data (on the retrieval grid) and the measured S5P tropospheric vertical NO₂ columns have been conservatively remapped to the original COSMO-CLM/MESSy grid to preserve the exact values and make them comparable.

¹²The molar mass of dry air is 0.0289647 kg mol⁻¹.

Now, the results can be further evaluated using statistical methods such as calculating monthly means or probability density functions. These values allow for a direct comparison of the tropospheric vertical columns between the model data and the satellite data, which is done in the next subsection.

4.2.1.1 Europe

Compared to the S5P data, the geographical distribution of tropospheric NO₂ simulated by CM50 and CM12 for JJA 2018 is well represented in Europe, as shown in Figure 4.2. Both COSMO instances represent hotspots of NO₂ in regions like the Benelux area, the Po Valley, and cities like Paris. However, a quantitative comparison (Fig. 4.2, lower panels) reveals that both, CM50 and CM12, underestimate the levels of NO₂ in heavily polluted areas, including the Benelux region, the Ruhr area, the Po Valley, Poland, and Southern Germany. Conversely, in rural areas, the simulated tropospheric NO₂ column is frequently overestimated, with Central and Southern France and Central Italy being prominent extremes. The bias of NO₂ in CM12 is slightly smaller than in CM50.

Figure 4.3 presents the histogram of the probability densities of CM50 and CM12, which indicate that in CM12, tropospheric NO₂ is generally larger than in CM50, particularly for vertical NO₂ columns above 2.0×10^{-5} mol m⁻². Nevertheless, the distribution of tropospheric NO₂ is largely similar throughout the range of values. The probability densities of the Sentinel-5P data reveal that, in comparison with the COSMO-CLM/MESSy data, the maximum frequency of tropospheric NO₂ values is shifted towards smaller vertical NO₂ columns.

4.2.1.2 East Asia

Figure 4.4 illustrates the strong North-South gradient of tropospheric NO₂ in East Asia, which is captured by CM50 and CM12. The retrieved geographical distribution of tropospheric NO₂ in JJA 2018 is generally well represented by both COSMO model instances, adequately representing hotspots, such as the Pearl River Delta, Shanghai, Taiwan, and Chongqing in East China. However, tropospheric NO₂ is significantly overestimated within major polluted areas and their edges with steep NO₂ gradients, as shown in the lower left and right panels of Figure 4.4. Conversely, in rural areas such as East China and parts of South China, tropospheric NO₂ is slightly underestimated, as indicated by the gray and bluish background color in the lower panels of Figure 4.4.

In Figure 4.5, the histogram of the probability densities of the tropospheric NO₂ column for CM50 and CM12 are compared to those of the Sentinel-5P observations. The figure indicates that below a threshold of 4×10^{-5} mol m⁻², CM50 and CM12 underestimate the frequency of NO₂ columns in comparison to Sentinel-5P observations, suggesting that the COSMO-CLM/MESSy model shows more smaller NO₂ columns, particularly in rural areas. Conversely, above this threshold, in CM50 and CM12 the frequencies are slightly shifted to larger tropospheric NO₂ columns in comparison to the S5P observations. This applies particularly to plumes with high values, such as those observed in North China. It is

hypothesised that the EDGAR v5.0 data set overestimates anthropogenic NO emissions.

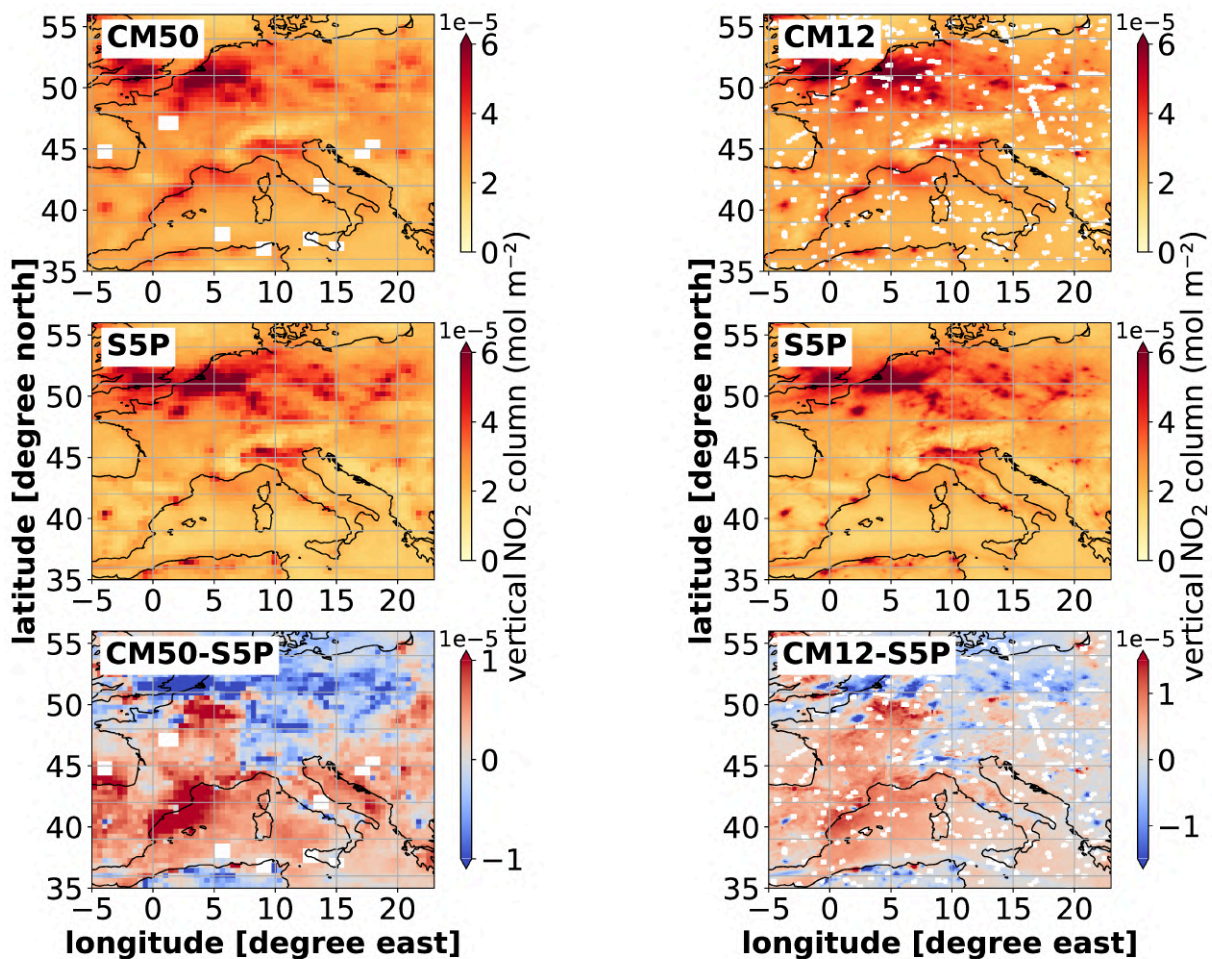


Figure 4.2: Shown is the tropospheric column of NO₂ in units of mol m⁻² over Central Europe for the JJA 2018 period, resulting from CM50 and CM12 model instances (upper panels), as well as the conservative remapped Sentinel-5P (S5P) data onto the COSMO-CLM/MESSy grids (central panels). For S5P data the quality flag has been taken into account to exclude cloudy pixels. Additionally, the differences between the model and satellite data (CM50-S5P and CM12-S5P) are shown. The undefined values in the model output of SORBIT in CM50 and CM12 are indicated by white pixels, which have been explained in section 3.3.7.

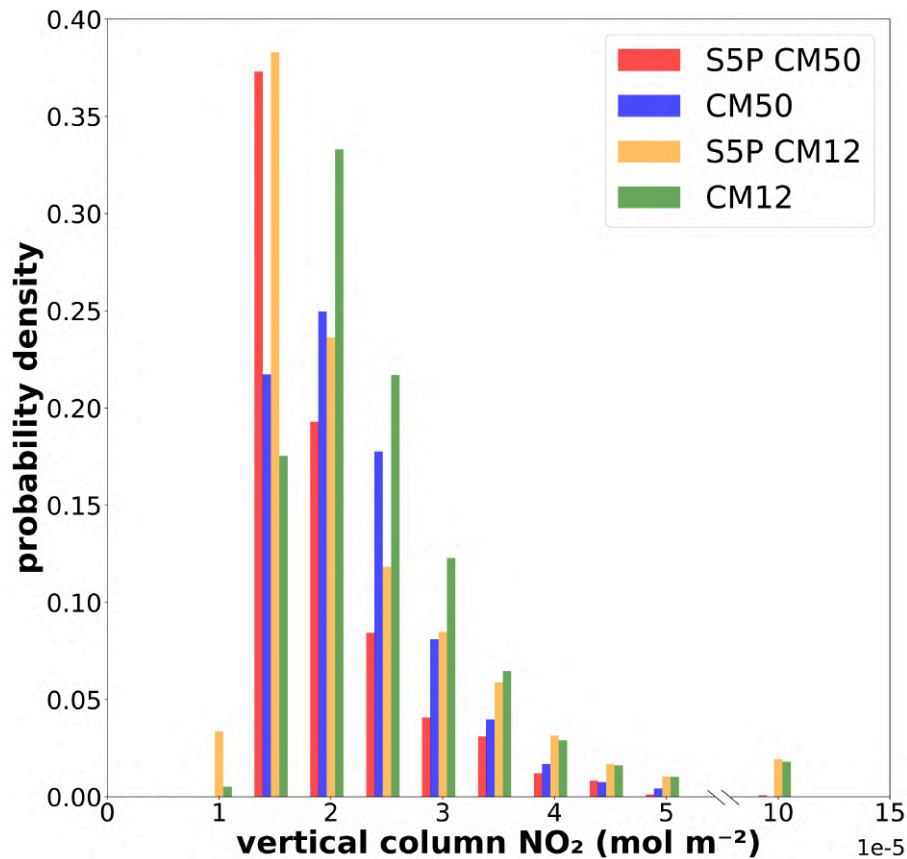


Figure 4.3: Histogram of the probability density of the tropospheric vertical NO₂ column (in units of 10^{-5} mol m⁻²) for Central Europe during JJA 2018 as Simulated by CM50 (blue) and CM12 (green). The probability density of the Sentinel-5P data is also shown, conservatively remapped onto both the CM50 (red) and CM12 (orange) grids, respectively. The probability densities of CM50 and CM12 are weighted based on the grid box area. The bin size is 0.5×10^{-5} mol m⁻² for values less than or equal to 5×10^{-5} mol m⁻² and 10×10^{-5} mol m⁻² for values larger than this threshold. Note that the x-axis is discontinuous.

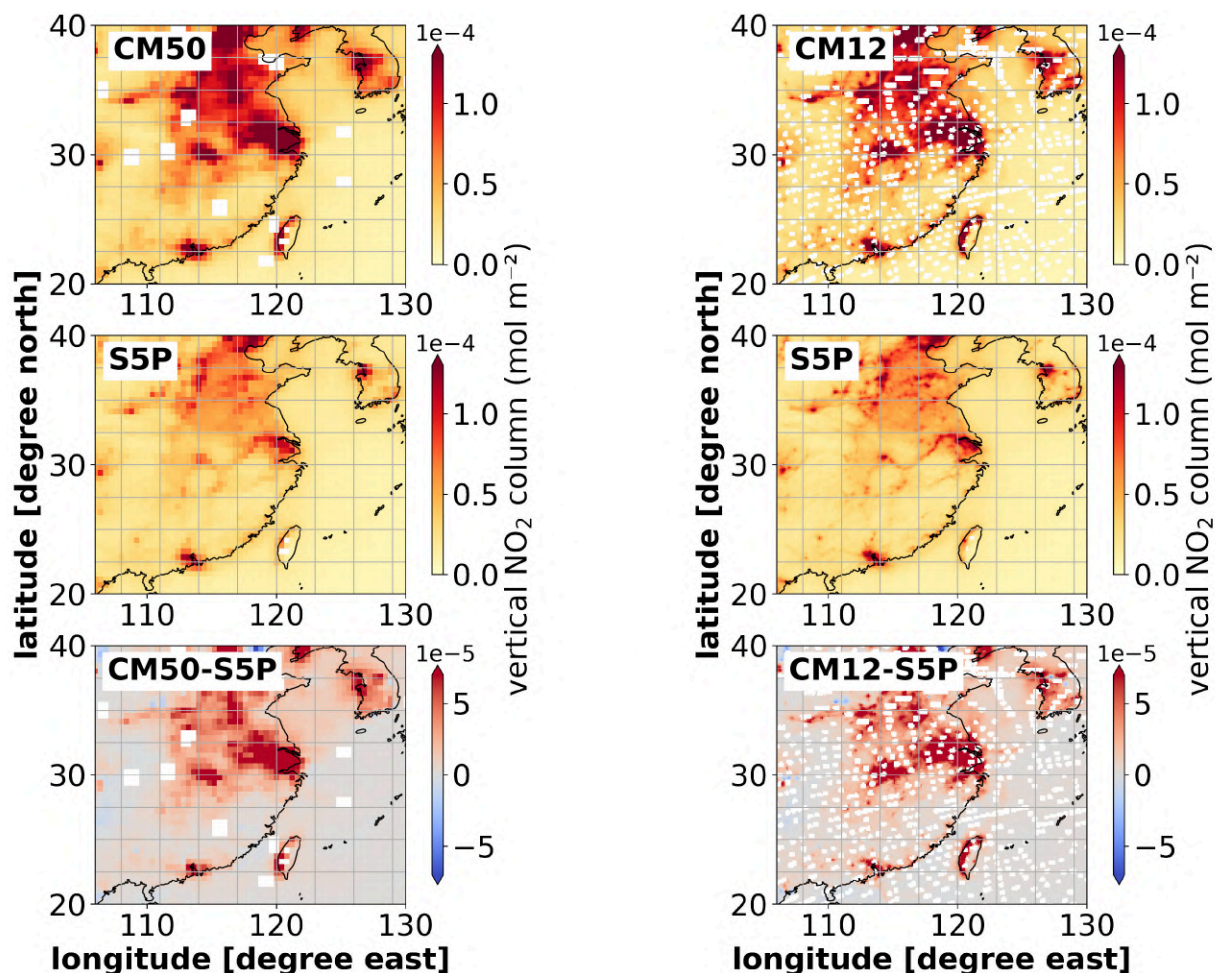


Figure 4.4: Shown is the tropospheric column of NO₂ in units of mol m^{-2} over East Asia for the JJA 2018 period, resulting from CM50 and CM12 model instances (upper panels), as well as the Sentinel-5P (S5P) data that have been re-mapped by conservative remapping onto the COSMO-CLM/MESSy grids (central panels). For S5P data the quality flag has been taken into account to exclude cloudy pixels. Additionally, the differences between the model and satellite data (CM50-S5P and CM12-S5P) are shown. Note that the colourbar of the model data and Sentinel 5P data with a scale of 10^{-4} differs from that of the differences (lower panels) with a scale of 10^{-5} . The undefined values in the model output of SORBIT in CM50 and CM12 are indicated by white pixels, which have been explained in section 3.3.7.

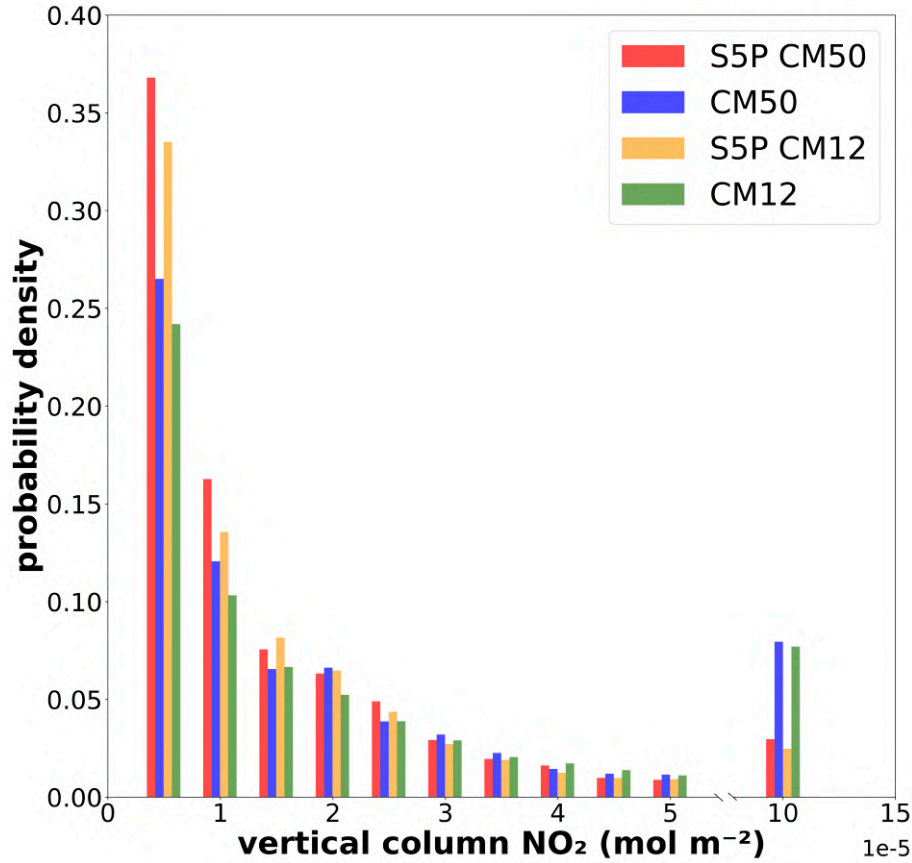


Figure 4.5: Histogram of the probability density of the Tropospheric Vertical NO₂ Column (in units of 10⁻⁵ mol m⁻²) for East Asia during JJA 2018 as Simulated by CM50 (blue) and CM12 (green). The probability density of the Sentinel-5P data is also shown, conservatively remapped onto both the CM50 (red) and CM12 (orange) grids, respectively. The probability densities of CM50 and CM12 are weighted based on the grid box area. The bin size is 0.5x10⁻⁵ mol m⁻² for values less than or equal to 5x10⁻⁵ mol m⁻² and 10x10⁻⁵ mol m⁻² for values larger than this threshold. Note that the x-axis is discontinuous.

4.2.2 Model results compared to satellite observations: Ozone

For the evaluation of simulated tropospheric O_3 , pre-processed Level-3 products from Sentinel-5P are utilised, which integrated tropospheric ozone based on tropopause pressure data from ERA5 reanalysis data. The integration of tropospheric O_3 column from the model data is performed using the same ERA5 tropopause pressure to avoid systematic errors resulting from differences in tropopause heights.

4.2.2.1 Europe

Figure 4.6 shows the vertical column of tropospheric O_3 data from CM50 (upper left) and CM12 (upper right) over Central Europe during JJA 2018. The central panels show the tropospheric ozone columns as measured by Sentinel-5P. The comparison between the model and satellite data reveals that CM50 overestimates tropospheric O_3 in most of Central Europe (lower left), with the highest values of up to 0.003 mol m^{-2} in areas such as Benelux, Northern France, the Po Valley, and the Balearic Islands. However, it slightly underestimates tropospheric O_3 in Central Italy and the Balkans. On the other hand, CM12 exhibits an even larger overestimation, with values of up to 0.005 mol m^{-2} (lower right), and a similar geographical distribution of this bias compared to CM50.

Figure 4.7 displays the PDF of the vertical O_3 column for Europe (JJA 2018) of CM50 and CM12, as well as those of the Sentinel-5P observations conservatively remapped onto the CM50 and CM12 grids, respectively. CM50 generally exhibits larger O_3 values compared to CM12. However, the PDFs of CM50 and CM12 show the largest frequencies of tropospheric O_3 columns over Europe at larger tropospheric O_3 columns than the satellite observations (represented in red and orange). In the case of CM12, the frequencies are slightly shifted to smaller tropospheric O_3 columns than those of CM50.

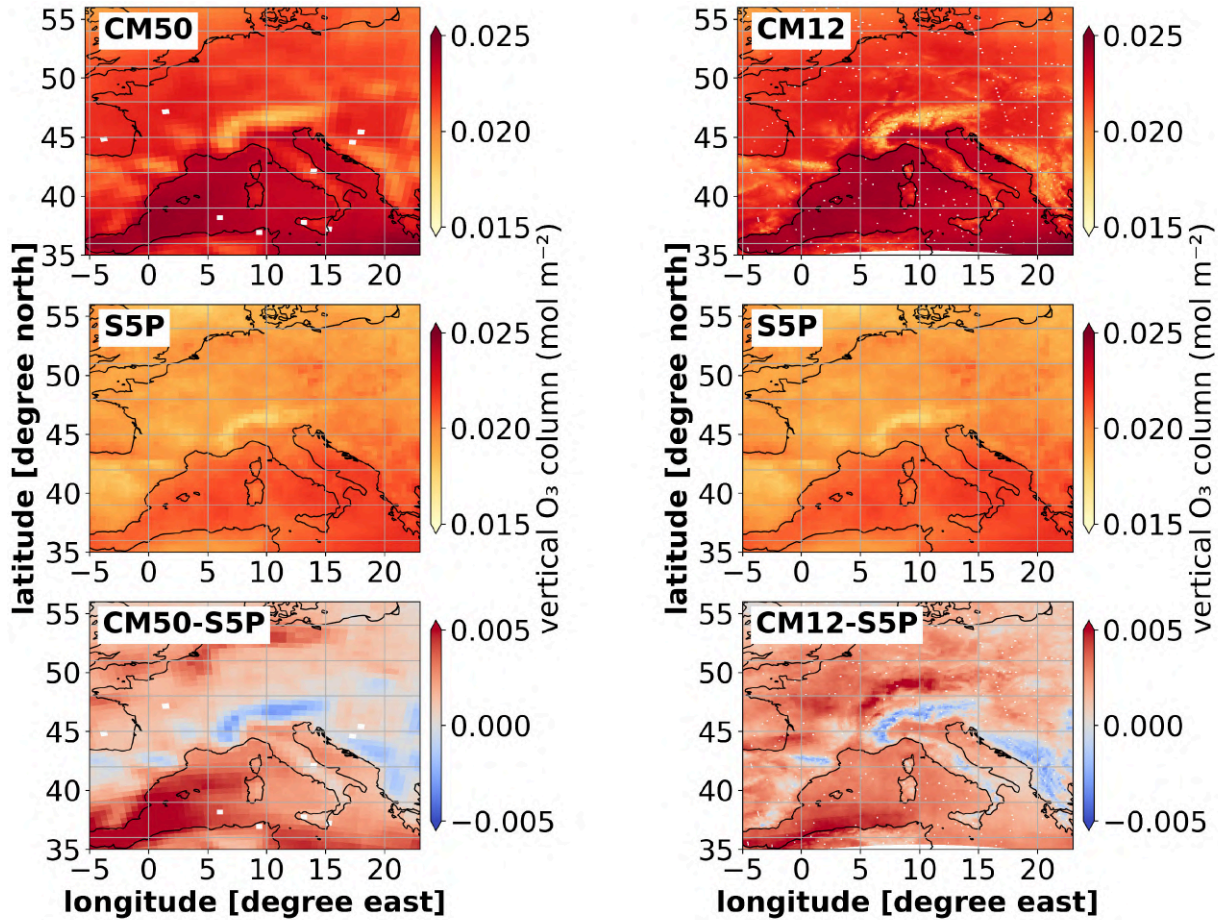


Figure 4.6: Shown is the tropospheric column of O₃ in units of mol m⁻² over Central Europe for the JJA 2018 period, resulting from CM50 and CM12 model instances (upper panels), as well as the Sentinel-5P (S5P) data that have been re-mapped by conservative remapping onto the COSMO-CLM/MESSy grids (central panels). For S5P data the quality flag has been taken into account to exclude cloudy pixels. Additionally, the differences between the model and satellite data (CM50-S5P and CM12-S5P) are shown. Note that the colourbar for the model data and Sentinel 5P data is differently scaled compared to the colourbar for the differences in the lower panels. The undefined values in the model output of SORBIT in CM50 and CM12 are indicated by white pixels, which have been explained in section 3.3.7.

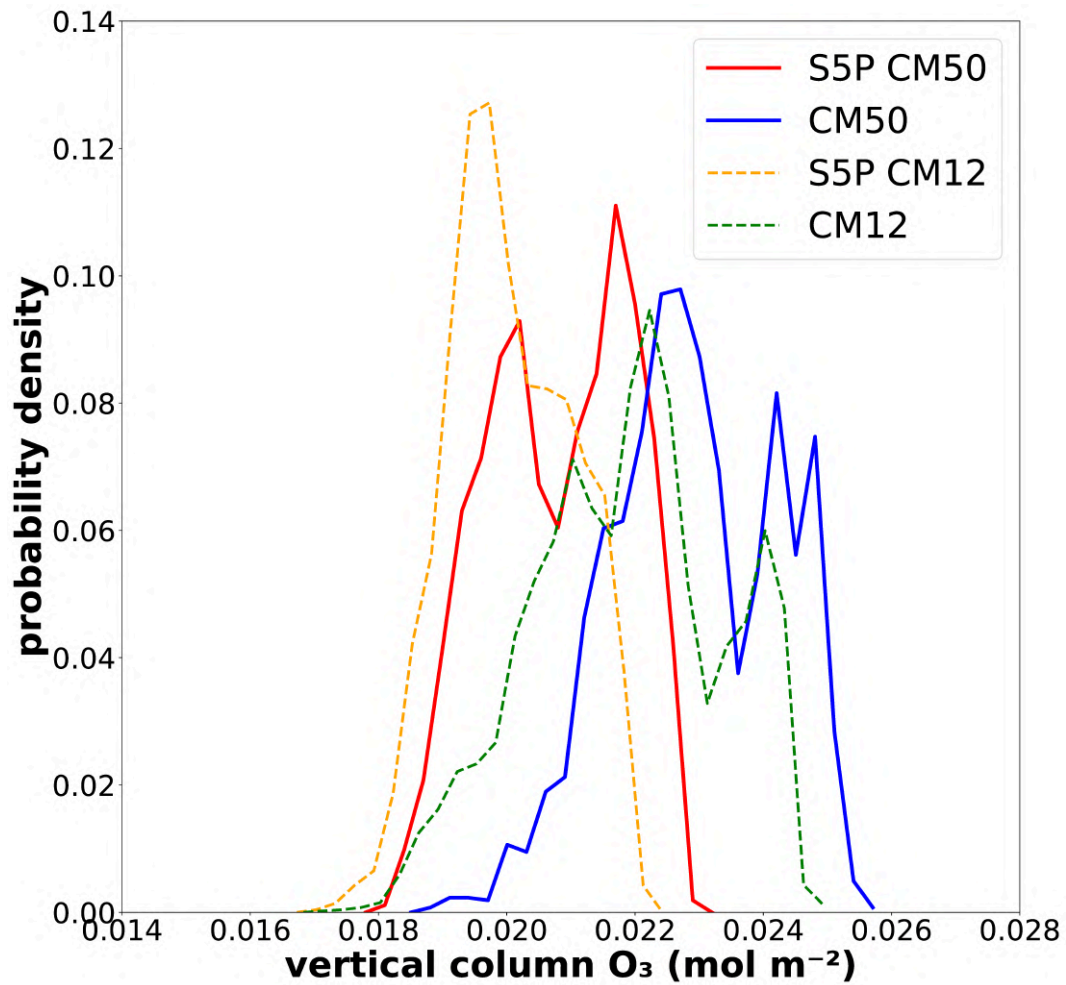


Figure 4.7: Probability density function (PDF) of the tropospheric vertical O_3 column (mol m^{-2}) for Central Europe during JJA 2018 as simulated by CM50 (blue) and CM12 (green dashed). The Sentinel-5P data PDF is also shown, which is conservatively remapped on both, the CM50 (red) and CM12 (orange dashed) grids, respectively. PDFs of CM50 and CM12 are weighted based on the grid box area. The bin size is 0.003.

4.2.2.2 East Asia

Figure 4.8 shows the vertical column of tropospheric O_3 simulated by CM50 and CM12 for JJA 2018 in East Asia. The largest tropospheric O_3 columns are simulated in North and Central China, with a South-North gradient in both cases. The central panels display the data retrieved by Sentinel-5P, interpolated on each COSMO-CLM/MESSy grid, respectively. The results show a similar South-North gradient but with smaller values. A comparison between the model and satellite data indicates that CM50 overestimates tropospheric O_3 , particularly in Central and parts of Southwest China (CM50-S5P), with values of up to 0.006 mol m^{-2} . However, the overestimation is less pronounced along the coast. Similarly, the ozone bias simulated by CM12 has a similar geographical distribution as that of CM50, but the underestimation of tropospheric O_3 in Southwest China is lower than that of CM50.

Figure 4.9 shows the PDFs of tropospheric O_3 in East Asia (JJA 2018) as simulated with CM50 and CM12, as well as of the interpolated Sentinel-5P observations on the respective COSMO-CLM/MESSy grid. The PDFs exhibit a bimodal distribution, indicating that regions with low O_3 values around 0.01 mol m^{-2} dominate a significant portion of East Asia and are well represented by both COSMO-CLM/MESSy model instances, CM50 and CM12. Tropospheric O_3 columns ranging from 0.012 – 0.017 mol m^{-2} are less frequent. The second peak of the probability density occurs between 0.020 and 0.024 mol m^{-2} . For large values, the frequencies for CM50 and CM12 are shifted to larger tropospheric O_3 columns than the S5P observations. In summary, CM50 and CM12 capture the geographical distribution of tropospheric O_3 and low values. Areas with high levels of O_3 have larger frequencies in CM50 and CM12 than in the S5P observations.

In order to assess the impact of tropopause height on the resulting tropospheric ozone column, Figure 4.10 compares two integration methods (M1 and M2) for Europe. The upper panels display the integration of tropospheric O_3 based on tropopause pressure from the COSMO-CLM/MESSy model output, while the central panels show the same integration based on tropopause pressure from ERA5 reanalysis data. The two integration methods, which use different tropopause pressures, result in a tropospheric O_3 column bias of up to 0.001 mol m^{-2} (10–20 %) in CM50 and CM12. The slightly larger differences between M1 and M2 at the edges, which appear as stripes, need further investigation. Since tropopause height can differ between models (e.g., COSMO, ECMWF, EMAC), using an inconsistent tropopause height from another model can cause a bias because a fraction of stratospheric ozone might or might not be integrated into the tropospheric ozone column.

Based on the information in Figure 4.10, a certain percentage of the O_3 bias can be attributed to variations in the free troposphere. It should be noted that even though the model and Sentinel-5P Level-3 product use the same tropopause pressure to integrate tropospheric O_3 , differences in the free troposphere can still occur.

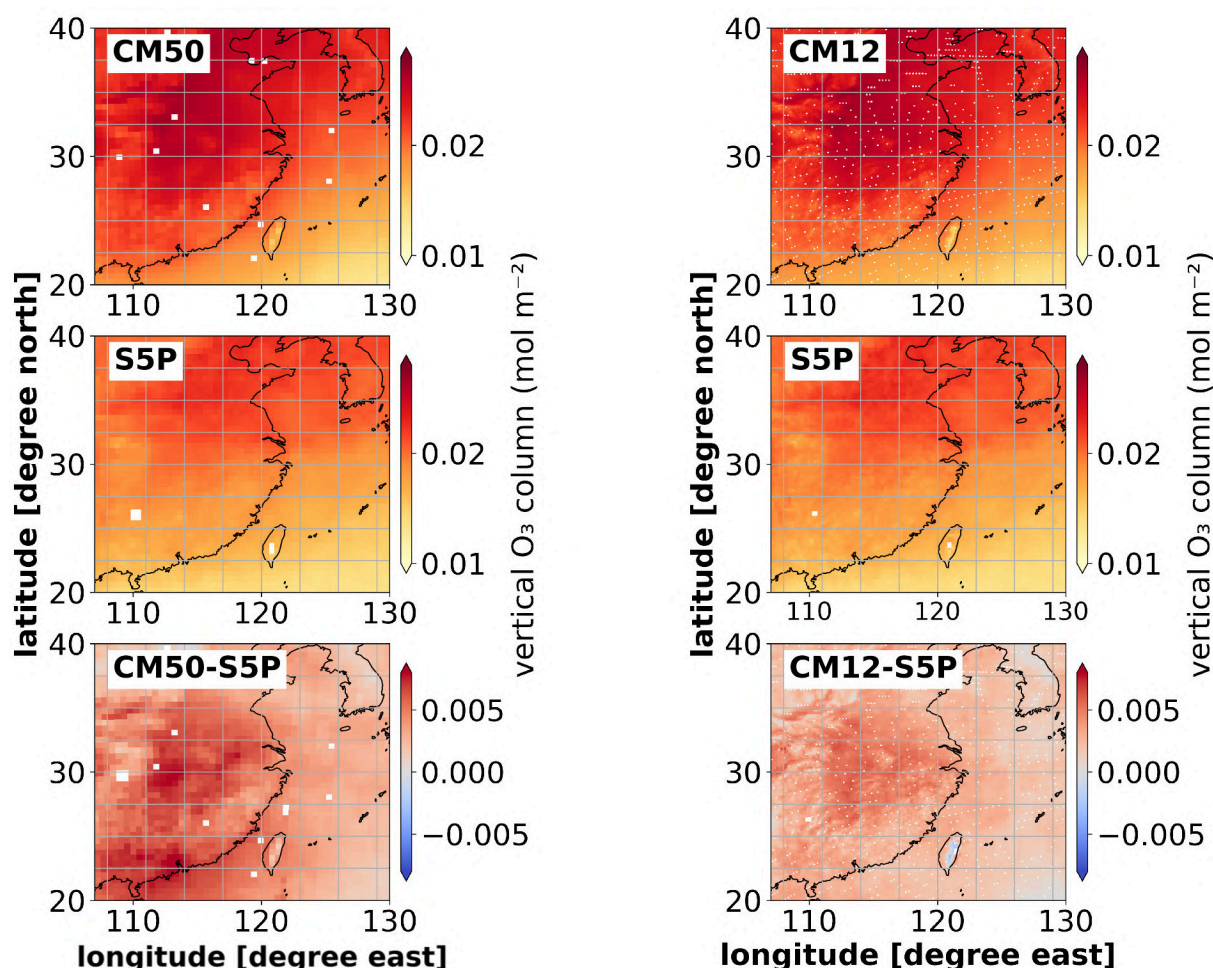


Figure 4.8: Shown is the tropospheric column of O_3 in units of mol m^{-2} over East Asia for the JJA 2018 period, resulting from CM50 and CM12 model instances (upper panels), as well as the Sentinel-5P (S5P) data that have been re-mapped by conservative remapping onto the COSMO-CLM/MESSy grids (central panels). For S5P data the quality flag has been taken into account to exclude cloudy pixels. Additionally, the differences between the model and satellite data (CM50-S5P and CM12-S5P) are shown. Note that the colourbar for the model data and Sentinel 5P data is differently scaled compared to the colourbar for the differences in the lower panels. The undefined values in the model output of SORBIT in CM50 and CM12 are indicated by white pixels, which have been explained in section 3.3.7.

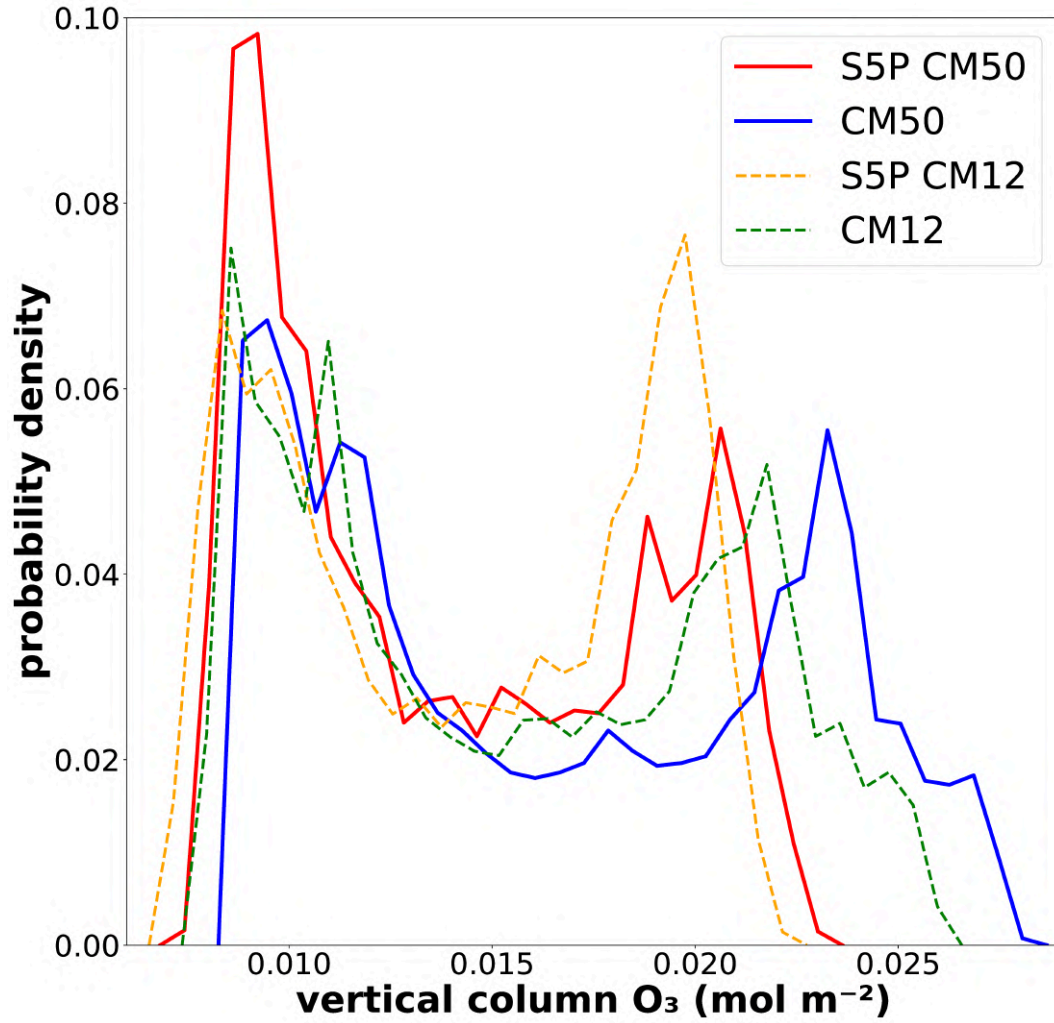


Figure 4.9: Probability density function (PDF) of the tropospheric vertical O_3 column (mol m^{-2}) over East Asia during JJA 2018 as simulated by CM50 (blue) and CM12 (green dashed). The Sentinel-5P data PDF is also shown, which is conservatively remapped on both, the CM50 (red) and CM12 (orange dashed) grids, respectively. PDFs of CM50 and CM12 are weighted based on the grid box area. The bin size is 0.006.

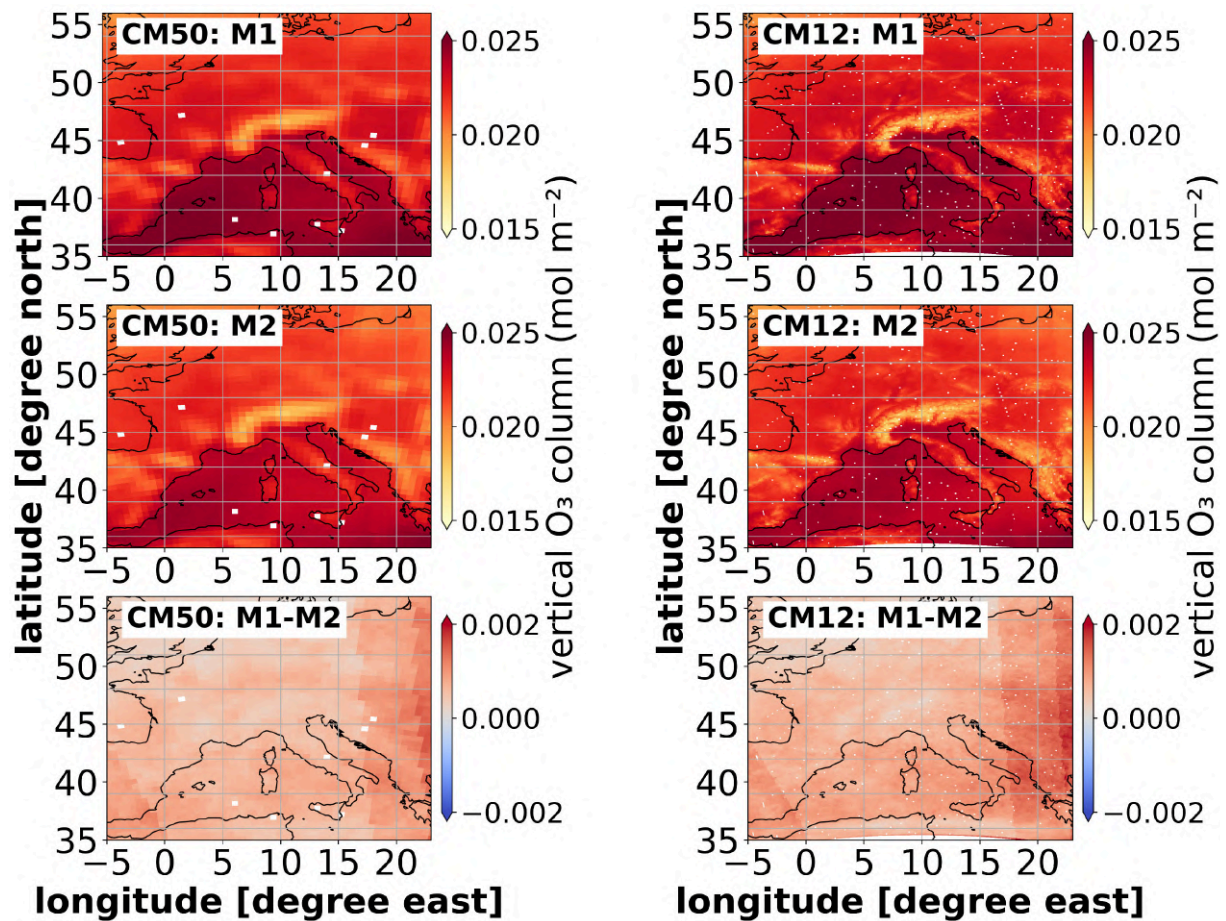


Figure 4.10: Tropospheric O₃ column in units of mol m⁻² over Central Europe for JJA 2018, simulated by CM50 and CM12. For the integration of the tropospheric O₃ column two different methods are compared. In method M1 O₃ is calculated based on the tropopause pressure from the COSMO-CLM/MESSy model output (upper panels), M2 is based on the tropopause pressure from the ERA5 reanalysis data (middle panels). M1-M2 shows the difference between both results (lower panel). Note that the colourbar for the model data and Sentinel 5P data is differently scaled compared to the colourbar for the differences in the lower panels. The undefined values in the model output of SORBIT in CM50 and CM12 are indicated by white pixels, which have been explained in section 3.3.7.

4.3 Ground-Level Observations

4.3.1 D21 Ozone Dataset

To assess the ground-level O_3 mixing ratios simulated by the MECO(n) model for Europe and East Asia, the results from the CM50 model instance are compared to the data product developed by Delang et al. [2021] further abbreviated as D21. D21 utilised the TOAR database, which contains a vast amount of O_3 measurements collected at different stations, and combined the results from nine atmospheric chemistry models, mostly from the first phase of the Chemistry-Climate Model Initiative (CCMI). The M³Fusion method¹³ was employed to create a composite of all nine atmospheric chemistry models, which corrects the model biases and searches a linear combination of model results that minimises the root mean square error as compared to the observations [Delang et al., 2021]. The observations of surface ozone span from 1970 to 2017, with fewer data available for 2016 and 2017, and are aggregated hourly.

Figure 4.11a displays the seasonal daily maximum 8-hour mixing ratio of ground-level O_3 (OSDMA8) in nmol mol^{-1} for CM50, while Figure 4.11b shows the same variable for data product D21 in 2017 from Delang et al. [2021]. The OSDMA8 is calculated as the annual maximum of the six-month running mean of the monthly average daily maximum 8-hour mixing ratio [Delang et al., 2021]. The geographical distribution of OSDMA8 across Europe is well captured by MECO(n), as is evident from the comparison. In Figure 4.11c, the D21 data is interpolated onto the CM50 grid, and the difference between CM50 minus D21 is computed. To illustrate the spatial variations between CM50 and D21, the difference is adjusted by subtracting $16.5 \text{ nmol mol}^{-1}$ (i.e., de-biased). This bias is $4\text{--}6 \text{ nmol mol}^{-1}$ higher than the average over the model domain in rural regions like the Alps, parts of the Iberian Peninsula, Wales, and the Balkan region. Conversely, the ozone bias in polluted regions like the Ruhr area, Benelux, parts of France, and the Po Valley is generally lower by $3\text{--}7 \text{ nmol mol}^{-1}$ than the average.

Figure 4.12 shows the same as Figure 4.11, but for East Asia. In Figure 4.12c, the D21 grid is interpolated onto the CM50 grid, and the difference is computed and adjusted by subtracting the positive bias of 21 nmol mol^{-1} . The comparison reveals that the ozone bias over North China is around $21 \pm 5 \text{ nmol mol}^{-1}$. In South China and Taiwan, CM50 overestimates O_3 around $20\text{--}25 \text{ nmol mol}^{-1}$ more than the mean bias of 21 nmol mol^{-1} . Generally, there exists a South-North gradient of the O_3 bias between CM50 and D21.

The evaluation of the model data with the D21 dataset for ground-level O_3 is consistent with the overestimation of O_3 in Europe and East Asia in CM50 found by the Sentinel-5P assessment of tropospheric O_3 (see section 4.2.2).

¹³A new statistical approach for combining observations and multiple model output.

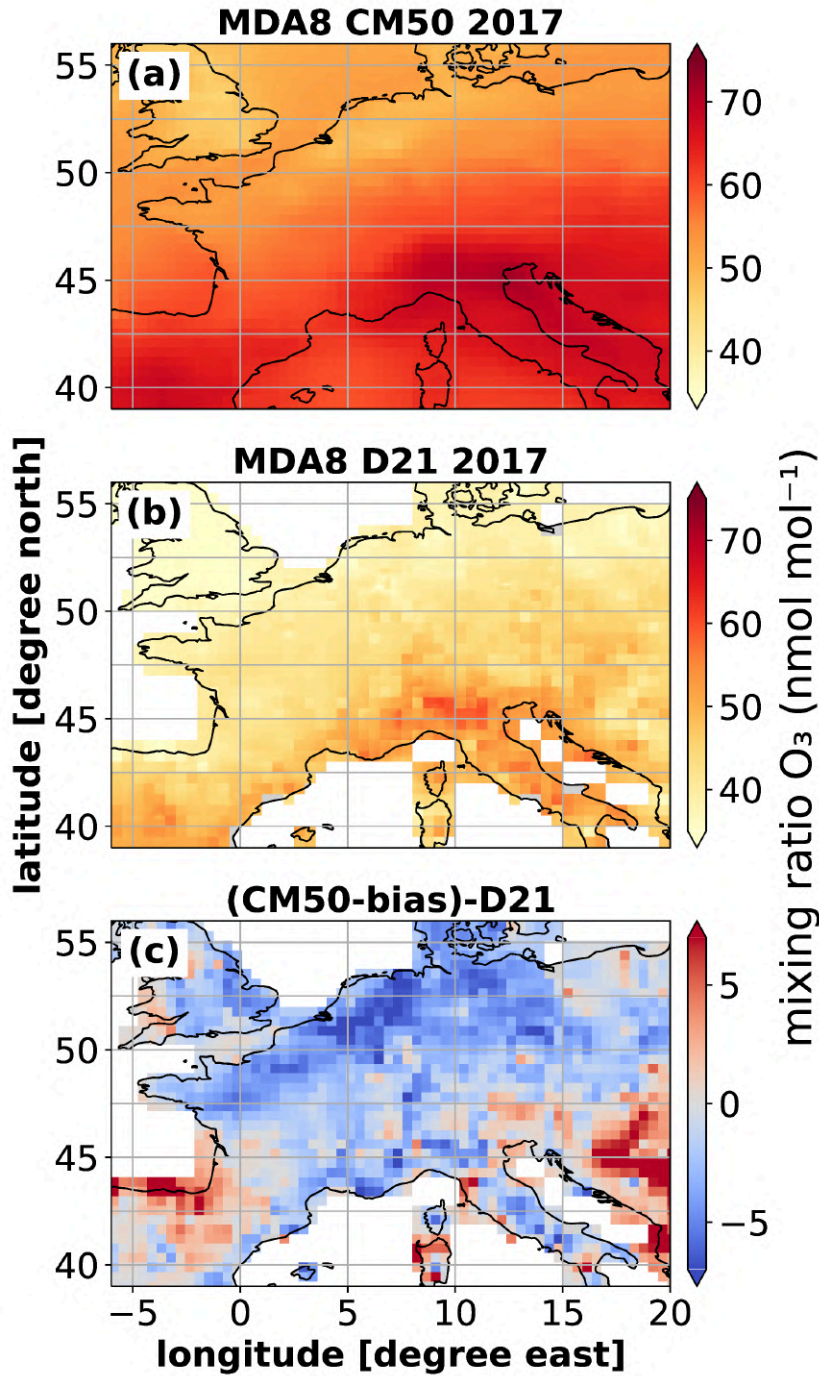


Figure 4.11: Comparison of the seasonal daily maximum 8-hour ground-level O_3 mixing ratio for Central Europe in 2017 of (a) CM50 ($0.44^\circ \times 0.44^\circ$) with the (b) TOAR database ($0.5^\circ \times 0.5^\circ$; Delang et al. 2021). For a better visibility of the spatial differences, the mean bias (MB) of $16.5\ nmol\ mol^{-1}$ is subtracted from the CM50 results and then the (c) difference between (de-biased) CM50 results minus the D21 data set has been calculated.

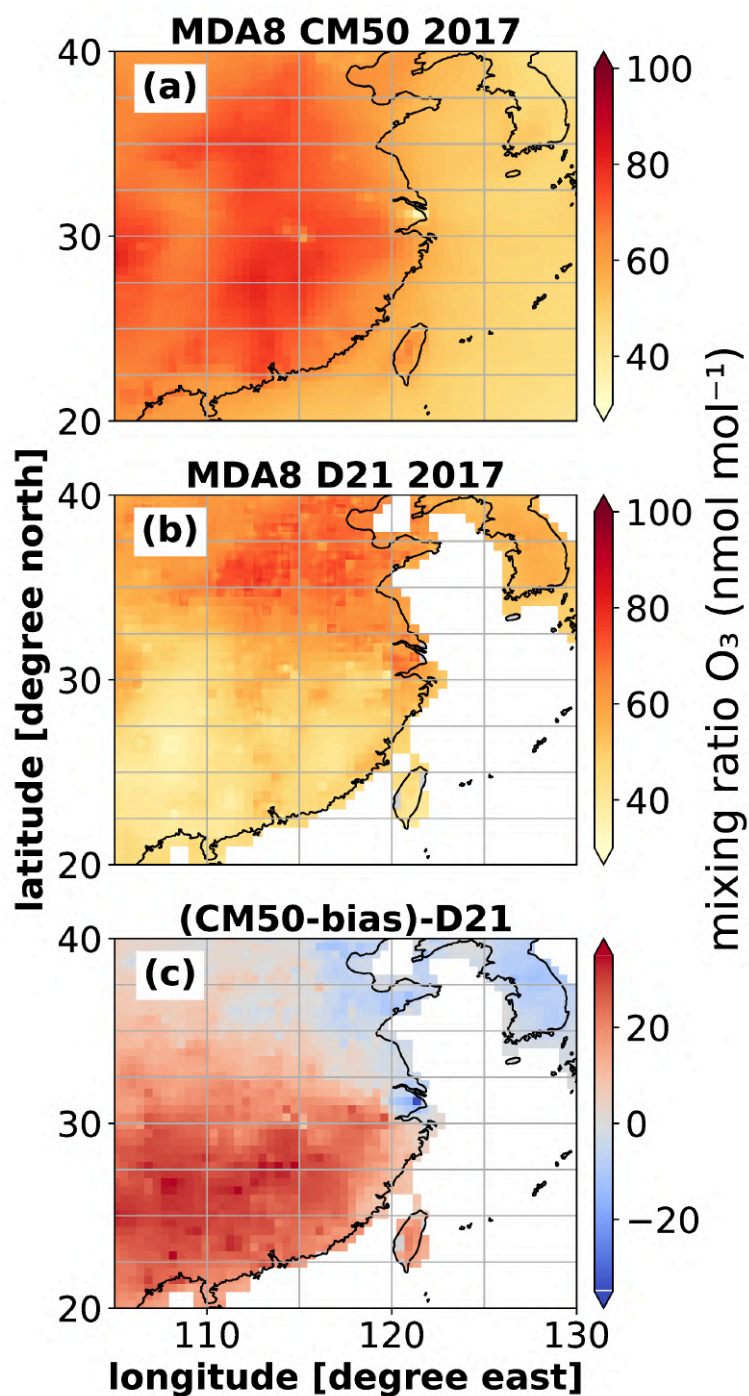


Figure 4.12: Comparison of the seasonal daily maximum 8-hour ground-level O_3 mixing ratio for East Asia in 2017 of (a) CM50 ($0.44^\circ \times 0.44^\circ$) with the (b) TOAR database ($0.5^\circ \times 0.5^\circ$; Delang et al. 2021). For a better visibility of the spatial differences, the MB of $21.0\ nmol\ mol^{-1}$ is subtracted from the CM50 results and then the (c) difference between (de-biased) CM50 results minus the D21 data set has been calculated.

4.3.2 Air Quality Stations

With the here applied spatial resolution of the nested regional model, it cannot be expected that observed steep gradients near strong sources (e.g. at traffic sites or near industrial sites) are reproduced. Therefore, I restrict the evaluation to stations labelled as 'background' or 'rural'. Several data points are missing, likely due to technical issues during the measurements, and these have been excluded from the analysis. For a direct comparison of the model results with the measurements, I sampled the model data at the positions of the measurement stations, using a nearest neighbor approach, from hourly model output of CM12 [e.g., Xu et al., 2023].

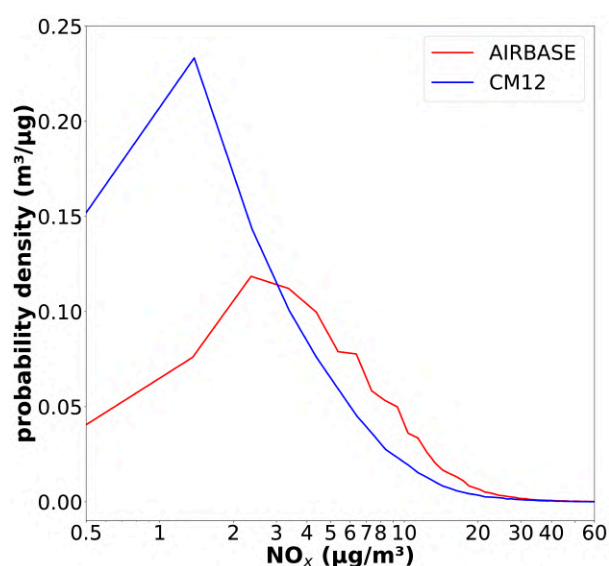


Figure 4.13: Probability density function of the hourly ground-level NO_x concentrations in $\mu\text{g m}^{-3}$ of the model output of CM12 (blue) and the rural AIRBASE station data (red) for July 2017 in Europe.

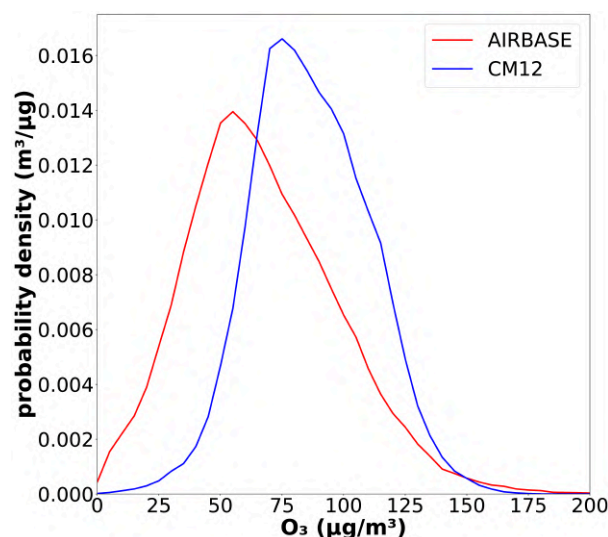


Figure 4.14: Probability density function of the hourly mean ground-level O_3 concentrations in $\mu\text{g m}^{-3}$ of the model output of CM12 (blue) and the rural AIRBASE station data (red) for July 2017 in Europe.

4.3.2.1 Airquality Stations Europe

In order to evaluate simulated ground-level O_3 concentrations, a comparison with observational data from the AIRBASE network is performed. AIRBASE is a European air quality database, maintained by the EEA (European Environment Agency)¹⁴ through its European topic centre on Air pollution and Climate Change mitigation [European Environment Agency, 2018]. The database contains air quality monitoring data and information submitted by participating countries throughout Europe.

Figures 4.13 and 4.14 show the observed and simulated probability density functions (PDFs) of NO_x and O_3 at 253 rural and background measurement stations in Europe,

¹⁴Data is available at <https://www.eea.europa.eu/data-and-maps/data/aqereporting-8>.

respectively. The comparison reveals that the frequency of observed NO_x concentrations below $3 \mu\text{g m}^{-3}$ is overestimated by CM12 (blue line), whereas that for larger NO_x concentrations it is underestimated. Compared to the observed, the simulated PDF of O_3 is shifted towards larger ozone concentrations. The model underestimates the frequency of small ozone values and overestimates the frequency of large ozone values, except for those above $150 \mu\text{g m}^{-3}$. The mean biases (MB) of simulated NO_x and O_3 (all stations), compared to the observations, are $-2.8 \mu\text{g m}^{-3}$ and $19.9 \mu\text{g m}^{-3}$, respectively. The Root Mean Square Errors (RMSE) of simulated NO_x and O_3 , compared to the observations, are $8.9 \mu\text{g m}^{-3}$ and $22.6 \mu\text{g m}^{-3}$, respectively. The MB and RMSE of ozone is comparable to previous evaluations of MECO(n) (Mertens et al. 2020b, their Table 7). The evaluation of the model results with the AIRBASE data for ground-level O_3 shows a relative overestimation of 32.8 % (MB), which is consistent with the D21 dataset, which shows an overestimation of 28.8 % in Europe (see section 4.3.1).

4.3.2.2 Airquality Stations East Asia

In order to evaluate ground-level O_3 of the COSMO-CLM/MESSy model output in East Asia, a comparison with observational data from the World Air Quality Index (AQICN) project is performed. All air quality data for East Asia arise from the AQICN network, which is part of the Environmental Protection Agency (EPA)¹⁵. For China 153 rural and background stations are selected. Figure 4.15 depicts the diurnal cycle of ground-level NO_2 . Although CM12 represents the diurnal cycle of NO_2 very well, it tends to overestimate NO_2 during the night and early morning hours (0:00–9:00 local solar time) by approximately $2.5 \text{ nmol mol}^{-1}$. Conversely, during the day, CM12 underestimates NO_2 by roughly $-2.5 \text{ nmol mol}^{-1}$. The root mean square error (RMSE) for the diurnal cycle of NO_2 is relatively low, at $1.9 \text{ nmol mol}^{-1}$. However, the observed amplitude of NO_2 is overestimated by CM12, with $9.5 \text{ nmol mol}^{-1}$ compared to the observed amplitude of 4 nmol mol^{-1} . CM12 systematically overestimates ground-level O_3 throughout the day compared to the EPA stations, with a RMSE of $29.9 \text{ nmol mol}^{-1}$ (Fig. 4.16). This overestimation is consistent with the analysis based on the D21 dataset, for which CM50 overestimates ground-level O_3 by about $21.0 \text{ nmol mol}^{-1}$ throughout 2017 (see section 4.3.1). However, CM12 accurately captures the diurnal cycle of O_3 , except for a 1–2 hours lag of the simulated maximum compared to the EPA observations.

In the morning hours at 6:00 local solar time, CM12 overestimates the mixing ratios of O_3 and NO_2 at most of the EPA stations. Only at a few stations does CM12 show good agreement (Fig. B.27, p. 182). The overestimation of O_3 could be caused by an underestimation of O_3 depletion (e.g., O_3 titration) in CM12 during that time. During MDA8 ozone the overestimation of the O_3 mixing ratios in CM12 decreases in comparison with the morning hours (Fig. B.28, p. 182). When compared to EPA air quality observations, CM12 is better at representing MDA8 O_3 than O_3 during the morning hours.

The evaluation of the model results with the EPA data for ground-level O_3 in comparison

¹⁵Data is available at <https://aqicn.org/map/china/>, last access: 02.03.2023 (Environmental Protection Agency 2018).

with the results for the D21 dataset is consistent for East Asia. For both, the models results show a relative overestimation (MB) of ground-level O_3 with 44.8 % (MB) and 38.1 %, respectively (see section 4.3.1).

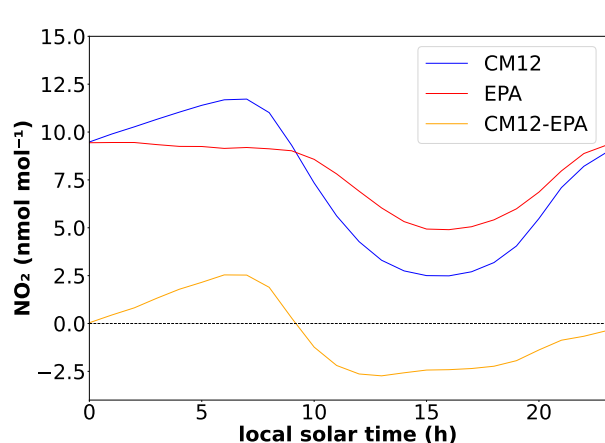


Figure 4.15: Observed (EPA, red) and simulated (CM12, blue) diurnal cycle of the hourly ground-level NO_2 mixing ratios (in nmol mol^{-1}) during JJA 2018 averaged over 153 rural EPA stations. The difference CM12-EPA is shown in orange.

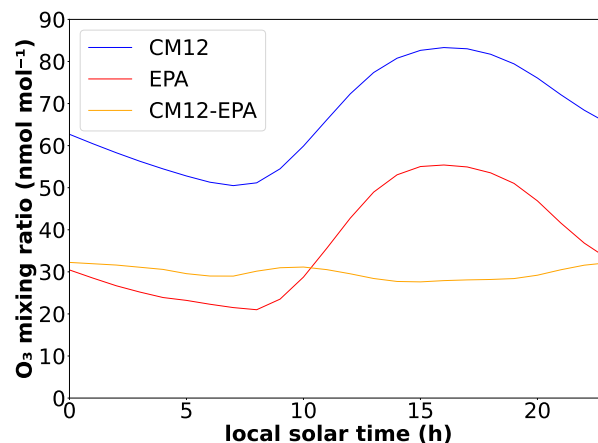


Figure 4.16: Observed (EPA, red) and simulated (CM12, blue) diurnal cycle of the hourly ground-level O_3 mixing ratios (in nmol mol^{-1}) during JJA 2018 averaged over 153 rural EPA stations. The difference CM12-EPA is shown in orange.

4.4 Observations from campaigns

This evaluation concentrates on specific study areas using measurements from in situ flight data (see section 4.4.1) and shipborne MAX-DOAS measurements (see section 4.4.2).

4.4.1 HALO in situ measurements during EMeRGe measurement campaigns

The goal of the Effect of Megacities on the Transport and Transformation of Pollutants on the Regional to Global Scales (EMeRGe) campaigns was to measure downwind plumes from major polluted regions and to study their transport and transformation [Andrés Hernández et al., 2022]. A detailed description of the instrumentation is provided by Andrés Hernández et al. [2022] and Ziereis et al. [2022]. For my analyses only O_3 and NO_y in-situ measurement data from EMeRGe Europe and East Asia have been used. For the evaluation, the S4D model output (see section 3.3.6) is vertically interpolated on the model pressure levels and then sampled by using the nearest neighbor method, based on the measured pressure.

This section first provides a quantitative comparison of all flights conducted during both campaigns, followed by a detailed evaluation of one flight per campaign that occurred within my defined study areas. It is important to note that a point-to-point intercomparison between the aircraft in-situ measurements and model data is still limited, despite the

fact that the model system is operated in specified dynamics (SD) mode. Thus, specific features such as city and power plant plumes can be shifted in time (or space) compared to the observations [see also discussion in Andrés Hernández et al., 2022].

4.4.1.1 EMeRGe Europe

In July 2017, the EMeRGe Europe flight measurement campaign was conducted using HALO flights that covered Central Europe, Western Europe, South France, and Central Italy (Fig. B.29, p. 182).

Overall, CM12 represents NO_y and O_3 compared to the in situ measurements from EMeRGe Europe well (Figs. B.30–B.33, see p. 183). Despite this, the results indicate, that the model performance, compared to the observations, varies strongly for each flight. CM12 better represents small NO_y mixing ratios up to 3 nmol mol^{-1} during all flights than larger mixing ratios, which are often underestimated. The summary listed in Table 4.1 shows that the NO_y mixing ratio of the flights on the 13th and 28th of July 2017 have the smallest RMSE, with $0.75 \text{ nmol mol}^{-1}$ each. The strongest correlations between simulated (CM12) and observed NO_y , with a R^2 0.47 and 0.62 result for the flights on the 11th and 13th of July 2017, respectively. The RMSE between simulated (CM12) and observed NO_y (all flights) is $2.9 \text{ nmol mol}^{-1}$, and the model data moderately correlate with the in situ data with a R^2 of 0.4. For three flights the model (CM12) overestimates NO_y with a MB of $0.5 \text{ nmol mol}^{-1}$, for four flights CM12 underestimates NO_y by $-0.8 \text{ nmol mol}^{-1}$ (see Table 4.1).

During EMeRGe Europe, the instruments on board of the HALO aircraft measured ozone in a range of $20\text{--}100 \text{ nmol mol}^{-1}$. CM12 tends to overestimate the O_3 along all flights. The smallest RMSE for O_3 (compared to the observations) is simulated along the flight tracks on the flights on July 11th, 17th, 24th, and 26th, with values ranging from $11.9\text{--}14.4 \text{ nmol mol}^{-1}$. The MB for O_3 is rather small and ranges from $5.3\text{--}11.8 \text{ nmol mol}^{-1}$. The strongest correlation between CM12 and the in situ data appears for the flights on July 11th, 13th, and 17th, with a R^2 ranging from 0.54–0.70. Overall, CM12 represents O_3 well, although it tends to slightly overestimate it with a MB of $10.6 \text{ nmol mol}^{-1}$. Some simulated results deviate considerably from the observed data, and even no correlations ($R^2=0$) between the two are present for some flights. A possible reason for this is that HALO crossed downwind plumes which are displaced in time and/or space in the model results or that not all sources have been taken into account for the CM12 simulation. In particular the displacements of simulated features cause a double penalty problem, causing deviations of model simulations to appear larger than they actually are. Moreover, very small scale features observed by the instrumentation on board the HALO aircraft cannot be resolved by CM12 with its $12 \text{ km} \times 12 \text{ km}$ grid resolution.

Due to these limitations, this study focuses on a more qualitative analysis of only one flight date in Europe, while two additional flights and their analyses are presented in the Appendix B.2.1 (p. 168). Figure 4.17 depicts the comparison of the observational data with CM12 model results for the Po Valley at the 11th of July 2017. It indicates, that NO_y at 725 hPa (left panel) is well represented by the model and enhancements of

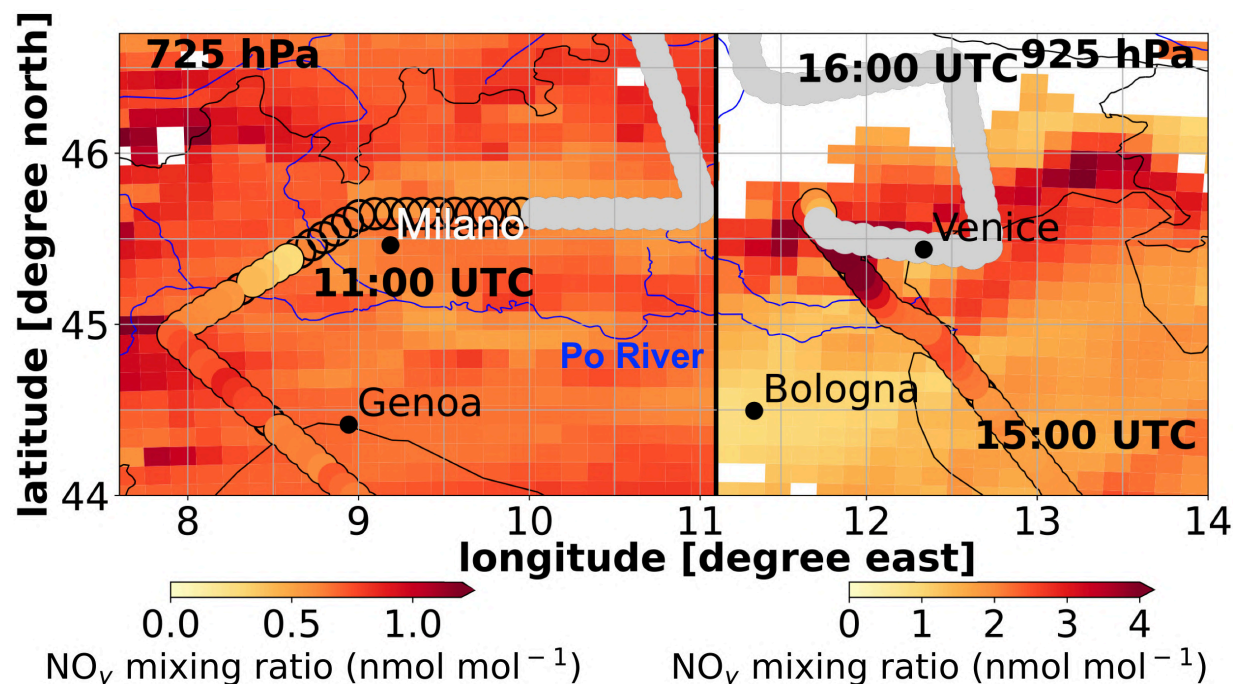


Figure 4.17: CM12 simulated NO_y mixing ratios in nmol mol^{-1} (background color) at 725 hPa (11 UTC) and 925 hPa (15 UTC), respectively, and the HALO in situ measurements (filled circles) for the flight date 11.07.2017 in the Po Valley. The grey filled circles mask the measurement data, when HALO leaves the shown pressure level. The white spots mark the grid points in which the surface pressure is lower than 725 hPa (left) and 925 hPa (right), respectively. Unfilled circles mark the missing data.

NO_y west of Genoa are reproduced. The NO_y outflow of the Po Valley west of Venice at 925 hPa agrees geographically and temporally very well (right panel). The vertical profiles of NO_y displayed in Figures 4.19 and 4.21 confirm the agreement between measurements and simulation results.

Compared to NO_y , O_3 is mostly overestimated, as shown for the pressure levels at 725 hPa and 925 hPa, respectively (Fig. 4.18). Figure 4.20 and 4.22 confirm the overestimation of O_3 at 725 hPa in CM12 and show large O_3 values above 700 hPa, which have not been measured by HALO. This is caused by differences between the large-scale meteorological conditions in the model results compared to the real world, which causes an area with large O_3 mixing ratios above Northern Italy (as explained above in section 4.4.1).

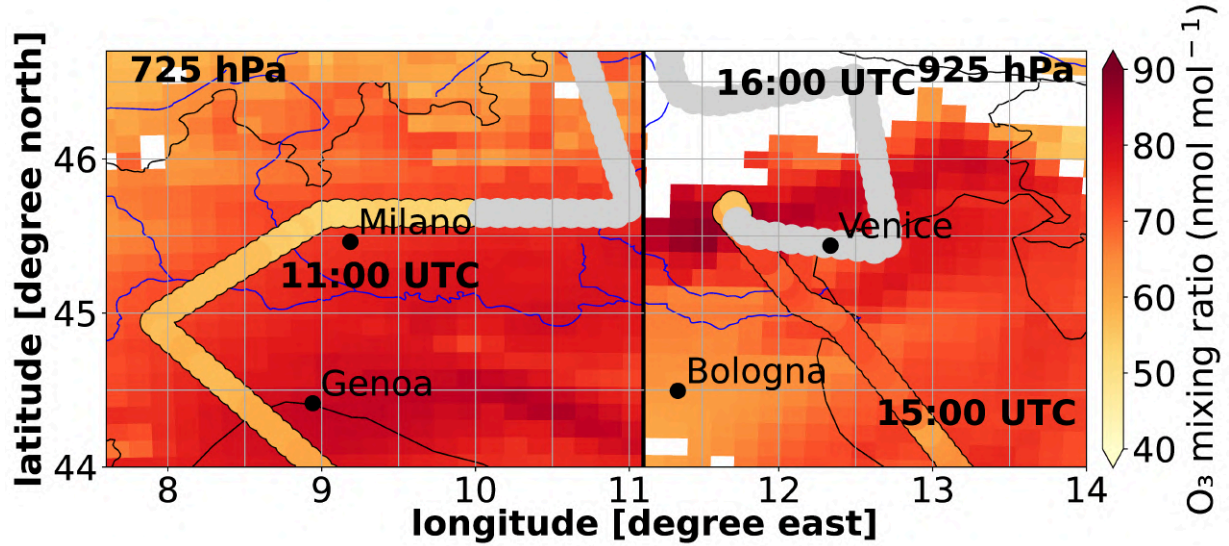


Figure 4.18: CM12 simulated O_3 mixing ratios in nmol mol^{-1} (background color) at 725 hPa (11 UTC) and 925 hPa (15 UTC), respectively, and the HALO in situ measurements (filled circles) for the flight date 11.07.2017 in the Po Valley. The grey filled circles mask the measurement data, when HALO leaves the shown pressure level. The white spots mark the grid points in which the surface pressure is lower than 725 hPa (left) and 925 hPa (right), respectively.

Table 4.1: RMSE, MB and squared Pearson correlation coefficient (R^2) of CM12 simulation results compared to observations from the EMeRGE Europe campaign, for NO_y and O_3 , respectively. The MB is calculated separately for negative and positive biases.

Flight	NO_y				O_3			
	MB	MB	RMSE	R^2	MB	MB	RMSE	R^2
unit	nmol mol^{-1}	%	nmol mol^{-1}		nmol mol^{-1}	%	nmol mol^{-1}	
11.07.2017	0.6	42.6	0.8	0.47	11.8	15.4	14.4	0.54
13.07.2017	0.3	24.2	0.7	0.62	10.6	15.7	14.4	0.70
17.07.2017	-0.6	-49.7	1.3	0.29	13.0	22.9	18.0	0.57
20.07.2017	-0.5	-23.9	3.8	0.08	5.0	7.4	16.0	0.01
24.07.2017	-0.3	-40.2	2.0	0.03	5.3	8.8	11.9	0.38
26.07.2017	-1.9	-111.1	8.4	0.00	7.8	14.1	14.1	0.37
28.07.2017	0.5	26.9	0.8	0.09	11.2	17.7	18.2	0.18
Mean	-0.8/0.5	-56.2/31.2	2.9	0.40	10.6	14.6	17.5	0.58

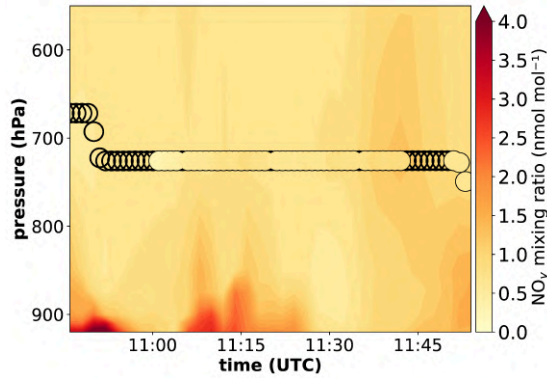


Figure 4.19: Comparison between simulated (CM12) NO_y mixing ratios in nmol mol^{-1} sampled along the flight path (background color) with the on board in situ measurements (filled circles) for the flight date 11.07.2017 in the Po Valley. Unfilled circles mark the missing data.

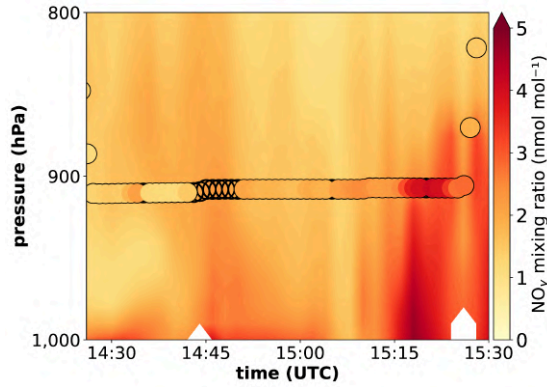


Figure 4.21: Comparison between simulated (CM12) NO_y mixing ratios in nmol mol^{-1} sampled along the flight path of CM12 (background color) with the on board in situ measurements (filled circles) for the flight date 11.07.2017 in the Po Valley. Unfilled circles mark the missing data.

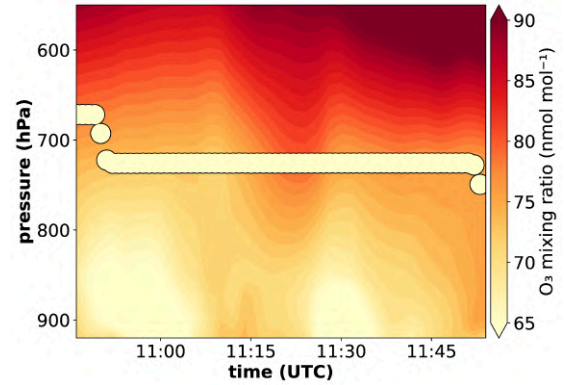


Figure 4.20: Comparison between simulated (CM12) O_3 mixing ratios in nmol mol^{-1} sampled along the flight path (background color) with the on board in situ measurements (filled circles) for the flight date 11.07.2017 in the Po Valley.

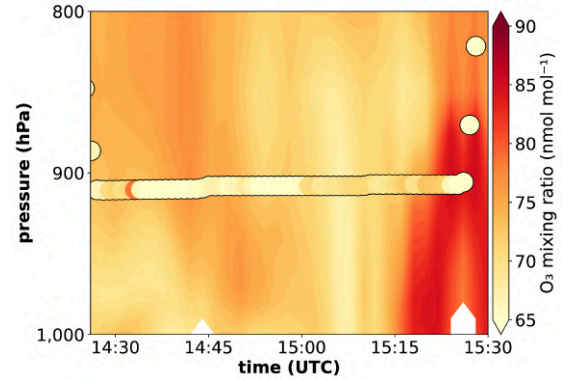


Figure 4.22: Comparison between simulated (CM12) O_3 mixing ratios in nmol mol^{-1} sampled along the flight path of CM12 (background color) with the on board in situ measurements (filled circles) for the flight date 11.07.2017 in the Po Valley.

4.4.1.2 EMeRGe Asia

The EMeRGe Asia flight measurement campaign was conducted in March and April 2018 across East Asia (see Fig. B.34, p. 184). The flights primarily covered the areas between Thailand, the Philippines, Taiwan and Japan, with the aim of investigating the impact of pollution outflow from megacities, conurbations, and major population centers on a regional scale. My study focuses on the outflow of polluted areas such as Shanghai Delta and Taiwan.

The comparison between results from CM12 and the in situ measurements of NO_y for all 11 flights conducted during EMeRGe Asia is done in the following (Figs. B.35, B.37 and B.39, pp. 184–185). The distribution of NO_y in East Asia is very in-homogeneous and characterised by large gradients (see Chapter 3, Fig. 3.1b). At least with respect to the EMeRGe in-situ data, CM12 overestimates NO_y for large mixing ratios, whereas smaller mixing ratios are better represented. The RMSE for most flights (7 out of 11) is between 3 and 7 nmol mol^{-1} , with the smallest deviation occurring on 28th March and 7th April 2018 (see Table 4.2). Overall, there is an overestimation of NO_y by CM12, with a MB of 2.7 nmol mol^{-1} . The correlation of CM12 with the in situ data is only moderate, with a coefficient of 0.49.

The same comparison is done for O_3 (Figs. B.36, B.38 and B.40, pp. 184–185). It shows that CM12 overestimates O_3 along all flight tracks, with a MB of 18.2 nmol mol^{-1} (see Table 4.2). However, for the 12th, 24th, and 26th March, CM12 shows a smaller overestimation of O_3 within the range of 5.6–8.0 nmol mol^{-1} . Only on the 7th of April, CM12 underestimates O_3 by -5.7 nmol mol^{-1} . The RMSE is relatively large, about 22.7 nmol mol^{-1} for all flights. The correlation between the CM12 output and the in situ data is weak, with a correlation coefficient of 0.24 for all flights. The strongest correlation with 0.54–0.59 for O_3 with CM12 is found for the flights on the 12th and 20th March. It is worth noting that during four flights, the simulated O_3 values exhibit no correlation with the observations.

The reason for this is that the downwind plumes that HALO crossed are displaced in time and/or space in the model results. The displacement of simulated features causes a double penalty problem, where deviations in model simulations appear larger than they actually are, resulting in an overestimation of discrepancies between model results and observations (for more details, see subsection 4.4.1.1). In the following, a detailed evaluation is only done for one flight. Additional flights are further investigated in the Appendix, specifically in section B.2.2 (p. 168).

The comparison of observational data with CM12 model output above the coast of Taiwan on March 22nd, 2018 is shown in Figure 4.23 and 4.25. This round flight between Tainan and Taichung was conducted to measure local plumes. The model shows a good representation of NO_y at 975 hPa along the coast of Taiwan, and reproduces enhancements of NO_y between Tainan and Taichung, but slightly overestimates them. The reason for this is the large gradient of NO_y between the coast and the mainland, which is larger than 12 nmol mol^{-1} within 3 model grid boxes in CM12.

The topography within the vicinity of the west coast of Taiwan largely exceeds the height of the planetary boundary layer (BL), as illustrated in Fig. B.41 (p. 186). This, in

Table 4.2: RMSE, MB and squared Pearson correlation coefficient (R^2) of CM12 simulation results compared to observations from the EMERGE Asia campaign, for NO_y and O_3 , respectively. The MB is calculated separately for negative and positive biases.

	NO_y				O_3			
Flight	MB	MB	RMSE	R^2	MB	MB	RMSE	R^2
unit	nmol mol ⁻¹	%	nmol mol ⁻¹		nmol mol ⁻¹	%	nmol mol ⁻¹	
12.03.2018	0.8	43.9	3.5	0.61	8.0	12.9	13.7	0.54
17.03.2018	2.9	66.1	5.0	0.19	25.0	30.1	26.1	0.43
19.03.2018	2.0	61.7	4.4	0.04	26.5	31.1	30.2	0.08
20.03.2018	2.9	79.8	7.0	0.05	21.9	27.6	24.1	0.59
22.03.2018	4.2	53.9	5.7	0.31	19.9	23.7	21.4	0.00
24.03.2018	2.6	41.1	5.5	0.10	7.9	10.8	18.5	0.07
26.03.2018	4.8	65.9	9.6	0.26	5.6	7.7	13.9	0.02
28.03.2018	1.2	47.5	2.2	0.45	19.7	24.6	24.2	0.08
30.03.2018	1.6	55.6	3.0	0.30	15.3	19.9	22.9	0.00
03.04.2018	6.5	80.1	8.8	0.12	34.7	39.9	39.7	0.02
07.04.2018	0.4	18.8	1.6	0.73	-5.7	-8.5	16.1	0.01
Mean	2.7	55.9	5.1	0.49	-5.7/18.2	-8.5/20.8	22.7	0.24

turn, favours the trapping of ground-level emissions within the BL along the coast, leading to significant emission gradients.

Figure 4.25 confirms the agreement between simulated and observed NO_y between around 08:30 UTC, i.e. the plume above the mainland, despite the strong gradient. Furthermore, CM12 reproduces the in situ measurements of the background NO_y above the Taiwan Strait.

The vertical representation of NO_y in Figure 4.27 shows the agreement between the CM12 model output and the in situ data. Although the plume pattern simulated by CM12 appears at the same time as for the in situ data at 7:30 UTC and 8:30 UTC, it appears at lower levels. This vertical displacements might be caused by the model's underestimated Boundary Layer (BL) height, which causes the simulated NO_y plume to remain lower than the observed. This finding is in line with [Szintai and Kaufmann, 2014]'s conclusion that the height of well-developed boundary layers (≈ 2500 m) in the COSMO model is mostly underestimated.

Additionally, the in situ data exhibit larger NO_y mixing ratios at 925 hPa and 900 hPa than those simulated by CM12. For a better comparison between the in situ and model data, the background of Figure 4.24 shows the comparison between the in situ data and CM12 output for O_3 at the west coast of Taiwan on March 22nd 2018. The results indicate that CM12 overestimates O_3 mixing ratios above the Taiwan Strait by 20–25 nmol mol⁻¹. However, between the north of Tainan and the south of Taichung on the mainland, CM12 shows very good agreement with the in situ data of O_3 . This is consistent with Figure 4.26, which shows a slight overestimation of O_3 simulated by CM12 above the ocean.

The vertical representation of O_3 is shown in Figure 4.28 and indicates an overall good agreement between the simulated and observed patterns, but also illustrates differences between in situ data and the CM12 model output. The NO_y overestimated by CM12 causes the large O_3 mixing ratios at 7:30 UTC and 8:30 UTC. Moreover, the simulated extremum of the plume along this flight track lags about 15 minutes behind the measurements (see section 4.4.1).

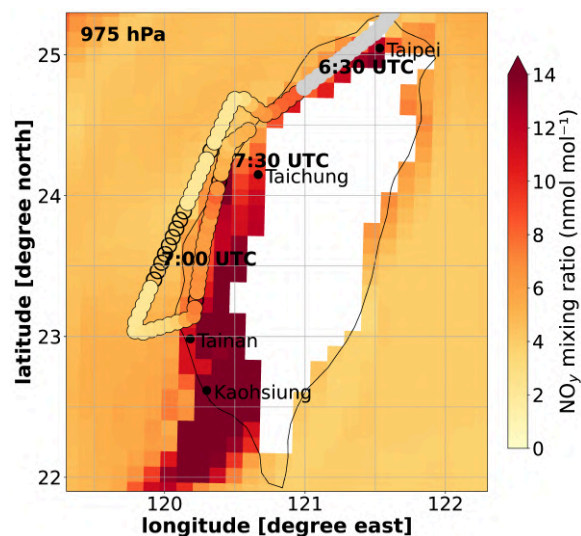


Figure 4.23: CM12 simulated NO_y mixing ratios in nmol mol^{-1} at 6 UTC (background color) and at 975 hPa, and the HALO in situ measurements (filled circles) for the flight date 22.03.2018 in Taiwan. Unfilled circles mark the missing data. The white spots mark the grid points in which the surface pressure is lower than 975 hPa. The grey filled circles mask the measurement data, when HALO leaves the shown pressure level.

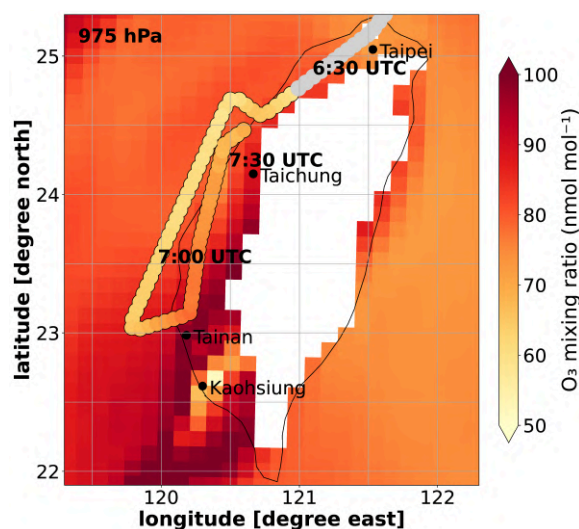


Figure 4.24: CM12 simulated O_3 mixing ratios in nmol mol^{-1} at 6 UTC (background color) and at 975 hPa, and the HALO in situ measurements (filled circles) for the flight date 22.03.2018 in Taiwan. The white spots mark the grid points in which the surface pressure is lower than 975 hPa. The grey filled circles mask the measurement data, when HALO leaves the shown pressure level.

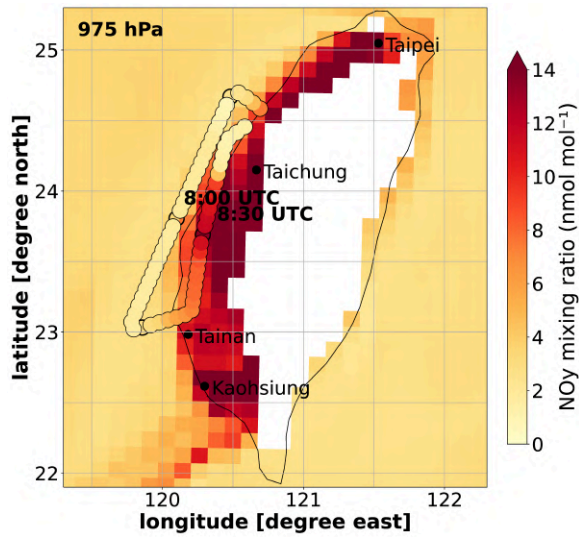


Figure 4.25: CM12 simulated NO_y mixing ratios in nmol mol^{-1} at 9 UTC (background color) and at 975 hPa, and the HALO in situ measurements (filled circles) for the flight date 22.03.2018 in Taiwan. The white spots mark the grid points in which the surface pressure is lower than 975 hPa.

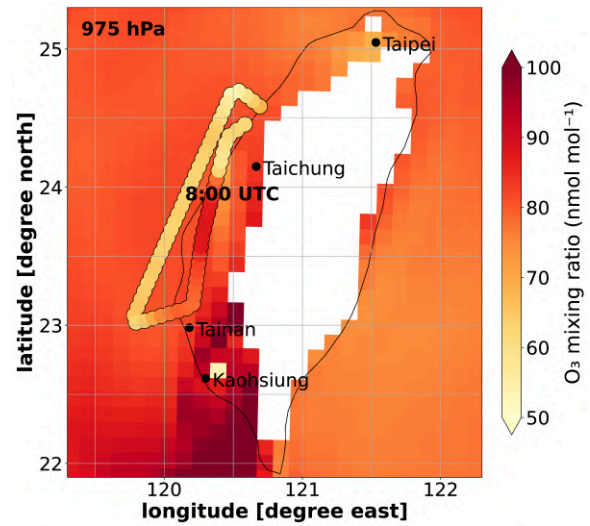


Figure 4.26: CM12 simulated O_3 mixing ratios in nmol mol^{-1} at 9 UTC (background color) and at 975 hPa, and the HALO in situ measurements (filled circles) for the flight date 22.03.2018 in Taiwan. The white spots mark the grid points in which the surface pressure is lower than 975 hPa.

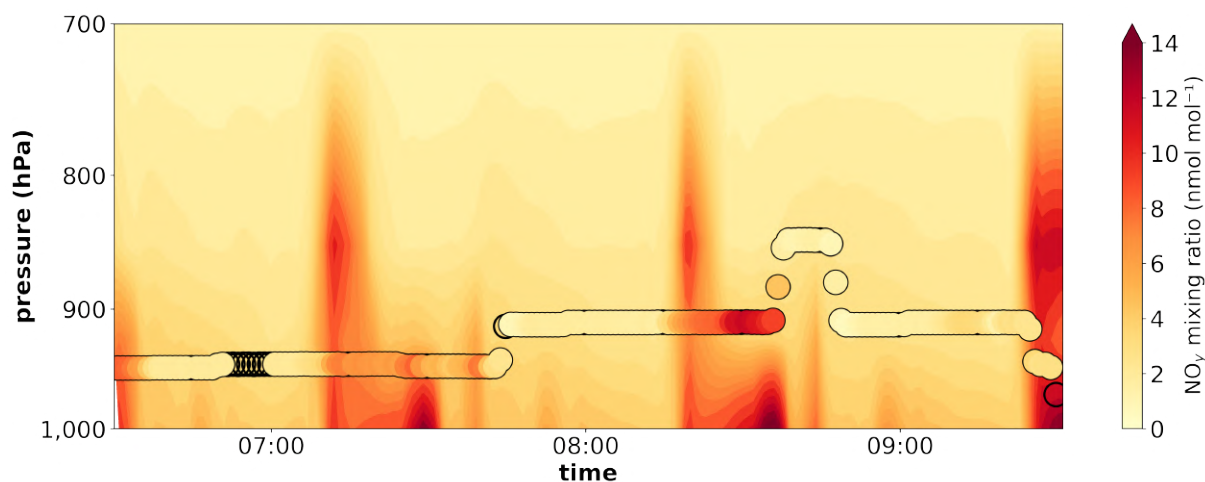


Figure 4.27: Comparison between model results of NO_y mixing ratios in nmol mol^{-1} sampled along the flight path (background color) with the on board in situ measurements (filled circles) for the flight date 22.03.2018.

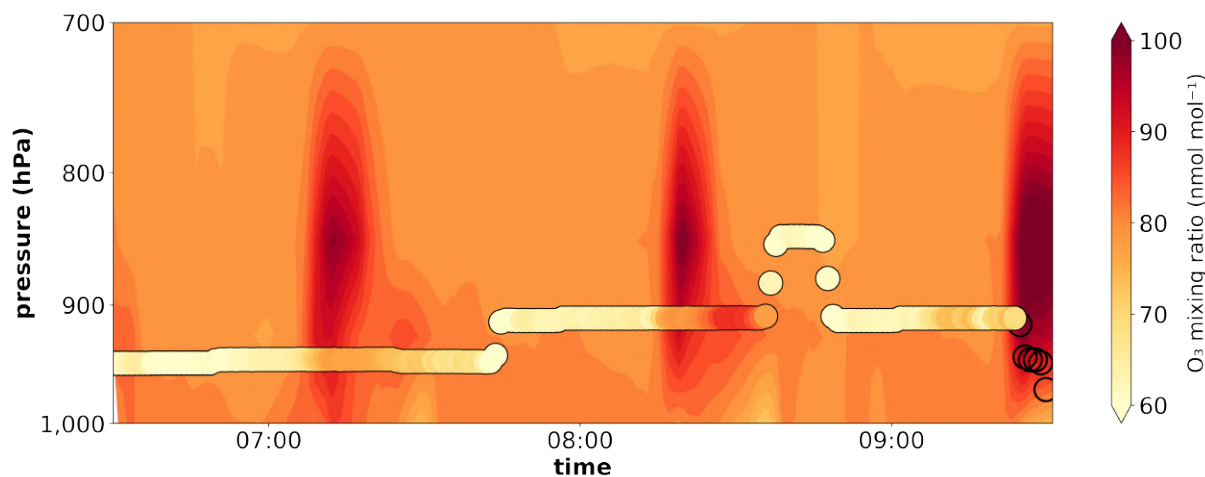


Figure 4.28: Comparison between simulated (CM12) O_3 mixing ratios in nmol mol^{-1} sampled along the flight path (background color) with the on board in situ measurements (filled circles) for the flight date 22.03.2018.

4.4.2 MAX-DOAS measurements over the East China Sea

Ship-based multi-axis differential optical absorption spectroscopy (MAX-DOAS) measurements had been taken over the East China Sea from 2nd to 29th June 2017, as reported by Tan et al. [2018]. Figure 4.29 shows all shipping routes along which the measurements conducted throughout the campaign. The authors used the differential optical absorption spectroscopy (DOAS) technique to retrieve the tropospheric slant column densities (SCDs) of NO_2 and formaldehyde (HCHO) from the measured spectra. By adopting a simple geometric approach, they converted the SCDs of the observed trace gases at 15° and 30° elevation angle into tropospheric vertical column densities (VCDs). In this study, the VCDs of NO_2 combined from both elevation angles are considered for the comparison with the model results.

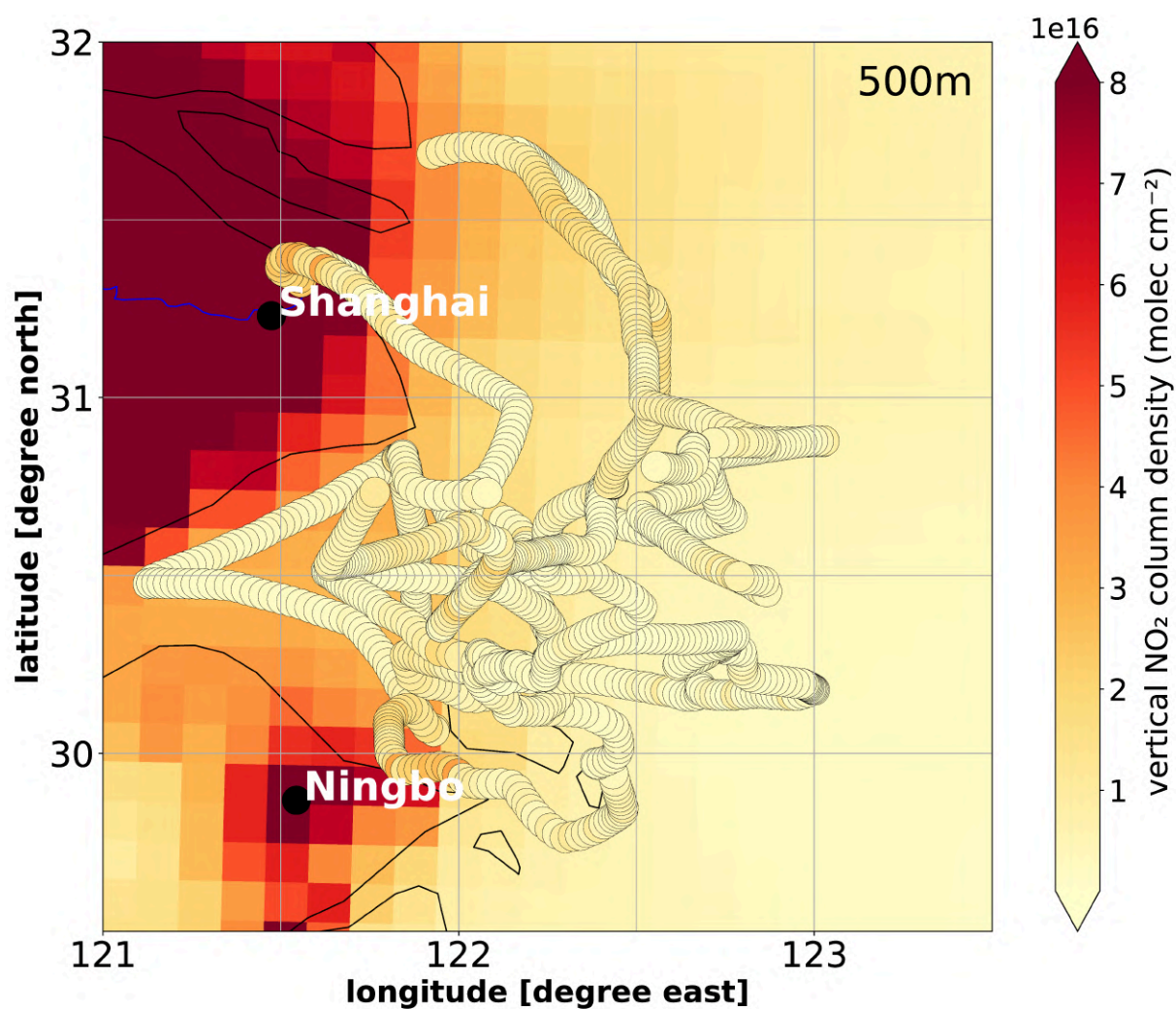


Figure 4.29: Comparison between mean model results of NO₂ vertical column densities in molecules cm⁻² integrated up to 500 m (background color) with the MAX DOAS ship-based measurements (filled circles) for the campaign between 2nd and 29th of June 2017. The time resolution of the shown MAX-DOAS NO₂ measurements is 8 minutes.

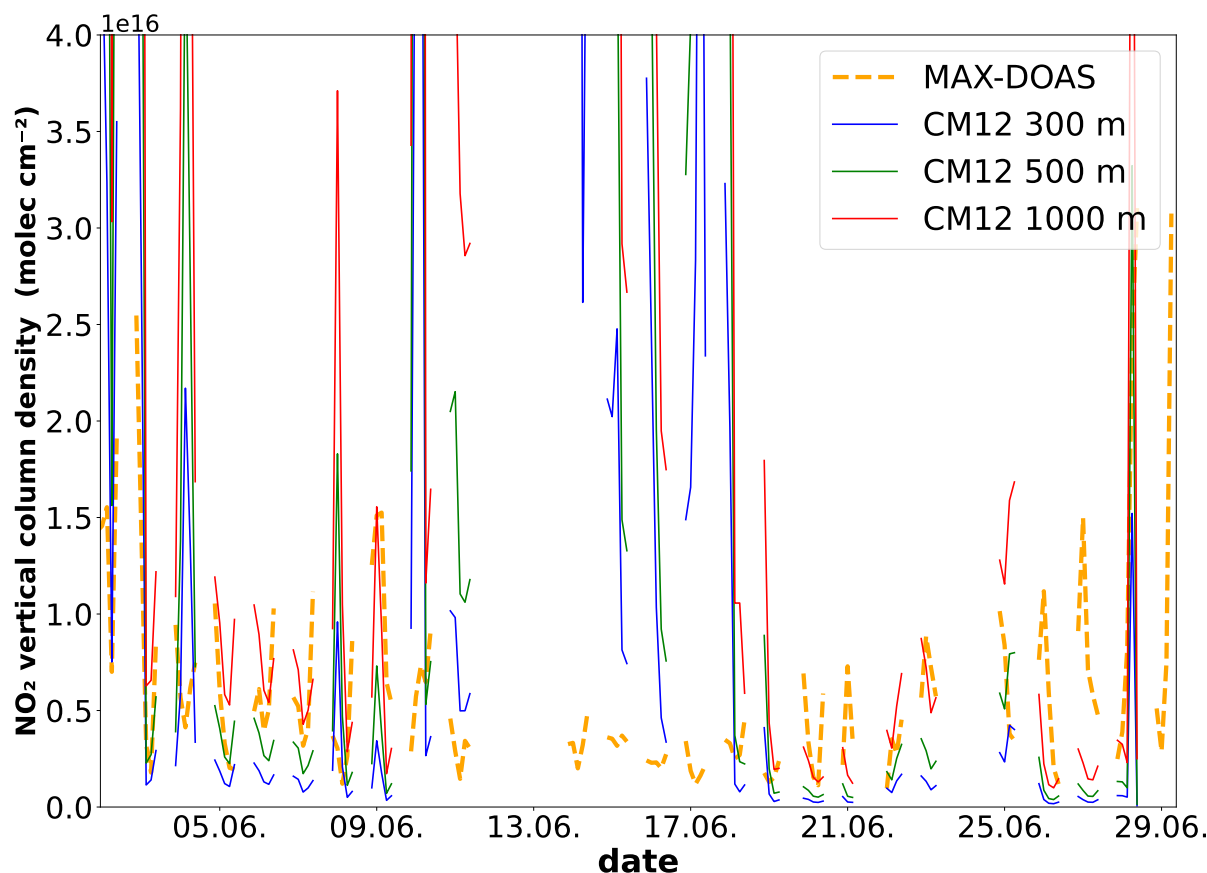


Figure 4.30: Timeseries of the simulated (CM12) NO_2 vertical column densities as 3h means in molecules cm^{-2} (blue) with the MAX-DOAS ship-based measurements (dashed orange) for the whole campaign between 2nd and 29th of June 2017.

The data from the CM12 model is converted from nmol mol^{-1} to molecules cm^{-2} and integrated vertically. Since the height up to which MAX-DOAS measures NO_2 is unknown, and the sensitivity of the MAX-DOAS instruments decreases with height [Li et al., 2020b], different integration heights are assumed to estimate the uncertainty. The geographical illustration of NO_2 VCDs in Figure 4.29 are calculated for an integration height of 500 m. The majority of offshore NO_2 vertical column densities (VCDs) fall below or around 1×10^{16} molecules cm^{-2} , as depicted in Figure 4.29. These findings are similar to those reported by Li et al. [2020b], who recorded NO_2 VCDs of approximately 1.0×10^{16} molecules cm^{-2} over the Qingdao offshore area. My model results are consistent with those obtained over the Tai'an region during May–June 2006, which are slightly lower at 0.94×10^{16} molecules cm^{-2} , according to Irie et al. [2008].

Over the Jiaozhou Bay, Li et al. [2020b] found NO_2 VCDs of up to 3.7×10^{16} molecules cm^{-2} , which is considerably larger than the model results. Similarly, the model results show maximum NO_2 VCDs of up to 8×10^{16} molecules cm^{-2} in the vicinity of Shanghai and Ningbo, indicating significant NO_2 pollution in the surrounding regions of megacities. In general the calculated NO_2 VCDs from the model results are comparable

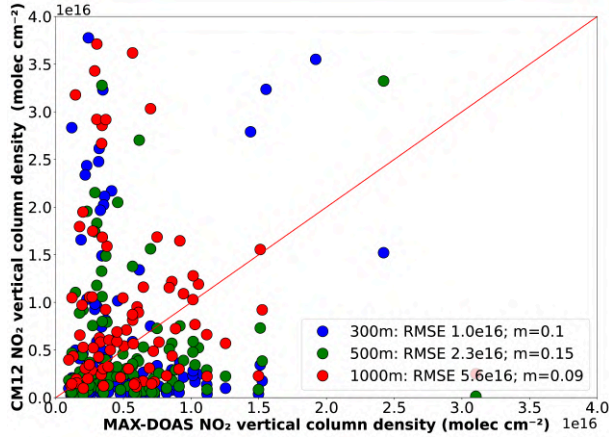


Figure 4.31: Comparison between model results of the NO_2 vertical column densities in molecules cm^{-2} (vertical-axis) with the MAX-DOAS ship-based measurements (horizontal-axis) for the campaign between 2nd and 29th of June 2017. Shown are the results for three different integration heights: 300m (blue), 500m (green) and 1000m (red). Data are 3-hourly averages.

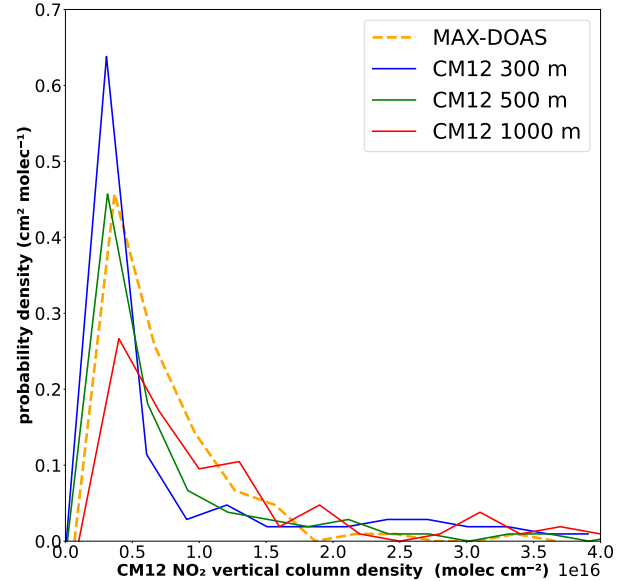


Figure 4.32: PDF's of the 1 hourly averages of the NO_2 vertical column densities in molecules cm^{-2} . CM12 model results sampled along the ship tracks and integrated up to 300 m, 500 m, and 1000 m are shown in blue, green and red, respectively, MAX-DOAS observations are shown in dashed orange.

with the literature, showing the best agreement offshore.

Figure 4.30 shows the model results over time along the ship route, integrated between the lowest model layer and three different altitudes: 300 m, 500 m, and 1000 m. The results indicate that the CM12 instance underestimates NO_2 in the lower troposphere for integration heights of 300 m and 500 m, with a few exceptions on June 10th, 15–17th, and 29th. These simulated NO_2 plumes are not detected in reality. However, outside of enhanced NO_2 plumes, the CM12 model data integrated up to 1000 m slightly overestimate NO_2 . The direct comparison between the MAX-DOAS observations and the CM12 model results is shown by Figure 4.31. Since the slopes for each integration height are far from 1, they are inconclusive in finding the best fit for the integration height. The root mean square error (RMSE) of the CM12 model results integrated up to 300 m is 1.0×10^{16} molecules cm^{-2} . Integrated up to 500 m and 1000 m, the RMSE increases to 2.3×10^{16} molecules cm^{-2} and 5.6×10^{16} molecules cm^{-2} , respectively.

The probability density functions (PDFs; Figure 4.32) indicate that the peak of the NO_2 VCD's frequencies around 0.5×10^{16} molecules cm^{-2} for all CM12 integration heights is consistent with the MAX-DOAS observations. Specifically, the PDF of the CM12 results integrated up to 500 m corresponds very well with the MAX-DOAS based PDF, in particular for small ($< 0.5 \times 10^{16}$ molecules cm^{-2}) vertical column density values. Values in the range between 0.5 and 2.0×10^{16} molecules cm^{-2} are underrepresented by the CM12 integrals

up to 300 m and 500 m. Conversely, larger NO_2 values above 2.0×10^{16} molecules cm^{-2} are more frequently simulated by the model, independent of the chosen integration height.

Out of the PDF and the RMSE it can be inferred that an integration height for the CM12 model data somewhere between 300 m and 500 m minimises the RMSE deviation of the model results from the MAX-DOAS observations.

Various potential causes of uncertainty may account for the systematic deviations of simulated NO_2 columns from the MAX-DOAS observations. Enhanced NO_2 observations are potentially caused by the ship's exhaust being transported into the viewing angle of the MAX-DOAS instrument, depending on the wind direction. Such enhanced observations are not captured by the model. Furthermore as discussed above (see section 4.4.1), the CM12 model might not simulate accurately the transport of plumes in time and space, but with a certain displacement from the exact position (and time) of the measurement. Moreover, the emission inventories used as boundary conditions (see section 3.3.9) for the model simulations might not represent correctly all local sources. And last, but not least, the intercomparison of model results and MAX-DOAS observations is methodologically limited by the fact that the integration height, which strongly affects the model-derived results and the measurements itself, is not exactly known. Additionally, the underestimation of the height of well-developed boundary layers by the COSMO model, as explained in section 4.4.1.2, may also contribute to the analysed deviations of model results from the observations [Szintai and Kaufmann, 2014].

4.5 Discussion and Summary of the Model Evaluation

4.5.1 Europe

My evaluation of the model results for Europe reveals that CM50 and CM12 perform well in representing the geographical distribution of NO_2 , NO_y , and O_3 . Table 4.3 summarises the intercomparison of model results (CM12) with the used observational data for Europe. The analysis of satellite data (TROPOMI on board of Sentinel-5P) for vertical tropospheric columns shows that CM50 and CM12 tend to overestimate NO_2 columns in rural areas during summers of 2017 and 2018, while underestimating it in urban regions like Benelux, Po Valley, Berlin, London, and Paris, with an overall MB of 0.1×10^{-5} mol m^{-2} (5.8 %). Similarly, CM50 and CM12 tend to systematically overestimate O_3 in comparison to the Sentinel-5P data, except in some areas like South Italy and the Balkans, with an overall MB of 0.002 mol m^{-2} (9.5 %). This is consistent with the evaluation of ground-level O_3 in CM50 using the D21 dataset, which indicates an overestimation within CM50 by a mean bias of 16.5 nmol mol^{-1} in 2017. The overestimation of ground-level O_3 appears especially in urban regions, and to a lesser extent in rural areas. Data from air quality stations (AIRBASE) in rural areas show that NO_x is underestimated and O_3 is overestimated by CM12 [Mertens et al., 2016a, 2020a], with MBs of -2.8 $\mu\text{g}/\text{m}^{-3}$ (RMSE: 8.9 $\mu\text{g}/\text{m}^{-3}$) and 19.9 $\mu\text{g}/\text{m}^{-3}$ (RMSE: 32.8 $\mu\text{g}/\text{m}^{-3}$), respectively. The relative MBs for NO_x and O_3 are 31.5 % and 32.8 % (Table 4.3), respectively. The RMSE for O_3 is consistent with the

findings of Mertens et al. [2020b], who reported $29.2 \mu\text{g m}^{-3}$ for the years 2008–2010. The relative MB of O_3 in this study is slightly larger with 32.8 % than that reported by Mertens et al. [2020b] with 26.6 %. Most probably, this is because Mertens et al. [2020b] used a different emission inventory and evaluated the AIRBASE data for the years 2008–2010. The relative MB of NO_x in comparison with AIRBASE (31.5 %) is similar with the MB derived from the EMerGe observations (31.2 %, see Table 4.3).

The comparison with simulation results reveals that CM12 underestimates NO_y during four flights with a MB of $-0.8 \text{ nmol mol}^{-1}$. The qualitative analysis, however, shows that CM12 represents the geographical patterns of NO_y , but tends to underestimate the NO_y mixing ratio near city centers, while only slightly underestimating it in rural areas. The MBs of O_3 simulated by CM12 consistently show a systematic overestimation of the ozone mixing ratio throughout Europe (Table 4.3). Reasons for the ozone bias have been discussed in previous publications [Mertens et al., 2016b, 2021]. One main reason is a too strong vertical mixing during night, which leads to too large ozone mixing ratios. This is a common problem in many models [Travis and Jacob, 2019]. Main reasons for the underestimations of NO_x are the horizontal resolution of the model, leading to a dilution of emissions over a large area, and emission inventories, which might underestimate the emissions. Another possible reason for the underestimation of NO_x in CM12 could be an overestimation of OH and the wet deposition processes, which remove NO_x via HNO_3 from the system. Despite the analysed discrepancies between model results and observational data, CM50 and CM12 are overall capable of representing NO_2 , NO_y , and O_3 across Europe in sufficient quality to justify a further analysis of the chemical regimes and the contributions of different source sectors to ozone, in the view of the scientific focus of my study.

Table 4.3: RMSE and MB for NO_2/NO_x , NO_y and O_3 as simulated by CM50 and CM12 in comparison with different data sets in Europe.

Study	NO_2/NO_x			NO_y			O_3		
	MB	MB(%)	RMSE	MB	MB(%)	RMSE	MB	MB(%)	RMSE
S5P (mol m^{-2})	0.1×10^{-5}	5.8	0.5×10^{-5}			0.002	9.5	0.0025	
D21 (nmol mol^{-1})							16.5	28.8	20.8
AIRBASE ($\mu\text{g/m}^{-3}$)	-2.8	-31.5	8.9				19.9	32.8	22.6
EMerGe (nmol mol^{-1})				-0.8/ 0.5	-56.2/ 31.2	2.9	10.6	14.6	17.5

4.5.2 East Asia

The evaluation of the model results for East Asia shows that CM50 and CM12 overall reproduce the geographical patterns of NO_2 , NO_y , and O_3 . Table 4.4 summarises the

intercomparison of model results (CM12) with the used observational data for East Asia. The analysis of vertical tropospheric columns using S5P satellite data reveals a considerable overestimation of NO_2 by the model in and around mega cities throughout East Asia with an overall MB of $0.6 \times 10^{-5} \text{ mol m}^{-2}$ (26.9 %).

In contrast, in rural regions such as the Ningxia region and south of the Sichuan Basin, CM50 and CM12 slightly underestimate NO_2 . Compared to Sentinel-5P data, CM50 and CM12 exhibit a systematic overestimation of tropospheric O_3 with a MB of $0.0075 \text{ mol m}^{-2}$ (10.9 %), particularly in Central China, but to a lesser extent at the coast. This finding is corroborated by the analysis of the D21 data set, which indicates a MB of $21.0 \text{ nmol mol}^{-1}$ across East Asia with a North-South gradient. The comparison of model results with data from rural EPA stations across East Asia further confirms this result, with ground-level measurements biased by the model of $29.8 \text{ nmol mol}^{-1}$ on average (Table 4.4). On the other hand, CM12 underestimates NO_2 by about $-0.5 \text{ nmol mol}^{-1}$ (i.e., about -7 %) compared to the rural EPA stations. However, in comparison to the observations from the EMeRGe Asia campaign, CM12 overestimates NO_y by approximately $2.7 \text{ nmol mol}^{-1}$ (55.9 %). A direct comparison of the observation data and their MBs is not possible since the EMeRGe Asia campaign mostly took place above the sea within city plumes, while the EPA stations measure inland and rural. Additionally, NO_2 is a smaller contributor to NO_y .

The comparison between the model results simulated by CM12 and the observations from EMeRGe Asia yields an O_3 MB of $18.2 \text{ nmol mol}^{-1}$. In relative terms, the MB of O_3 simulated by CM12 compared to the EMeRGe Asia observations is 20.8 %, and up to 44.8 % for the comparison with air quality measurements (EPA stations). Moreover, a comparison of MAX-DOAS data with CM12 indicates that NO_2 is overestimated by 56.6 % in the lower troposphere along the shore of Shanghai and offshore (integration height of 500m). The vertical NO_2 column densities (VCDs) obtained in CM12 are consistent with the findings reported by Li et al. [2020b], especially in offshore areas.

Liu and Wang [2020] assessed the performance of the CMAQ model by comparing it with data from the China National Environmental Monitoring Center for NO_2 . They found a bias of $-1.8 \text{ nmol mol}^{-1}$ across East Asia for the year 2017. The underestimation of NO_2 in CM12, by about $-0.5 \text{ nmol mol}^{-1}$ when compared to the EPA stations, is smaller and not directly comparable to the results from Liu and Wang [2020], as they used 1480 stations for the entire year of 2017.

Ye et al. [2022] evaluated the performance of the GEOS-CHEM chemistry transport model (CTM) in simulating ozone concentrations for East Asia. By comparing the model output with measurements from the nationwide monitoring network, they estimated an ozone bias of 40 % during the summer of 2018, which mostly occurs on wet/cloudy days. This finding is consistent with the results of the current study, with an O_3 MB of 44.8 % when comparing CM12 results with observations from EPA stations across East Asia. According to Ye et al. [2022], there are three primary factors responsible for the high ozone biases observed in the GEOS-CHEM CTM. These factors are cloud optical depth (COD), relative humidity, and precipitation. The COD affects the photolysis rates, and thus directly the O_3 formation and depletion (see section 2.2). As shown by Finkelstein et al. [2000] and Altimir et al. [2006], the dry deposition of O_3 is enhanced on the wet canopy

when the ambient humidity is high or the canopy has been moistened by precipitation. Typical reasons for the ozone bias in many models have already been discussed in section 4.5.1 and will not be repeated here.

The comparison with other literature indicates that MECO(n) is not superior or inferior to other chemistry-climate models in representing NO_2 , NO_y , and O_3 in East Asia. The analysis shows that CM50 and CM12 provide reliable geographic representations of NO_2 , NO_y , and O_3 , but CM12 overestimates O_3 even more in East Asia than in Europe. The primary causes of the underestimation of NO_x seem to be attributed to the horizontal resolution of the model and the underestimation in the emission inventories (see details in section 4.5.1).

Although there are discrepancies between the model results and observational data, CM50 and CM12 are generally able to adequately represent NO_2 , NO_y , and O_3 across East Asia. In line with the scientific focus of my study, there is a justification for further analysing the chemical regimes and the contributions of different source sectors to ozone.

Table 4.4: RMSE and MB for NO_2/NO_x , NO_y and O_3 as simulated by CM50 and CM12 in comparison with different data sets in East Asia. The MAX-DOAS data is shown for an integration height of 500m.

Study	NO_2/NO_x			NO_y			O_3		
	MB	MB(%)	RMSE	MB	MB(%)	RMSE	MB	MB(%)	RMSE
S5P (mol m^{-2})	0.6×10^{-5}	26.9	3.7×10^{-5}			0.0017	10.9	0.0075	
D21 (nmol mol^{-1})							21.0	38.1	25.2
EPA (nmol mol^{-1})	-0.5	-7.0	1.9				29.8	44.8	29.9
EMerGe (nmol mol^{-1})				2.7	55.9	5.1	18.2	20.8	22.7
MAX-DOAS (molec cm^{-2})	0.7×10^{16}	56.6	2.3×10^{16}						

Chapter 5

Comparison of the ozone chemistry in Europe and East Asia

This Chapter focuses on investigating O_3 contributions from different emission sectors in Europe and East Asia. First, both regions are analysed in detail (sections 5.1.1 and 5.2.1), and afterwards their O_3 chemical regimes are intercompared (section 5.3). Section 5.4 assesses and discusses the ozone mitigation potential for study areas in Europe and East Asia and discusses the uncertainties associated with the model results.

5.1 Contribution of different emission sectors to ground-level O_3 in Europe¹⁶

5.1.1 Contributions during summer 2017–2018 in Europe

The analysis shown in this section bases on the simulation EUREF, with a focus on the finest instance CM12 (see section 3.4). In the following, contributions to ozone from land transport, anthropogenic non-traffic, and biogenic emissions are analysed, because these are the sectors with the largest contribution to ground-level O_3 in Europe [e.g. Karamchandani et al., 2017, Mertens et al., 2018, Butler et al., 2018, Lupaşcu and Butler, 2019, Mertens et al., 2020a]. Contributions from other emission sectors are either summarised as residual or not shown. Five different study areas with rather large and rather low air pollution in Europe are defined (see Table 5.1 (p. 84), Table C.7 and Fig. 5.15, left panel). Besides Europe (whole domain), the Po Valley, Benelux, a region on the Iberian Peninsula, and West Ireland are considered. The latter two are chosen to represent rural regions and a region which is dominated by inflow (West Ireland).

The analysis focuses on two years (2017 and 2018) summer average (JJA, June, July, and August). The main focus is to investigate, which emission sectors contribute most to ozone levels in the considered regions. Of special importance is the distinction between

¹⁶Results described in this section have been submitted to the Atmospheric Chemistry and Physics (ACP) journal with multiple co-authors [Kilian et al., 2023]. The manuscript is currently under review.

Table 5.1: Definition of the regions in Europe, which are analysed in this study in detail. The last column lists the type of the chemical regime of each region.

Region	Code	Latitude	Longitude	Type of regime
Europe	EU	33.5° to 56.6° N	8.3° W to 23.2° W	mixed
Po Valley	PO	45° to 46.5° N	7° to 14° E	polluted basin
Benelux	BEN	50° to 53° N	3° to 7° E	polluted coastal
West Ireland	IRE	51° to 55° N	8° to 12° W	inflow
Iberian Peninsula	IBE	37° to 42° N	4.5° to 8.5° W	rural

the geographical origin of the emissions to discriminate between the contributions which can be attributed to long-range transport and to regional emission sources. As first step, the contributions of the ozone precursors are analysed in detail. The largest contribution of anthropogenic emissions to ground-level NO_y in Europe are simulated in the Benelux regions (see Fig. 5.1, upper and middle right). Here, the contribution of land transport and anthropogenic non-traffic emissions to ground-level NO_y are up to 3–8 nmol mol^{-1} and 2–8 nmol mol^{-1} , respectively. The contributions from landtransport in the Po Valley are around 2–8 nmol mol^{-1} , and those from anthropogenic non-traffic are 1–4 nmol mol^{-1} . Most of the contributions to ground-level NO_y in Europe arise from European emissions, only a very small share from long-range transported emissions. For NMHC (see section 2.3) this is different: here the anthropogenic non-traffic emissions (30–100 nmol mol^{-1}) from the long-range transport and the biogenic sector (up to 30 nmol mol^{-1}) are the largest contributors to ground-level NMHC in the Benelux region and the Po Valley. Contributions from land transport emissions are in the range of 3–8 nmol mol^{-1} (Fig. C.43, p. 188).

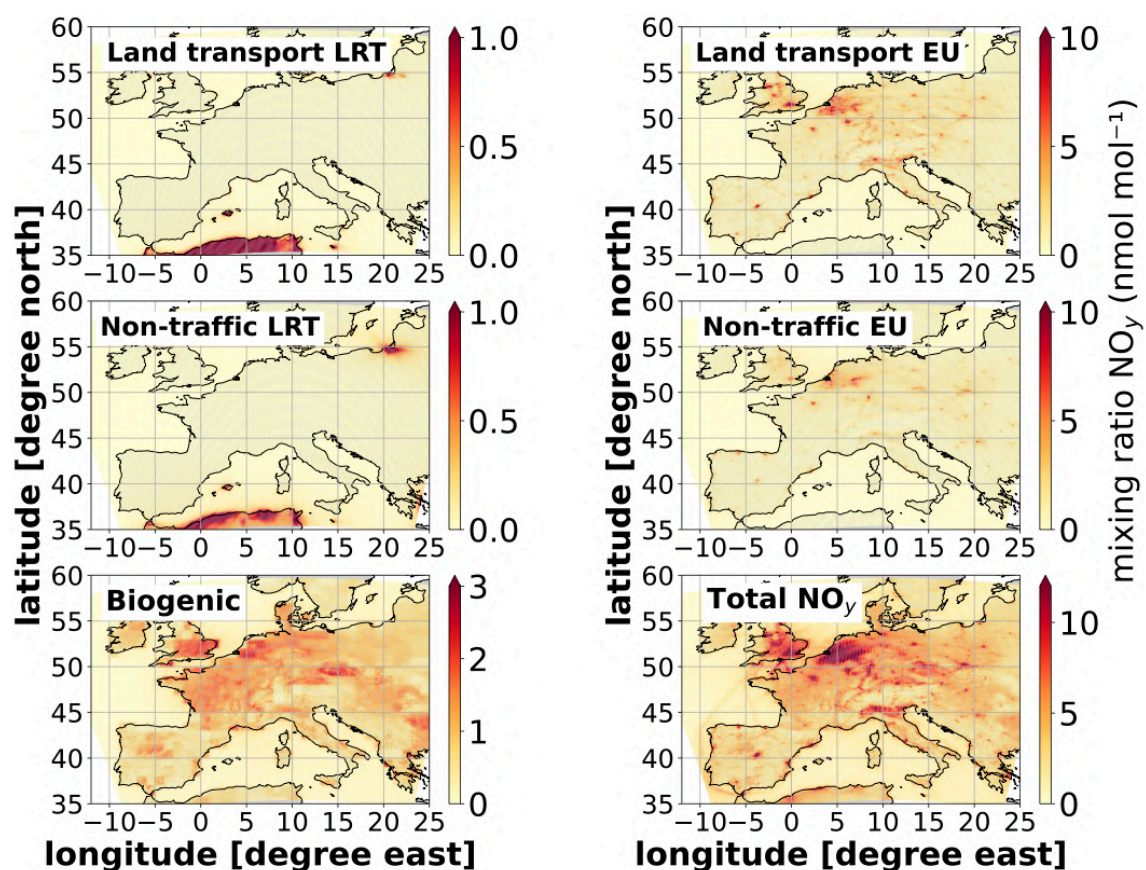


Figure 5.1: Seasonal mean (JJA 2017–2018) absolute contributions of NO_y as mixing ratios in $nmol\ mol^{-1}$ from long-range transported (LRT: Rest of the World + North America + East Asia) NO_y and European NO_y emissions by sectors, and total NO_y (lower right) as simulated with CM12. Note that the colour scales of the panels differ.

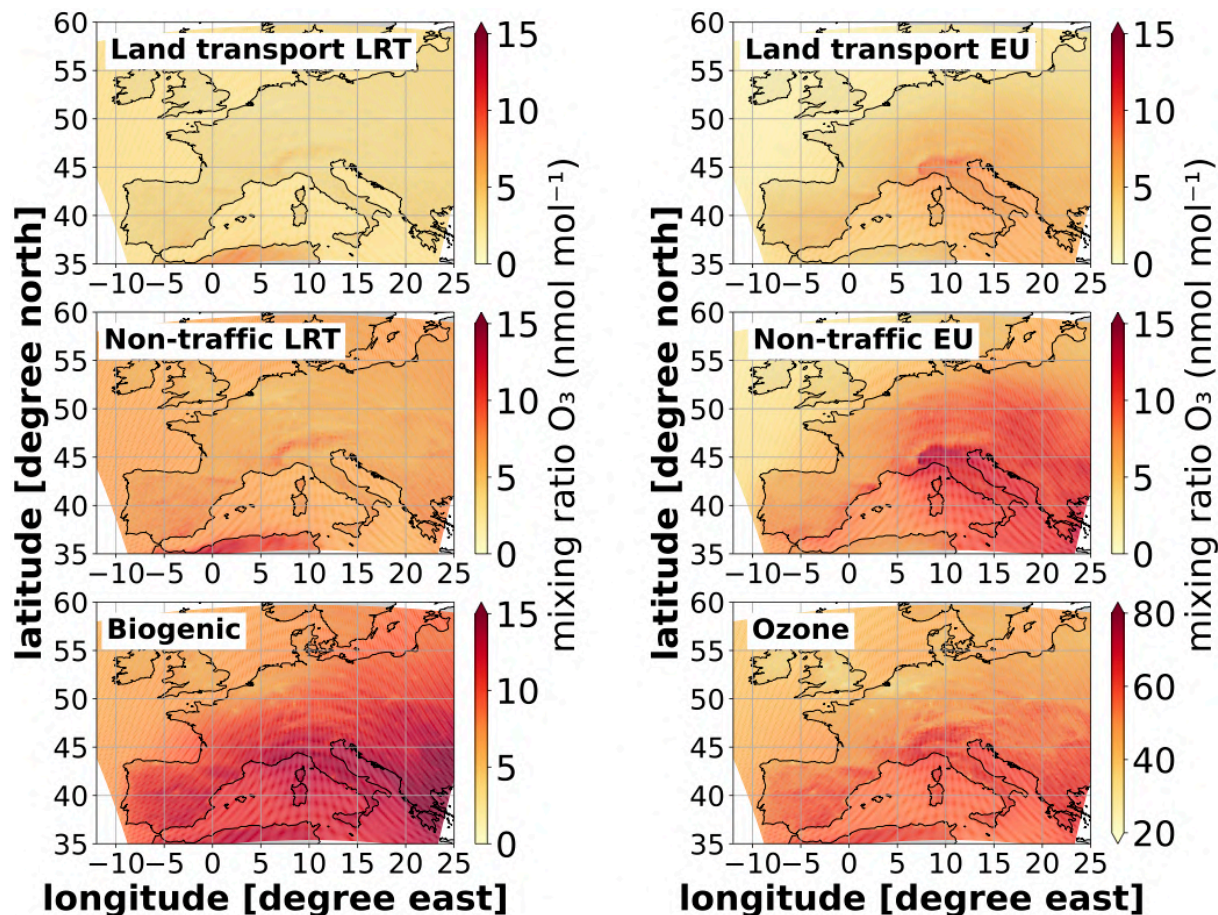


Figure 5.2: Seasonal mean (JJA 2017–2018) absolute contributions as mixing ratios in nmol mol^{-1} to O_3 from long-range transported (LRT: ROW + NA + EA) and European emissions as simulated with CM12. Note that the colour scales of the panels differ.

Figure 5.2 shows the absolute contributions to ozone of the various sectors as simulated by CM12 in Central Europe for JJA 2017–2018. The results of CM12 show slightly larger contributions in hot spot regions compared to those of CM50 (Fig. C.44, p. 189), but the distributions and order of magnitudes agree well between CM50 and CM12. In general, the emissions from European anthropogenic non-traffic emissions (O_3^{ieu}), European land-transport (O_3^{teu}) and from biogenic emissions (O_3^{soi}) are the largest contributors to ground-level O_3 in Europe. These contributions also show a positive gradient in North-West to South-East direction. The distribution of the contribution to ozone from long-range transported emissions is more homogeneous and largest in South Europe. Reasons for the peak over South Europe are transport of air masses from the African continent (tagged as ROW) to Europe (especially Southern Iberian Peninsula) and descent of air masses transported from North America over the Mediterranean [Stohl et al., 2002, Eckhardt et al., 2004].

The source attribution method yields contributions to ozone of the individual emission sources and calculates the ozone production and loss rates for each emission sector, from

5.1 Contribution of different emission sectors to ground-level O₃ in Europe 87

which I calculate the net ozone production for each emission sector (i) defined as:

$$PO_{3i}^{\text{net}} = \text{ProdO}_{3i} - \text{LossO}_{3i} \quad (5.1)$$

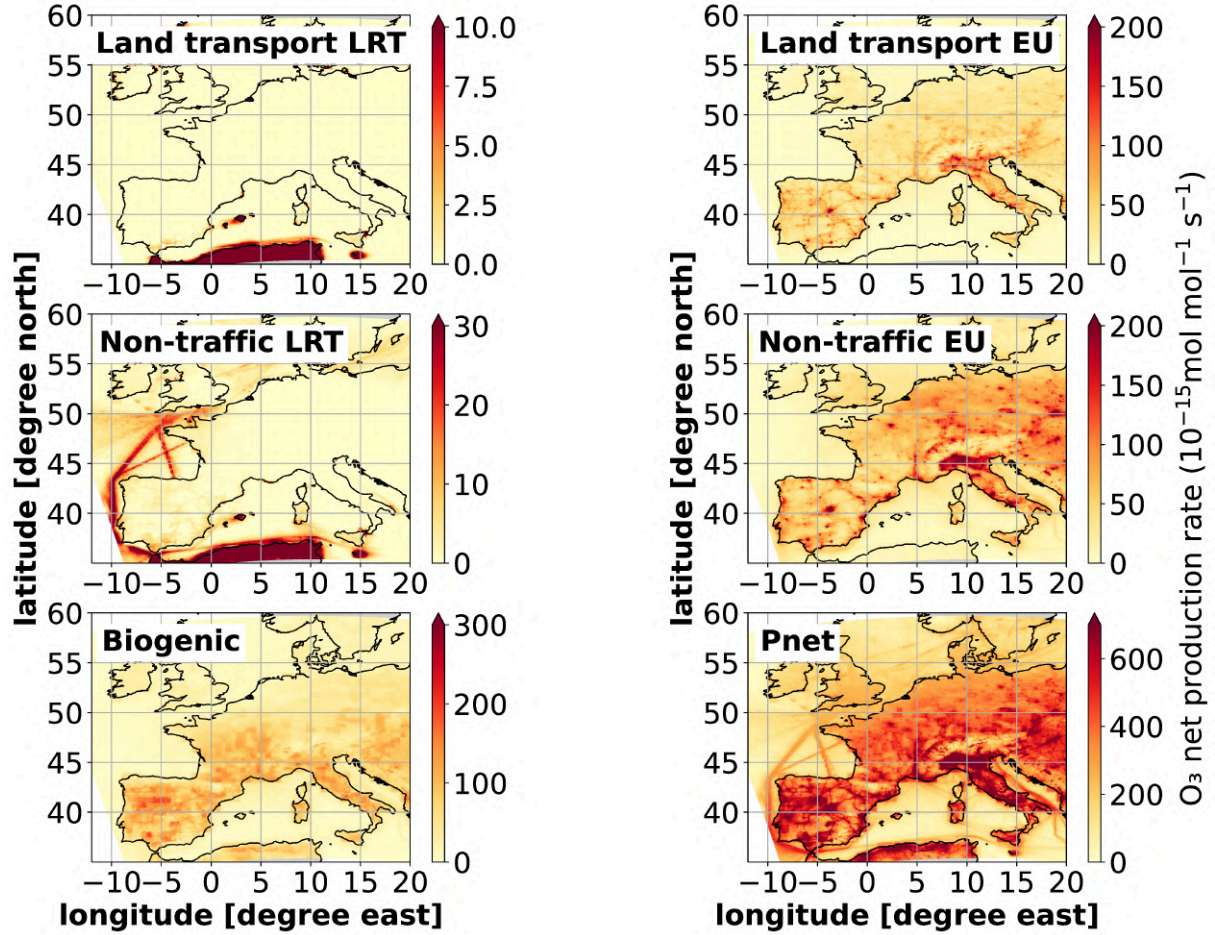


Figure 5.3: Seasonal mean (JJA 2017–2018) of the ozone net production rate ($P_{\text{net}} = \text{Production} - \text{Loss}$; see chemical mechanism in Appendix: ProdO_3 and LossO_3) in $10^{-15} \text{ mol mol}^{-1} \text{ s}^{-1}$ from long-range transported (LRT: ROW + NA + EA) and European sectors. Note that the colour scales of the panels differ.

Figure 5.3 shows the total PO_3^{net} (lower right panel) and PO_{3i}^{net} for the most important emission sectors (land transport, anthropogenic non-traffic, and biogenic) separated between impact from European emissions (EU) and emissions from other regions (LRT=NA+EA+ROW). Typically, the seasonal diurnal mean of PO_3^{net} exhibits positivity throughout the summer 2017–2018, while showing increased negativity in the winter season, as indicated by previous research [Kondo et al., 2004]. The surplus of tropospheric O₃ during summer is concurrently subject to transport mechanisms that disperse it away from the region of origin.

Total PO_3^{net} shows a clear North-South gradient, indicating much larger net ozone production in Southern Europe than in Northern Europe. Accordingly, also PO_3^{net} in the Po Valley is much larger as in Benelux. Ozone production from European land transport emissions peak in the Po Valley and some larger cities in Southern Europe (Madrid, Rome, Naples). Similarly, also $\text{PO}_{3i}^{\text{net}}$ from European anthropogenic non-traffic emissions peak in the Po Valley and around hot-spots, mainly in South- and Eastern Europe. Ozone production from biogenic sources is largest over the Iberian Peninsula. In-situ production from anthropogenic precursors over Europe from LRT plays almost no role in Europe; only along the ship lanes in the Atlantic ozone production from LRT takes place. This production is due to reactions of NO_y from shipping with NMHC emissions from evaporation of gas/oil transported with ships (not the shipping emissions itself). This NMHC evaporation is categorised as anthropogenic non-traffic emissions from the rest of the world (see Fig. C.43, p. 188) as they take place over the oceans.

Figure 5.4 shows the area-averaged contributions to ozone for each study area to ground-level O_3 for JJA 2017–2018. Since Central Europe has already been analysed previously on a large scale (Fig. 5.2), it is not displayed separately as a distinct study area in this figure. Not explicitly shown sources are summarised as 'residual'.

A detailed breakdown of the contributions from the 'residual' category are given in the Appendix (Figs. C.45–C.48, pp. 189–191). In the following, absolute and relative ozone contributions are analysed. Absolute contributions provide information on the total amount of ozone that is produced as a result of emissions. However, this measure does not take into account the background mixing ratio of O_3 in the atmosphere. For example, a city with large emissions may cause large absolute contributions to ozone, but if it is located in an area with naturally large mixing ratios of ozone, its contribution on the overall ozone mixing ratio might be relatively small. Relative ozone contributions allow to assess the importance of certain ozone contribution in comparison to the overall amount of ozone.

In the Po Valley, the absolute ozone contribution from European land transport emissions (red bars) is with around 8 nmol mol^{-1} larger than in the Benelux region with around 3 nmol mol^{-1} . Similarly, absolute contributions from European anthropogenic non-traffic emissions are larger in the Po Valley (12 nmol mol^{-1}) than in Benelux (6 nmol mol^{-1}). This is consistent with the differences between the net ozone production rates in both regions shown above. In contrast, NO_y and NMHC emissions from European land transport and anthropogenic non-traffic are larger in the Benelux region than in the Po Valley (Figs. 5.1 and C.43, p. 188). Ireland shows almost no ozone contributions from European anthropogenic sources. Instead, shipping, biogenic (which is tagged as a global source) and the residual (mainly biomass burning and CH_4) dominate ozone in the inflow region (see Fig. C.47, p. 190).

Ozone contributions from global shipping emissions are similar in the Benelux region and the Po Valley with around 3 nmol mol^{-1} . Absolute ozone contributions from global biogenic emissions (O_3^{soi}) are largest in the Po Valley with more than 12 nmol mol^{-1} , and only half of that in the Benelux region with 6 nmol mol^{-1} . Accordingly, ozone contributions from biogenic emissions (O_3^{soi}) in the Po Valley are twice as large as in the Benelux region. This agrees with the contribution to the ozone net production rate from biogenic emissions

in the Po Valley, which is up to 3 times larger than in the Benelux region (Fig. 5.3, lower left panel). While in the Benelux region soil-NO_x emissions are larger than in the Po Valley, biogenic emissions of isoprene are larger in the Po Valley than in the Benelux region (see Figs. C.49 and C.50, pp. 191). Since the tagging mechanism in this study combines different ozone precursors, it cannot be distinguished, if the ozone contribution from soil emissions (O₃^{soi}) arises mostly from NO_x or isoprene emissions in each region.

The absolute contributions to ground-level ozone of sources summarised as residual are 16 nmol mol⁻¹ in the Po Valley and 12 nmol mol⁻¹ in the Benelux region, respectively. In both regions the relative contributions of the sectors summarised as residual are similar with the most important contributions from CH₄, biomass burning and lightning-NO_x (see Figs. C.45-C.48, pp. 189-191).

The relative ozone contributions from European land transport (O₃^{teu}) and anthropogenic non-traffic (O₃^{ieu}) emissions in the Po Valley are 12 % and 19 %, respectively (Fig. 5.5). In accordance with the absolute contributions and the larger net ozone production in the Po Valley compared to Benelux, also these relative contributions are larger than in Benelux (7 % O₃^{teu}, and 15 % O₃^{ieu}). The relative ozone contributions of the sum of land transport emissions from other regions are slightly smaller with 5 % in the Po Valley than in the Benelux region with 6 %. The emissions from land transport in North-America contribute with 3 % and 4 % similarly to ground-level O₃ in the Po Valley and in the Benelux region, respectively. East Asian land transport emissions contribute only 1 % to ground-level O₃ in both regions, because transport times are similar or larger to the lifetimes of the ozone precursors. Furthermore, air masses from East Asia are also strongly diluted and mixed with other emissions during the transport. In the Po Valley, the relative ozone contributions from anthropogenic non-traffic emissions from other regions of the world are 9 %, in more detail 3 % originate from NA, 4 % from ROW and 2 % from EA. In the Benelux region, even larger relative ozone contributions from anthropogenic non-traffic LRT emissions of 13 % are simulated. The relative contributions to ozone of ROW and NA are slightly smaller as in the Po Valley, both with 5 %. The remaining part (3 %) arises from East Asia. These contributions are favoured by the coastal location and the large-scale weather pattern of the Benelux region, which is mostly dominated by fronts. During the intercontinental transport from NA, ozone and precursors are diluted during the advection across the Atlantic. This leads to lower mixing ratios of long-range transported NO_y and O₃ arising from North-America and therefore to a uniform distribution across Europe (Fig. 5.2). The relative contribution from biogenic emissions to ozone is 22 % in the Po Valley, 20 % over the Iberian Peninsula and 19 % in the Benelux. Accordingly, biogenic emissions are one of the most important contributor to ground-level O₃ in these regions.

The relative contribution from shipping emissions to ground-level O₃ is around 9 % in Benelux, which is around twice as much as in the Po Valley (5 %). This is due to the coastal location and strong influence of the shipping emissions over the North Sea. Ozone over West Ireland has even slightly larger relative contributions from shipping emissions compared to Benelux, because of the proximity to important Atlantic shipping routes.

Figure 5.5 shows that in all four study areas the residual non-anthropogenic sectors

(blue bar) contribute to ozone by 27–37 %. Ozone contributions from methane emissions ($\text{O}_3^{\text{CH}_4}$) and from biogenic emissions (O_3^{bio}) are the largest contributions with 7–14 % and 5–10 % to ground-level O_3 , respectively (see Figs. C.45–C.48 in the Appendix, pp. 189–191). Ozone contributions from lightning emissions (O_3^{lig}) and from stratosphere–troposphere exchange O_3^{str} are also very important sectors to ground-level O_3 and their relative contributions to ground-level O_3 are quite uniformly distributed across Europe with 5–8 % and 3–5 %, respectively.

The results show that in Benelux and the Po Valley ozone contributions from European anthropogenic emissions (land transport and non-traffic) contribute the largest shares with 9 nmol mol^{-1} and 20 nmol mol^{-1} , respectively. This comparison shows that the mitigation potential for the European anthropogenic sector in the Benelux region is more limited than in the Po Valley, because much less ozone is produced in-situ from regional emissions. Instead, ozone is more dominated by long-range transport and shipping in Benelux compared to the Po Valley.

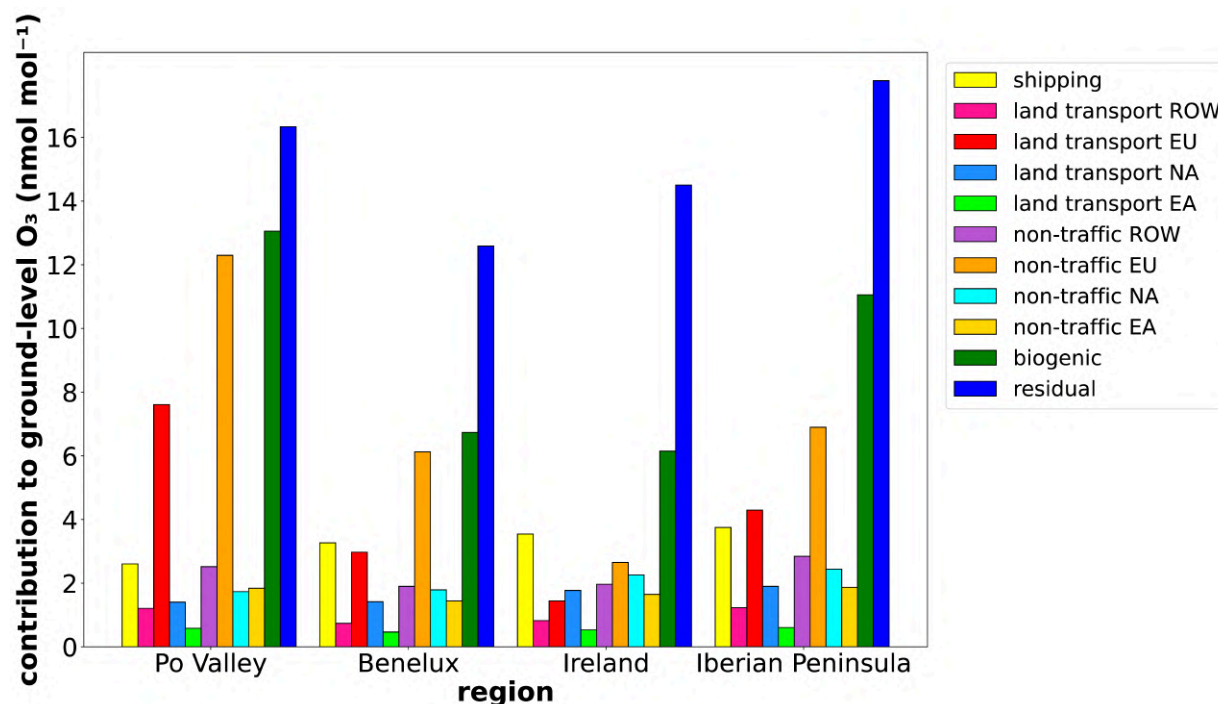


Figure 5.4: Seasonal mean absolute contribution of different emissions sectors and regions to ground-level ozone in the four European regions Benelux, Po Valley, West Ireland and Iberian Peninsula for JJA 2017–2018 as simulated with CM12. The residual sector is defined in Figs. C.45–C.48, pp. 189–191

5.1 Contribution of different emission sectors to ground-level O₃ in Europe 91

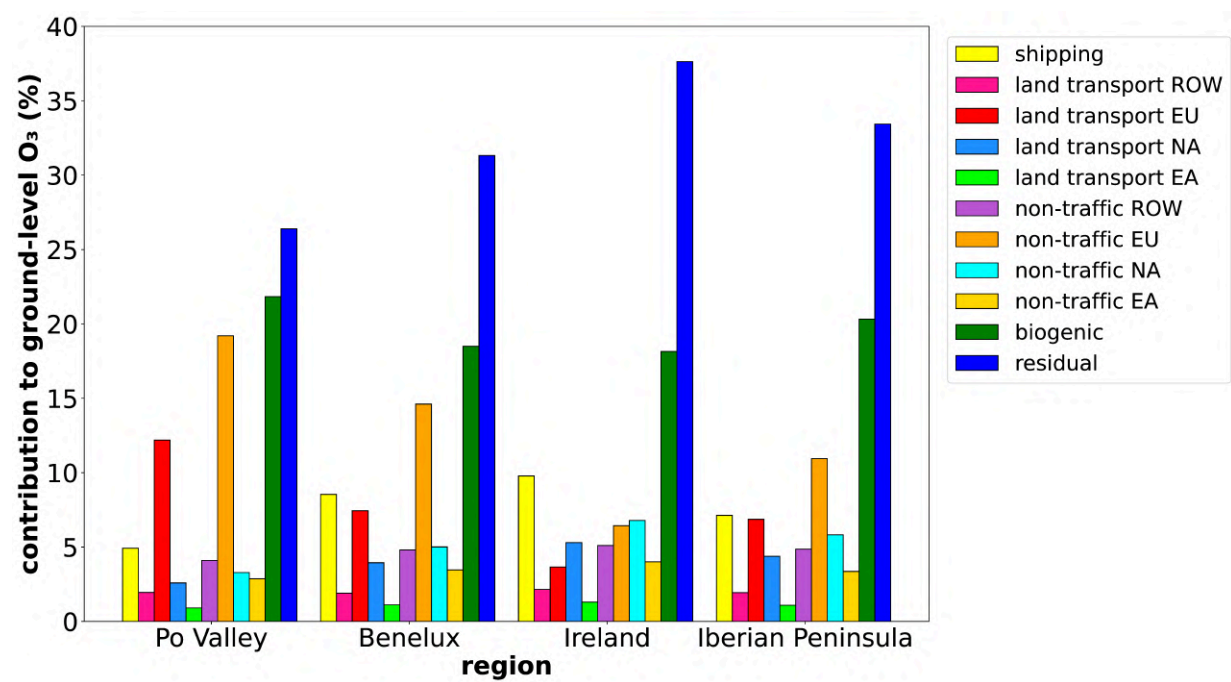


Figure 5.5: Seasonal mean relative contribution of different emissions sectors and regions to ground level ozone in the four European regions Benelux, Po Valley, West Ireland and Iberian Peninsula for JJA 2017–2018 as simulated with CM12.

5.1.2 Contributions during periods of large ozone values in Europe

Especially for human health, periods of enhanced ozone values are most harmful. Such large ozone values can occur, for example, during stagnant conditions during heat waves. During these periods, contributions to ozone can differ strongly from seasonal mean values [e.g. Mertens et al., 2020a, Lupaşcu et al., 2022]. Firstly, the contributions at the 95th, 90th, and 75th percentiles of ozone, based on 1-hourly model output, have been calculated. Secondly, the following analyses showcase the 25th and 75th percentiles, along with the median, for these three distinct percentiles. The analyses are performed for Central Europe and for the four study regions (see Table 5.1).

Figure 5.6 shows the absolute contributions of land transport, anthropogenic non-traffic and biogenic emissions at different percentiles of ozone (see Fig. C.51 in the Appendix for relative contributions, p. 193). As the ozone values can have a large geographical spread, the results are presented as box-whisker plots to indicate the variation of contributions within the regions. The results show that contributions of O_3^{teu} (1–13 nmol mol⁻¹, 2–18%) and O_3^{ieu} (1–23 nmol mol⁻¹, 3–33 %) have a large geographical variation over Europe, while the variations of the contribution from long-range transport are much smaller (compare also Fig. C.51, p. 193). The large spread is favoured by an in-homogeneous distribution of the emission sources resulting in a strong variation of the net ozone production.

In accordance with Mertens et al. [2020b] contributions from land transport, anthropogenic non-traffic and biogenic sources increase in the regions Europe, Benelux, Po Valley and Iberian Peninsula with increasing ozone percentiles. Compared to Mertens et al. [2020b], however, the additional information about the geographical origins of the emissions shows that the increase of the contributions of land transport and anthropogenic emissions is caused by emissions from within Europe. Here, absolute contributions from European land transport emissions increase up to 16 nmol mol⁻¹ (20 %) for the 95th percentile of ozone. Contributions of European anthropogenic non-traffic emissions increase up to 25 nmol mol⁻¹ (35 %) at the 95th percentile of ozone.

The contributions of both emission sectors (European land transport and anthropogenic non-traffic) from long-range transport remain relatively constant at all ozone percentiles. As Figure 5.6 shows, the difference between contributions from long-range transport and from European emissions is largest in the Po Valley, where the net ozone production is also the highest. Accordingly, large ozone values can be reduced very well by reductions of European emissions. Compared to this, the differences between contributions from long-range transport and European emissions is much smaller in Benelux and over the Iberian Peninsula. In both regions the contributions from European emissions is only slightly larger as the contribution from long-range transport (especially at the 95th percentile). Larger contributions from German emissions to large ozone levels in Germany have also been reported by Lupaşcu et al. [2022]. The results indicate that the overall potential to reduce large ozone values by reduction of European emissions is much smaller in Benelux and over the Iberian Peninsula compared to the Po Valley. This is also in accordance with contribution analyses of peak ozone values over the Iberian Peninsula by Pay et al. [2019].

5.1 Contribution of different emission sectors to ground-level O₃ in Europe 93

Compared to Po Valley, Benelux and the Iberian Peninsula, the contributions from long-range transport and European emissions are very similar in Ireland. There, the contributions from land transport and anthropogenic non-traffic long-range transport emissions show no increase for increasing ozone percentiles. The contributions from biogenic emissions, however, show a small increase.

An important metric for ozone exceedences is the maximum daily 8-hour average ozone (MDA8), therefore the ozone contributions to MDA8 are investigated (see section 2.1). To do so, MDA8 is calculated for JJA 2017–2018. Based on the MDA8 values, contributions are investigated for the maximum MDA8, the mean MDA8 values and the minimum MDA8 values (Fig. 5.7). These maximum, mean and minimum MDA8 values (Fig. C.52, p. 194) are analysed for whole Europe and the considered regions (Table 5.1). Similar as for the percentiles, the contributions are analysed as box-whisker plots to indicate the geographical spread within the regions. For a better comparability of the anthropogenic emissions with biogenic emissions, the contributions of the anthropogenic emissions in Figure 5.7 are the sum of contributions from all regions (e.g. $O_3^{\text{teu}} + O_3^{\text{tna}} + O_3^{\text{tra}} + O_3^{\text{tea}}$). A figure with the same analysis distinguishing between contributions from European emissions and long-range transport is part of the Appendix (Fig. C.53, p. 195).

The monthly maxima of MDA8 over the whole domain range from 50–95 nmol mol⁻¹ (Fig. C.52, p. 194). Contributions to the maximum MDA8 of land transport emissions (sum of all regions) range between 7–19 nmol mol⁻¹, contributions from anthropogenic non-traffic between 14–32 nmol mol⁻¹, and contributions from biogenic emissions between 5–31 nmol mol⁻¹. The analysis largely confirms the findings from the analysis of the ozone percentiles. From minimum to maximum MDA8 values, the absolute contributions of land transport, anthropogenic non-traffic and biogenic emissions increase over Benelux, Po Valley and the Iberian Peninsula. Over the Po Valley large MDA8 values are strongly driven by European emissions, while over Benelux and over the Iberian Peninsula also long-range transport plays a role (see Fig. C.53, p. 195). For Ireland, the minimum, maximum and mean MDA8 values change only slightly. The corresponding O₃ contributions of the three emission sectors are nearly constant between minimum and maximum MDA8.

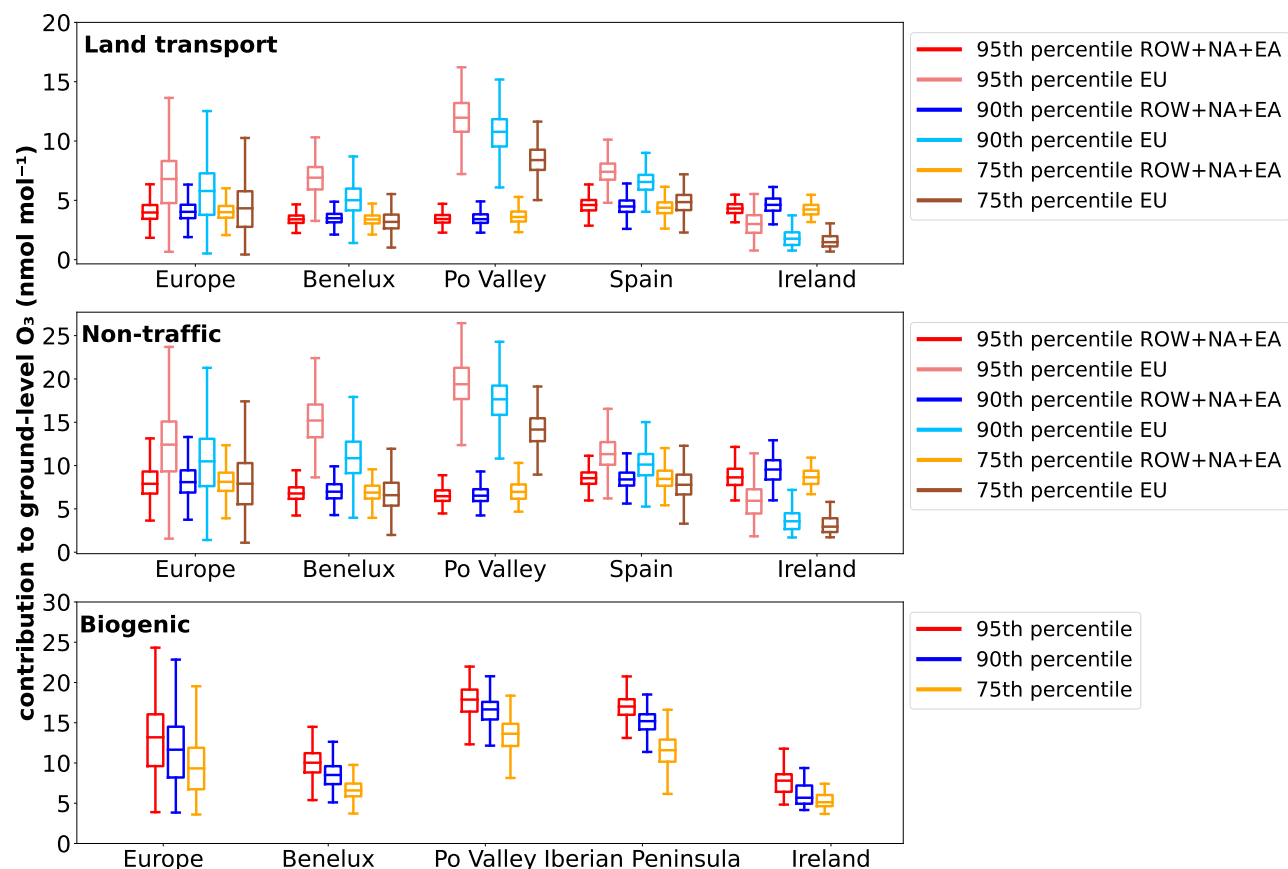


Figure 5.6: Box-whisker plot showing the contributions (in $nmol\ mol^{-1}$) of the most important emission sources for the 95th, 90th, and 75th percentiles of ozone as simulated by CM12 for JJA 2017–2018. The upper panel shows the regional absolute contributions of O_3^{teu} (labeled EU) and the sum of long-range transported absolute contributions of O_3^{tra} , O_3^{tna} and O_3^{tea} (labeled ROW+NA+EA). The middle panel shows the absolute contributions of O_3^{ieu} (labeled EU) and the sum of long-range transported absolute contributions of O_3^{ind} , O_3^{ina} and O_3^{iea} (labeled ROW+NA+EA). The lower panel shows the absolute contributions of O_3^{soi} . The lower and upper ends of the boxes indicate the 25th and 75th percentile of the underlying regional distribution, respectively, the bar the median, and the whiskers are defined as ± 1.5 the interquartile range of the contributions of all grid boxes within the indicated region.

5.1 Contribution of different emission sectors to ground-level O₃ in Europe 95

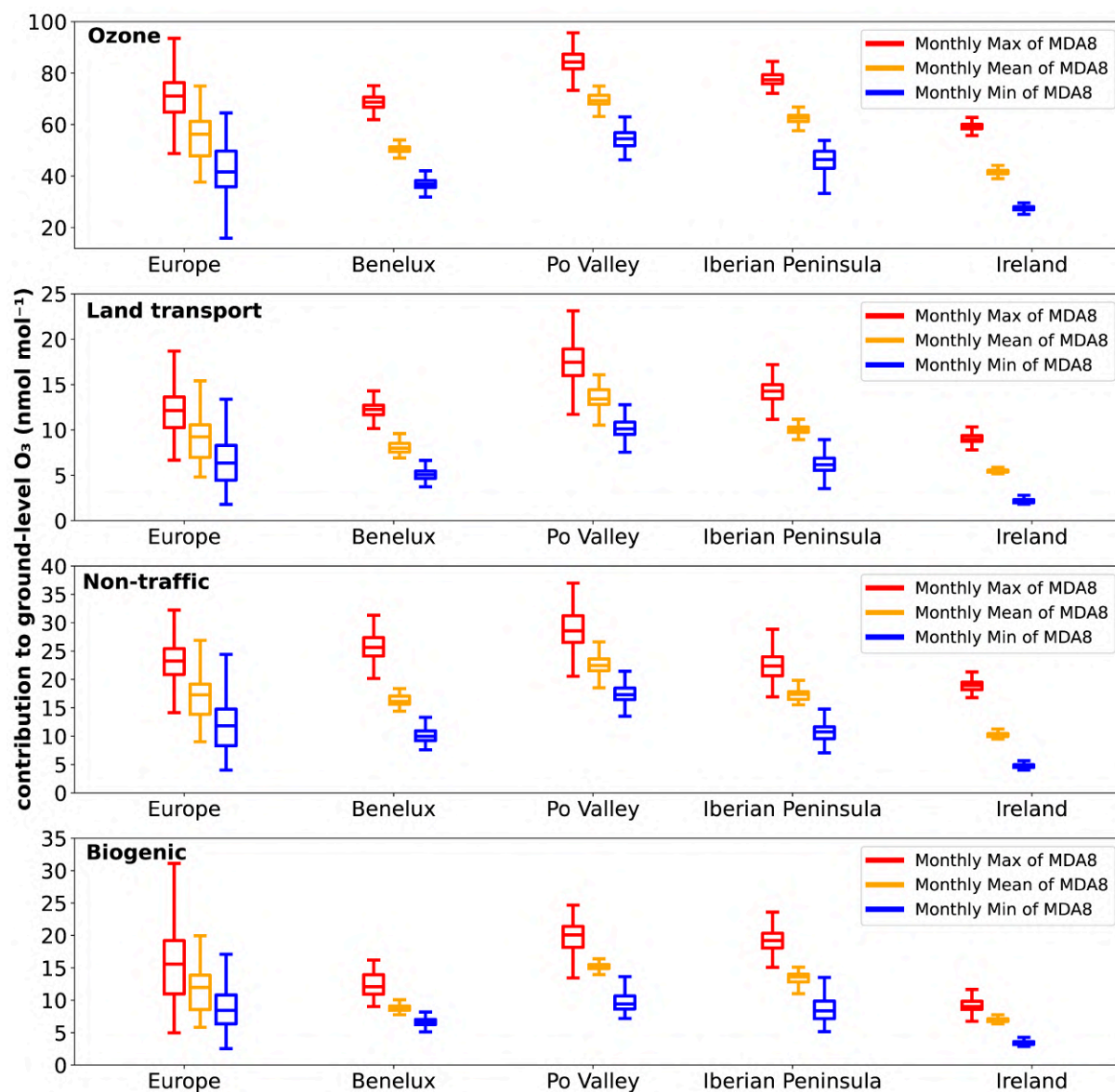


Figure 5.7: Box-whisker plot showing the contributions in nmol mol⁻¹ of the most important emission sources of ozone as simulated by CM12 for JJA 2017–2018 in Europe. Shown are ozone and the contributions of land transport, anthropogenic non-traffic, and biogenic emissions to ground-level ozone during the seasonal maximum of the maximum daily 8-h average (MDA8) (upper panel), the seasonal mean of MDA8 (middle panel) and the seasonal minimum of MDA8 (lower panel) as ozone mixing ratio in nmol mol⁻¹ based on 1-hourly model output. The lower and upper ends of the boxes indicate the 25th and 75th percentile of corresponding regional distribution, respectively, the bar the median, and the whiskers are defined as ± 1.5 the interquartile range of the contributions of all grid boxes within the indicated region.

5.2 Contribution of different emission sectors to ground-level ozone in East Asia

5.2.1 Contributions during summer 2017–2018 in East Asia

In this section, the analysis bases on the ASIAREF simulation, with a focus on the instance CM12 (section 3.4). As for Europe, the contributions to O_3 in East Asia are separated into contributions from regional and LRT emissions. Again, contributions to ozone from land transport, anthropogenic non-traffic, and biogenic emissions are analysed, because these are the sectors with the largest contribution to ground-level O_3 in East Asia [e.g. Li et al., 2012, Wang et al., 2014, Li et al., 2016, 2019, Wang et al., 2019]. Since the largest ozone levels occur during summer, my analysis is for JJA 2017 and 2018.

As in the previous section, the contributions of the ozone precursors are analysed in detail for different study areas. Table 5.2 displays five study areas in East Asia, the Pearl River Delta (PEA), the Yangtze Delta (YAN), and Taiwan (TAI), which are mainly polluted areas (Table C.8, p. 187). The geographical location of each study area is displayed in Figures 5.15 or C.42 (right panel, p.188). The Sichuan Basin (BAS) represents an area that is significantly impacted by orography and captures emissions especially during inversion weather conditions. Ningxia (RUR), situated in the northwest of Wuhan, is defined by a predominantly rural area with fewer emission sources (Fig. C.42, right panel, p. 188).

Table 5.2: Definition of the regions in East Asia, which are analysed in this study in detail. The last column lists the type of the chemical regime of each region.

Region	Code	Latitude	Longitude	Type of regime
East Asia	EA	0.5° to 40.4° N	105.7 to 141.0° E	mixed
Pearl Delta	PEA	22.1° to 23.3° N	112.5° to 114.5° E	polluted coastal
Yangtze Delta	YAN	30.0° to 32.3° N	119.6° to 122.3° E	polluted coastal
Taiwan	TAI	21.4° to 25.8° N	119.0° to 122.5° E	inflow/polluted coastal
Sichuan Basin	BAS	27.0° to 33.0° N	105.7° to 108.0° E	polluted basin
Ningxia	RUR	35.3° to 39.4° N	105.7° to 107.6° E	rural

Figure 5.8 shows, that in East Asia in JJA 2017–2018, the Pearl River Delta, the Yangtze Delta, and Taiwan show the largest contributions to ground-level NO_y from land transport and anthropogenic non-traffic emissions, reaching up to 6–22 $nmol\ mol^{-1}$ and 14–40 $nmol\ mol^{-1}$, respectively. The Sichuan Basin exhibits lower contributions, with around 3–16 $nmol\ mol^{-1}$ from the land transport, and 4–18 $nmol\ mol^{-1}$ from the anthropogenic non-traffic sector (Fig. 5.8). The vast majority of ground-level NO_y in East Asia originates

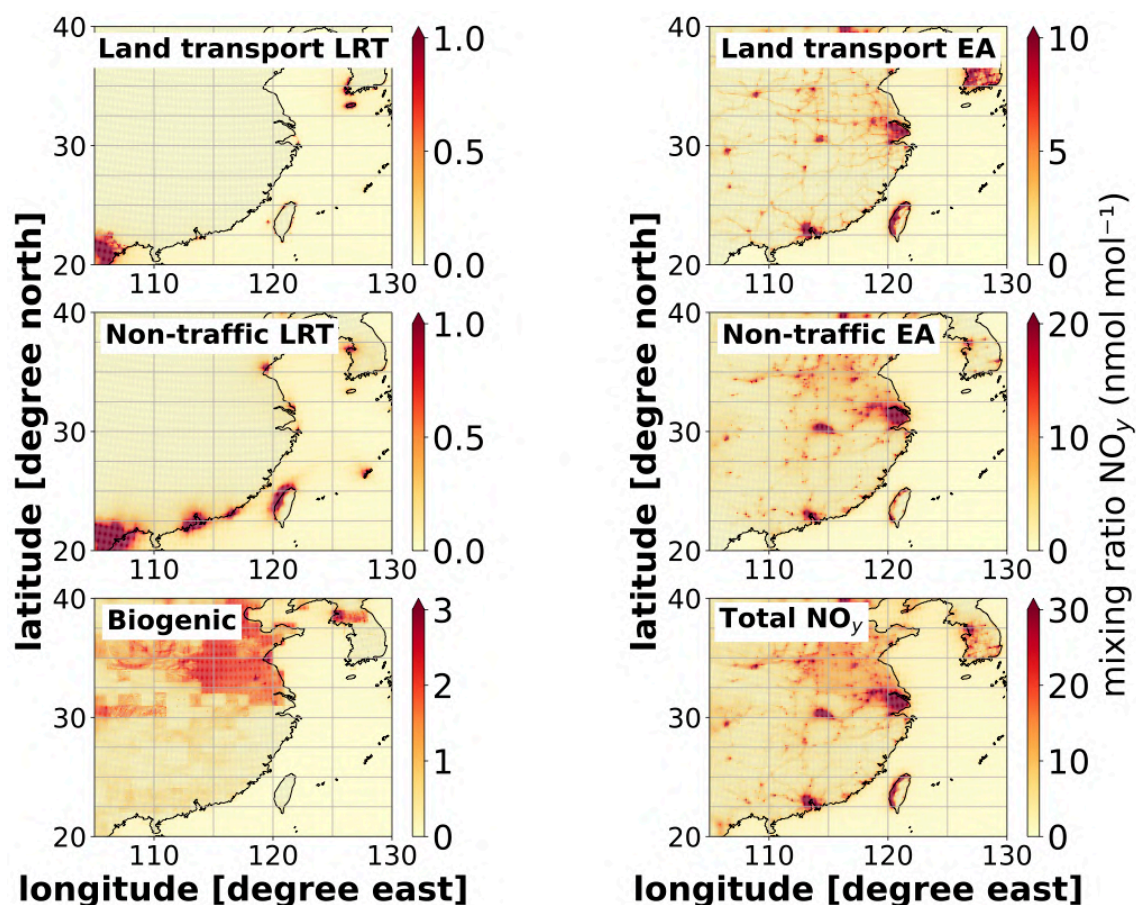


Figure 5.8: Seasonal mean absolute contributions of NO_y as mixing ratios in nmol mol^{-1} for JJA 2017–2018 from long-range transported (LRT: Rest of the World + North America + Europe) NO_y and East Asian NO_y emissions by sectors and total NO_y (lower right) as simulated with CM12. Note that the colour scales of the panels differ.

from regional emissions, with only a small portion resulting from long-range transport. The NO_y contributions along the Chinese coast attributed to long-range transport are an artefact, and are caused by a different land-sea mask between the EDGAR v5.0 emissions, and the flag file used for the source attribution in SCALC (see Appendix A.1.3, p. 141).

For NMHC the geographical distribution is similar to that of NO_y : here the land transport ($30\text{--}90 \text{ nmol mol}^{-1}$) and the anthropogenic non-traffic sector ($80\text{--}200 \text{ nmol mol}^{-1}$) are the largest contributors to ground-level NMHC in the Pearl Delta, Yangtze Delta and Taiwan. Contributions from biogenic emissions are in the range of $15\text{--}30 \text{ nmol mol}^{-1}$ (Fig. C.54, p. 196). In the Sichuan Basin anthropogenic NMHC emissions are clearly lower, but biogenic NMHC emissions are more important.

Figure 5.9 shows the absolute contributions to ozone of the most important emission sectors as simulated by CM12 in East Asia for JJA 2017–2018. Again, the results for CM12 show slightly larger contributions in hot spot regions compared to those of CM50 (Fig. C.55, p. 197), but the distributions and orders of magnitude agree well between CM50

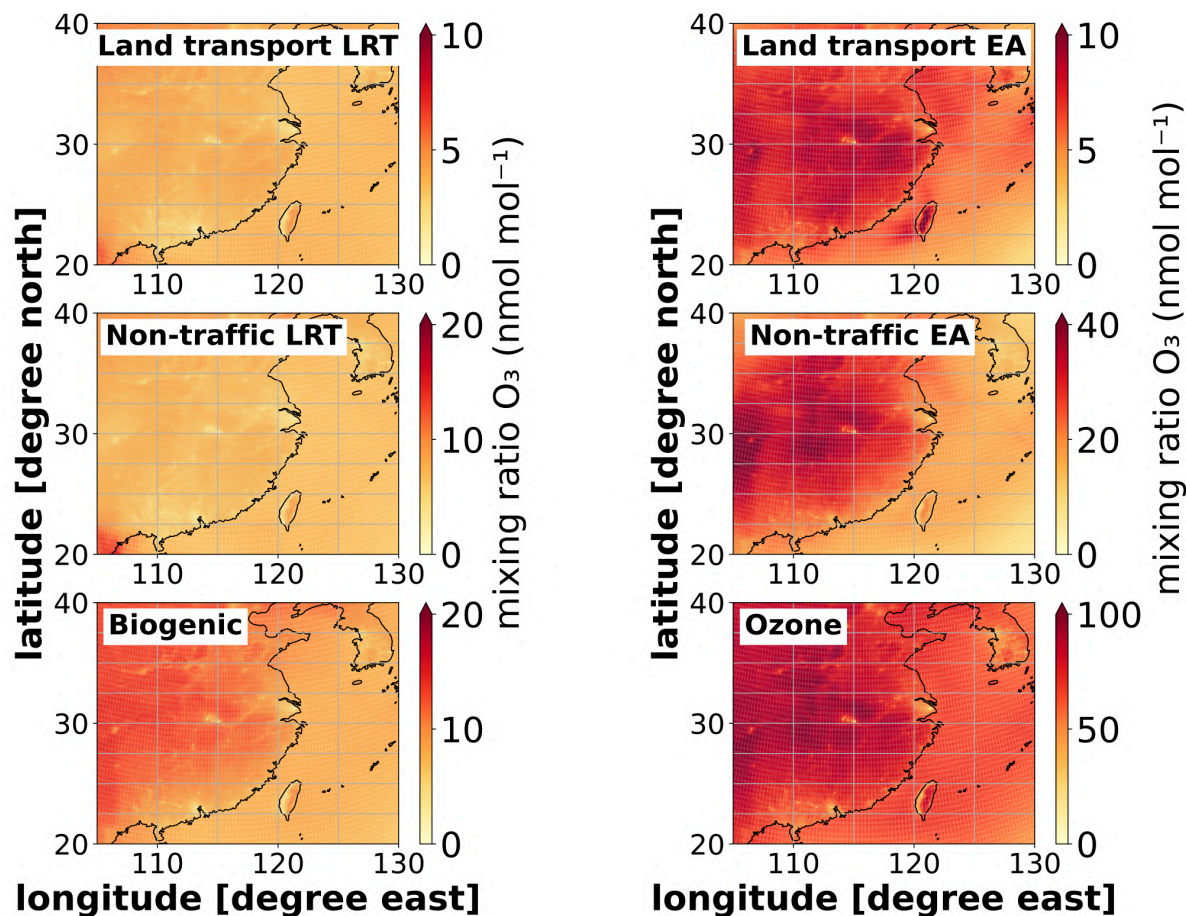


Figure 5.9: Seasonal mean absolute contribution as mixing ratios in nmol mol^{-1} of O_3 for JJA 2017–2018 from long-range transported (LRT: ROW + NA + EA) and East Asian emissions as simulated with CM12. Note that the colour scales of the panels differ.

and CM12 (shown for Europe in section 5.1.1). In general, the emissions from East Asian land transport emissions (O_3^{tea}), East Asian anthropogenic non-traffic (O_3^{iea}), and from biogenic emissions (O_3^{soi}) are the largest contributors to ground-level O_3 in East Asia.

These contributions show a positive gradient in South-East to North-West direction from the coast to the inland. The distribution of the contribution to ozone from long-range transported emissions is more homogeneous with the smallest values in city centres as Shanghai and Wuhan. Here, in the vicinity of large NO emissions, O_3 titration takes place and reduces the mixing ratio of O_3 (see reaction R9, p. 9).

Figure 5.10 displays $\text{PO}_{3i}^{\text{net}}$ for the primary emission sectors in East Asia, such as land transport, anthropogenic non-traffic, and biogenic, separated by their contribution from East Asian emissions (EA) and emissions from other regions (LRT). The $\text{PO}_{3i}^{\text{net}}$ ozone production for each emission sector (i) is defined by equation 5.1. The $\text{PO}_{3i}^{\text{net}}$ values exhibit a clear South-North gradient, with much larger net ozone production in North China than in South China. Moreover, the $\text{PO}_{3i}^{\text{net}}$ in the Pearl Delta is larger than in

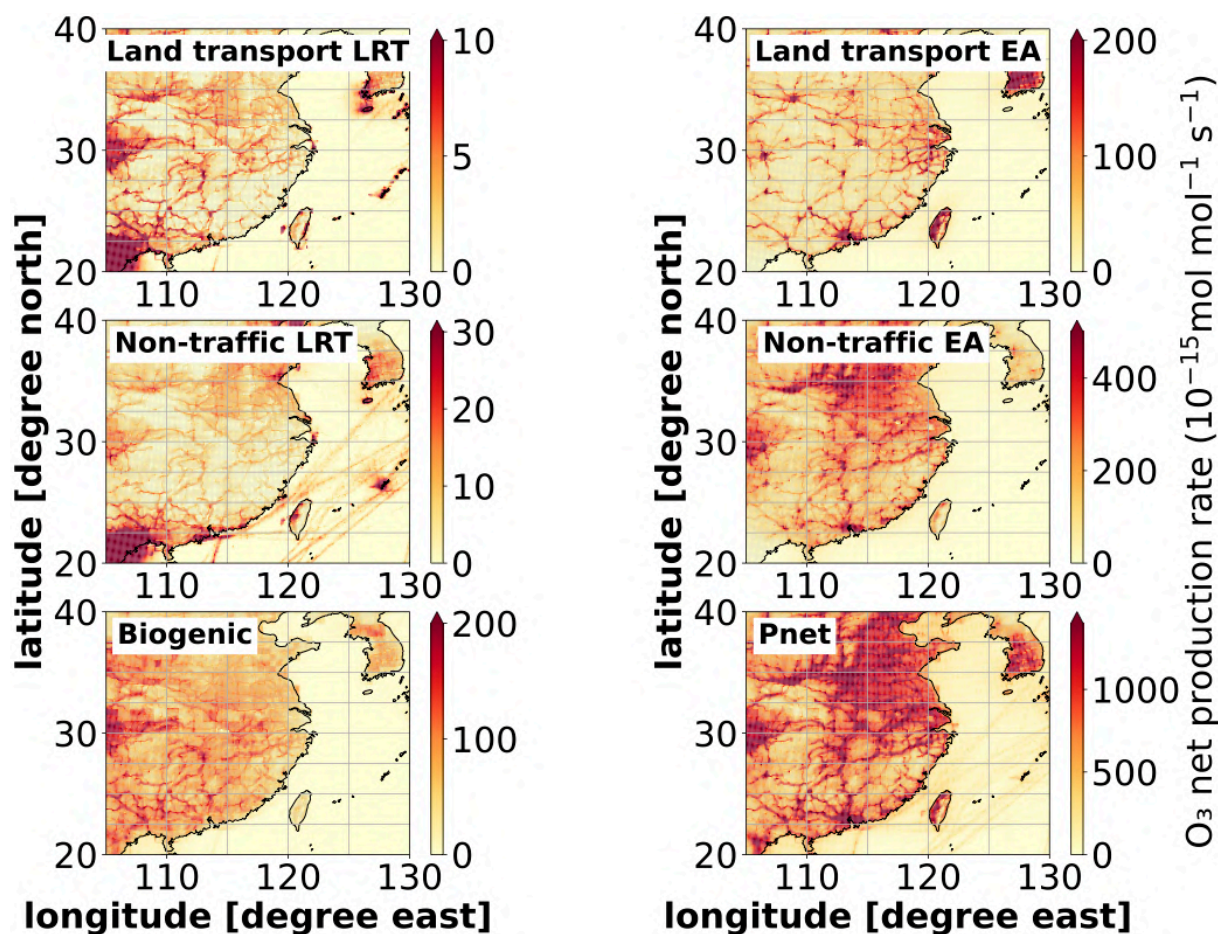


Figure 5.10: Seasonal mean (JJA 2017–2018) of the ozone net production rate ($P_{\text{net}} = \text{Production} - \text{Loss}$ in East Asia; see chemical mechanism in Appendix: ProdO_3 and LossO_3) in $10^{-15} \text{ mol mol}^{-1} \text{ s}^{-1}$ from long-range transported (LRT: ROW + NA + EU) and European sectors. Note that the colour scales of the panels differ.

the Yangtze Delta and Taiwan. The ozone production from East Asian land transport emissions peaks in the Pearl Delta, Taiwan, and some megacities across China, such as Wuhan, Chongqing, and Xi'An. Similarly, the $\text{PO}_{3i}^{\text{net}}$ from East Asian anthropogenic non-traffic emissions peaks in the Pearl Delta, the Sichuan Basin, and large areas in North China along the Wei and Yellow River Valley. In these regions, the largest regional anthropogenic non-traffic NO_y and NMHC emissions in East Asia occur (Figs. 5.8 and C.54, p. 196). The biogenic sources' ozone production is largest in the Sichuan Basin and some rural areas in the Northwest of China (Ningxia). Here, also in-situ production from anthropogenic precursors over East Asia from LRT plays an important role in the Sichuan Basin and the province Guandong.

Throughout the country, in-situ production from LRT anthropogenic emissions is large along significant transport links and some ship lanes in the Taiwan Strait and parts of the South China Sea. The larger production along the ship lanes results from the reactions of

NO_y shipping emissions with NMHC from industrial and land transport emissions outside East Asia. Large ozone production rates from LRT along the transport links are caused by the reservoir species peroxyacetyl nitrates (PAN) from LRT. Here, contributions of anthropogenic LRT emissions to the formation of PAN are 3–4 times larger, than from anthropogenic East Asian emissions (Fig. C.56, p. 198). PAN is formed outside East Asia, as a secondary pollutant, and its relatively long lifetime enables the transport to East Asia. It enhances indirectly the ozone formation after being photolysed, and reacting with OH. The photolysis of PAN forms NO_2 and RO_2 , which are important precursors of O_3 (see sections 2.2 and R23, p. 12). As a result, long-range transport of PAN contributes to O_3 formation in East Asia (Fig. C.56, p. 198).

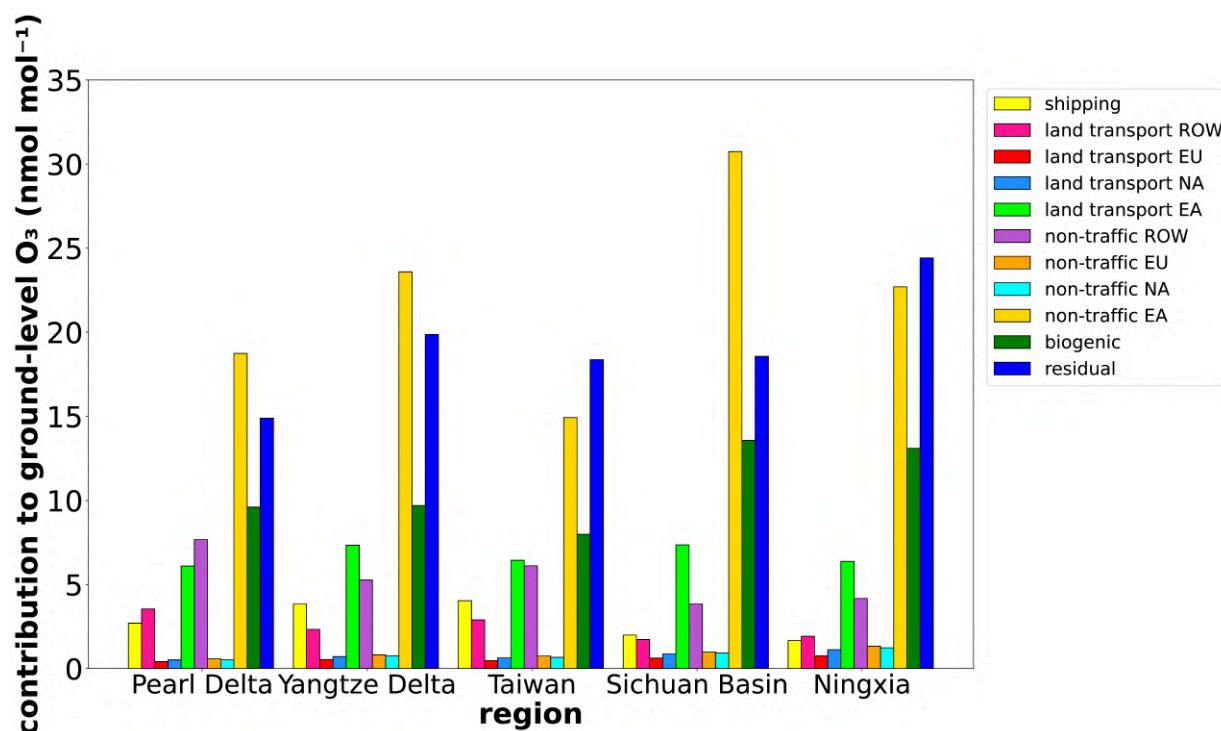


Figure 5.11: Seasonal mean absolute contributions of different emissions sectors and regions to ground level ozone in the five regions Pearl River Delta, Yangtze Delta, Taiwan, Sichuan Basin and Ningxia for JJA 2017–2018 as simulated with CM12.

In Figure 5.11 the CM12 simulated contributions to ground-level O_3 in each study area during JJA 2017–2018 are presented as area-averaged values. Since East Asia has already been analysed previously on a larger scale (Fig. 5.9), here it is not explicitly presented again as a distinct study area. Other emission sectors that are not explicitly shown are combined and presented as “residual”. Additional information on these sectors can be found in the Appendix, specifically in Figures C.57–C.60 (pp. 198–200). Over the three major polluted coastal regions - Pearl Delta, Yangtze Delta, and Taiwan - absolute contributions to O_3 from East Asian land transport (O_3^{tea}) and anthropogenic non-traffic emissions (O_3^{iea}), range from 6–8 nmol mol^{-1} and 15–23 nmol mol^{-1} , respectively, with the largest absolute

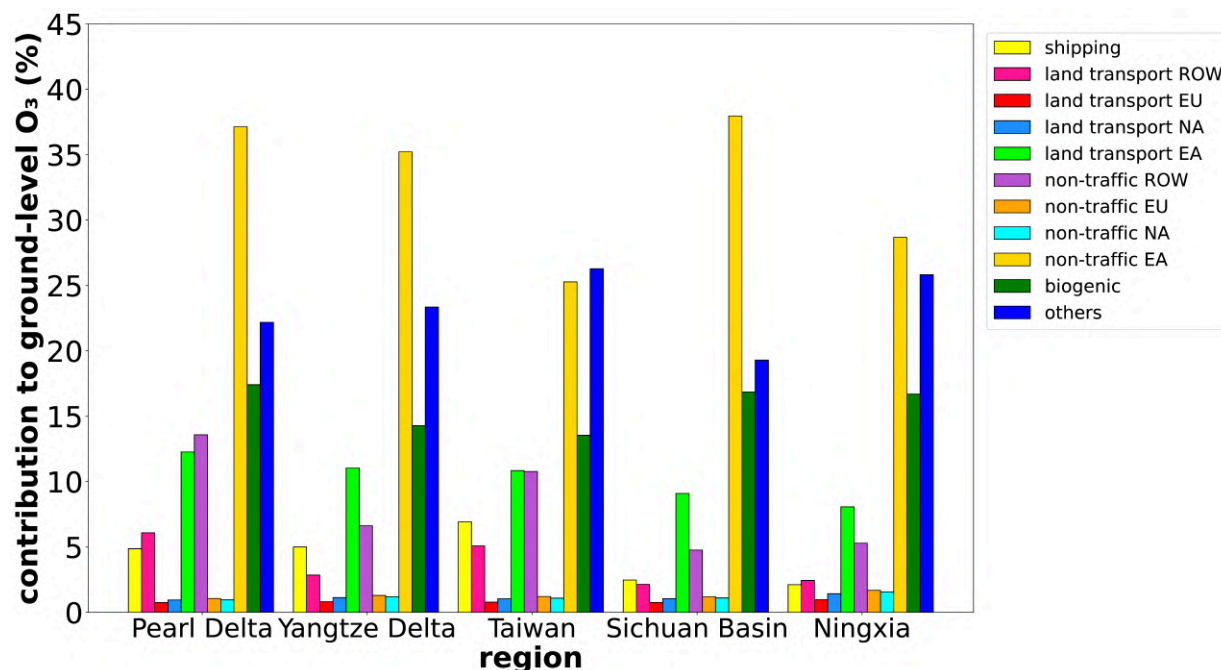


Figure 5.12: Seasonal mean relative contributions of different emissions sectors and regions to ground level ozone in the five regions Pearl River Delta, Yangtze Delta, Taiwan, Sichuan Basin and Ningxia for JJA 2017–2018 as simulated with CM12.

contributions arising in the Yangtze Delta.

The formation of O₃ in Taiwan and the Pearl Delta is significantly influenced by East Asian land transport and non-traffic anthropogenic emissions, as shown in Figure 5.10, whereas O₃ net production rates are rather small for the Yangtze Delta. Here, large local NO emissions deplete O₃ by titration.

Biogenic emissions contribute to O₃ at similar levels, with values ranging from 8–10 nmol mol⁻¹ in the Pearl Delta, the Yangtze Delta and Taiwan. The contributions from anthropogenic (land transport and anthropogenic non-traffic) LRT emissions are relatively small, with values ranging from 3–4 nmol mol⁻¹ and 7–8 nmol mol⁻¹, respectively. Among the three regions, the Pearl Delta has the largest O₃ contributions from LRT emissions. Here, anthropogenic LRT emissions enhance the local ozone production in particular (Fig. 5.10). Conversely, the ozone contribution from shipping emissions (O₃^{shp}) is slightly larger in Taiwan and the Yangtze Delta (3–4 nmol mol⁻¹) than in the Pearl Delta (2 nmol mol⁻¹). In the Yangtze Delta, the contributions to O₃ from the residual sectors (blue) are the largest and almost reach the order of magnitude of O₃ contributions from East Asian anthropogenic non-traffic emissions (O₃^{iea}) (Fig. 5.11).

The Sichuan Basin is a good example of a heavily polluted region, where the local topography supports high mixing ratios of ozone precursors across the area, due to the boundary layer capturing city plumes during periods of reduced wind. The topography around the Sichuan Basin mostly exceeds 1500 m above sea level (Fig. B.41, left panel, p. 186). Since the seasonal planetary boundary layer height (PBLH) in the Sichuan Basin in JJA 2017–

2018 is between 1000–1250 m above mean sea level (see Fig. B.41, p. 186), the topography favours the capturing of emissions in the basin. Consequently, East Asian land transport and anthropogenic non-traffic emissions contribute the most to O_3 in the Sichuan Basin, with absolute contributions of 8 nmol mol^{-1} and 32 nmol mol^{-1} respectively, surpassing all other study areas. Ningxia, a rural region located in the continental Northwest of China, shows slightly smaller ozone contributions from East Asian land transport (O_3^{tea}) and anthropogenic non-traffic emissions (O_3^{iea}) of 7 nmol mol^{-1} and 22 nmol mol^{-1} , respectively. Biogenic emissions also play an important role in local O_3 formation in Ningxia (Fig. 5.10). With contributions of 12 nmol mol^{-1} and 13 nmol mol^{-1} , they are comparable to those in the Sichuan Basin and larger than those in the three coastal regions. This agrees with the net O_3 production from biogenic emissions in the Ningxia and Sichuan Basin, which is up to two times larger than in the coastal study areas (Fig. 5.10, lower left panel). While in the rural region Ningxia and in the Sichuan Basin soil- NO_x emissions are larger than in the River Deltas and Taiwan, biogenic emissions of isoprene are larger in the Yangtze Delta as in the Sichuan Basin (see Figs. C.62 and C.63, p. 201).

The residual for all five study areas shows, that for each area, O_3 contributions from methane emissions ($O_3^{\text{CH}_4}$) are the most significant contribution to ground-level O_3 , with a range of $5\text{--}6 \text{ nmol mol}^{-1}$ (6–10%). O_3 contributions from lightning emissions (O_3^{lig}) are the second most important contributor, ranging from $3\text{--}6 \text{ nmol mol}^{-1}$ (5–8%), followed by O_3 contributions from stratosphere–troposphere exchange (O_3^{str}) and from biomass burning emissions (O_3^{bio}). It is noteworthy that the anthropogenic (excluding air traffic) and biogenic contributions collectively account for about 73–81 % of the ground-level O_3 in the study areas. Details about the residuals can be found in the Appendix in Figures C.57–C.60 on pages 198–200.

As shown in Figure 5.12, the relative O_3 contributions from East Asian land transport (O_3^{tea}) and East Asian anthropogenic non-traffic emissions (O_3^{iea}) to ozone in the Yangtze Delta, and Taiwan are comparable, at around 10–12 % and 25–35 %, respectively. The Pearl Delta has larger O_3^{tea} and O_3^{iea} contributions with up to 12 % and 37 %, respectively. All three regions exhibit O_3 contributions from biogenic emissions (O_3^{soi}), at around 13–17 %. Land transport and anthropogenic non-traffic emissions from long-range transport contribute only moderately to ozone in the Yangtze Delta and Taiwan with 5–7 % and 9–13 %, respectively. In relative contributions, over the Pearl Delta the largest shares to O_3 come from land transport and anthropogenic non-traffic LRT emissions with 8 % and 15 %, respectively.

In the Sichuan Basin, the relative contribution from East Asian land transport emissions (O_3^{tea}) is comparable to other highly polluted regions, but the contribution from East Asian anthropogenic non-traffic emissions (O_3^{iea}) is larger, up to 37 %. In relative terms, Ningxia has the smallest contribution of O_3^{tea} (7%) compared to all other study areas, and a similar contribution of O_3^{iea} as Taiwan, at around 27 %.

In general, the results show that the Sichuan Basin and the Pearl Delta exhibit the largest relative ozone contribution of 46 % (40 nmol mol^{-1}) and 49 % (25 nmol mol^{-1}) from East Asian anthropogenic emissions (land transport + non-traffic) in East Asia. In the Yangtze Delta, Ningxia and Taiwan, this relative ozone contribution is smaller, ranging from 35–

46 % (21–32 nmol mol⁻¹). This comparison indicates that the mitigation potential for the East Asian anthropogenic sector's on ozone in the Yangtze Delta, Taiwan, and Ningxia is more limited than in the Sichuan Basin and Pearl Delta, as much less ozone is produced in-situ from regional emissions. In relative terms, in the Yangtze Delta and Taiwan, the ozone contributions from anthropogenic LRT and shipping emissions, as well as from the residual sector, are more important than in the Sichuan Basin and Pearl Delta. This limits the mitigation potential for the East Asian anthropogenic sector in the Yangtze Delta and Taiwan in comparison to the Pearl Delta (see Fig. 5.11).

5.2.2 Contributions during periods of large ozone values in East Asia

East Asia with its subtropical climate and large anthropogenic emissions, experiences significant ozone mixing ratios. In the following, contributions during large ozone mixing ratios are analysed with the same methods as described in section 5.1.2.

Figure 5.13 illustrates the absolute contributions of land transport, anthropogenic non-traffic, and biogenic emissions at different ozone percentiles, while their relative contributions can be found in Figure C.64 in the Appendix (p. 202). The results show that the contributions from East Asian land transport (1–22 nmol mol⁻¹, 1–23%) and East Asian anthropogenic non-traffic emissions (1–72 nmol mol⁻¹, 1–63 %) vary considerably across East Asia, with the contributions from long-range transport exhibiting less variation (also see Fig. 5.9). This broad range is caused by the in-homogeneous distribution of emission sources and large spread of the net ozone production (Fig. 5.10). The absolute contributions from East Asian land transport emissions increase for increasing ozone percentiles the most in the Pearl Delta, the Yangtze Delta, in Taiwan and the Sichuan Basin. This increase is substantially smaller in the rural Ningxia region. The largest contributions from East Asian land transport emissions (O_3^{tea}) for the 95th and 90th percentiles occur in the Pearl and the Yangtze Delta. Furthermore, an increase with increasing ozone percentiles of contributions from East Asian anthropogenic non-traffic emissions (O_3^{iea}) can be derived over all five study areas. The Sichuan Basin, Ningxia and the Pearl Delta show the largest contributions from East Asian anthropogenic non-traffic emissions (O_3^{iea}) for the 95th and 90th percentiles.

The contributions from biogenic emissions (O_3^{soi}) also show an increase with higher ozone percentiles across all study areas, with the largest values observed in the Sichuan Basin and Ningxia.

Especially in the Sichuan Basin, the contributions from LRT emissions to O_3 show small variations across all ozone percentiles for the anthropogenic (land transport and non-traffic) sector. Conversely, as shown in Figure 5.13, the largest disparity between contributions from long-range transport and East Asian emissions is observed in the Sichuan Basin and the Pearl Delta, where the net ozone production is also the largest. These results indicate that the overall potential to reduce large ozone values by reduction of East Asian emissions is larger in the Pearl Delta and Sichuan Basin, compared to Taiwan and the Yangtze Delta.

This is also in accordance with the study conducted by Yang et al. [2020], who found that the Sichuan Basin has a large potential for mitigating ozone because local anthropogenic emissions (e.g., transportation and industry) are the dominant sources of ozone formation in the basin.

In contrast, Taiwan exhibits quite large contributions from long-range transport emissions to ground-level O_3 , which limits the potential of mitigating large ozone values. This finding is consistent with results by Chou et al. [2006] and Chen et al. [2022], who showed that reducing anthropogenic emissions in the upwind regions of Taiwan can significantly contribute to reducing ozone in Taiwan, because the long-range transport of precursor emissions contributes considerably to ozone.

In the following, ozone contributions during MDA8 are investigated, with the same method as used in section 5.1.2. The analysis of the seasonal maxima, mean and minima for MDA8 ozone in JJA 2017–2018 is done for whole East Asia and each study area (Fig. C.65, p. 203). A figure with the same analysis differentiating between contributions from East Asian emissions and long-range transport is part of the Appendix (Fig. C.66, p. 204).

Figure 5.14 shows the absolute ozone contributions during MDA8 ozone as box-whisker plots (relative contribution are shown in Figure C.67 in the Appendix, p. 205). The monthly maxima of MDA8 over East Asia range from 25–160 nmol mol^{-1} (Fig. 5.14). Contributions to the maximum MDA8 ozone of land transport emissions range between 2–26 nmol mol^{-1} , contributions from anthropogenic non-traffic emissions between 5–85 nmol mol^{-1} and contributions from biogenic emissions between 3–20 nmol mol^{-1} . The analysis largely confirms the findings from the analysis of the percentiles. From minimum to maximum MDA8 values the absolute contributions of land transport, anthropogenic non-traffic and biogenic emissions increase over the Pearl Delta, the Yangtze Delta, Taiwan and the Sichuan Basin, with the smallest increase above the Ningxia region. This increase is largest in the Pearl Delta for the contributions from regional anthropogenic emissions, which means, large MDA8 values are strongly driven by East Asian emissions, while over Taiwan and the Pearl Delta the long-range transport plays a more important role (see Fig. C.66, p. 204). This finding is in accordance with the study by Li et al. [2019], who applied a source attribution method over the Yangtze River Delta and found that industry and vehicle emissions are major anthropogenic sources of ozone during high ozone levels in this area. In the Sichuan Basin, this effect is slightly smaller, and large MDA8 values are weaker driven by East Asian emissions. Nevertheless, East Asian emissions are still important for the mean ozone mixing ratios in the Sichuan Basin, but more constant throughout the whole summer months and thus less limited to specific extreme ozone events. Hence, mitigating ozone during MDA8 ozone events in the Sichuan Basin is more limited than in the Pearl Delta. In Ningxia the minimum, maximum, and mean MDA8 values change less than in the Pearl Delta and Sichuan Basin, and especially the contributions from anthropogenic LRT emissions hardly vary with MDA8.

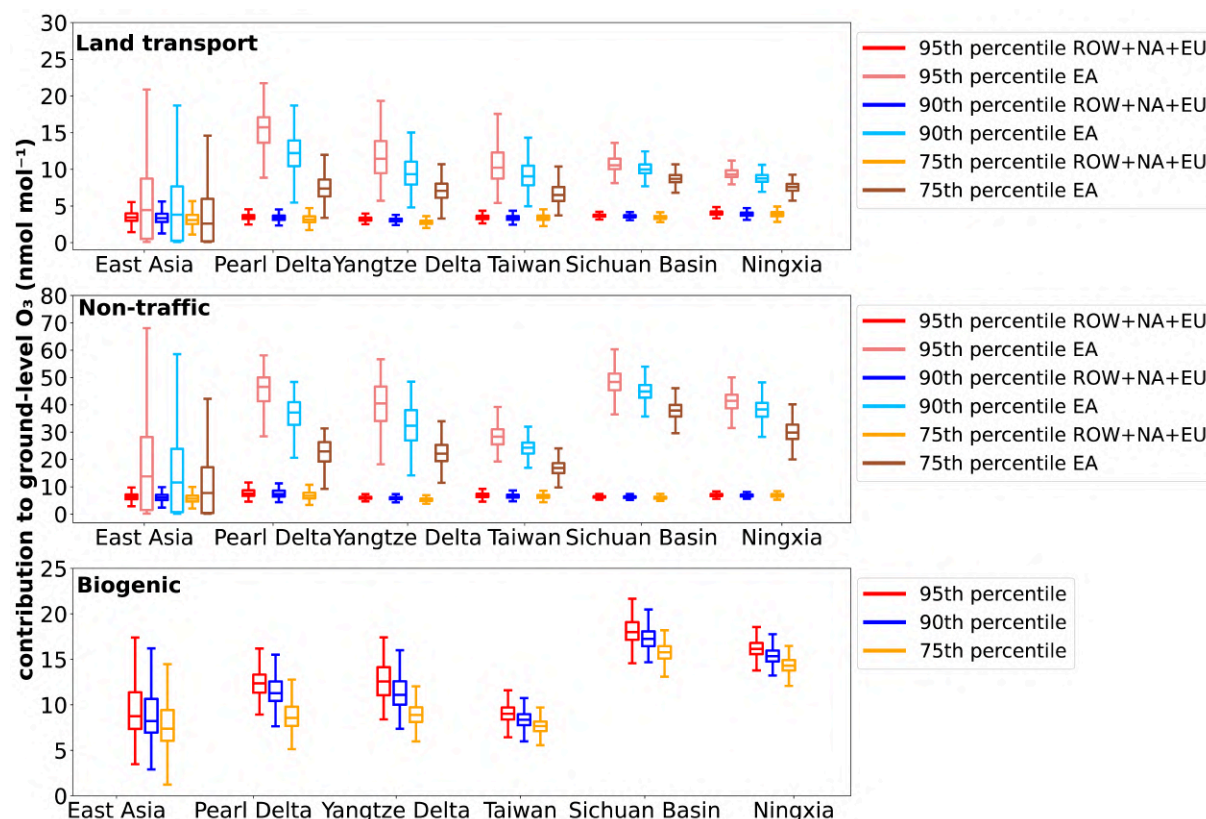


Figure 5.13: Box-whisker plot showing the seasonal mean (JJA 2017–2018) contributions in nmol mol^{-1} of the most important emission sources at the 95th, 90th, and 75th percentiles of ozone as simulated by CM12 in East Asia. The upper panel shows the absolute regional contributions of O_3^{tea} and the sum of long-range transported absolute contributions of O_3^{tra} , O_3^{tna} and O_3^{teu} . The middle panel shows the regional absolute contributions of O_3^{iea} and the sum of long-range transported absolute contributions of O_3^{ind} , O_3^{ina} and O_3^{ieu} . The lower panel shows the absolute contributions of O_3^{soi} . The lower and upper ends of the boxes indicate the 25th and 75th percentile of the corresponding regional distribution, respectively, the bar the median, and the whiskers are defined as ± 1.5 the interquartile range of the contributions of all grid boxes within the indicated region.

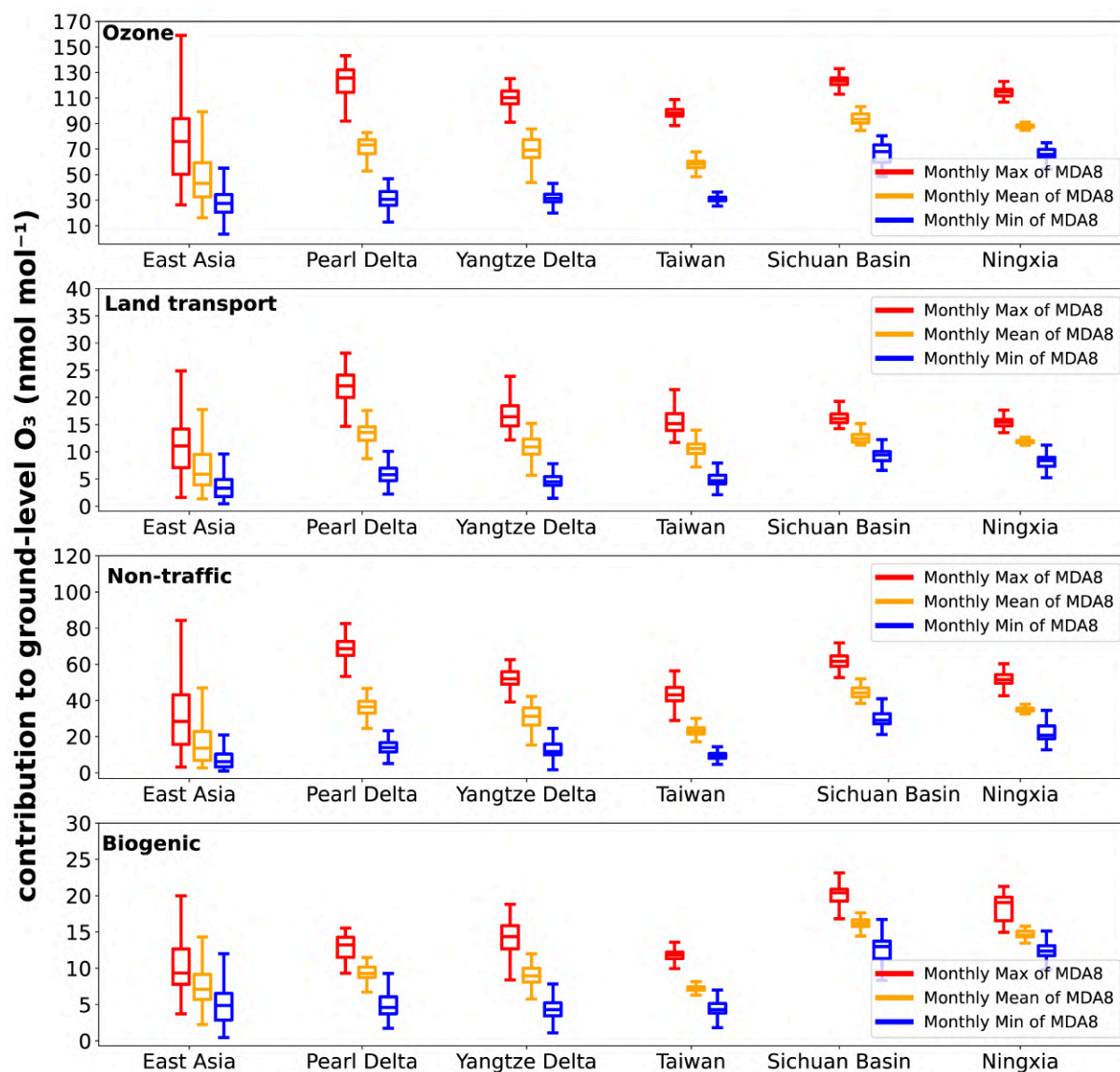


Figure 5.14: Box-whisker plot showing the contributions in nmol mol⁻¹ of the most important emission sources of ozone as simulated by CM12 for JJA 2017–2018 in East Asia. Shown are ozone and the contributions of land transport, anthropogenic non-traffic and biogenic emissions to ground-level ozone during the seasonal maximum of the maximum daily 8-h average (MDA8) (upper panel), the seasonal mean of MDA8 (middle panel) and the seasonal minimum of MDA8 (lower panel) as ozone mixing ratio in nmol mol⁻¹ based on 1-hourly model output. The lower and upper ends of the boxes indicate the 25th and 75th percentile corresponding regional distribution, respectively, the bar the median, and the whiskers are defined as ± 1.5 the interquartile range of the contributions of all grid boxes within the indicated region.

5.3 Comparison of the study areas in Europe and East Asia

In sections 5.1.1 and 5.2.1 I analysed the O_3 contributions from anthropogenic and biogenic emissions in Europe and East Asia. The aim of this section is to compare the O_3 chemical regimes between the study areas in more detail. To accomplish this, different measures are used to compare the efficiency and sensitivity of O_3 formation to NO_x and VOCs between Europe and East Asia. Section 5.4 assesses and discusses the ozone mitigation potential for certain study areas in Europe and East Asia. I compare the ozone production efficiency (see section 2.2.1, Equation 2.5) for the CM12 model results between Europe and East Asia. The ozone production efficiency (OPE) conceptually quantifies the number of O_3 production cycles undergone by one molecule of NO_x before it is transformed into HNO_3 .

Figure 5.15 presents the OPE values for Europe and East Asia. High values indicate that one NO_x molecule forms several O_3 molecules, while small OPEs indicate that one NO_x molecule forms fewer O_3 molecules. The OPE increases from North to South direction in both, Europe and East Asia. In highly polluted regions like the Benelux region, Southern England, and above the English Channel, O_3 production is less efficient, with an OPE range of 6–20. Similar OPE values are also observed in major polluted areas of East Asia, such as the Yangtze River Delta, the Pearl River Delta, and the west coast of Taiwan. Thus, the O_3 formation is rather inefficient next to large NO emission sources in coastal, heavily polluted areas of Europe and East Asia (see Fig. C.42, p. 188).

The strong gradient of the OPE along the coastline in many regions is caused by larger OH mixing ratios offshore compared to inland (factor of 2–3, see also Fig. C.68, p. 206), which enhance the loss of NO_2 via OH into the reservoir species HNO_3 (R26, p. 12). Hence, there is a reduced availability of NO_2 for O_3 formation. Figure 5.16 shows the monthly production of O_3 by the reaction chain, starting with the reaction R18 (upper panels; p. 11) and the production of HNO_3 (lower panels; reaction R26). These individual terms are utilised in the calculation of the OPE. Figure 5.16 confirms the finding explained above, showing a larger monthly production of HNO_3 along the coastline compared to inland in the CM12 model results. This results in a larger denominator in the OPE term. The OH mixing ratio above the sea is usually larger due to the increased humidity over the sea (see Fig. C.69, p. 206), which enhance the production of OH through the photolysis of water vapor. Further inland, less OH is available, which reduces the conversion of NO_2 into HNO_3 and enhances O_3 formation leading to larger OPEs.

Figure 5.15 shows that a steep topography around polluted basins, such as the Po Valley and the Sichuan Basin (Fig. B.41, left panel, p. 186), leads to a slow down of the O_3 production at their lowest planes (small OPEs of 10–20). As described in section 5.2.1, during calm conditions, the planetary boundary layer of a basin tends to trap NO_x emissions, resulting in larger mixing ratios compared to lowlands. With increasing altitude above mean sea level (see Fig. B.41, left panel, p. 186), NO_x mixing ratios decrease, and the OPE increases, up to 40–50 (Fig. 5.15).

In rural regions located far from significant NO_x emission sources, such as the Iberian

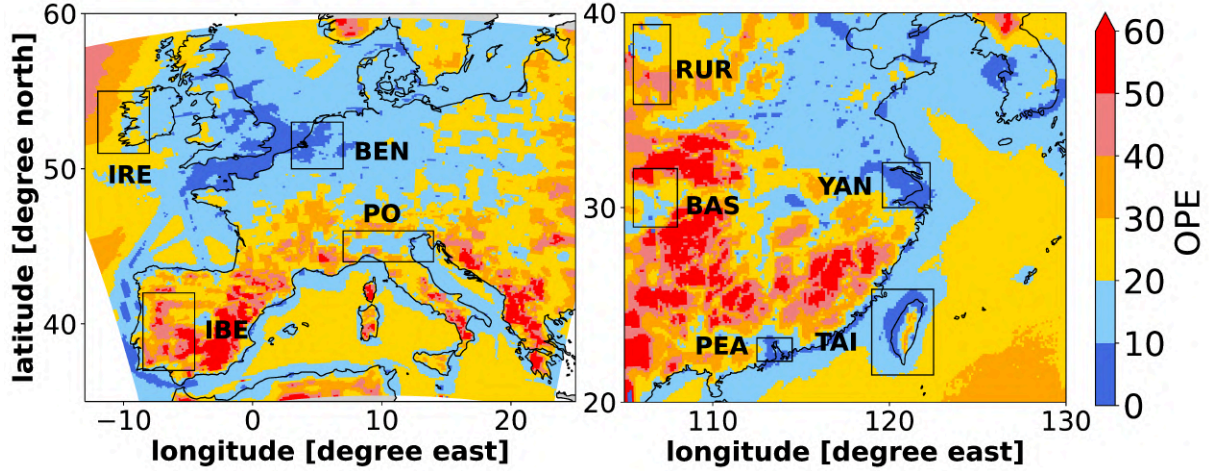


Figure 5.15: Ozone production efficiency (OPE) in JJA 2017–2018 for Europe (left) and East Asia (right) in CM12. Rectangles mark the study areas for Europe, labelled according to Table 5.1. East Asian study areas are labelled according to Table 5.2.

Peninsula and West Ireland, as well as Ningxia, O_3 formation is highly efficient, with an OPE range of 10–60. Similar OPE values also occur in the Balkans, parts of the Iberian Peninsula, and Southern Italy, ranging from 40–60. Therefore, rural regions exhibit significantly higher OPE values than polluted study areas, which is in line with several studies [e.g. Kleinman, 1994, Olszyna et al., 1994, Ninneman et al., 2017, 2019].

Figure 5.17 shows the OPE and the corresponding NO_x and NMHC mixing ratios for all study areas in Europe and East Asia. As described above, the OPE decreases for increasing NO_x mixing ratios. In addition, an increase in NMHC at a given NO_x level leads to an increase in the OPE. Here, an increasing NMHC mixing ratio increases the probability of O_3 formation via additional pathways next to reaction R18 (p. 11). This happens due to the competition of OH around NO_x and NMHCs. In general, the distribution of the NO_x and NMHC mixing ratios and their respective OPE in the Benelux region, is comparable to the East Asian study areas Pearl Delta, Yangtze Delta, and Taiwan. At large NO_x and NMHC mixing ratios, the ozone production is less efficient (low OPE). In the Po Valley, small OPE values (0–20) and large OPE values (up to 40) are quite uniformly distributed across all NO_x values, and the decrease of the OPE with increasing NO_x mixing ratios is weaker. The same applies to the OPE in the Sichuan Basin. Rural regions, such as Ireland, the Iberian Peninsula, and Ningxia, are located far away from major emission sources. In these regions, the mixing ratios of NO_x and NMHCs are more uniformly distributed, and the OPE decreases with increasing NO_x and NMHC mixing ratios.

In summary, the O_3 production efficiency in polluted areas is generally low and decreases as NO_x mixing ratios increase. This is because the conversion of NO_2 into HNO_3 is large, leading to a reduction in O_3 formation. The same applies to both basins in Europe and East Asia, but here, the decrease in OPE with increasing NO_x mixing ratios is weaker. However, in certain rural study areas (e.g. Ningxia), the OPE is generally larger for similar

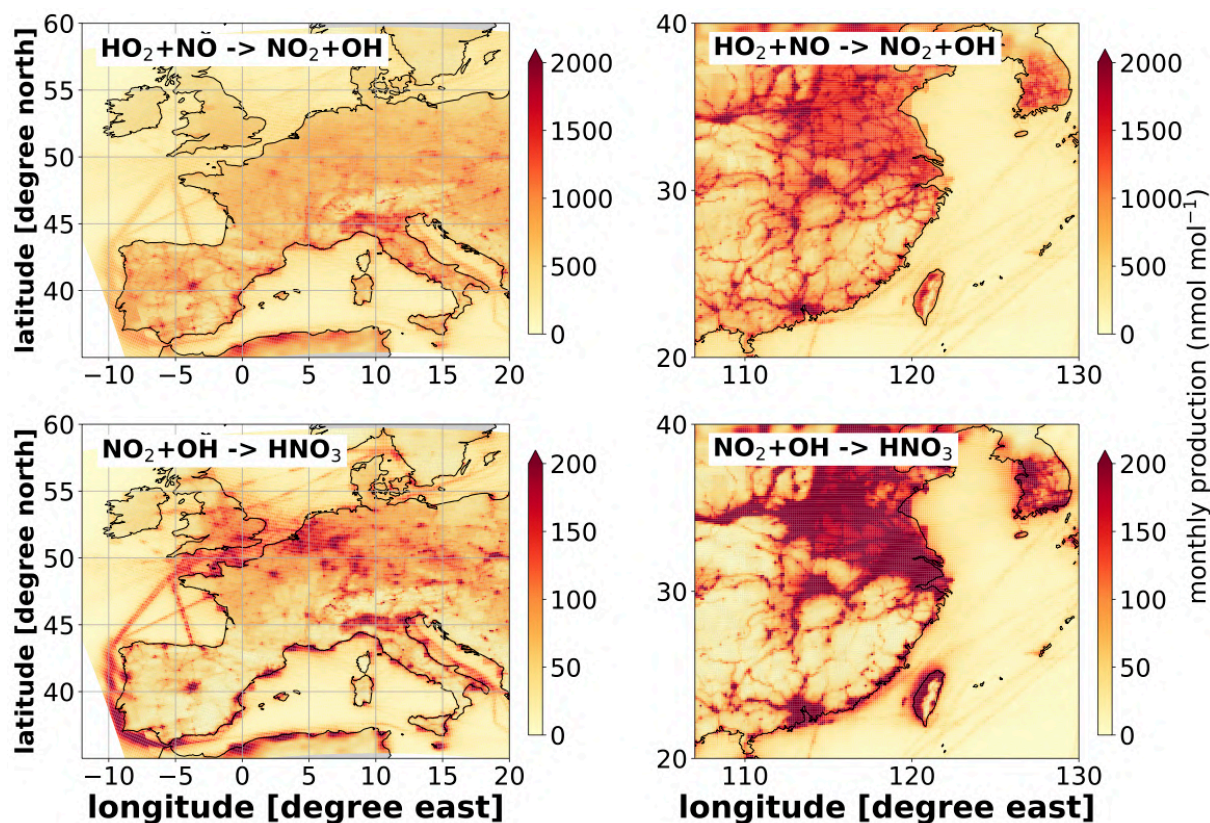


Figure 5.16: Seasonal mean (JJA 2017–2018) of the monthly production of reaction R18 (upper panels; p. 11) and of reaction R26 (lower panels; p. 12) in nmol mol⁻¹ for CM12 for Europe (left) and East Asia (right).

NO_x and NMHC mixing ratios as in the polluted regions. Here, less NO_2 is converted into HNO_3 , making it available for O_3 formation. This leads to a more efficient O_3 formation in the Po Valley, Sichuan Basin and Ningxia compared to the Benelux region, Yangtze Delta, Pearl Delta, and the west coast of Taiwan.

When directly comparing the OPE with other studies, it is important to keep in mind that differences in the definition of the OPE can make the comparison challenging. In the global study of Dahlmann et al. [2011], they calculated OPE values ranging from 10 to 30 in Europe and confirmed that the OPE is lower for ground-based source emissions in polluted areas than in remote regions, which is consistent with the present findings. A quantitative comparison with my results is limited because Dahlmann et al. [2011] used a coarser resolved global model, which can affect the OPE. Similarly, Moiseenko et al. [2018] determined surface OPEs ranging from 10–30 during European summer months, which agrees with the present results. Additionally, Sillman [2000] discovered that OPE values in NO_x plumes are minimal, ranging from 1–5, and increase with distance from the plume (as seen in the Benelux region and Yangtze River Delta). The CM12 results are in line with these studies, indicating large OPE values far away from highly polluted areas and small OPE values within NO_x plumes.

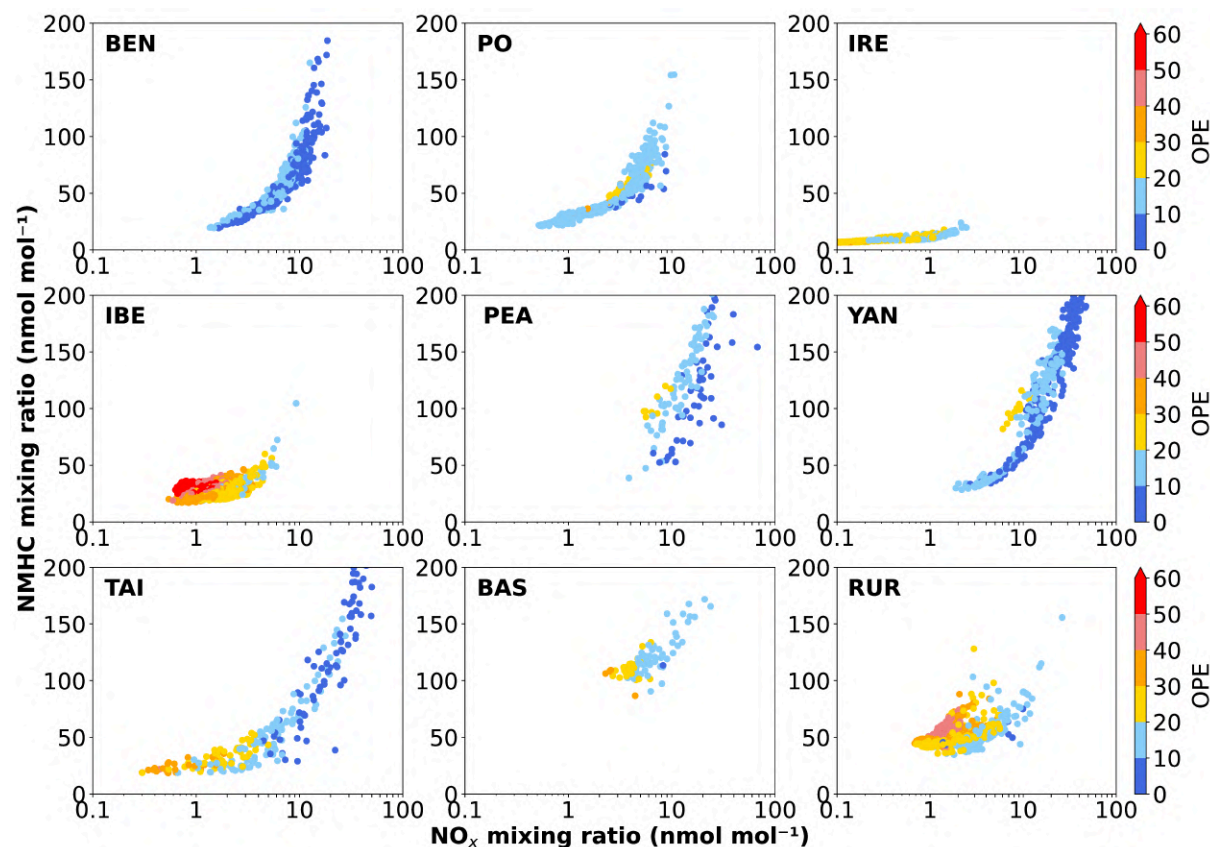


Figure 5.17: Relation of OPE with the NO_x and NMHC mixing ratio in amount of C in nmol mol^{-1} as simulated by CM12 in JJA 2017–2018 for the European and East Asian study areas as scatter plots. Study areas for Europe labelled according to Table 5.1. East Asian study areas labelled according to Table 5.2. NMHC mixing ratios above $200 \text{ nmol mol}^{-1}$ are not shown here. Here, Taiwan (TAI) is only represented over land, with the ocean excluded. The Po Valley (PO) and Sichuan Basin (BAS) are only shown for elevations lower than 150 m and 350 m, respectively.

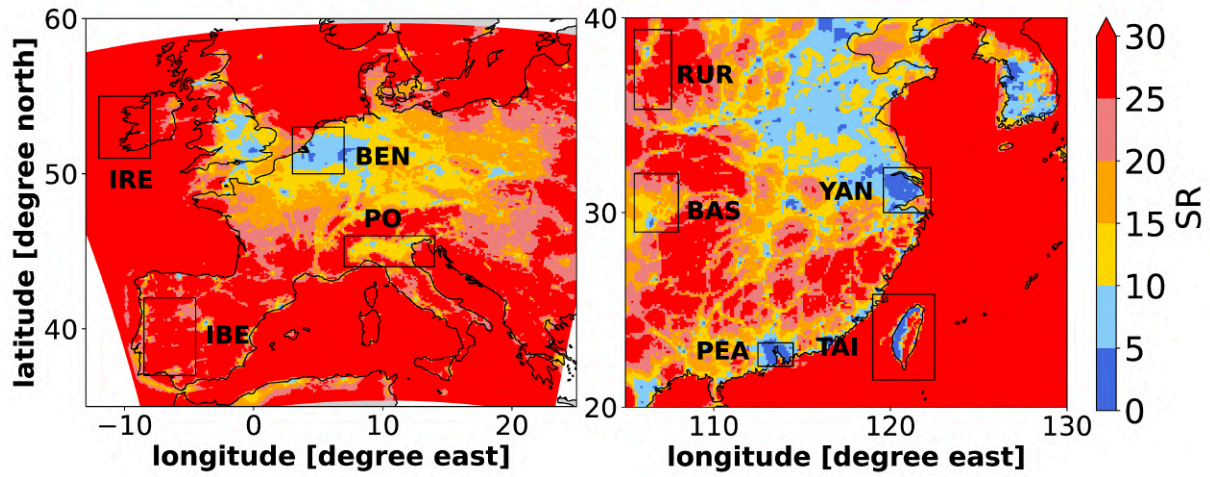


Figure 5.18: SR of CM12 in JJA 2017–2018 for Europe (left) and East Asia (right). Rectangles mark the study areas for Europe, labelled according to Table 5.1. East Asian study areas are labelled according to Table 5.2.

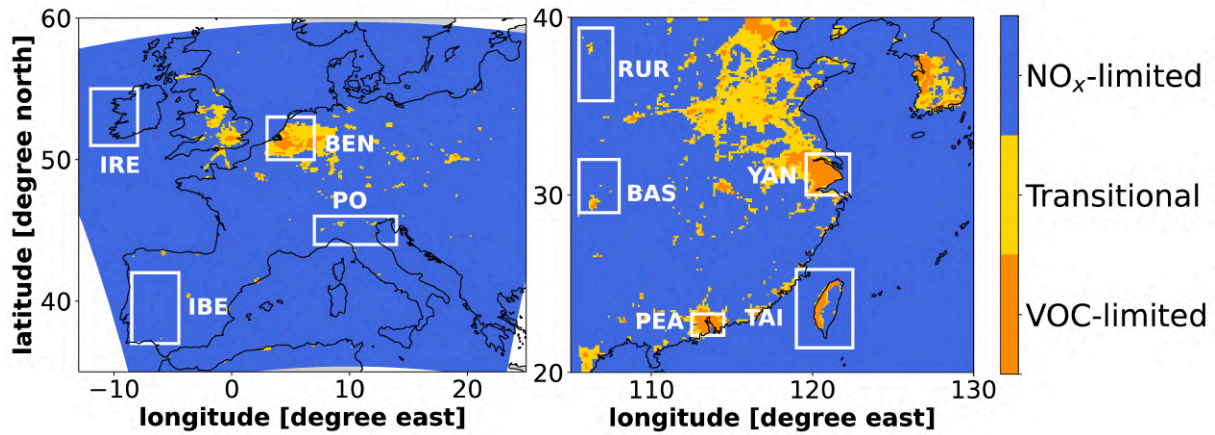


Figure 5.19: Chemical regimes classified after their Sillman ratio, into VOC-limited (< 6), transitional (6–8) and NO_x -limited regime (> 8) for CM12 in JJA 2017–2018 for Europe (left) and East Asia (right) Sillman et al. [1998]. Rectangles mark the study areas for Europe, labelled according to Table 5.1. East Asian study areas are labelled according to Table 5.2.

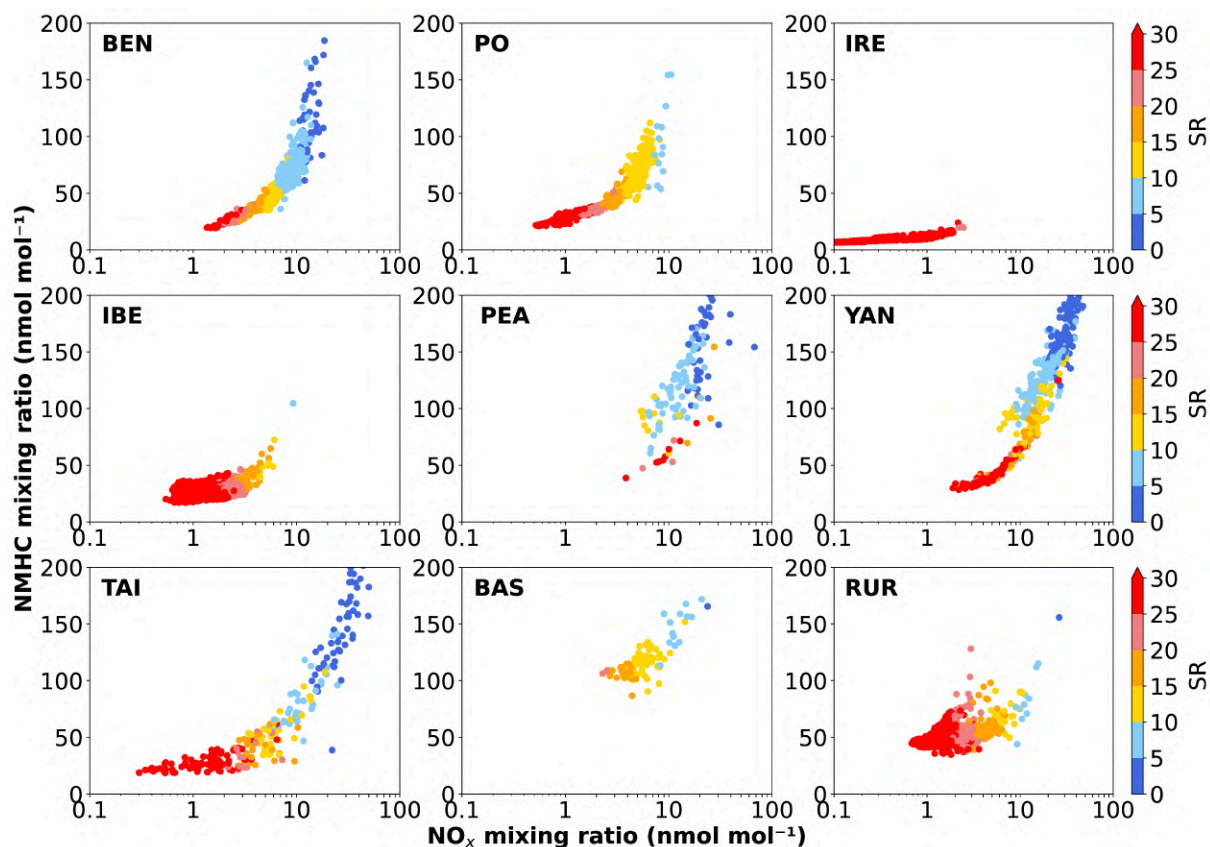


Figure 5.20: Relation of SR with the NO_x and NMHC mixing ratio in amount of C in nmol mol^{-1} as simulated by CM12 in JJA 2017–2018 for the European and East Asian study areas as scatter plots. Study areas for Europe labelled according to Table 5.1. East Asian study areas labelled according to Table 5.2. NMHC mixing ratios above $200 \text{ nmol mol}^{-1}$ are not shown here. Here, Taiwan (TAI) is only represented over land, with the ocean excluded. The Po Valley (PO) and Sichuan Basin (BAS) are only shown for elevations lower than 150 m and 350 m, respectively.

In order to assess, whether the O_3 production is NO_x - or VOC-limited, the Sillman Ratio (SR) as introduced by Sillman [1995] is analysed in the following:

$$SR = \frac{[O_3]}{[NO_y]}, \quad (5.2)$$

where $[O_3]$ represents the concentration of ozone and $[NO_y]$ the concentration of the total reactive nitrogen (see equation A.2 in section A.1.2, p. 137). Sillman [1995] introduced different NO_x -VOC indicators, but in this study only the ratio between O_3 and NO_y is analysed.

In Figure 5.18, the SR (Equation 5.2) for Europe and East Asia during JJA 2017–2018 is displayed. The Benelux region, the Pearl Delta, the Yangtze Delta, and the west coast of Taiwan exhibit small SRs, mostly ranging from 1 to 5. The Po Valley and the Sichuan Basin show larger SRs with a greater geographical variation, mostly between 5–20, with values exceeding 30 at the basin edges. In rural regions of Europe, the SRs are generally larger, with values of 15–30, apart from local plumes. According to Sillman [1995] and Sillman et al. [1998], small SRs point to a VOC-limited regime, while larger SRs indicate a NO_x -limited regime. Sillman et al. [1998] determined thresholds for these regimes but underlined their dependency on surrounding conditions (e.g., decrease of thresholds with increasing ozone mixing ratio). Therefore, these thresholds are quite complex and only applicable to specific conditions, which is why they should be used with caution, while keeping these limitations in mind.

Figure 5.19 attempts to classify the study areas into three regimes based on their SR: VOC-limited (<6), transitional ($6-8$), and NO_x -limited (>8) Sillman [1995], Sillman et al. [1998], Sillman [1999]. Based on these thresholds, the O_3 production in the Benelux region is mostly VOC-limited. This classification indicates similar results for the Yangtze River Delta, the Pearl River Delta, and the west coast of Taiwan. Apart from polluted areas, the O_3 chemical regime is transitional and not clearly NO_x - or VOC-limited. In contrast, the O_3 formation in rural areas such as Ireland and the Iberian Peninsula are mostly limited by NO_x , similar to Ningxia.

Figure 5.20 illustrates the relationship between the SR and the mixing ratios of NO_x and NMHCs. Across all study areas, the SR decreases with increasing NO_x and NMHC values. Large SRs, ranging from 20 to above 30, are mostly observed at low NO_x and NMHC mixing ratios, indicating that the chemical regime is certainly NO_x -limited. A transition from NO_x - to VOC-limited within a region can be especially observed in the Benelux region, the Pearl Delta, the Yangtze Delta, and Taiwan.

After analysing the effects of NO_x and VOC mixing ratios on O_3 formation, it is crucial to assess the role of photolysis in O_3 formation (as described in section 2.2) compared to the depletion of O_3 by titration in Europe and East Asia. The Leighton Ratio quantifies the deviation of O_3 from the hypothetical photostationary state of a system composed primarily of NO_x and O_3 (see section 2.1, Equation 2.2; Leighton [1961]).

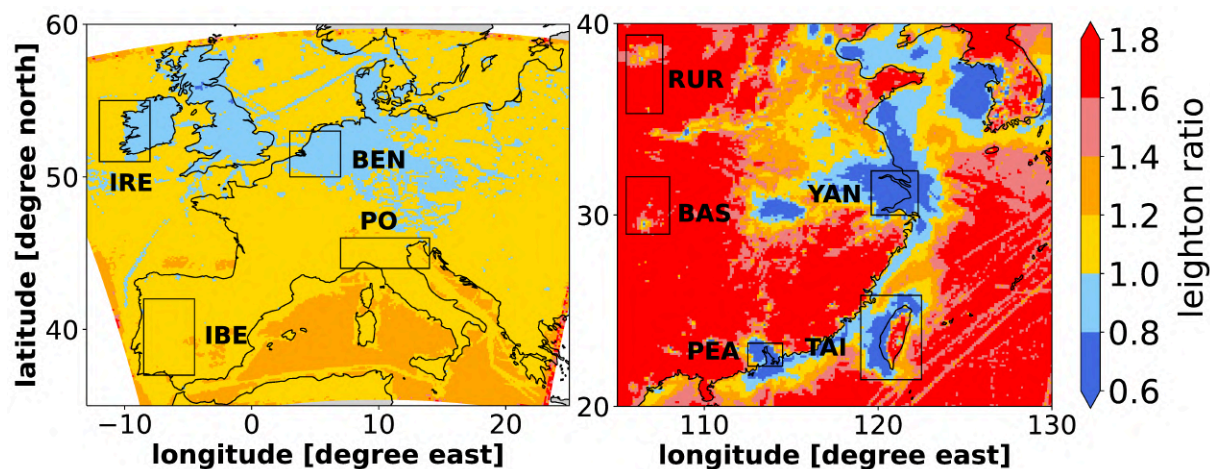


Figure 5.21: Illustration of the Leighton Ratio (ϕ) for CM12 during JJA 2017–2018 for Europe (left) and East Asia (right). A Leighton Ratio of 1 indicates that the system is in a photostationary state, while $\phi < 1$ indicates significant local emissions of NO. Conversely, according to Chate et al. [2014], a $\phi > 1$ suggests the domination of the conversion of NO to NO₂ in the presence of RO₂ and other reactions that deplete O₃, in addition to reaction R9. Rectangles mark the study areas for Europe, labelled according to Table 5.1. East Asian study areas are labelled according to Table 5.2.

Figure 5.21 presents the Leighton Ratio for Europe and East Asia during JJA 2017–2018. The Leighton Ratios indicate that O₃ is mostly in a photostationary state ($\phi \approx 1$) in Central Europe. In contrast, in East Asia, O₃ is almost never in a photostationary state, except in the transition zones between heavily polluted and more rural areas. This is because in East Asia, either large NO sources enhance the titration of O₃ ($\phi < 1$), or NO reacts less with O₃, and the formation pathways via HO₂ and RO₂ become more important for O₃ formation through photolysis of NO₂ ($\phi > 1$).

Coastal major polluted areas in East Asia show rather small Leighton Ratios between 0.5–0.8, indicating large local emissions of NO (Fig. C.42, right panel, p. 188). Here, the titration of O₃ by NO is larger than the O₃ formation by the photolysis of NO₂. The rest of East Asia, except for megacities such as Wuhan, shows large Leighton Ratios between 1.3–1.8. According to Chate et al. [2014], this suggests that NO tends to be converted to NO₂ in the presence of RO₂, which weakens the removal of NO₂ into HNO₃. As a result, these areas exhibit a large NO₂-NO ratio (Fig. C.70, p. 207).

Figure 5.22 illustrates the relationship between the Leighton Ratio and the NO_x and NMHC mixing ratios. Most of the study areas in Europe and East Asia show a decrease in the Leighton Ratio as the NO_x and NMHC values increase. In Europe, this decrease is relatively small, with only the Benelux region tending towards Leighton Ratios of 0.8 for very large NO_x and NMHC mixing ratios.

In the Benelux region, large NO sources favour O₃ titration, and the ozone formation via the photolysis of NO₂ is relatively weak due to the rapid removal of NO₂ into HNO₃ (see Fig. 5.16, lower left panel). The same applies to the Yangtze Delta, the Pearl River

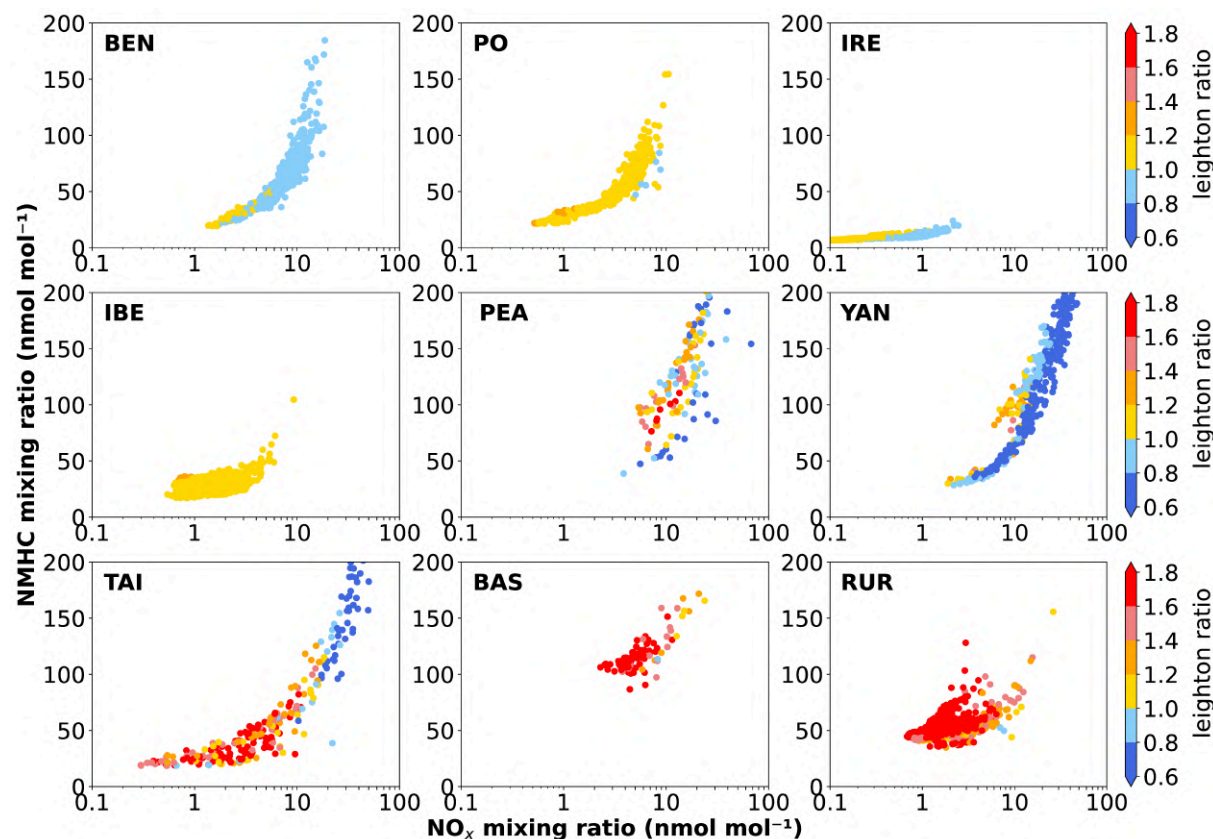


Figure 5.22: Relation of Leighton Ratio with the NO_x and NMHC mixing ratio in amount of C in nmol mol^{-1} as simulated by CM12 in JJA 2017–2018 for the European and East Asian study areas as scatter plots. Study areas for Europe labelled according to Table 5.1. East Asian study areas labelled according to Table 5.2. NMHC mixing ratios above $200 \text{ nmol mol}^{-1}$ are not shown here. Here, Taiwan (TAI) is only represented over land, with the ocean excluded. The Po Valley (PO) and Sichuan Basin (BAS) are only shown for elevations lower than 150 m and 350 m, respectively.

Delta, and the west coast of Taiwan.

In contrast, the Leighton Ratio over the Iberian Peninsula reaches up to 1.2, and O_3 only deviates slightly from the photochemical state. Here, the O_3 formation via the RO_2 pathway is more favoured [Chate et al., 2014], which, combined with small NO sources, results in more ozone formation via photolysis than O_3 titration by NO. The same applies to the Sichuan Basin and the rural area of Ningxia in East Asia. Here, the Leighton Ratios are the largest, reaching up to 1.8, due to increased O_3 formation via RO_2 , which weakens the sink of NO_2 and makes it available for O_3 formation. My results for the Leighton Ratios in rural areas are consistent with the findings of other studies, which have shown Leighton Ratios ranging from 1.2 to 3.0 [Ridley et al., 1992, Cantrell et al., 1997, Rohrer et al., 1998, Hosaynali Beygi et al., 2011].

In summary, the results indicate that the efficiency of O_3 production in the vicinity of large NO sources is low (less than 10) in parts of the Benelux region (BEN) and the major polluted areas of the Pearl Delta (PEA), Yangtze Delta (YAN), and the west coast

of Taiwan (TAI). This is because NO_2 is rapidly removed by OH into HNO_3 (Fig. 5.16, middle left panel), resulting in less O_3 formation. In these study areas, the titration of O_3 is larger than the ozone formation via photolysis of NO_2 ($\phi < 1$). This is consistent with the Sillman Ratio, which indicates that in these study areas, O_3 formation is limited by VOCs, which means O_3 formation decreases with increasing NO_x mixing ratios.

In most rural study areas of Europe and East Asia, the OPE is large because less NO_2 is removed, making it available for O_3 formation via photolysis. This effect is more prominent in East Asia, with Leighton Ratios ranging from 1.2 to 1.8, compared to Europe, where Leighton Ratios reach up to 1.2. The larger Leighton Ratios in East Asia suggest that the conversion of NO to NO_2 in the presence of RO_2 [Chate et al., 2014] is more favoured than in Europe. In most rural study areas in Europe, O_3 is in a photostationary state, meaning that the mixing ratios of O_3 , NO, and NO_2 primarily depend on the photolysis of NO_2 . The formation of O_3 in almost all rural study areas in Europe and East Asia is primarily limited by NO_x . This means that the O_3 formation increases as the NO_x mixing ratios increase and is largely independent of VOCs.

Table 5.3: Seasonal means (JJA 2017–2018) of the absolute and relative O_3 contributions from regional anthropogenic emissions ($\text{O}_3^{\text{reg.-anth.}}$: O_3^{teu} and O_3^{ieu} or O_3^{tea} and O_3^{iea} , respectively), and medians of the OPE, the SR, the Leighton Ratio and the dominant regime, based on Figure 5.19 for all study areas. Study areas are grouped after their chemical regime and within each group in descending order of their relative O_3 contributions from regional anthropogenic emissions. * Only the west coast of Taiwan is VOC-limited, which is discussed in the text. Apart from the west coast of Taiwan, the O_3 formation is mostly NO_x -limited.

Region	Code	$\text{O}_3^{\text{reg.-anth.}}$	$\text{O}_3^{\text{reg.-anth.}}$	OPE	SR	Dominant Regime	Leighton Ratio
unit		nmol	mol ⁻¹ %				
Pearl Delta	PEA	25	49	9.9	4.5	VOC-limited	0.6
Yangtze Delta	YAN	32	46	8.9	7.6	VOC-limited	0.5
Benelux	BEN	9	22	15.5	8.7	VOC-limited	1.0
Sichuan Basin	BAS	40	46	23.9	17.8	NO_x -limited	1.8
Taiwan	TAI	21	36	12.6	53.3	NO_x -limited*	1.0
Ningxia	RUR	29	35	26.5	26.8	NO_x -limited	1.8
Po Valley	PO	20	31	19.5	12.9	NO_x -limited	1.1
Iberian Peninsula	IBE	11	19	16.3	30.0	NO_x -limited	1.1
Ireland	IRE	4	9	23.4	152.2	NO_x -limited	1.1

5.4 Summary and Discussion

All three sections indicate that some study areas in Europe and East Asia are comparable in terms of their O_3 contributions and O_3 chemical regimes, but also point out their differences.

Table 5.3 summarises all results from sections 5.1–5.3. In the Benelux region and the Po Valley, the largest contributions to ground-level ozone come from European emissions (land transport and non-traffic) with 22 % (9 nmol mol⁻¹) and 31 % (20 nmol mol⁻¹), respectively. In East Asia, the Sichuan Basin and the Pearl River Delta exhibit the largest relative ozone contributions of 46 % (40 nmol mol⁻¹) and 49 % (25 nmol mol⁻¹) from East Asian anthropogenic emissions (land transport + non-traffic). This shows that absolute O_3 contributions from regional emissions in the Sichuan Basin are two times larger than in the Po Valley. In relative terms, almost one half (Sichuan Basin) and one third (Po Valley) of ground-level O_3 is contributed by regional anthropogenic emissions, respectively. Over the Po Valley, large MDA8 values are strongly driven by regional emissions, while over Benelux and the Iberian Peninsula, long-range transport plays an important role. The same applies to the Pearl River Delta, where large MDA8 values are also strongly driven by regional emissions, while over Taiwan and the Yangtze Delta the long-range transport is important. In the Sichuan Basin, mixing ratios of MDA8 ozone are less driven by regional emissions than in the Po Valley.

This comparison shows that the mitigation potential for reducing regional emissions in the European anthropogenic sector is more limited in the Benelux region compared to the Po Valley. This is because less ozone is produced in-situ from regional anthropogenic emissions in the Benelux region. Instead, ozone is more dominated by long-range transport and shipping in Benelux compared to the Po Valley. The O_3 contributions from regional anthropogenic emissions indicate that the mitigation potential by regional emissions in the Sichuan Basin, especially during MDA8 ozone events, is more limited than in the Pearl River Delta.

Overall, the Pearl River Delta has large O_3 contributions from regional anthropogenic emissions, resulting in the largest mitigation potential by regional emissions in East Asia. Here, the mitigation potential by regional emissions is even larger than in the Sichuan Basin and the Po Valley (Table 5.3). In rural and inflow areas, such as Ireland, the Iberian Peninsula, Taiwan, and Ningxia, O_3 contributions from anthropogenic LRT, shipping, and residual emissions play a more important role than in the other regions, which clearly limits the mitigation potential of O_3 by regional emissions.

To assess whether the mitigation potential can be achieved by reducing either regional NO_x or VOC emissions, the results of section 5.3 are further analysed.

The OPE shows, that over the Pearl River Delta, which has the largest ozone mitigation potential, local ozone formation by NO_x is rather inefficient (Table 5.3). The same applies to the Yangtze Delta and the Benelux region. These three study areas seem to be in a comparable chemical regime for O_3 formation (VOC-limited). In a VOC-limited regime, a reduction of regional NO_x emissions could initially increase, rather than mitigate, O_3 . The only option (in addition to the NO_x emissions) for a direct mitigation effect on O_3 would be

the reduction of anthropogenic VOC emissions (e.g., from solvents in industrial processes or incomplete combustion processes). In such regions, (e.g., Pearl River Delta, see Table 5.3), the regional NO_x emissions would need to be reduced to such an extent that the O_3 formation shifts from a VOC- to a NO_x -limited regime. In a NO_x -limited regime (e.g., Po Valley), a reduction of regional NO_x emissions could immediately reduce ozone. In the Po Valley, this reduction could lead to a mitigation of large MDA8 events during the summer months. This is limited over the Iberian Peninsula and Ireland, where O_3 contributions from anthropogenic LRT emissions play a more important role than from anthropogenic regional emissions. In general, my study design does not allow for a detailed investigation of how large a specific reduction in regional NO_x or VOC emissions should be to achieve a corresponding mitigation of O_3 . For this, a follow-up study applying the tagging and perturbation method needs to be conducted (see section 7).

Chemistry-climate models are associated with various uncertainties, so it is important to consider all presented results in light of these uncertainties. As analysed in Chapter 4, the model tends to overestimate NO_x in Europe and East Asia when compared to satellite data and other observations. The main source of these differences is typically the uncertainties in the emission inventories, which represent NO_x , CO, NMHCs, and other precursors in my simulations. The uncertainties of soil NO_x emissions [Vinken et al., 2014] and biogenic VOC emissions [Ashworth et al., 2010, Li et al., 2020a] are particularly large.

Additionally, each chemistry-climate model is based on different chemical mechanisms, which introduce various assumptions, simplifications, as well as variations in the VOC speciation. However, it is not straightforward to determine how changes in ozone precursors would affect O_3 mixing ratios. It is important to note that the sensitivity of O_3 formation to NO_x and VOC emissions is a major source of uncertainty in simulating the relationship between O_3 and precursor emissions [Sillman, 1999]. Furthermore, the chemical sinks and dynamics in chemistry-climate models can differ.

Moreover, the tagging approach used in this study introduces additional uncertainties as it employs a simplified family concept. Other tagging approaches may have different assumptions. For example, different approaches, such as tagging NO_x and VOCs separately or simultaneously, can result in larger differences in the contributions from specific sources. For example, tagging of NO_x only, leads to larger contributions of NO_x sources to ozone compared to the tagging approach used in this study [e.g., Karamchandani et al., 2017, Butler et al., 2018, Mertens et al., 2020b]. This is because the competition with other VOC sources is not taken into account in the NO_x -only tagging approach. This makes it rather challenging to directly compare tagging results from different studies. Overall, the sources of uncertainties in chemistry-climate models are diverse, and as a result, my model's results may differ from those of other models. As shown in the previous sections, the uncertainties in the MECO(n) model are neither superior nor inferior to those of other chemistry-climate models in different studies.

Thus, the MECO(n) model system is a robust resource for comparing O_3 contributions on a global and regional scale and evaluating the chemical regime of O_3 .

Chapter 6

Sensitivity Simulations

In this Chapter, the effect of different representations of biomass burning and biogenic VOC emissions on the anthropogenic O_3 contributions is investigated. For this, the results of the sensitivity simulations performed with the submodels BIOBURN (EUBB and ASIABB) and MEGAN (EUMEGAN), described in section 3.4, are analysed and compared with the reference simulations (EUREF and ASIAREF), respectively.

6.1 Sensitivity Study with BIOBURN: EUBB and ASIABB

As a preliminary step, the evaluation of the new implementation in BIOBURN (see section 3.3.3) against the GFASv1.2 dataset is conducted in this study using prescribed static injection heights. This evaluation serves as a base before the vertical representation of biomass burning emissions with local injection heights can be addressed in a future study (see section 1.1). Thus, this section aims to demonstrate that the online calculation of the biomass burning flux using the BIOBURN submodel (described in section 3.3.3) yields comparable results to those of the GFASv1.2 dataset. In particular, the investigation focuses on the effect of the differences in biomass burning emissions between both representations on the anthropogenic O_3 contributions.

Since the calculation of biomass burning fluxes (BB_{flux}) in BIOBURN is based on the same equation (3.1) used to derive the original BB_{flux} provided by the GFASv1.2 dataset, both simulations are expected to yield comparable global totals. Although the same equation is applied in both methods for BIOBURN in BB (EUBB and ASIABB) and for the GFASv1.2 dataset used in REF (EUREF and ASIAREF), respectively, the order of operations has been changed in BIOBURN. The calculation of the BB_{flux} in BB is done after regridding DM, EF, FT, and VF by `IMPORT_GRID` onto the EMAC/COSMO grids. The resulting data is then transferred to BIOBURN to calculate the multiplication of the fields dependent on the species, as shown in Equation 3.1. In the REF simulations, the BB_{flux} from GFAS is regridded onto the EMAC/COSMO grids using `IMPORT_GRID`, and is then transferred into OFFEMIS, which uses the channel object to calculate tracer

Table 6.1: Global totals of the GFASv1.2 data set and the calculated totals by OFFEMIS and BIOBURN in EMAC in 2017 in Tg a^{-1} (species) for all relevant species.

Species	GFASv1.2	BB (EMAC)	REF (EMAC)	BB-REF
unit	Tg a^{-1}	Tg a^{-1}	Tg a^{-1}	%
CO	280.4	278.0	280.6	-1
NO _x	8.4	8.3	8.4	-1
SO ₂	1.9	2.0	1.9	4
NH ₃	4.1	3.9	4.1	-6
C ₂ H ₄		2.4	3.7	-35
C ₂ H ₆		1.4	2.1	-33
C ₃ H ₆		1.1	1.7	-35
C ₃ H ₈		0.4	0.7	-43
NC ₄ H ₁₀		0.6	0.8	-25
CH ₃ COCH ₃		1.4	0.9	-36
CH ₃ COOH		3.1	4.8	-35
CH ₃ OH		3.2	4.8	-33
HCOOH		1.7	2.6	-35
MEK		1.2	3.2	-62

tendencies (see section 3.3.5). This rearrangement produces non-binary identical results, causing a local redistribution of the biomass burning fluxes in BB, in case FT and DM differ from those used for the calculation of the GFASv1.2 dataset. These differences are mostly cancelled out when considering the global totals. In addition, it is not entirely known which input data such as the firetype, were used by the authors to create the GFASv1.2 dataset (see section 3.3.3). Table 6.1 shows the comparison of the global totals of the BB_{flux} for the EMAC instance in BB and REF, respectively, for different species. For both simulations in BB (EUBB and ASIABB) and REF (EUREF and ASIAREF), respectively, the global totals of the BB_{flux} in the EMAC instance lead, by definition, to the same results. In the comparison between BB and REF, only small differences (-6–4 %) are observed for CO, NO_x, SO₂, and NH₃. The totals of the NMHCs are considerably smaller in BB, mostly between 25–43 %. These differences are primarily caused by a wrong NMHC speciation used in the reference simulations. The fractions of the NMHC speciation in REF are wrongly scaled by the factor 161/210 because the biomass burning NMHC flux in REF was mistakenly scaled to kg C [von Kuhlmann et al., 2003]. This explains why the NMHC flux in REF is on average 27 % larger than in BB.

Figures 6.1 and 6.2 show the annual mean biomass burning flux of NO_x for 2017–2018 in EMAC and CM50 for Europe (EUBB) and East Asia (ASIABB). Although different species of the biomass burning flux exhibit various deviations (as explained for example for NMVOCs above), in this study, only NO_x is presented. The geographical patterns of the biomass burning NO_x flux in CM50 over Europe and East Asia are in line with those of EMAC. The largest emission fluxes from biomass burning (in EMAC and CM50) appear in the South of Europe and East Asia, respectively, as well as in parts of Northeast China

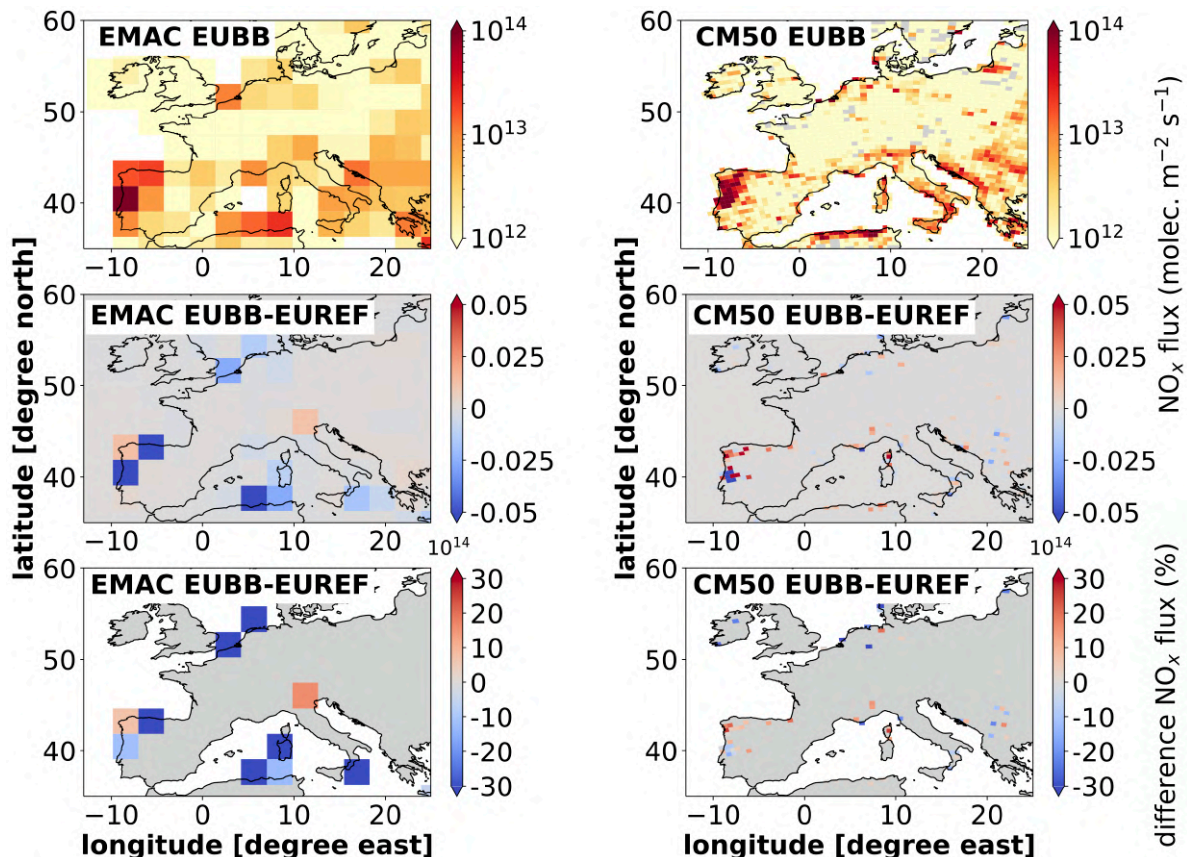


Figure 6.1: Annual mean (2017–2018) of the vertically summed NO_x biomass burning fluxes in $10^{14} \text{ molec m}^{-2} \text{ s}^{-1}$ of the model results from EUBB for the instances EMAC (upper left) and CM50 (upper right) for Europe, respectively. Absolute differences between EUBB minus EUREF are shown in the middle left (EMAC) and middle right (CM50) panels, respectively. Relative differences in % between EUBB and EUREF are only calculated and plotted (middle panels) for absolute differences $>0.01 \text{ molec m}^{-2} \text{ s}^{-1}$ and $<-0.01 \text{ molec m}^{-2} \text{ s}^{-1}$ and shown in the lower left (EMAC) and lower right (CM50) panels, respectively.

for BB and REF.

In general, the EMAC instance of BB for Europe and East Asia shows regionally smaller biomass burning fluxes compared to REF. The absolute differences are usually rather small, but in some locations relatively large (more than $\pm 30 \%$). In CM50 of EUBB, absolute differences of the biomass burning fluxes with REF are also rather small, but regionally relatively large ($\pm 30 \%$). The same applies for the CM50 instance of ASIABB. The largest differences between BB and REF occur along the coast and at the strongest gradients of the dry particulate matter (DM). These differences are primarily a consequence of the different spatial firetype distributions used in BIOBURN and the calculation of the GFASv1.2 dataset. In BIOBURN the firetype is used from a dataset based on Kaiser et al. [2012], which is remapped by an index regridding that considers the fraction of each grid box of a specific firetype (e.g., tropical forest or savanna). This dataset includes the land-

sea mask, with the “firetype” class labelled as water (including lakes). Index regridding means that grid boxes with a fraction of only 1 % land and 99 % water receive only the land fraction of 1 % of the biomass burning flux (see Figs. C.71 and C.72, pp. 208–209). In other words, during the regridding in REF, each grid box received 100 % of the biomass burning flux as prescribed by the GFASv1.2 dataset. Although the GFASv1.2 algorithm also incorporates a land-sea mask, the specific dataset and its resolution are not known. This potentially explains a part of the differences in biomass burning fluxes between BB and REF. The influence of the land-sea fraction within BIOBURN is evident above the island landscape off the coast of the Pearl River Delta (122° E, 30° N). In ASIAREF (EMAC), the biomass burning flux is distributed across the entire grid box. In ASIABB (EMAC), however, the biomass burning flux depends on the land-sea fraction (represented by FT) and is significantly smaller compared to ASIAREF (refer to Fig. C.72, p. 209). This leads to local shifts in biomass burning fluxes between BB and REF.

In order to evaluate the new implementation (described in section 3.3.3) of the vertical distribution of biomass burning fluxes in BB, a comparison with the REF simulations is made. In REF, the vertical distribution of biomass burning fluxes from GFASv1.2 is done manually in the pre-processing (see section 3.3.9). Figure 6.3 depicts the IMPORT_GRID output of the vertical representation of the biomass burning NO_x flux on the 6 defined levels by VF [Dentener et al., 2006], as a zonal mean for 2017–2018. The differences between BB and REF are rather low, with a maximum of ± 2 % between 50–60° N at all levels. In the Tropics, the differences are only marginal, in the range of ± 0.5 %. Overall, the vertical cross-section shows that the new implementation of the vertical fraction in BIOBURN yields comparable results, and only has a small effect on the differences of the biomass burning flux between BB and REF.

Nevertheless, even small differences in the biomass burning fluxes affect the chemistry and thus the ozone formation. In both, Europe and East Asia, the total ground-level O_3 in BB is slightly smaller with up to $-0.3 \text{ nmol mol}^{-1}$ in comparison to REF (Figs. C.73 and C.74, pp. 210–211). Since the BB simulations include lower biomass burning emissions of NMHCs, the O_3 contribution from biomass burning emissions to O_3 is smaller in BB compared to REF for Europe and East Asia (Fig. C.75, p. 212). This indicates that the smaller O_3 mixing ratios in BB are mostly caused by fewer biomass burning emissions of NMHCs. In general, the effect of differences in biomass burning emissions on the O_3 contributions to ground-level O_3 is more prominent in East Asia than in Europe. Overall, the differences in O_3 contributions from regional, long-range transported anthropogenic, and biogenic emissions between BB and REF are negative and positive for different sectors throughout Europe and East Asia during JJA 2017–2018 (Figs. C.73 and C.74, pp. 210–211).

In the following, a detailed analysis of each study area is conducted to examine the shift in O_3 contribution among the emission sectors due to differences in biomass burning emissions. Here, the specific focus is set on the change of O_3 contributions from anthropogenic emissions.

Figures 6.4 and 6.5 show the absolute differences of the O_3 contributions for all study areas in Europe and East Asia as simulated by CM50 (for relative differences, see Figs. C.76

and C.77, pp. 213). In Europe in all study areas, the O_3 contribution from biomass burning emissions are smaller in EUBB by up to $-0.15 \text{ nmol mol}^{-1}$ (-0.2 percentage points (%p)) than in EUREF (Fig. C.76, p. 213). The O_3 contributions from all other emission sectors are even smaller in EUBB by about $0.01\text{--}0.05 \text{ nmol mol}^{-1}$. Only O_3 contributions from European anthropogenic non-traffic and biogenic emissions are slightly larger in EUBB than in EUREF. This is because the biogenic and anthropogenic non-traffic sectors have the largest contributions to NMHCs in Europe and East Asia (see Figs. C.43 and C.54, pp. 188 and 196). Their NMHCs compete with NMHCs from the biomass burning sector, and since the biomass burning sector emits fewer NMHCs in EUBB, both sectors take over their O_3 formation, resulting in larger absolute O_3 contributions of up to $0.02 \text{ nmol mol}^{-1}$ (0.1 %p) in Europe (Fig. C.76, p. 213).

The same applies to East Asia, which exhibits a similar sensitivity with comparable smaller O_3 contributions from biomass burning emissions in ASIABB of up to $0.2 \text{ nmol mol}^{-1}$ (0.25 %p) across all study areas. In general, the O_3 contributions from the residual and biogenic sectors are larger in ASIABB than in ASIAREF, while the contributions from the anthropogenic sector remain the same or are smaller, with one exception. The contribution of the anthropogenic sectors to O_3 formation is smaller in BB than in REF over the Pearl River Delta, possibly because the biomass burning sector has replaced their previously important role in O_3 formation. This hypothesis requires further investigations through a more comprehensive sensitivity study and is not further analysed here.

In summary, the analysis demonstrates that the GFASv1.2 dataset could successfully be replaced by the BIOBURN submodel. However, the uncertainties between both methods are not larger than the uncertainties typically associated with emission inventories representing biomass burning emissions [e.g., Pan et al., 2020]. The sensitivity of the O_3 contributions to the differences in biomass burning emissions (BB and REF) between Europe and East Asia is not larger than that obtained by using two different emission inventories, as shown in several studies [e.g., Mertens et al., 2020b]. Although incorrect scaling factors are used for the biomass burning NMHC emissions in this study, the effect on the anthropogenic O_3 contributions is negligible when compared to the results of the anthropogenic O_3 contributions presented in this thesis. The findings demonstrate the robustness of anthropogenic O_3 contributions when considering changes in the representation of biomass burning emissions in the MECO(n) model.

6.2 Sensitivity Study with MEGAN: EUMEGAN

MEGAN allows for the representation of biogenic VOC emissions depending on the meteorological conditions (see section 3.3.4), which replaces the previous approach of using a climatology based on the GEIA dataset. Therefore, the MEGAN submodel was tested for the first time within the MECO(n) model system. In order to evaluate the effect of biogenic fluxes calculated by the MEGAN submodel on the O_3 chemistry, the EUMEGAN simulation was conducted using a MECO(1) setup for Europe. Due to computational limitations and limited time, the sensitivity simulation was only performed for Europe. Nevertheless,

this study preliminarily shows how different representations of biogenic emissions affect O_3 contributions from anthropogenic emissions in Europe. In the EUMEGAN simulation, I replaced the GEIA dataset representing biogenic emissions in EUREF with the MEGAN submodel (see section 3.4 for more details).

MEGAN calculates biogenic emission fluxes for a grid cell based on various meteorological parameters, out of which emission factors for different vegetation types and climate conditions are calculated (see section 3.3.4). Therefore, the biogenic emission fluxes in MEGAN depend on the Leaf Area Index (LAI), the light (solar angle), the temperature, humidity and wind. In addition the soil moisture and various other parameters affect the biogenic emission flux calculated in MEGAN, which makes the calculation rather complex and increases its spatial and temporal variability in EUMEGAN in comparison to EUREF. Thus, the following comparison of EUMEGAN and EUREF is based on two completely different data sources. The detailed preparatory work for the MEGAN namelist with global and regional scaling is described in section 3.3.4, the GEIA dataset is described in section 3.3.9.

Table 6.2: Global annual totals of biogenic emissions in EUMEGAN and EUREF as simulated by EMAC for 2017 in Tg (species) a^{-1} for all species. The totals in EUREF are representing the totals of the GEIA dataset based on the year 2000 [Guenther et al., 1995] and listed in the Supplement (Table 1) of Pozzer et al. [2007]. The desired totals are based on a T42 climatology (personal communication A. Pozzer).

Species	Desired 2000	EUMEGAN	EUREF 2017	EUMEGAN-
unit	$Tg\ a^{-1}$	2017 $Tg\ a^{-1}$	(GEIA) $Tg\ a^{-1}$	EUREF %
CO	97.36	101.25	112.58	10
C ₂ H ₄	21.10	21.94	12.55	43
C ₂ H ₆	0.32	0.33	0.56	-41
C ₃ H ₆	12.98	14.10	3.53	299
C ₃ H ₈	0.16	0.17	0.36	-53
NC ₄ H ₁₀	0.24	0.25	0.41	-39
CH ₃ COCH ₃	31.62	33.44	41.29	-19
CH ₃ COOH	3.15	3.27	3.51	-7
CH ₃ OH	96.91	100.66	61.89	-63
HCOOH	3.15	3.27	5.78	-43
C ₅ H ₈	598.00	416.46	¹⁷ 358	16

Table 6.2 lists the global annual totals of biogenic emissions in EUMEGAN for the year 2017, which are based on climatological data for the year 2000 (see section 3.3.4). In 2017, the global totals of biogenic emissions in the EMAC instance of EUMEGAN are on average 5 % larger for all species compared to those in 2000. Table 6.2 lists the direct comparison of global annual totals of biogenic emissions in EUMEGAN and in EUREF

¹⁷C₅H₈ was calculated by the ONEMIS submodel. This submodel calculates 2D emission fluxes for gas-phase tracers (i.e., soil emissions; see Table A.1, p. 138) and updates the tracer tendencies accordingly [Kerkweg et al., 2006a].

for 2017. The totals of the biogenic emissions in EUMEGAN (T42 climatology for the year 2000; see section 3.3.4) and EUREF (GEIA emission inventory for the year 2000; see Fig. C.78, upper panels, p. 214) are based on two different data sources. This is different for C_5H_8 , which is not taken from the GEIA dataset in EUREF, but is instead calculated by the ONEMIS submodel. This submodel calculates 2D emission fluxes for gas-phase tracers, such as soil emissions (see Table A.1, p. 138), and updates the tracer tendencies accordingly [Kerkweg et al., 2006a].

Therefore, this study compares the C_5H_8 output from MEGAN with the results calculated by ONEMIS, which shows a difference of 16 %. Generally, the differences in data sources explain the rather large differences between EUMEGAN and EUREF (see Table 6.2). A few species, such as CO, C_2H_4 , and C_2H_6 , have even larger differences in global totals in EUMEGAN than in EUREF, but the majority of the biogenic species have smaller totals in EUMEGAN by up to -60 %.

Figure 6.6 shows the annual mean of the biogenic CO flux as simulated by EMAC and CM50 in EUMEGAN for 2017. Although the biogenic fluxes in EUREF and EUMEGAN are calculated based on the same equations, the biogenic fluxes in EUMEGAN is either larger or smaller compared to EUREF. To limit the scope of this section, only CO is presented. Since the biogenic fluxes in EUMEGAN are calculated using a parametrisation that depends on the meteorological conditions and in EUREF represented by the GEIA climatology, the geographical patterns differ. Regionally in CM50, above East and South Germany down to South Poland, as well as above parts of the Iberian Peninsula, the biogenic CO flux is considerable smaller in EUMEGAN than in EUREF (Fig. C.78, p. 214). Relatively, the differences in EMAC and CM50 often exceed ± 30 %, which is expectable due to the reasons explained above.

However, in most of Central Europe, the absolute differences of the biogenic emission flux of CO in EUMEGAN are very small (absolute value $< 0.1 \text{ nmol m}^{-2} \text{ s}^{-1}$) and the biogenic emission flux of CO is rather well represented (Fig. C.78, p. 214). MEGAN does not parameterise biogenic emissions above the ocean. Therefore, in EUMEGAN, the biogenic fluxes of the respective species over the ocean are included by using the biogenic emission fluxes from the GEIA dataset, which are calculated in OFFEMIS. Thus the differences of the biogenic emission flux between EUMEGAN and EUREF above the ocean are zero.

Due to the complexity of the processes leading to biogenic VOC emissions, emissions from biogenic sources have large uncertainties [e.g. Guenther et al., 1995, Simpson et al., 1995, Li et al., 2020a]. Li et al. [2020a] reported rather large uncertainties of biogenic VOC emissions of between - 36.5–4.6 %. This makes the comparison with monthly means from a climatology as used in EUREF challenging. Even though the estimations used for the GEIA dataset are based on a calculation approach comparable to that of MEGAN [see model description by Guenther et al., 1995].

The differences of the biogenic fluxes in EUMEGAN in comparison to EUREF affect the O_3 chemistry resulting in changes in ozone. Ozone in EUMEGAN is regionally slightly larger with up to 1 nmol mol^{-1} , mostly in Central and West Europe, but is slightly smaller in Southeast Europe (Fig. C.79, p. 215). It is important to analyse which sectors con-

tribute the most to this ozone change. The geographical pattern of the O_3 change in EUMEGAN is particularly similar to the differences in the O_3 contributions from biogenic emissions. These contributions in EUMEGAN are larger in Northwest Europe and smaller in Southeast Europe than in EUREF, by up to $\pm 0.5 \text{ nmol mol}^{-1}$. In general, the O_3 contributions from the anthropogenic sectors are less affected, but are also slightly changed by the non-linear competing effects between the sectors.

Figure 6.7 provides an overview of the differences between EUMEGAN and EUREF regarding O_3 contributions during JJA 2017 as simulated by CM50 for the European study areas (see Fig. C.80 for relative differences, p. 216). Different regions exhibit distinct changes in the contributions. Using MEGAN in COSMO leads to smaller O_3 contributions from biogenic emissions in all study areas, except in the Po Valley. Additionally, some O_3 contributions from anthropogenic emissions are slightly larger in EUMEGAN than in EUREF. The larger O_3 contributions from biogenic emissions in EUMEGAN are particularly noticeable in rural regions such as Ireland and above the Iberian Peninsula, with $0.3\text{--}0.4 \text{ nmol mol}^{-1}$ ($0.4\text{--}0.8 \text{ \%p}$). In the polluted Benelux region, O_3 contributions from biogenic emissions in EUMEGAN are only slightly larger with $0.2 \text{ nmol mol}^{-1}$ (0.25 \%p), and O_3 contributions from European land transport are similarly larger. However, in the Po Valley, O_3 contributions from biogenic emissions in EUMEGAN are smaller than in EUREF by around $-0.2 \text{ nmol mol}^{-1}$ (-0.4 \%p). Here, larger O_3 contributions from European anthropogenic non-traffic emissions are particularly noticeable, because the non-linearity of O_3 formation causes competing effects between the sectors and shifts the O_3 contributions among each other.

Overall, the differences in O_3 contributions resulting from the use of MEGAN in the MECO(n) model system, referred to as EUMEGAN, are not larger than the differences observed when using different anthropogenic emission inventories [e.g., Mertens et al., 2020b]. For example, Mertens et al. [2020b] reported differences in O_3 contributions from anthropogenic emissions during the summer months of 2008–2010, ranging from approximately 2–3 % above France and Middle Europe. In this study, the differences in biogenic emission fluxes of VOCs caused by the MEGAN submodel have a minimal impact on the O_3 contributions from anthropogenic emissions (mostly $-0.1\text{--}0.4 \text{ nmol mol}^{-1}$ or $-0.1\text{--}0.5 \text{ \%p}$) and can be considered negligible when compared to the substantial anthropogenic O_3 contributions observed in this study (typically $10\text{--}20 \text{ nmol mol}^{-1}$ or $20\text{--}30 \text{ \%}$ in polluted areas). Therefore, MEGAN proves to be a suitable parametrisation for representing biogenic emission fluxes dependent on meteorology, without significantly altering the O_3 contributions, particularly those from anthropogenic emissions. This makes MEGAN a powerful submodel for future climate studies investigating O_3 contributions from anthropogenic emissions in Europe under different climate conditions.

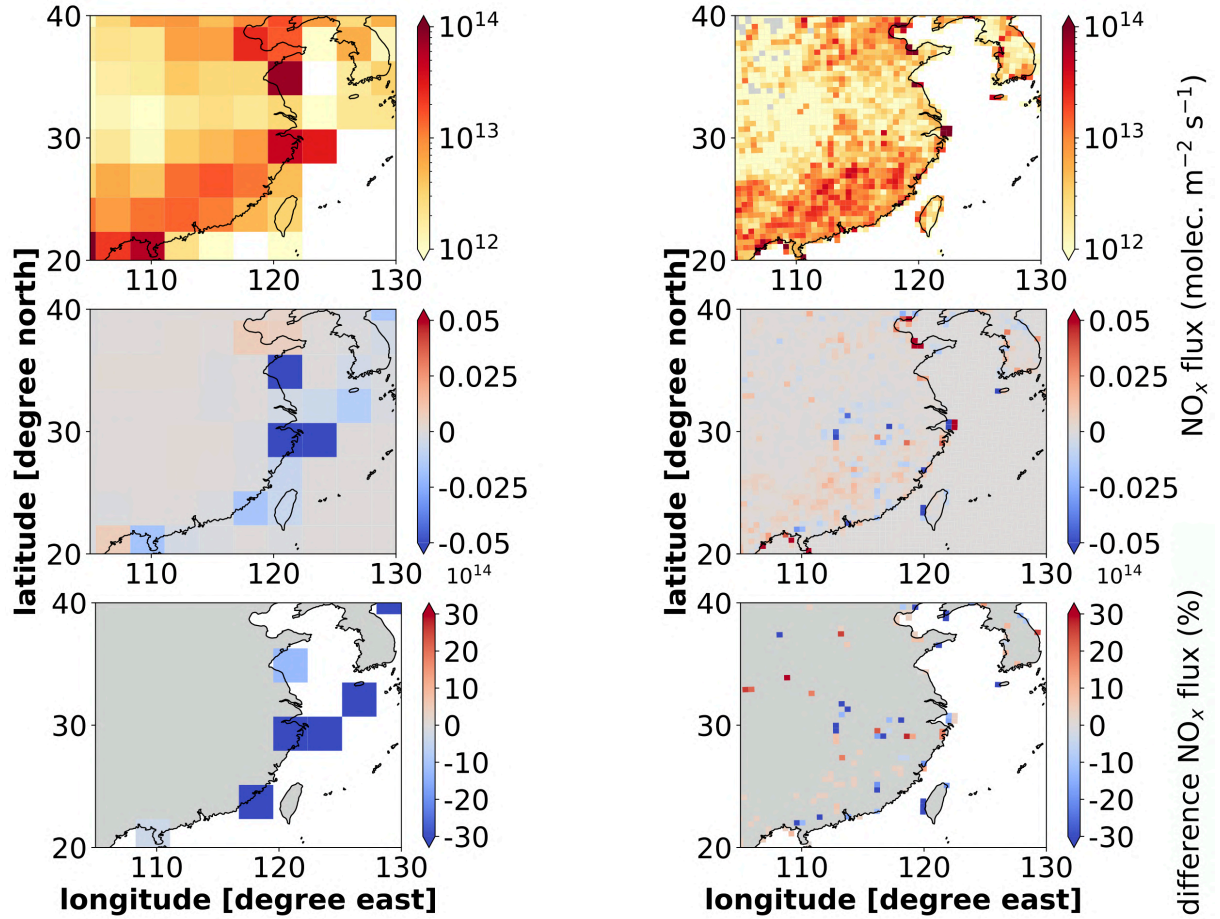


Figure 6.2: Annual mean (2017–2018) of the vertically summed NO_x biomass burning fluxes in 10^{14} molec $\text{m}^{-2} \text{s}^{-1}$ of the model results from ASIABB for the instances EMAC (upper left) and CM50 (upper right) for East Asia, respectively. Absolute differences between ASIABB minus ASIAREF are shown in the middle left (EMAC) and middle right (CM50) panels, respectively. Relative differences in % between ASIABB and ASIAREF are only calculated and plotted (middle panels) for absolute differences >0.01 molec $\text{m}^{-2} \text{s}^{-1}$ and <-0.01 molec $\text{m}^{-2} \text{s}^{-1}$ and shown in the lower left (EMAC) and lower right (CM50) panels, respectively.

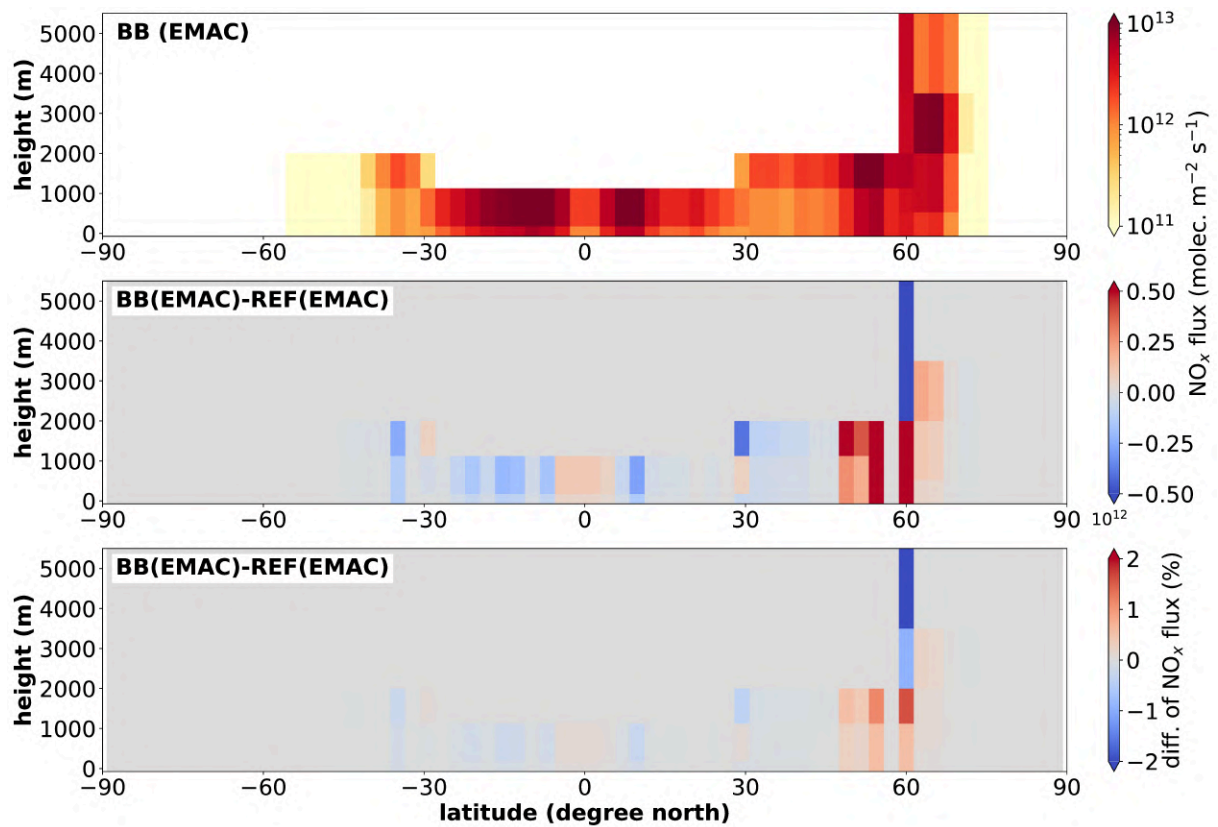


Figure 6.3: Vertical zonal cross section of the mean NO_x biomass burning flux in $10^{12} \text{ molec m}^{-2} \text{ s}^{-1}$ as simulated by EMAC in both BB simulations (upper panel) for 2017–2018. Absolute vertical differences between BB minus REF are shown in the middle panel. Relative vertical differences in % between BB and REF are shown in the lower panel.

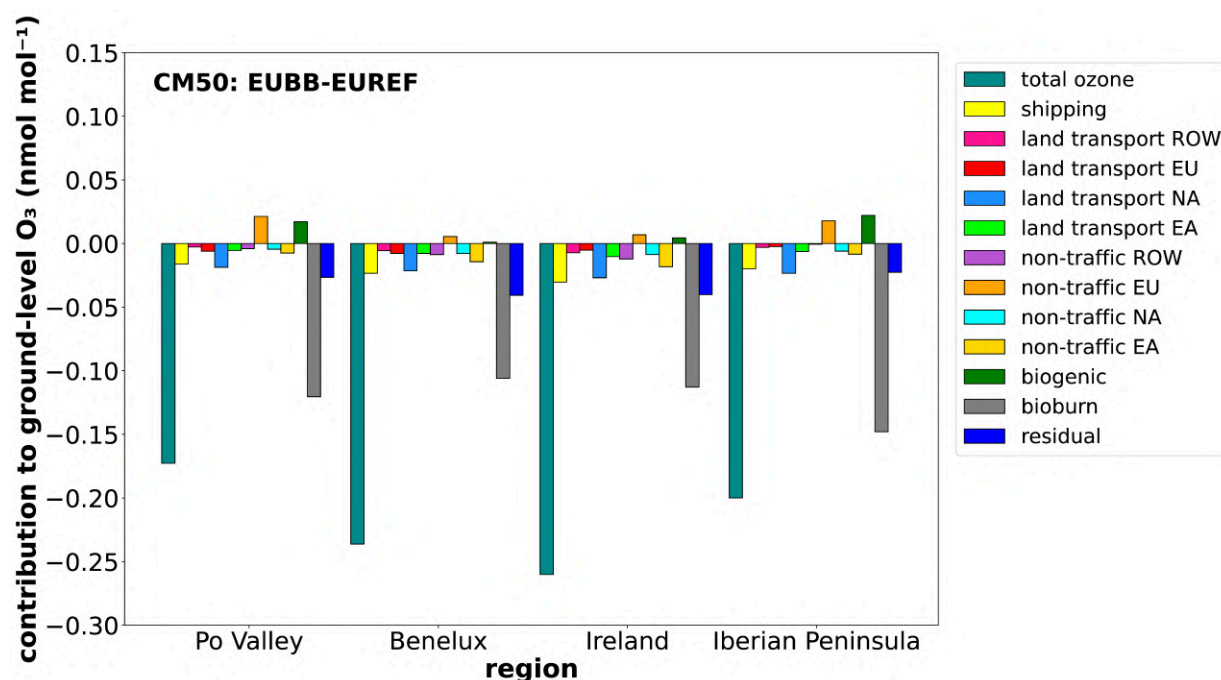


Figure 6.4: Seasonal mean (JJA 2017–2018) of the differences between EUBB minus EUREF of total ozone and the absolute contributions of different emissions sectors and regions to ground level ozone in four European study areas as simulated with CM50.

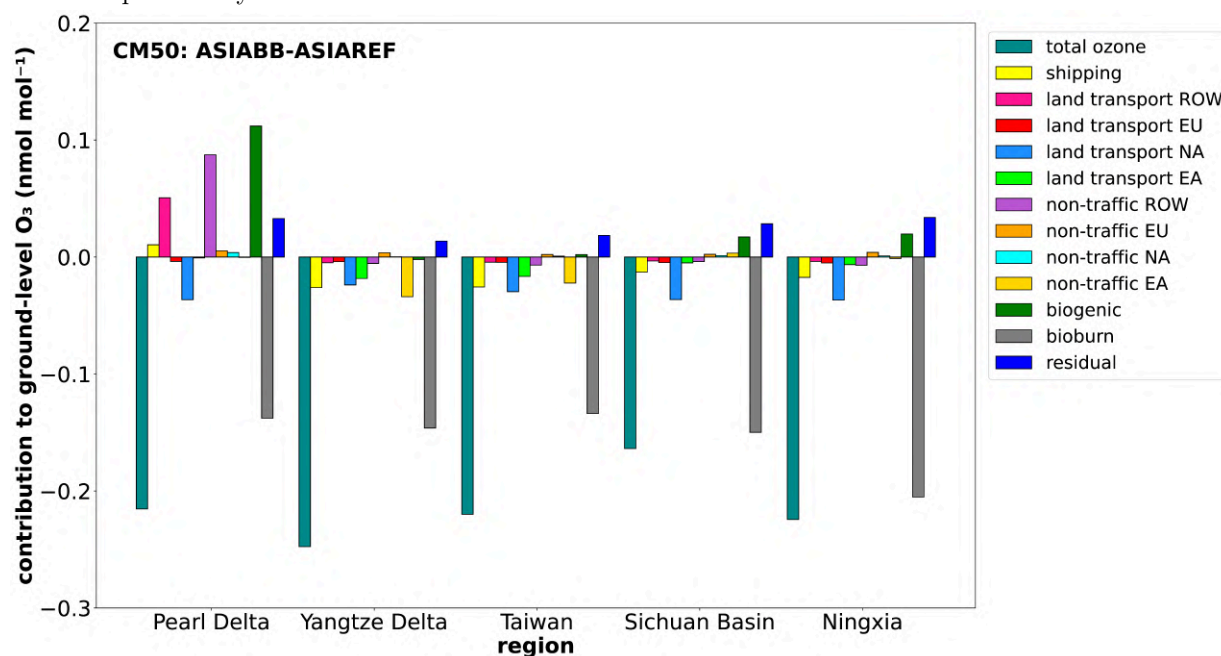


Figure 6.5: Seasonal mean (JJA 2017–2018) of the differences between ASIABB minus ASIAREF of total ozone and the absolute contributions of different emissions sectors and regions to ground level ozone in four Asian study areas as simulated with CM50.

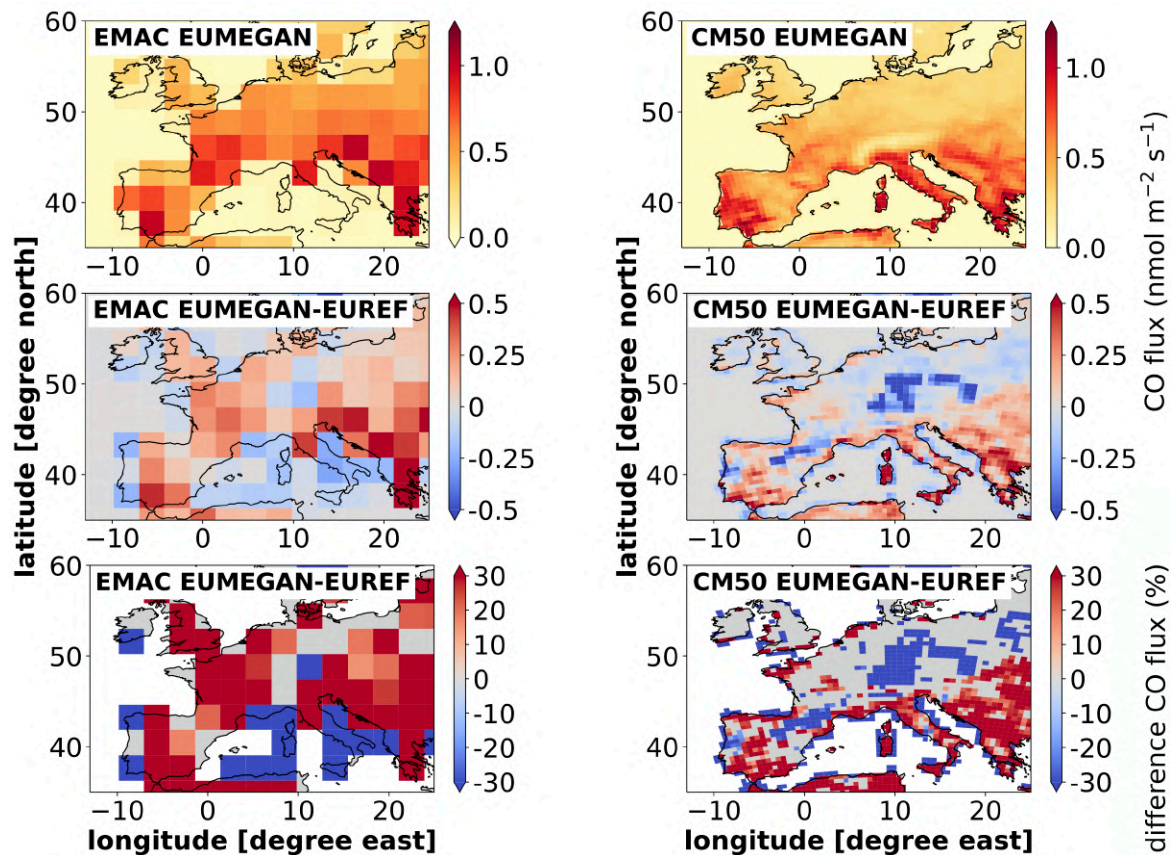


Figure 6.6: Annual mean (2017) of the simulated biogenic CO flux in $\text{nmol m}^{-2} \text{s}^{-1}$ from EUMEGAN for the instances EMAC (upper left) and CM50 (upper right) for Europe, respectively. Biogenic emission fluxes over the ocean are not parameterised by MEGAN and, therefore, are included in EUMEGAN using the GEIA dataset calculated via OFFEMIS. Absolute differences between EUMEGAN minus EUREF are shown in the middle left (EMAC) and middle right (CM50) panels, respectively. Relative differences in % between EUMEGAN and EUREF are only calculated for absolute differences $>0.1 \text{ nmol m}^{-2} \text{s}^{-1}$ and $<-0.1 \text{ nmol m}^{-2} \text{s}^{-1}$ and shown in the lower left (EMAC) and lower right (CM50) panels, respectively.

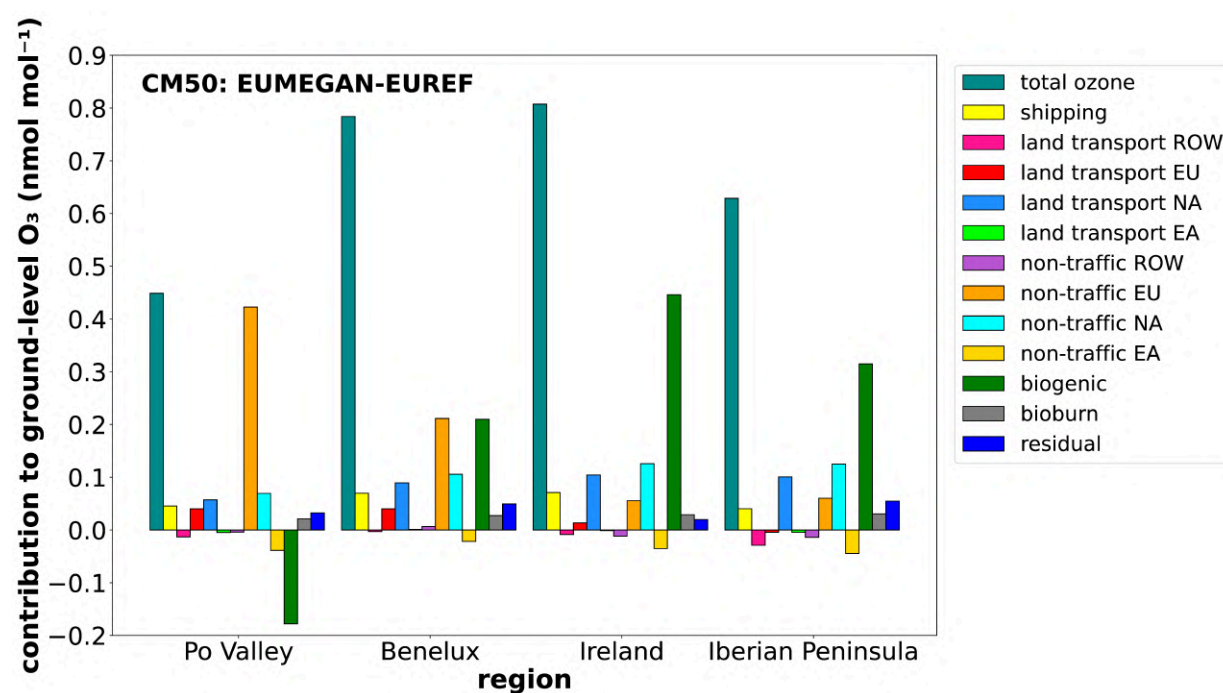


Figure 6.7: Seasonal mean (JJA 2017) of the differences between EUBB minus EUREF of total ozone and the absolute contributions of different emissions sectors and regions to ground level ozone in four European study areas as simulated with CM50.

Chapter 7

Conclusions and Outlook

This Chapter answers the scientific questions formulated in section 1.2 and briefly summarises the major findings of this study. In the end, it provides an outlook on further questions that could not be answered within the scope of this study.

Q1: How do various emission sectors contribute to ground-level NO_y and O_3 in Europe and how does this differ in comparison to East Asia?

A1: In Europe and East Asia, the largest contributions to ground-level NO_y come from the anthropogenic sector (land transport and non-traffic). In Europe, the contributions to NO_y from the land transport sector are larger than those from the anthropogenic non-traffic sector. In the most polluted areas (e.g., Benelux region), the largest NO_y contributions from the land transport sector are up to 8 nmol mol^{-1} .

In East Asia, the opposite is true. Here, in general, contributions to NO_y from the anthropogenic non-traffic sector are mostly larger than from the land transport sector. Locally, in major polluted regions (e.g., Pearl River Delta), contributions to NO_y from the anthropogenic non-traffic sector (up to 40 nmol mol^{-1}) are twice as large as those from the land transport sector (up to 22 nmol mol^{-1}). In general, in these areas, contributions to ground-level NO_y from the anthropogenic sector are absolutely 4–5 times larger in East Asia than in Europe. In Europe, contributions to NO_y from the biogenic sector are rather small, with up to 2 nmol mol^{-1} , primarily located over Central Europe and France. This is similar to East Asia, where contributions to NO_y from the biogenic sector are up to 3 nmol mol^{-1} , and mostly concentrated on the northern part of China.

In Europe, the importance of different sectors in contributing to ground-level O_3 differs between the regions. In Central and Southeast Europe, the largest contributions to O_3 come from the anthropogenic non-traffic and biogenic sectors, and contributions from the land transport sector are less important. In rural regions (e.g., the Iberian Peninsula), the anthropogenic sector is less important, and the biogenic sector plays a more crucial role in O_3 contribution. Here, contributions to ground-level O_3

from the shipping sector are more important. In East Asia, contributions to ground-level O_3 from the regional anthropogenic non-traffic sector are even larger than in Europe, and contributions from the regional land transport sector are approximately one third of the contributions from the anthropogenic non-traffic sector. The role of the biogenic sector in East Asia is comparable to that in Europe. Along the coasts of East Asia, contributions to ground-level O_3 from the shipping sector are relatively smaller than those in Europe.

Q2: How large are the contributions from regional emissions compared to the contributions from long-range transported emissions to ground-level O_3 in Europe and how does this differ in East Asia?

A2: In the Po Valley, O_3 contributions from anthropogenic emissions (land transport and non-traffic) are dominated by regional (European) emissions, accounting for 20 nmol mol^{-1} (31 %). In coastal regions such as Benelux, regional anthropogenic emissions account for only half of the anthropogenic O_3 contributions, with 9 nmol mol^{-1} (22 %), and the rest comes from anthropogenic LRT (long-range transport) emissions. The same applies to more rural and coastal regions such as the Iberian Peninsula and Ireland, where inflow is important, and regional anthropogenic emissions are smaller. Here, contributions to O_3 from anthropogenic LRT emissions (18–20 %) play a crucial role.

In East Asia, O_3 contributions from anthropogenic emissions are even more dominated by regional (East Asian) emissions than in Europe. The Sichuan Basin, the Yangtze River Delta and the Pearl River Delta exhibit the largest absolute and relative ozone contributions from regional anthropogenic emissions of $25\text{--}40 \text{ nmol mol}^{-1}$ (46–49 %). For example, the absolute O_3 contributions from regional anthropogenic emissions in the Sichuan Basin are two times larger than in the Po Valley. In East Asia, anthropogenic long-range transport (LRT) emissions contribute to ground-level ozone in coastal areas to a comparable extent as in Europe, accounting for 13–21 %. However, in rural regions where the inflow of anthropogenic LRT emissions is shielded by the Himalayan mountains in the west, the contributions from anthropogenic LRT emissions to ozone levels are less important.

Q3: How does the O_3 chemistry differs between Europe and East Asia?

A3: In major polluted coastal areas in Europe and East Asia, O_3 deviates from the photostationary state due to large NO sources (Leighton Ratio <1). Here, the titration of O_3 is larger than the formation of O_3 via the photolysis of NO_2 because the rapid conversion of NO_2 into HNO_3 leads to a very low ozone production efficiency (<10). The formation of O_3 is limited by the availability of VOCs. In these regions, a reduction of regional NO_x emissions could initially increase, rather than mitigate, O_3 . In addition to reducing NO_x emissions, a direct approach to mitigate O_3 would be to concurrently reduce anthropogenic VOC emissions.

In the Sichuan Basin in East Asia, O_3 deviates even more from the photostationary state than in the Po Valley in Europe. Here, NO_2 is removed from the system into HNO_3 , which decreases the ozone production efficiency. In most rural areas in Europe, O_3 is in a photostationary state. However, in rural regions in East Asia, the opposite applies, and O_3 strongly deviates from the photostationary state (Leighton Ratio > 1). This is because additional O_3 formation pathways involving RO_2 become more important, thereby reducing the conversion of NO_2 into HNO_3 . In rural areas in Europe and East Asia, the formation of O_3 is limited by the availability of NO_x . Therefore, reducing NO_x emissions in these regions can help mitigate ground-level O_3 .

Q4: How robust are the simulated anthropogenic O_3 contributions in the MECO(n) model when the previous implementations of emissions from biomass burning and biogenic VOC emissions are replaced with improved representations of these processes?

A4: The effect of different representations of biomass burning emissions on anthropogenic O_3 contributions is negligible for both, Europe and East Asia. In Europe, most of the anthropogenic O_3 contributions are only slightly affected by the differences in the biomass burning fluxes, with smaller or larger O_3 contributions of $\pm 0.02 \text{ nmol mol}^{-1}$ (up to 0.1 %). In East Asia, the sensitivity of anthropogenic O_3 contributions to differences in biomass burning emissions is slightly larger, with a range of ± 0.05 – $0.1 \text{ nmol mol}^{-1}$ (up to 0.25 %).

The meteorologically dependent representation of biogenic VOC emissions has only minor effect on anthropogenic O_3 contributions in Europe, resulting in slightly larger O_3 contributions of up to $0.45 \text{ nmol mol}^{-1}$ (0.5%), but mostly even smaller differences. Overall, these differences are considered to be negligible when compared to the magnitude of the anthropogenic O_3 contributions presented in this thesis. These findings demonstrate the robustness of anthropogenic O_3 contributions when considering changes in the representation of biomass burning and biogenic VOC emissions in the MECO(n) model.

From these findings, further questions arise that could not be answered by this study. In the following, I conclude my thesis with a (incomplete) list of tasks for further works:

- The tagging regions used in this study are limited to continents. Further subdivision into regions or even countries would enable the identification of specific countries with the largest O_3 contributions from regional (or national) anthropogenic emissions. Based on this, the countries with the largest mitigation potential by reducing their regional anthropogenic emissions could be determined.
- In a future study, a perturbation method could be applied to assess which source should be prioritised for mitigation options, as it would lead to the largest reduction in ground-level O_3 in Europe and East Asia. The same study could quantify the resulting change in ozone caused by reducing certain anthropogenic emissions, such as NO_x and VOCs.

- The inclusion of a third, more refined COSMO instance (e.g., with a resolution of 7 km) would enable a more detailed exploration of local processes in the study areas defined in this research. However, the extension of the setup is limited by constraints in computing power and memory.
- The BIOBURN submodel should be further developed to incorporate satellite instrument-derived injection heights, replacing the currently used prescribed static injection heights with local injection heights. This modification will result in changes to the emissions distributions, and the effect on the derived ozone contributions needs to be assessed.
- The application of MEGAN for biogenic emissions allows an improved assessment of ozone contributions, considering the effects of climate change and land use. With MEGAN, both factors will influence biogenic emissions (replacing the previously used climatological emissions), potentially leading to changes in simulated ozone contributions.

Appendices

A.1 Appendix Tables and Descriptions

A.1.1 Definition of NO_y in the TAGGING submodel

Overview on the family of NO_y in the TAGGING submodel [Supplement Table 1, Grewe et al., 2017].

$$\begin{aligned}\text{NO}_y = & \text{N} + \text{NO} + \text{NO}_2 + \text{NO}_3 + \text{HNO}_3 + \text{HNO}_4 \\ & + \text{HONO} + \text{NACA} + 2 \cdot \text{N}_2\text{O}_5 + \text{MPAN} + \text{ISON} + \text{LC}_4\text{H}_9\text{NO}_3 \\ & + \text{IC}_3\text{H}_7\text{NO}_3 + \text{BrNO}_3 + \text{ClNO}_3.\end{aligned}\tag{A.1}$$

A.1.2 Definition of NO_y in the Evaluation Chapter

NO_x is part of the total reactive nitrogen denoted by NO_y . For the evaluation in Chapter 4 in this study, I define NO_y as the family of all reactive nitrogen species present in the (model) atmosphere as:

$$\begin{aligned}\text{NO}_y = & \text{NO}_x + \text{NO}_z = \text{NO} + \text{NO}_2 + \text{N} + \text{HNO}_3 + \text{HNO}_4 \\ & + \text{HONO} + 2 \cdot \text{N}_2\text{O}_5 + \text{PAN} + \text{HNO} + \text{ISON} + \text{LC}_4\text{H}_9\text{NO}_3 \\ & + \text{IC}_3\text{H}_7\text{NO}_3 + \text{BrNO}_2 + \text{BrNO}_3 + \text{ClNO}_2 + \text{ClNO}_3.\end{aligned}\tag{A.2}$$

Table A.1: List of all submodels used in the model setup for EMAC and COSMO for the reference simulations EUREF and ASIAREF.

Submodel	EMAC	COSMO	Description	Reference
AEROOPT	x		AERosol OPTical properties	Dietmüller et al. [2016]
AIRSEA	x	x	deposition and emission over ocean	Pozzer et al. [2006]
CH4	x		oxidation of methane	
CLOUD	x		cloud parametrisation	Roeckner et al. [2006a], Jöckel et al. [2006]
CLOUDOPT	x		cloud optical properties	Dietmüller et al. [2016]
CONVECT	x		process of convection	Tost et al. [2006b]
CVTRANS	x	x	tracer transport due to convection	Tost et al. [2010]
DRADON	x	x	emission and decay of ^{222}Rn	Jöckel et al. [2010]
DDEP	x	x	gas phase and aerosol tracer dry deposition	Kerkweg et al. [2006a]
E5VDIFF	x		land-atmosphere exchange and vertical diffusion	
EC2COSMO	x		additional ECHAM5 fields for COSMO coupling	Kerkweg and Jöckel [2012]
GWAVE	x		gravity wave drag parametrisation	Roeckner et al. [2006b]
JVAL	x	x	photolysis rate coefficients	Sander et al. [2014]
LNOX	x		parameterisation lightning NO_x	Tost et al. [2007]
MECCA	x	x	tropospheric and stratospheric chemistry	Sander et al. [2019]
MMD2WAY		x	coupling of the MECO(n) model instances	Kerkweg and Jöckel [2012], Kerkweg et al. [2018]
MSBM	x		heterogeneous reaction rates	Jöckel et al. [2010]
OFFEMIS	x	x	reads emission fluxes in 2D and 3D from netCDF-files	Jöckel et al. [2006]
ONEMIS	x	x	2D emission fluxes for gas-phase tracers	Kerkweg et al. [2006a]
ORBIT	x	x	orbital parameters of the Earth orbit	Jöckel et al. [2016]

Table A.4: Fractional distribution (in %) of emission heights for biomass burning (GFAS v1.2) [Dentener et al., 2006].

Region	Level [m]					
	50	300	750	1500	2500	4500
Tropical (30° S–30° N)	20.	40.	40.	0.	0.	0
Temperate (30° N–60° N, 30° S–60° S)	20.	20.	20.	40.	0.	0
Boreal (Eurasia)	10.	10.	20.	20.	40.	0
Boreal (Canada)	10.	10.	10.	10.	20.	40

A.1.3 Tagging regions and the submodel SCALC

For the tagging in my MECO(n) setup, I defined three tagging regions namely Europe (EU), North America (NA) and East Asia (EA) to distinguish between emissions from regional sources (i.e. same continent) and from long-range transport (see Figure A.2). The notation for tagged ozone in this study is described in detail in Table 3.3. The source attribution by this tagging regions Europe, North America and East Asia is enabled by the Simple CALCulations (SCALC) submodel. The goal is to subdivide the global emission files, which are used as input of the model, into regional parts corresponding to the individual regions. Kern [2013] describes the submodel in detail, which allows the multiplication of two "channel objects", here applied in order to prepare the emissions for the tagging by the source regions (see Appendix C in Kern 2013). The anthropogenic emission inventory EDGAR is multiplied with a flag file containing 1 for the specific tagging region and 0 everywhere else. This generates new emission channel objects, where emissions are enabled in the tagged region and set to zero everywhere else. It is ensured that all emissions at the coastline end up in the respective category through regridding, and the total amount of emissions remains the same.

A.1.4 Detailed description of BIOBURN

The burnt dry particulate matter DM for each grid cell is defined as

$$DM = \sum_{i=1}^8 \delta_{i,l} \beta_i \hat{\rho}, \quad (A.3)$$

where $l \in [1,8]$ denotes the land cover class of each grid cell, δ is Kronecker's delta, β_i is the conversion factor to calculate the dry matter combustion rate estimate for eight land cover classes, and $\hat{\rho}$ the fire radiative power (FRP) density estimate [Wuest, 2009, Kaiser et al., 2012]. Figure 3.3 shows the used land cover classes as a global map, which are derived from the dominant burning land cover type in each grid cell [Kaiser et al., 2012]. The emission factor EF [g(species)kg⁻¹(DM)] depends on the fuel type and the land cover type. Originally, $\hat{\rho}$ is calculated as daily mean, and FT and EF are constant throughout the time.

Table A.5: Emission factors [g(species)kg⁻¹(DM)] for the species in BIOBURN based on Kaiser et al. [2012]. Shown are only the species of biomass burning, which are emitted in the applied model. M is the molar mass (g mol⁻¹), GS the global scaling factor and EF shows the emission factor for different firetypes: (5) agriculture (with organic soil), (6) tropical forest, (7) peat, (8) extra-tropical forest and (9) extra-tropical forest (with organic soil).

Species	units	M	GS	EF(5)	EF(6)	EF(7)	EF(8)	EF(9)
C	g m ⁻² s ⁻¹	12.01	1.0	0.45	0.45	0.45	0.45	0.45
CO	molec. m ⁻² s ⁻¹	28.01	1.0	92.1477	100.8533	210.0000	105.5509	105.5509
NO_x	molec. m ⁻² s ⁻¹	30.01	1.0	2.2938	2.2557	1.0000	3.4053	3.4053
SO₂	molec. m ⁻² s ⁻¹	64.07	1.0	0.3679	0.7110	0.7110	0.9990	0.9990
NH₃	molec. m ⁻² s ⁻¹	17.03	1.0	1.6200	0.9355	19.9200	1.6335	1.6335
C₂H₄	molec. m ⁻² s ⁻¹	24.02	0.1460	9.8925	7.0008	12.070	5.6886	5.6886
C₂H₆	molec. m ⁻² s ⁻¹	24.02	0.0777	9.8925	7.0008	12.0700	5.6886	5.6886
C₃H₆	molec. m ⁻² s ⁻¹	36.03	0.0651	9.8925	7.0008	12.0700	5.6886	5.6886
C₃H₈	molec. m ⁻² s ⁻¹	36.03	0.0247	9.8925	7.0008	12.0700	5.6886	5.6886
NC₄H₁₀	molec. m ⁻² s ⁻¹	48.04	0.0320	9.8925	7.0008	12.0700	5.6886	5.6886
CH₃CHO	molec. m ⁻² s ⁻¹	24.02	0.0371	9.8925	7.0008	12.0700	5.6886	5.6886
CH₃COCH₃	molec. m ⁻² s ⁻¹	36.03	0.0384	9.8925	7.0008	12.0700	5.6886	5.6886
CH₃CO₂H	molec. m ⁻² s ⁻¹	24.02	0.0871	9.8925	7.0008	12.0700	5.6886	5.6886
CH₃OH	molec. m ⁻² s ⁻¹	12.01	0.0824	9.8925	7.0008	12.0700	5.6886	5.6886
HCHO	molec. m ⁻² s ⁻¹	12.01	0.0467	9.8925	7.0008	12.0700	5.6886	5.6886
HCOOH	molec. m ⁻² s ⁻¹	12.01	0.0310	9.8925	7.0008	12.0700	5.6886	5.6886
MEK	molec. m ⁻² s ⁻¹	48.04	0.0983	9.8925	7.0008	12.0700	5.6886	5.6886

Table A.6: Emission factors [g(species)kg⁻¹(DM)] for the species in BIOBURN based on Kaiser et al. [2012]. Shown are only the species of biomass burning, which are emitted in the applied model. M is the molar mass (g mol⁻¹), GS the global scaling factor and EF(number) shows the emission factor of different firetypes: (1) water, (2) savanna, (3) savanna (with organic soil) and (4) agriculture.

Species	units	M	GS	EF(1)	EF(2)	EF(2)	EF(4)
C	g m ⁻² s ⁻¹	1.0	0.0	0.0	0.45	0.45	0.45
CO	molec. m ⁻² s ⁻¹	28.01	1.0	0.0	61.4832	61.4832	92.1477
NO_x	molec. m ⁻² s ⁻¹	30.01	1.0	0.0	2.1240	2.1240	2.2938
SO₂	molec. m ⁻² s ⁻¹	64.07	1.0	0.0	0.7110	0.9990	0.9990
NH₃	molec. m ⁻² s ⁻¹	17.03	1.0	0.0	0.7361	0.7361	1.6200
C₂H₄	molec. m ⁻² s ⁻¹	24.02	0.1460	0.0	3.4103	3.4103	9.8925
C₂H₆	molec. m ⁻² s ⁻¹	24.02	0.0777	0.0	3.4103	3.4103	9.8925
C₃H₆	molec. m ⁻² s ⁻¹	36.03	0.0651	0.0	3.4103	3.4103	9.8925
C₃H₈	molec. m ⁻² s ⁻¹	36.03	0.0247	0.0	3.4103	3.4103	9.8925
NC₄H₁₀	molec. m ⁻² s ⁻¹	48.04	0.0320	0.0	3.4103	3.4103	9.8925
CH₃CHO	molec. m ⁻² s ⁻¹	24.02	0.0371	0.0	3.4103	3.4103	9.8925
CH₃COCH₃	molec. m ⁻² s ⁻¹	36.03	0.0384	0.0	3.4103	3.4103	9.8925
CH₃CO₂H	molec. m ⁻² s ⁻¹	24.02	0.0871	0.0	3.4103	3.4103	9.8925
CH₃OH	molec. m ⁻² s ⁻¹	12.01	0.0824	0.0	3.4103	3.4103	9.8925
HCHO	molec. m ⁻² s ⁻¹	12.01	0.0467	0.0	3.4103	3.4103	9.8925
HCOOH	molec. m ⁻² s ⁻¹	12.01	0.0310	0.0	3.4103	3.4103	9.8925
MEK	molec. m ⁻² s ⁻¹	48.04	0.0983	0.0	3.4103	3.4103	9.8925

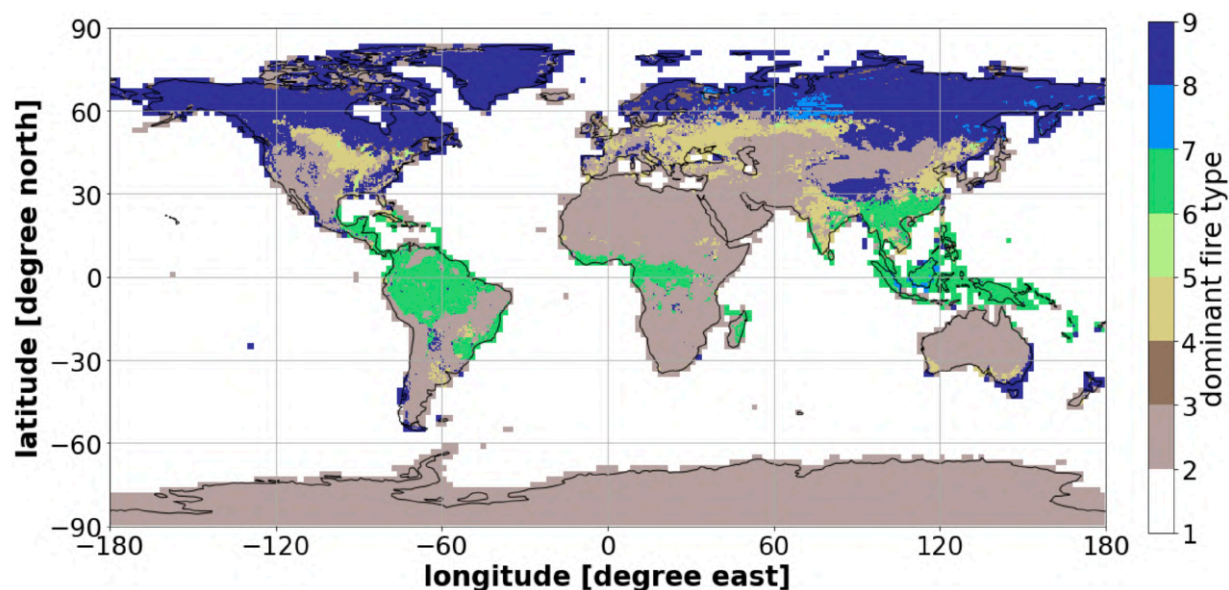


Figure A.1: Land cover class map based on dominant fire type in GFAS and organic soil and peat maps after Kaiser et al. [2012]. The grid resolution is 0.5° in latitude and longitude. The dominant firetypes are defined as (1) water, (2) savanna, (3) savanna with organic soil and (4) agriculture, (5) agriculture with organic soil, (6) tropical forest, (7) peat, (8) extra-tropical forest, and (9) extra-tropical forest with organic soil.

A.1.5 Mechanism of the gas phase chemistry

The document presented below has been automatically generated during the creation of the gas phase mechanism with MECCA [Sander et al., 2011]. Only the essential sections of the document are displayed, while the full version is included in the Supplement that accompanies the manuscript submitted to ACP by Kilian et al. in 2023:

The Chemical Mechanism of MECCA

KPP version: 2.2.3_rs3

MECCA version: 4.4.0.m1

Date: August 3, 2022

Batch file: CCMI2-base-02-tag.bat

Integrator: rosenbrock_mz

Gas equation file: gas.eqn

Replacement file: mim1-CCMI2-base-02

Selected reactions:

“(((Tr && (G || Het) && !I) || St) && !Hg)”

Number of aerosol phases: 0

Number of species in selected mechanism:

Gas phase: 205

Aqueous phase: 0

All species: 205

Number of reactions in selected mechanism:

Gas phase (Gnnn): 265

Aqueous phase (Annn): 0

Henry (Hnnn): 0

Photolysis (Jnnn): 82

Aqueous phase photolysis (PHnnn): 0

Heterogeneous (HETnnn): 12

Equilibria (EQnn): 0

Isotope exchange (IEXnnn): 0

Tagging equations (TAGnnn): 0

Dummy (Dnn): 0

All equations: 359

Table 1: Gas phase reactions

#	labels	reaction	rate coefficient	reference
G1000	UpStTrG	$O_2 + O(^1D) \rightarrow O(^3P) + O_2$	$3.3E-11 \cdot \text{EXP}(55./\text{temp})$	Burkholder et al. (2015)
G1001	UpStTrG	$O_2 + O(^3P) \rightarrow O_3$	$6.0E-34 \cdot ((\text{temp}/300.)^{**}(-2.4))$ *cair	Burkholder et al. (2015)
G1002a	UpStG	$O_3 + O(^1D) \rightarrow 2.0 \text{ } \alpha 3\text{lossxo} + 2.0 \text{ LossO3O} + 2.0 \text{ LossO3}$ + 2 O_2	$1.2E-10$	Burkholder et al. (2015)*
G1003	UpStG	$O_3 + O(^3P) \rightarrow 2.0 \text{ } \alpha 3\text{lossxo} + 2.0 \text{ LossO3O} + 2.0 \text{ LossO3}$ + 2 O_2	$8.0E-12 \cdot \text{EXP}(-2060./\text{temp})$	Burkholder et al. (2015)
G2100	UpStTrG	$H + O_2 \rightarrow 1.0 \text{ LossG2100} + HO_2$	$k_3rd(\text{temp}, \text{cair}, 4.4E-32, 1.3,$ $7.5E-11, -0.2, 0.6)$	Burkholder et al. (2015)
G2101	UpStG	$H + O_3 \rightarrow 1.0 \text{ } \alpha 3\text{lossxo} + 1.0 \text{ LossO3H} + 1.0 \text{ LossO3} +$ $OH + O_2$	$1.4E-10 \cdot \text{EXP}(-470./\text{temp})$	Burkholder et al. (2015)
G2102	UpStG	$H_2 + O(^1D) \rightarrow 1.0 \text{ } \alpha 3\text{lossxo} + 1.0 \text{ LossO3H} + 1.0 \text{ LossO3}$ + $H + OH$	$1.2E-10$	Burkholder et al. (2015)
G2103	UpStG	$OH + O(^3P) \rightarrow 1.0 \text{ LossG2103} + 1.0 \text{ } \alpha 3\text{lossoh} + 1.0$ $\text{LossO3H} + 1.0 \text{ LossO3} + H + O_2$	$1.8E-11 \cdot \text{EXP}(180./\text{temp})$	Burkholder et al. (2015)
G2104	UpStTrG	$OH + O_3 \rightarrow 1.0 \text{ LossG2104} + 1.0 \text{ } \alpha 3\text{lossoh} + 1.0 \text{ LossO3H}$ + $\text{LossOH} + 1.0 \text{ LossO3} + HO_2 + O_2$	$1.7E-12 \cdot \text{EXP}(-940./\text{temp})$	Burkholder et al. (2015)
G2105	UpStTrG	$OH + H_2 \rightarrow 1.0 \text{ LossG2105} + \text{ProdH2O} + H_2O + H$	$2.8E-12 \cdot \text{EXP}(-1800./\text{temp})$	Burkholder et al. (2015)
G2106	UpStG	$HO_2 + O(^3P) \rightarrow 1. \text{ LossG2106} + 1.0 \text{ } \alpha 3\text{lossho2} + 1.0$ $\text{LossO3H} + 1.0 \text{ LossO3} + OH + O_2$	$3.E-11 \cdot \text{EXP}(200./\text{temp})$	Burkholder et al. (2015)
G2107	UpStTrG	$HO_2 + O_3 \rightarrow 1. \text{ LossG2107} + 1.0 \text{ } \alpha 3\text{lossho2} + 1.0 \text{ LossO3H}$ + $\text{LossHO2} + 1.0 \text{ LossO3} + OH + 2 \text{ } O_2$	$1.E-14 \cdot \text{EXP}(-490./\text{temp})$	Burkholder et al. (2015)
G2108a	UpStG	$HO_2 + H \rightarrow 2 \text{ } OH$	$7.2E-11$	Burkholder et al. (2015)
G2108b	UpStG	$HO_2 + H \rightarrow H_2 + O_2$	$6.9E-12$	Burkholder et al. (2015)
G2108c	UpStG	$HO_2 + H \rightarrow 1.0 \text{ } \alpha 3\text{prodho2} + \text{ProdH2O} + 1.0 \text{ ProdO3} +$ $O(^3P) + H_2O$	$1.6E-12$	Burkholder et al. (2015)
G2109	UpStTrG	$HO_2 + OH \rightarrow 1. \text{ LossG2109} + \text{ProdH2O} + H_2O + O_2$	$4.8E-11 \cdot \text{EXP}(250./\text{temp})$	Burkholder et al. (2015)
G2110	UpStTrG	$HO_2 + HO_2 \rightarrow 1. \text{ LossG2110} + H_2O_2 + O_2$	k_HO2_HO2	Burkholder et al. (2015)*
G2111	UpStTrG	$H_2O + O(^1D) \rightarrow 1. \text{ LossG2111} + 1.0 \text{ } \alpha 3\text{lossxo} + \text{LossH2O}$ + $1.0 \text{ LossO3O} + \text{LossO1D} + 1.0 \text{ LossO3} + 2 \text{ } OH$	$1.63E-10 \cdot \text{EXP}(60./\text{temp})$	Burkholder et al. (2015)
G2112	UpStTrG	$H_2O_2 + OH \rightarrow 1. \text{ LossG2112} + \text{ProdH2O} + H_2O + HO_2$	$1.8E-12$	Burkholder et al. (2015)
G3100	UpStGN	$N + O_2 \rightarrow 1.0 \text{ } \alpha 3\text{prodnoy} + 1.0 \text{ ProdO3} + NO + O(^3P)$	$1.5E-11 \cdot \text{EXP}(-3600./\text{temp})$	Burkholder et al. (2015)
G3101	UpStTrGN	$N_2 + O(^1D) \rightarrow O(^3P) + N_2$	$2.15E-11 \cdot \text{EXP}(110./\text{temp})$	Burkholder et al. (2015)

Table 1: Gas phase reactions (... continued)

#	labels	reaction	rate coefficient	reference
G3102a	UpStGN	$\text{N}_2\text{O} + \text{O}(^1\text{D}) \rightarrow 1.0 \text{ } \alpha 3\text{lossxo} + \text{noproductN2O} + 1.0 \text{ LossO3O}$ $+ 1.0 \text{ LossO3} + 2 \text{ NO}$	$7.259\text{E}-11 \cdot \text{EXP}(20./\text{temp})$	Burkholder et al. (2015)
G3102b	StGN	$\text{N}_2\text{O} + \text{O}(^1\text{D}) \rightarrow 1.0 \text{ } \alpha 3\text{lossxo} + 1.0 \text{ LossO3O} + 1.0 \text{ LossO3}$ $+ \text{N}_2 + \text{O}_2$	$4.641\text{E}-11 \cdot \text{EXP}(20./\text{temp})$	Burkholder et al. (2015)
G3103	UpStTrGN	$\text{NO} + \text{O}_3 \rightarrow \text{NO}_2 + \text{O}_2$	$3.0\text{E}-12 \cdot \text{EXP}(-1500./\text{temp})$	Burkholder et al. (2015)
G3104	UpStGN	$\text{NO} + \text{N} \rightarrow 1.0 \text{ } \alpha 3\text{prodnoy} + 1.0 \text{ ProdO3} + \text{O}(^3\text{P}) + \text{N}_2$	$2.1\text{E}-11 \cdot \text{EXP}(100./\text{temp})$	Burkholder et al. (2015)
G3105	UpStGN	$\text{NO}_2 + \text{O}(^3\text{P}) \rightarrow 2.0 \text{ } \alpha 3\text{lossno} + 2.0 \text{ LossO3N} + 2.0 \text{ LossO3}$ $+ \text{NO} + \text{O}_2$	$5.1\text{E}-12 \cdot \text{EXP}(210./\text{temp})$	Burkholder et al. (2015)
G3106	StTrGN	$\text{NO}_2 + \text{O}_3 \rightarrow \text{NO}_3 + \text{O}_2$	$1.2\text{E}-13 \cdot \text{EXP}(-2450./\text{temp})$	Burkholder et al. (2015)
G3107	UpStGN	$\text{NO}_2 + \text{N} \rightarrow \text{N}_2\text{O} + \text{O}(^3\text{P})$	$5.8\text{E}-12 \cdot \text{EXP}(220./\text{temp})$	Burkholder et al. (2015)
G3108	StTrGN	$\text{NO}_3 + \text{NO} \rightarrow 2 \text{ NO}_2$	$1.5\text{E}-11 \cdot \text{EXP}(170./\text{temp})$	Burkholder et al. (2015)
G3109	UpStTrGN	$\text{NO}_3 + \text{NO}_2 \rightarrow \text{N}_2\text{O}_5$	$k_{\text{N03_N02}}$	Burkholder et al. (2015)*
G3110	StTrGN	$\text{N}_2\text{O}_5 \rightarrow \text{NO}_2 + \text{NO}_3$	$k_{\text{N03_N02}} / (5.8\text{E}-27 \cdot \text{EXP}(10840./\text{temp}))$	Burkholder et al. (2015)*
G3200	TrGN	$\text{NO} + \text{OH} \rightarrow 1. \text{ LossG3200} + \text{HONO}$	$k_{\text{3rd}}(\text{temp}, \text{cair}, 7.0\text{E}-31, 2.6, 3.6\text{E}-11, 0.1, 0.6)$	Burkholder et al. (2015)
G3201	UpStTrGN	$\text{NO} + \text{HO}_2 \rightarrow 1. \text{ LossG3201} + 1.0 \text{ } \alpha 3\text{prodho2noy} + \text{ProdHO2} + 1.0 \text{ ProdO3} + \text{NO}_2 + \text{OH}$	$3.3\text{E}-12 \cdot \text{EXP}(270./\text{temp})$	Burkholder et al. (2015)
G3202	UpStTrGN	$\text{NO}_2 + \text{OH} \rightarrow 1. \text{ LossG3202} + \text{HNO}_3$	$k_{\text{3rd}}(\text{temp}, \text{cair}, 1.8\text{E}-30, 3.0, 2.8\text{E}-11, 0., 0.6)$	Burkholder et al. (2015)
G3203	StTrGN	$\text{NO}_2 + \text{HO}_2 \rightarrow 1. \text{ LossG3203} + \text{HNO}_4$	$k_{\text{N02_H02}}$	Burkholder et al. (2015)*
G3204	TrGN	$\text{NO}_3 + \text{HO}_2 \rightarrow 1.0 \text{ } \alpha 3\text{lossno} + 1.0 \text{ LossO3N} + 1.0 \text{ LossO3}$ $+ \text{NO}_2 + \text{OH} + \text{O}_2$	$3.5\text{E}-12$	Burkholder et al. (2015)
G3205	TrGN	$\text{HONO} + \text{OH} \rightarrow 1.0 \text{ } \alpha 3\text{prodohnoy} + \text{ProdH2O} + 1.0$ $\text{ProdO3} + \text{NO}_2 + \text{H}_2\text{O}$	$1.8\text{E}-11 \cdot \text{EXP}(-390./\text{temp})$	Burkholder et al. (2015)
G3206	StTrGN	$\text{HNO}_3 + \text{OH} \rightarrow 1.0 \text{ } \alpha 3\text{prodohnoy} + \text{ProdH2O} + 1.0$ $\text{ProdO3} + \text{H}_2\text{O} + \text{NO}_3$	$k_{\text{HN03_OH}}$	Dulitz et al. (2018)*
G3207	StTrGN	$\text{HNO}_4 \rightarrow 1. \text{ LossG3207} + \text{NO}_2 + \text{HO}_2$	$k_{\text{N02_H02}} / (2.1\text{E}-27 \cdot \text{EXP}(10900./\text{temp}))$	Burkholder et al. (2015)*
G3208	StTrGN	$\text{HNO}_4 + \text{OH} \rightarrow \text{ProdH2O} + \text{NO}_2 + \text{H}_2\text{O}$	$1.3\text{E}-12 \cdot \text{EXP}(380./\text{temp})$	Burkholder et al. (2015)
G3209	TrGN	$\text{NH}_3 + \text{OH} \rightarrow \text{ProdH2O} + \text{NH}_2 + \text{H}_2\text{O}$	$1.7\text{E}-12 \cdot \text{EXP}(-710./\text{temp})$	Kohlmann and Poppe (1999)
G3210	TrGN	$\text{NH}_2 + \text{O}_3 \rightarrow 1.0 \text{ } \alpha 3\text{lossxo} + 1.0 \text{ LossO3N} + 1.0 \text{ LossO3} + \text{NH}_2\text{O} + \text{O}_2$	$4.3\text{E}-12 \cdot \text{EXP}(-930./\text{temp})$	Kohlmann and Poppe (1999)
G3211	TrGN	$\text{NH}_2 + \text{HO}_2 \rightarrow \text{NH}_2\text{O} + \text{OH}$	$4.8\text{E}-07 \cdot \text{EXP}(-628./\text{temp}) * (\text{temp})^{**(-1.32)}$	Kohlmann and Poppe (1999)

Table 1: Gas phase reactions (... continued)

#	labels	reaction	rate coefficient	reference
G3212	TrGN	$\text{NH}_2 + \text{HO}_2 \rightarrow \text{ProdH}_2\text{O} + \text{HNO} + \text{H}_2\text{O}$	$9.4\text{E-}09 \cdot \text{EXP}(-356./\text{temp}) \cdot (\text{temp})^{**}(-1.12)$	Kohlmann and Poppe (1999)
G3213	TrGN	$\text{NH}_2 + \text{NO} \rightarrow \text{HO}_2 + \text{OH} + \text{N}_2$	$1.92\text{E-}12 \cdot ((\text{temp}/298.)^{**}(-1.5))$	Kohlmann and Poppe (1999)
G3214	TrGN	$\text{NH}_2 + \text{NO} \rightarrow \text{ProdH}_2\text{O} + \text{N}_2 + \text{H}_2\text{O}$	$1.41\text{E-}11 \cdot ((\text{temp}/298.)^{**}(-1.5))$	Kohlmann and Poppe (1999)
G3215	TrGN	$\text{NH}_2 + \text{NO}_2 \rightarrow 1.0 \text{ o3lossno} + \text{ProdH}_2\text{O} + 1.0 \text{ LossO}_3\text{N} + 1.0 \text{ LossO}_3$	$1.2\text{E-}11 \cdot ((\text{temp}/298.)^{**}(-2.0))$	Kohlmann and Poppe (1999)
G3216	TrGN	$\text{NH}_2 + \text{NO}_2 \rightarrow 1.0 \text{ o3lossno} + 1.0 \text{ LossO}_3\text{N} + 1.0 \text{ LossO}_3$ $+ \text{NH}_2\text{O} + \text{NO}$	$0.8\text{E-}11 \cdot ((\text{temp}/298.)^{**}(-2.0))$	Kohlmann and Poppe (1999)
G3217	TrGN	$\text{NH}_2\text{O} + \text{O}_3 \rightarrow 1.0 \text{ o3lossxo} + 1.0 \text{ LossO}_3\text{N} + 1.0 \text{ LossO}_3$ $+ \text{NH}_2 + \text{O}_2$	$1.2\text{E-}14$	Kohlmann and Poppe (1999)
G3218	TrGN	$\text{NH}_2\text{O} \rightarrow \text{NHOH}$	$1.3\text{E}3$	Kohlmann and Poppe (1999)
G3219	TrGN	$\text{HNO} + \text{OH} \rightarrow \text{ProdH}_2\text{O} + \text{NO} + \text{H}_2\text{O}$	$8.0\text{E-}11 \cdot \text{EXP}(-500./\text{temp})$	Kohlmann and Poppe (1999)
G3220	TrGN	$\text{HNO} + \text{NHOH} \rightarrow \text{NH}_2\text{OH} + \text{NO}$	$1.66\text{E-}12 \cdot \text{EXP}(-1500./\text{temp})$	Kohlmann and Poppe (1999)
G3221	TrGN	$\text{HNO} + \text{NO}_2 \rightarrow 1.0 \text{ o3lossno} + 1.0 \text{ LossO}_3\text{N} + 1.0 \text{ LossO}_3$ $+ \text{HONO} + \text{NO}$	$1.0\text{E-}12 \cdot \text{EXP}(-1000./\text{temp})$	Kohlmann and Poppe (1999)
G3222	TrGN	$\text{NHOH} + \text{OH} \rightarrow \text{ProdH}_2\text{O} + \text{HNO} + \text{H}_2\text{O}$	$1.66\text{E-}12$	Kohlmann and Poppe (1999)
G3223	TrGN	$\text{NH}_2\text{OH} + \text{OH} \rightarrow \text{ProdH}_2\text{O} + \text{NHOH} + \text{H}_2\text{O}$	$4.13\text{E-}11 \cdot \text{EXP}(-2138./\text{temp})$	Kohlmann and Poppe (1999)
G3224	TrGN	$\text{HNO} + \text{O}_2 \rightarrow \text{HO}_2 + \text{NO}$	$3.65\text{E-}14 \cdot \text{EXP}(-4600./\text{temp})$	Kohlmann and Poppe (1999)
G4100	UpStG	$\text{CH}_4 + \text{O}(^1\text{D}) \rightarrow 1.0 \text{ o3lossxo} + 1.0 \text{ LossO}_3\text{O} + 1.0 \text{ LossO}_3$ $+ .75 \text{ CH}_3\text{O}_2 + .75 \text{ OH} + .25 \text{ HCHO} + .4 \text{ H} + .05 \text{ H}_2$	$1.75\text{E-}10$	Sander et al. (2011)
G4101	StTrG	$\text{CH}_4 + \text{OH} \rightarrow 1. \text{ LossG4101} + \text{ProdH}_2\text{O} + \text{CH}_3\text{O}_2 + \text{H}_2\text{O}$	$1.85\text{E-}20 \cdot \text{EXP}(2.82 \cdot \text{LOG}(\text{temp}) - 987./\text{temp})$	Atkinson (2003)
G4102	TrG	$\text{CH}_3\text{OH} + \text{OH} \rightarrow 1. \text{ OHlossHO}_2\text{prodNMHC} + \text{HCHO} + \text{HO}_2$	$2.9\text{E-}12 \cdot \text{EXP}(-345./\text{temp})$	Sander et al. (2011)
G4103	StTrG	$\text{CH}_3\text{O}_2 + \text{HO}_2 \rightarrow 1. \text{ HO}_2\text{lossNMHC} + \text{CH}_3\text{OOH} + \text{O}_2$	$4.1\text{E-}13 \cdot \text{EXP}(750./\text{temp})$	Sander et al. (2011)*
G4104	UpStTrGN	$\text{CH}_3\text{O}_2 + \text{NO} \rightarrow 1. \text{ HO}_2\text{prodNMHCNOy} + \text{ProdMeO}_2 + \text{ProdMeO}_2 + 1.0 \text{ ProdO}_3 + \text{HCHO} + \text{NO}_2 + \text{HO}_2$	$2.8\text{E-}12 \cdot \text{EXP}(300./\text{temp})$	Sander et al. (2011)
G4105	TrGN	$\text{CH}_3\text{O}_2 + \text{NO}_3 \rightarrow 1. \text{ HO}_2\text{prodNMHCNOy} + 1.0 \text{ o3lossno}$ $+ 1.0 \text{ LossO}_3\text{R} + 1.0 \text{ LossO}_3 + \text{HCHO} + \text{HO}_2 + \text{NO}_2$	$1.3\text{E-}12$	Atkinson et al. (2006)
G4106a	StTrG	$\text{CH}_3\text{O}_2 + \text{CH}_3\text{O}_2 \rightarrow 2 \text{ HCHO} + 2 \text{ HO}_2$	$9.5\text{E-}14 \cdot \text{EXP}(390./\text{temp}) / (1 + 1./26.2 \cdot \text{EXP}(1130./\text{temp}))$	Sander et al. (2011)
G4106b	StTrG	$\text{CH}_3\text{O}_2 + \text{CH}_3\text{O}_2 \rightarrow \text{HCHO} + \text{CH}_3\text{OH} + \text{O}_2$	$9.5\text{E-}14 \cdot \text{EXP}(390./\text{temp}) / (1 + 26.2 \cdot \text{EXP}(1130./\text{temp}))$	Sander et al. (2011)
G4107	StTrG	$\text{CH}_3\text{OOH} + \text{OH} \rightarrow 0.7 \text{ OHlossNMHC} + \text{ProdH}_2\text{O} + .7 \text{ k_CH}_3\text{OOH_OH}$ $\text{CH}_3\text{O}_2 + .3 \text{ HCHO} + .3 \text{ OH} + \text{H}_2\text{O}$	$\text{k_CH}_3\text{OOH_OH}$	Wallington et al. (2018)

Table 1: Gas phase reactions (... continued)

#	labels	reaction	rate coefficient	reference
G4108	StTrG	HCHO + OH → 1. OHlossHO2prodNMHC + ProdH2O + CO + H ₂ O + HO ₂	9.52E-18*EXP(2.03*LOG(temp) + 636./temp)	Sivakumaran et al. (2003)
G4109	TrGN	HCHO + NO ₃ → 1. HO2prodNMHCNOy + 1.0 o3lossno + 1.0 LossO3R + 1.0 LossO3 + HNO ₃ + CO + HO ₂	3.4E-13*EXP(-1900./temp)	Sander et al. (2011)*
G4110	UpStTrG	CO + OH → 1. LossG4110 + H + CO ₂	(1.57E-13*cair*3.54E-33)	McCabe et al. (2001)
G4111	TrG	HCOOH + OH → 1. OHlossHO2prodNMHC + ProdH2O + CO ₂ + HO ₂ + H ₂ O	4.0E-13	Sander et al. (2011)
G4200	TrGC	C ₂ H ₆ + OH → 1. OHlossNMHC + ProdH2O + C ₂ H ₅ O ₂ + H ₂ O	1.49E-17*temp*temp*EXP(-499./temp)	Atkinson (2003)
G4201	TrGC	C ₂ H ₄ + O ₃ → 1.0 o3lossro + 1.0 LossO3R + 1.0 LossO3 + HCHO + .63 CO + .13 HO ₂ + 0.23125 HCOOH + 0.13875 HCHO + 0.13875 H ₂ O ₂ + .13 OH	1.2E-14*EXP(-2630./temp)	Sander et al. (2011)*
G4202	TrGC	C ₂ H ₄ + OH → 1. OHlossNMHC + .6666667 CH ₃ CH(O ₂)CH ₂ OH	k_3rd(temp, cair, 1.0E-28, 4.5, 7.5E-12, 0.85, 0.6)	Sander et al. (2011)
G4203	TrGC	C ₂ H ₅ O ₂ + HO ₂ → 1. HO2lossNMHC + C ₂ H ₅ OOH	7.5E-13*EXP(700./temp)	Sander et al. (2011)
G4204	TrGCN	C ₂ H ₅ O ₂ + NO → 1. HO2prodNMHCNOy + 1.0 o3prodro2 + ProdRO2 + 1.0 ProdO3 + CH ₃ CHO + HO ₂ + NO ₂	2.6E-12*EXP(365./temp)	Sander et al. (2011)
G4205	TrGCN	C ₂ H ₅ O ₂ + NO ₃ → 1. HO2prodNMHCNOy + 1.0 o3lossno + 1.0 LossO3R + 1.0 LossO3 + CH ₃ CHO + HO ₂ + NO ₂	2.3E-12	Wallington et al. (2018)
G4206	TrGC	C ₂ H ₅ O ₂ + CH ₃ O ₂ → .75 HCHO + HO ₂ + .75 CH ₃ CHO + .25 CH ₃ OH	1.6E-13*EXP(195./temp)	see note*
G4207	TrGC	C ₂ H ₅ OOH + OH → 0.3 OHlossNMHC + .3 C ₂ H ₅ O ₂ + .7 CH ₃ CHO + .7 OH	k_CH300H_OH	see note*
G4208	TrGC	CH ₃ CHO + OH → 1. OHlossNMHC + ProdH2O + CH ₃ C(O)OO + H ₂ O	4.4E-12*EXP(365./temp)	Atkinson et al. (2006)
G4209	TrGCN	CH ₃ CHO + NO ₃ → 1.0 o3lossno + 1.0 LossO3R + 1.0 LossO3 + CH ₃ C(O)OO + HNO ₃	1.4E-12*EXP(-1900./temp)	Sander et al. (2011)
G4210	TrGC	CH ₃ COOH + OH → 1. OHlossNMHC + ProdH2O + CH ₃ O ₂ + CO ₂ + H ₂ O	4.2E-14*EXP(855./temp)	Atkinson et al. (2006)
G4211a	TrGC	CH ₃ C(O)OO + HO ₂ → 1. HO2lossNMHC + 37.*EXP(660./temp)	4.3E-13*EXP(1040./temp)/(1.+1./37.*EXP(660./temp))	Tyndall et al. (2001a)
G4211b	TrGC	CH ₃ C(O)OO + HO ₂ → 1. HO2lossNMHC + 1.0 o3prodho2nmhc + 1.0 ProdO3 + CH ₃ COOH + O ₃	4.3E-13*EXP(1040./temp)/(1.+37.*EXP(-660./temp))	Tyndall et al. (2001a)
G4212	TrGCN	CH ₃ C(O)OO + NO → 1.0 o3prodro2 + ProdRO2 + 1.0 ProdO3 + CH ₃ O ₂ + CO ₂ + NO ₂	8.1E-12*EXP(270./temp)	Tyndall et al. (2001a)

Table 1: Gas phase reactions (... continued)

#	labels	reaction	rate coefficient	reference
G4213	TrGCN	$\text{CH}_3\text{C}(\text{O})\text{OO} + \text{NO}_2 \rightarrow \text{panprod} + \text{PAN}$		Sander et al. (2011)*
G4214	TrGCN	$\text{CH}_3\text{C}(\text{O})\text{OO} + \text{NO}_3 \rightarrow 1.0 \text{ o3lossno} + 1.0 \text{ LossO3R} + 1.0 \text{ LossO3}$	$k_{\text{CH3CO3_NO2}}$	Canosa-Mas et al. (1996)
G4215a	TrGC	$\text{LossO3} + \text{CH}_3\text{O}_2 + \text{NO}_2 + \text{CO}_2$	4.E-12	
G4215b	TrGC	$\text{CH}_3\text{C}(\text{O})\text{OO} + \text{CH}_3\text{O}_2 \rightarrow \text{HCHO} + \text{HO}_2 + \text{CH}_3\text{O}_2 + \text{CO}_2$	$0.9 \cdot 2.0\text{E}-12 \cdot \text{EXP}(500./\text{temp})$	Sander et al. (2011)
G4216	TrGC	$\text{CH}_3\text{C}(\text{O})\text{OO} + \text{CH}_3\text{O}_2 \rightarrow \text{CH}_3\text{COOH} + \text{HCHO}$	$0.1 \cdot 2.0\text{E}-12 \cdot \text{EXP}(500./\text{temp})$	Sander et al. (2011)
G4217	TrGC	$\text{CH}_3\text{C}(\text{O})\text{OO} + \text{C}_2\text{H}_5\text{O}_2 \rightarrow .82 \text{ CH}_3\text{O}_2 + \text{CH}_3\text{CHO} + .82 \text{ HO}_2 + .18 \text{ CH}_3\text{COOH}$	$4.9\text{E}-12 \cdot \text{EXP}(211./\text{temp})$	Wallington et al. (2018), Kirchner and Stockwell (1996)
G4218	TrGC	$\text{CH}_3\text{C}(\text{O})\text{OO} + \text{CH}_3\text{C}(\text{O})\text{OO} \rightarrow 2 \text{ CH}_3\text{O}_2 + 2 \text{ CO}_2 + \text{O}_2$	$2.5\text{E}-12 \cdot \text{EXP}(500./\text{temp})$	Tyndall et al. (2001a)
G4219	TrGCN	$\text{CH}_3\text{C}(\text{O})\text{OOH} + \text{OH} \rightarrow 1. \text{ OHlossNMHC} + \text{ProdH2O} + \text{CH}_3\text{C}(\text{O})\text{OO} + \text{H}_2\text{O}$	$0.6 \cdot k_{\text{CH300H_OH}}$	Rickard and Pascoe (2009)
G4220	TrGCN	$\text{NACA} + \text{OH} \rightarrow 1. \text{ OHlossNMHC} + \text{NO}_2 + \text{HCHO} + \text{CO}$	$5.6\text{E}-12 \cdot \text{EXP}(270./\text{temp})$	Pöschl et al. (2000)
G4221	TrGCN	$\text{PAN} + \text{OH} \rightarrow 1. \text{ OHlossNMHC} + \text{panloss} + \text{ProdH2O} + \text{HCHO} + \text{CO} + \text{NO}_2 + \text{H}_2\text{O}$	$9.50\text{E}-13 \cdot \text{EXP}(-650./\text{temp})$	Rickard and Pascoe (2009)
G4222	TrGC	$\text{PAN} \rightarrow \text{panloss} + \text{CH}_3\text{C}(\text{O})\text{OO} + \text{NO}_2$	$k_{\text{PAN_M}}$	Sander et al. (2011)*
G4300	TrGC	$\text{C}_2\text{H}_2 + \text{OH} \rightarrow \text{CH}_3\text{O}_2$	$k_{\text{3rd}}(\text{temp}, \text{cair}, 5.5\text{e}-30, 0.0, 8.3\text{e}-13, -2., 0.6)$	Sander et al. (2011)
G4301	TrGC	$\text{C}_3\text{H}_8 + \text{OH} \rightarrow 1. \text{ OHlossNMHC} + \text{ProdH2O} + .82 \text{ iC}_3\text{H}_7\text{O}_2 + .18 \text{ C}_2\text{H}_5\text{O}_2 + \text{H}_2\text{O}$	$1.65\text{E}-17 \cdot \text{temp} \cdot \text{temp} \cdot \text{EXP}(-87./\text{temp})$	Atkinson (2003)
G4302	TrGC	$\text{C}_3\text{H}_6 + \text{OH} \rightarrow 1. \text{ OHlossNMHC} + \text{CH}_3\text{CH}(\text{O}_2)\text{CH}_2\text{OH}$	$6.5\text{E}-15 \cdot \text{EXP}(-1900./\text{temp})$	Sander et al. (2011)
G4303	TrGCN	$\text{C}_3\text{H}_6 + \text{NO}_3 \rightarrow 1.0 \text{ o3lossno} + 1.0 \text{ LossO3R} + 1.0 \text{ LossO3} + \text{LC4H9NO3}$	$3\text{E}-11, 0., 0.5$	Wallington et al. (2018)
G4304	TrGC	$\text{iC}_3\text{H}_7\text{O}_2 + \text{HO}_2 \rightarrow 1. \text{ HO2lossNMHC} + \text{iC}_3\text{H}_7\text{OOH}$	$4.6\text{E}-13 \cdot \text{EXP}(-1155./\text{temp})$	Wallington et al. (2018)
G4305	TrGCN	$\text{iC}_3\text{H}_7\text{O}_2 + \text{NO} \rightarrow 0.96 \text{ HO2prodNMHCNOy} + 1.0 \text{ o3prodre2} + \text{ProdRO2} + 1.0 \text{ ProdO3} + .96 \text{ CH}_3\text{COCH}_3 + .96 \text{ HO}_2 + .96 \text{ NO}_2 + .04 \text{ iC}_3\text{H}_7\text{ONO}_2$	$k_{\text{PrO2_H02}}$ $k_{\text{PrO2_N0}}$	Atkinson (1997) Wallington et al. (2018)
G4306	TrGC	$\text{iC}_3\text{H}_7\text{O}_2 + \text{CH}_3\text{O}_2 \rightarrow \text{CH}_3\text{COCH}_3 + .8 \text{ HCHO} + .8 \text{ HO}_2$	$k_{\text{PrO2_CH3O2}}$	Kirchner and Stockwell (1996)
G4307	TrGC	$\text{iC}_3\text{H}_7\text{OOH} + \text{OH} \rightarrow 0.3 \text{ OHlossNMHC} + .3 \text{ iC}_3\text{H}_7\text{O}_2 + .7 \text{ CH}_3\text{COCH}_3 + .7 \text{ OH}$	$k_{\text{CH300H_OH}}$	see note*

Table 1: Gas phase reactions (... continued)

#	labels	reaction	rate coefficient	reference
G4308	TrGC	$\text{CH}_3\text{CH}(\text{O}_2)\text{CH}_2\text{OH} + \text{HO}_2 \rightarrow 1. \text{HO}_2\text{lossNMHC} +$ $\text{CH}_3\text{CH}(\text{OOH})\text{CH}_2\text{OH}$	$6.5\text{E-}13*\text{EXP}(650./\text{temp})$	Müller and Brasseur (1995)
G4309	TrGCN	$\text{CH}_3\text{CH}(\text{O}_2)\text{CH}_2\text{OH} + \text{NO} \rightarrow 0.98 \text{HO}_2\text{prodNMHCNO}_y +$ $1.0 \text{o3prod}_2 + \text{ProdRO}_2 + 1.0 \text{ProdO}_3 + .98 \text{CH}_3\text{CHO}$ $+ .98 \text{HCHO} + .98 \text{HO}_2 + .98 \text{NO}_2 + .02 \text{LC4H9NO}_3$	$4.2\text{E-}12*\text{EXP}(180./\text{temp})$	Müller and Brasseur (1995)
G4310	TrGC	$\text{CH}_3\text{CH}(\text{OOH})\text{CH}_2\text{OH} + \text{OH} \rightarrow 0.5 \text{OHlossNMHC} +$ $\text{ProdH}_2\text{O} + .5 \text{CH}_3\text{CH}(\text{O}_2)\text{CH}_2\text{OH} + .5 \text{CH}_3\text{COCH}_2\text{OH}$ $+ .5 \text{OH} + \text{H}_2\text{O}$	$3.8\text{E-}12*\text{EXP}(200./\text{temp})$	Müller and Brasseur (1995)
G4311	TrGC	$\text{CH}_3\text{COCH}_3 + \text{OH} \rightarrow 1. \text{OHlossNMHC} + \text{ProdH}_2\text{O} +$ $\text{CH}_3\text{COCH}_2\text{O}_2 + \text{H}_2\text{O}$	$1.33\text{E-}13+3.82\text{E-}11*\text{EXP}(-2000./\text{temp})$	Sander et al. (2011)
G4312	TrGC	$\text{CH}_3\text{COCH}_2\text{O}_2 + \text{HO}_2 \rightarrow 1. \text{HO}_2\text{lossNMHC} +$ $\text{CH}_3\text{COCH}_2\text{O}_2\text{H}$	$8.6\text{E-}13*\text{EXP}(700./\text{temp})$	Tyndall et al. (2001a)
G4313	TrGCN	$\text{CH}_3\text{COCH}_2\text{O}_2 + \text{NO} \rightarrow 1.0 \text{o3prod}_2 + \text{ProdRO}_2 + 1.0$ $\text{ProdO}_3 + \text{CH}_3\text{C}(\text{O})\text{OO} + \text{HCHO} + \text{NO}_2$	$2.9\text{E-}12*\text{EXP}(300./\text{temp})$	Sander et al. (2011)
G4314	TrGC	$\text{CH}_3\text{COCH}_2\text{O}_2 + \text{CH}_3\text{O}_2 \rightarrow .5 \text{MGLYOX} + .5 \text{CH}_3\text{OH} +$ $.3 \text{CH}_3\text{C}(\text{O})\text{OO} + .8 \text{HCHO} + .3 \text{HO}_2 + .2 \text{CH}_3\text{COCH}_2\text{OH}$	$7.5\text{E-}13*\text{EXP}(500./\text{temp})$	Tyndall et al. (2001a)
G4315	TrGC	$\text{CH}_3\text{COCH}_2\text{O}_2\text{H} + \text{OH} \rightarrow 0.3 \text{OHlossNMHC} + .3$ $\text{CH}_3\text{COCH}_2\text{O}_2 + .7 \text{MGLYOX} + .7 \text{OH}$	k_CH300H_OH	see note*
G4316	TrGC	$\text{CH}_3\text{COCH}_2\text{OH} + \text{OH} \rightarrow 1. \text{OHlossHO}_2\text{prodNMHC} +$ $\text{MGLYOX} + \text{HO}_2$	$2.15\text{E-}12*\text{EXP}(305./\text{temp})$	Dillon et al. (2006)
G4317	TrGC	$\text{MGLYOX} + \text{OH} \rightarrow 1. \text{OHlossNMHC} + \text{CH}_3\text{C}(\text{O})\text{OO} +$ CO	$8.4\text{E-}13*\text{EXP}(830./\text{temp})$	Tyndall et al. (1995)
G4320	TrGCN	$\text{iC}_3\text{H}_7\text{ONO}_2 + \text{OH} \rightarrow 1. \text{OHlossNMHC} + \text{CH}_3\text{COCH}_3 +$ NO_2	$6.2\text{E-}13*\text{EXP}(-230./\text{temp})$	Wallington et al. (2018)
G4400	TrGC	$\text{C}_4\text{H}_{10} + \text{OH} \rightarrow 1. \text{OHlossNMHC} + \text{ProdH}_2\text{O} + \text{LC}_4\text{H}_9\text{O}_2$ $+ \text{H}_2\text{O}$	$1.81\text{E-}17*\text{temp}*\text{temp}*\text{EXP}(114./\text{temp})$	Atkinson (2003)
G4401	TrGC	$\text{LC}_4\text{H}_9\text{O}_2 + \text{CH}_3\text{O}_2 \rightarrow .88 \text{MEK} + .68 \text{HCHO} + 1.23 \text{HO}_2$ $+ .12 \text{CH}_3\text{CHO} + .12 \text{C}_2\text{H}_5\text{O}_2 + .18 \text{CH}_3\text{OH}$	$\text{k_PrO}_2\text{_CH3O}_2$	see note*
G4402	TrGC	$\text{LC}_4\text{H}_9\text{O}_2 + \text{HO}_2 \rightarrow 1. \text{HO}_2\text{lossNMHC} + \text{LC}_4\text{H}_9\text{OOH}$	$\text{k_PrO}_2\text{_HO}_2$	see note*
G4403	TrGCN	$\text{LC}_4\text{H}_9\text{O}_2 + \text{NO} \rightarrow 0.56 \text{HO}_2\text{prodNMHCNO}_y + 1.0$ $\text{o3prod}_2 + \text{ProdRO}_2 + 1.0 \text{ProdO}_3 + .84 \text{NO}_2 + .56$ $\text{MEK} + .56 \text{HO}_2 + .28 \text{C}_2\text{H}_5\text{O}_2 + .28 \text{CH}_3\text{CHO} + .16$ LC4H9NO_3	$\text{k_PrO}_2\text{_NO}$	see note*

Table 1: Gas phase reactions (... continued)

#	labels	reaction	rate coefficient	reference
G4404	TrGC	LC ₄ H ₉ OOH + OH → 0.14999998 OHlossNMHC + 0.85 ProdH ₂ O + .15 LC ₄ H ₉ O ₂ + .85 MEK + .85 OH + .85 H ₂ O	k_CH300H_OH	see note*
G4405	TrGC	MVK + O ₃ → 1.0 o3lossro + 1.0 LossO ₃ R + 1.0 LossO ₃ + .45 HCOOH + .9 MGLYOX + .1 CH ₃ C(O)OO + .19 OH + .22 CO + .32 HO ₂	.5*(1.36E-15*EXP(-2112./temp) +7.51E-16*EXP(-1521./temp))	Pöschl et al. (2000)
G4406	TrGC	MVK + OH → 1. OHlossNMHC + MVKO ₂	.5*(4.1E-12*EXP(452./temp) +1.9E-11*EXP(175./temp))	Pöschl et al. (2000)
G4407	TrGC	MVKO ₂ + HO ₂ → 1. HO2lossNMHC + MVKOOH	1.82E-13*EXP(1300./temp)	Pöschl et al. (2000)
G4408	TrGCN	MVKO ₂ + NO → 0.75 HO2prodNMHCNOy + 1.0 o3prodro2 + ProdRO ₂ + 1.0 ProdO ₃ + NO ₂ + .25 CH ₃ C(O)OO + .25 CH ₃ COCH ₂ OH + .75 HCHO + .25 CO + .75 HO ₂ + .5 MGLYOX	2.54E-12*EXP(360./temp)	Pöschl et al. (2000)
G4409	TrGCN	MVKO ₂ + NO ₂ → MPAN	.25*k_3rd(temp, cair, 9.7E-29, 5.6, 9.3E-12, 1.5, 0.6)	Pöschl et al. (2000)
G4410	TrGC	MVKO ₂ + CH ₃ O ₂ → .5 MGLYOX + .375 CH ₃ COCH ₂ OH + .125 CH ₃ C(O)OO + 1.125 HCHO + .875 HO ₂ + .125 CO + .25 CH ₃ OH	2.E-12	von Kuhlmann (2001)
G4411	TrGC	MVKO ₂ + MVKO ₂ → CH ₃ COCH ₂ OH + MGLYOX + .5 CO + .5 HCHO + HO ₂	2.E-12	Pöschl et al. (2000)
G4412	TrGC	MVKOOH + OH → 1. OHlossNMHC + MVKO ₂	3.E-11	Pöschl et al. (2000)
G4413	TrGC	MEK + OH → 1. OHlossNMHC + LMEKO ₂	1.3E-12*EXP(-25./temp)	Wallington et al. (2018)
G4414	TrGC	LMEKO ₂ + HO ₂ → 1. HO2lossNMHC + LMEKOOH	k_PrO2_HO2	see note*
G4415	TrGCN	LMEKO ₂ + NO → 1.0 o3prodro2 + ProdRO ₂ + 1.0 ProdO ₃ + .985 CH ₃ CHO + .985 CH ₃ C(O)OO + .985 NO ₂ + .015 LC ₄ H ₉ NO ₃	k_PrO2_NO	see note*
G4416	TrGC	LMEKOOH + OH → 0.19999999 OHlossNMHC + .8 BIACET + .8 OH + .2 LMEKO ₂	k_CH300H_OH	see note*
G4417	TrGCN	LC ₄ H ₉ NO ₃ + OH → 1. OHlossNMHC + ProdH ₂ O + MEK + NO ₂ + H ₂ O	1.7E-12	Wallington et al. (2018)
G4418	TrGCN	MPAN + OH → 1. OHlossNMHC + CH ₃ COCH ₂ OH + NO ₂	3.2E-11	Orlando et al. (2002)
G4419	TrGCN	MPAN → MVKO ₂ + NO ₂	k_PAN_M	see note*

Table 1: Gas phase reactions (... continued)

#	labels	reaction	rate coefficient	reference
G4500	TrGC	$C_5H_8 + O_3 \rightarrow 1.0 \text{ } \alpha 3 \text{ lossro} + 1.0 \text{ LossO3R} + 1.0 \text{ LossO3} + .28 \text{ HCOOH} + .65 \text{ MVK} + .1 \text{ MVKO2} + .1 \text{ CH}_3\text{C(O)OO} + .14 \text{ CO} + .58 \text{ HCHO} + .09 \text{ H}_2\text{O}_2 + .08 \text{ CH}_3\text{O}_2 + .25 \text{ OH} + .25 \text{ HO}_2$	$7.86E-15 * \text{EXP}(-1913./\text{temp})$	Pöschl et al. (2000)
G4501	TrGC	$C_5H_8 + OH \rightarrow 1. \text{ OHlossNMHC} + \text{ISO2}$	$2.54E-11 * \text{EXP}(410./\text{temp})$	Pöschl et al. (2000)
G4502	TrGCN	$C_5H_8 + NO_3 \rightarrow 1.0 \text{ } \alpha 3 \text{ lossno} + 1.0 \text{ LossO3R} + 1.0 \text{ LossO3} + \text{ISON}$	$3.03E-12 * \text{EXP}(-446./\text{temp})$	Pöschl et al. (2000)
G4503	TrGC	$\text{ISO2} + \text{HO}_2 \rightarrow 1. \text{ HO2lossNMHC} + \text{ISOOH}$	$2.22E-13 * \text{EXP}(1300./\text{temp})$	Boyd et al. (2003)
G4504	TrGCN	$\text{ISO2} + \text{NO} \rightarrow 0.956 \text{ HO2prodNMHCNOy} + 1.0 \text{ } \alpha 3 \text{ prodro2} + \text{ProdRO2} + 1.0 \text{ ProdO3} + .956 \text{ NO}_2 + .956 \text{ MVK} + .956 \text{ HCHO} + .956 \text{ HO}_2 + .044 \text{ ISON}$	$2.54E-12 * \text{EXP}(360./\text{temp})$	Pöschl et al. (2000)
G4505	TrGC	$\text{ISO2} + \text{CH}_3\text{O}_2 \rightarrow .5 \text{ MVK} + 1.25 \text{ HCHO} + \text{HO}_2 + .25 \text{ MGLYOX} + .25 \text{ CH}_3\text{COCH}_2\text{OH} + .25 \text{ CH}_3\text{OH}$	$2.E-12$	von Kuhlmann (2001)
G4506	TrGC	$\text{ISO2} + \text{ISO2} \rightarrow 2 \text{ MVK} + \text{HCHO} + \text{HO}_2$	$2.E-12$	Pöschl et al. (2000)
G4507	TrGC	$\text{ISOOH} + \text{OH} \rightarrow \text{MVK} + \text{OH}$	$1.E-10$	Pöschl et al. (2000)
G4508	TrGCN	$\text{ISON} + \text{OH} \rightarrow 1. \text{ OHlossNMHC} + \text{CH}_3\text{COCH}_2\text{OH} + \text{NACA}$	$1.3E-11$	Pöschl et al. (2000)
G6100	UpStTrGCl	$\text{Cl} + \text{O}_3 \rightarrow \text{ClO} + \text{O}_2$	$2.8E-11 * \text{EXP}(-250./\text{temp})$	Atkinson et al. (2007)
G6101	UpStGCl	$\text{ClO} + \text{O}(^3\text{P}) \rightarrow 2.0 \text{ } \alpha 3 \text{ lossxo} + 2.0 \text{ LossO3Cl} + 2.0 \text{ LossO3} + \text{Cl} + \text{O}_2$	$2.5E-11 * \text{EXP}(110./\text{temp})$	Atkinson et al. (2007)
G6102a	StTrGCl	$\text{ClO} + \text{ClO} \rightarrow 2.0 \text{ } \alpha 3 \text{ lossxo} + 2.0 \text{ LossO3Cl} + 2.0 \text{ LossO3} + \text{Cl}_2 + \text{O}_2$	$1.0E-12 * \text{EXP}(-1590./\text{temp})$	Atkinson et al. (2007)
G6102b	StTrGCl	$\text{ClO} + \text{ClO} \rightarrow 2.0 \text{ } \alpha 3 \text{ lossxo} + 2.0 \text{ LossO3Cl} + 2.0 \text{ LossO3} + 2 \text{ Cl} + \text{O}_2$	$3.0E-11 * \text{EXP}(-2450./\text{temp})$	Atkinson et al. (2007)
G6102c	StTrGCl	$\text{ClO} + \text{ClO} \rightarrow 1.0 \text{ } \alpha 3 \text{ lossxo} + 1.0 \text{ LossO3Cl} + 1.0 \text{ LossO3} + \text{Cl} + \text{OCIO}$	$3.5E-13 * \text{EXP}(-1370./\text{temp})$	Atkinson et al. (2007)
G6102d	StTrGCl	$\text{ClO} + \text{ClO} \rightarrow \text{Cl}_2\text{O}_2$	k ClO ClO	Burkholder et al. (2015)
G6103	StTrGCl	$\text{Cl}_2\text{O}_2 \rightarrow \text{ClO} + \text{ClO}$	k ClO ClO / (2.16E-27 * EXP(8537./temp))	Burkholder et al. (2015)*
G6200	StGCl	$\text{Cl} + \text{H}_2 \rightarrow \text{HCl} + \text{H}$	$3.9E-11 * \text{EXP}(-2310./\text{temp})$	Atkinson et al. (2007)
G6201a	StGCl	$\text{Cl} + \text{HO}_2 \rightarrow \text{HCl} + \text{O}_2$	$4.4E-11 - 7.5E-11 * \text{EXP}(-620./\text{temp})$	Atkinson et al. (2007)
G6201b	StGCl	$\text{Cl} + \text{HO}_2 \rightarrow 1.0 \text{ } \alpha 3 \text{ prodho2} + 1.0 \text{ ProdO3} + \text{ClO} + \text{OH}$	$7.5E-11 * \text{EXP}(-620./\text{temp})$	Atkinson et al. (2007)
G6202	StTrGCl	$\text{Cl} + \text{H}_2\text{O}_2 \rightarrow \text{HCl} + \text{HO}_2$	$1.1E-11 * \text{EXP}(-980./\text{temp})$	Atkinson et al. (2007)
G6203	StGCl	$\text{ClO} + \text{OH} \rightarrow 1. \text{ LossG6203} + 1.0 \text{ } \alpha 3 \text{ lossolh} + 1.0 \text{ LossO3Cl} + 1.0 \text{ LossO3} + .94 \text{ Cl} + .94 \text{ HO}_2 + .06 \text{ HCl} + .06 \text{ O}_2$	$7.3E-12 * \text{EXP}(300./\text{temp})$	Atkinson et al. (2007)

Table 1: Gas phase reactions (... continued)

#	labels	reaction	rate coefficient	reference
G6204	StTrGCl	$\text{ClO} + \text{HO}_2 \rightarrow 1. \text{LossG6204} + \text{HOCl} + \text{O}_2$	$2.2\text{E}-12*\text{EXP}(340./\text{temp})$	Atkinson et al. (2007)*
G6205	StTrGCl	$\text{HCl} + \text{OH} \rightarrow \text{ProdH2O} + \text{Cl} + \text{H}_2\text{O}$	$1.7\text{E}-12*\text{EXP}(-230./\text{temp})$	Atkinson et al. (2007)
G6206	StGCl	$\text{HOCl} + \text{OH} \rightarrow \text{ProdH2O} + \text{ClO} + \text{H}_2\text{O}$	$3.0\text{E}-12*\text{EXP}(-500./\text{temp})$	Burkholder et al. (2015)
G6300	UpStTrGCIN	$\text{ClO} + \text{NO} \rightarrow \text{NO}_2 + \text{Cl}$	$6.2\text{E}-12*\text{EXP}(295./\text{temp})$	Atkinson et al. (2007)
G6301	StTrGCIN	$\text{ClO} + \text{NO}_2 \rightarrow \text{ClNO}_3$	$k_3\text{rd_iupac}(\text{temp}, \text{cair}, 1.6\text{E}-31, 3.4, 7\text{E}-11, 0., 0.4)$	Atkinson et al. (2007)
G6302	TrGCIN	$\text{ClNO}_3 \rightarrow \text{ClO} + \text{NO}_2$	$6.918\text{E}-7*\text{EXP}(-10909./\text{temp})*\text{cair}$	Anderson and Fahey (1990)
G6303	StGCIN	$\text{ClNO}_3 + \text{O}(^3\text{P}) \rightarrow \text{ClO} + \text{NO}_3$	$4.5\text{E}-12*\text{EXP}(-900./\text{temp})$	Atkinson et al. (2007)
G6304	StTrGCIN	$\text{ClNO}_3 + \text{Cl} \rightarrow \text{Cl}_2 + \text{NO}_3$	$6.2\text{E}-12*\text{EXP}(145./\text{temp})$	Atkinson et al. (2007)
G6400	StTrGCl	$\text{Cl} + \text{CH}_4 \rightarrow \text{HCl} + \text{CH}_3\text{O}_2$	$6.6\text{E}-12*\text{EXP}(-1240./\text{temp})$	Atkinson et al. (2006)
G6401	StTrGCl	$\text{Cl} + \text{HCHO} \rightarrow \text{HCl} + \text{CO} + \text{HO}_2$	$8.1\text{E}-11*\text{EXP}(-34./\text{temp})$	Atkinson et al. (2006)
G6402	StTrGCl	$\text{Cl} + \text{CH}_3\text{OOH} \rightarrow \text{HCHO} + \text{HCl} + \text{OH}$	$5.9\text{E}-11$	Atkinson et al. (2006)*
G6403	StTrGCl	$\text{ClO} + \text{CH}_3\text{O}_2 \rightarrow 1.0 \text{LossO3Cl} + 1.0 \text{LossO3}$ $+ \text{HO}_2 + \text{Cl} + \text{HCHO}$	$1.8\text{E}-12*\text{EXP}(-600./\text{temp})$	Burkholder et al. (2015)
G6404	StGCl	$\text{CCl}_4 + \text{O}(^1\text{D}) \rightarrow 4.0 \text{ProdLCl} + \text{LCARBON} + \text{ClO} + 3 \text{Cl}$	$3.3\text{E}-10$	Burkholder et al. (2015)
G6405	StGCl	$\text{CH}_3\text{Cl} + \text{O}(^1\text{D}) \rightarrow 1.0 \text{o3lossxo} + 1.0 \text{ProdLCl} + 1.0$ $\text{LossO3Cl} + 1.0 \text{LossO3} + \text{OH} + \text{Cl}$	$1.65\text{E}-10$	see note*
G6406	StGCl	$\text{CH}_3\text{Cl} + \text{OH} \rightarrow \text{ProdH2O} + 1.0 \text{ProdLCl} + \text{LCARBON}$ $+ \text{H}_2\text{O} + \text{Cl}$	$1.96\text{E}-12*\text{EXP}(-1200./\text{temp})$	Burkholder et al. (2015)
G6407	StGCCl	$\text{CH}_3\text{CCl}_3 + \text{O}(^1\text{D}) \rightarrow 1.0 \text{o3lossxo} + 3.0 \text{ProdLCl} + 1.0$ $\text{LossO3Cl} + 1.0 \text{LossO3} + 2 \text{LCARBON} + \text{OH} + 3 \text{Cl}$	$3.25\text{E}-10$	Burkholder et al. (2015)
G6408	StTrGCCl	$\text{CH}_3\text{CCl}_3 + \text{OH} \rightarrow \text{ProdH2O} + 3.0 \text{ProdLCl} + 2$ $\text{LCARBON} + \text{H}_2\text{O} + 3 \text{Cl}$	$1.64\text{E}-12*\text{EXP}(-1520./\text{temp})$	Burkholder et al. (2015)
G6409	TrGCCl	$\text{Cl} + \text{C}_2\text{H}_4 \rightarrow .6666667 \text{CH}_3\text{CH}(\text{O}_2)\text{CH}_2\text{OH} + \text{HCl}$	$k_3\text{rd_iupac}(\text{temp}, \text{cair}, 1.85\text{E}-29, 3.3, 6.0\text{E}-10, 0.0, 0.4)$	Atkinson et al. (2006)
G6410	TrGCCl	$\text{Cl} + \text{CH}_3\text{CHO} \rightarrow \text{HCl} + \text{CH}_3\text{C}(\text{O})\text{OO}$	$8.0\text{E}-11$	Atkinson et al. (2006)
G6411	TrGCCl	$\text{C}_2\text{H}_2 + \text{Cl} \rightarrow \text{LCARBON} + \text{CH}_3 + \text{HCl}$	$k_3\text{rd_iupac}(\text{temp}, \text{cair}, 6.1\text{E}-30, 3.0, 2.0\text{E}-10, 0., 0.6)$	Atkinson et al. (2006)
G6412	TrGCCl	$\text{C}_2\text{H}_6 + \text{Cl} \rightarrow \text{C}_2\text{H}_5\text{O}_2 + \text{HCl}$	$8.3\text{E}-11*\text{EXP}(-100./\text{temp})$	Atkinson et al. (2006)
G6500	StGCIF	$\text{CF}_2\text{Cl}_2 + \text{O}(^1\text{D}) \rightarrow 2.0 \text{ProdLCl} + \text{LCARBON} + 2$ $\text{LFLUORINE} + \text{ClO} + \text{Cl}$	$1.4\text{E}-10$	Burkholder et al. (2015)
G6501	StGCIF	$\text{CFCl}_3 + \text{O}(^1\text{D}) \rightarrow 3.0 \text{ProdLCl} + \text{LCARBON} + 2.3\text{E}-10$ $\text{LFLUORINE} + \text{ClO} + 2 \text{Cl}$		Burkholder et al. (2015)
G7100	StTrGBr	$\text{Br} + \text{O}_3 \rightarrow \text{BrO} + \text{O}_2$	$1.7\text{E}-11*\text{EXP}(-800./\text{temp})$	Atkinson et al. (2007)

Table 1: Gas phase reactions (... continued)

#	labels	reaction	rate coefficient	reference
G7101	StTGBr	$\text{BrO} + \text{O}(^3\text{P}) \rightarrow 2.0 \text{ } \alpha 3 \text{ lossxo} + 2.0 \text{ LossO3Br} + 2.0 \text{ LossO3}$	$1.9\text{E}-11 * \text{EXP}(230./\text{temp})$	Atkinson et al. (2007)
G7102a	StTGBr	$\text{BrO} + \text{BrO} \rightarrow 2.0 \text{ } \alpha 3 \text{ lossxo} + 2.0 \text{ LossO3Br} + 2.0 \text{ LossO3}$	$2.7\text{E}-12$	Atkinson et al. (2007)
G7102b	StTGBr	$\text{BrO} + \text{BrO} \rightarrow 2.0 \text{ } \alpha 3 \text{ lossxo} + 2.0 \text{ LossO3Br} + 2.0 \text{ LossO3}$	$2.9\text{E}-14 * \text{EXP}(840./\text{temp})$	Atkinson et al. (2007)
G7200	StTGBr	$\text{Br} + \text{HO}_2 \rightarrow \text{HBr} + \text{O}_2$	$7.7\text{E}-12 * \text{EXP}(-450./\text{temp})$	Atkinson et al. (2007)
G7201	StTGBr	$\text{BrO} + \text{HO}_2 \rightarrow 1. \text{ LossG7201} + \text{HOBBr} + \text{O}_2$	$4.5\text{E}-12 * \text{EXP}(500./\text{temp})$	Atkinson et al. (2007)
G7202	StTGBr	$\text{HBr} + \text{OH} \rightarrow \text{ProdH2O} + \text{Br} + \text{H}_2\text{O}$	$6.7\text{E}-12 * \text{EXP}(155./\text{temp})$	Atkinson et al. (2007)
G7203	StGBr	$\text{HOBr} + \text{O}(^3\text{P}) \rightarrow 1.0 \text{ } \alpha 3 \text{ lossxo} + 1.0 \text{ LossO3Br} + 1.0$ $\text{LossO3} + \text{OH} + \text{BrO}$	$1.2\text{E}-10 * \text{EXP}(-430./\text{temp})$	Atkinson et al. (2007)
G7204	StTGBr	$\text{Br}_2 + \text{OH} \rightarrow 1.0 \text{ } \alpha 3 \text{ prodoh} + 1.0 \text{ ProdO3} + \text{HOBBr} + \text{Br}$	$2.0\text{E}-11 * \text{EXP}(240./\text{temp})$	Atkinson et al. (2007)
G7300	TtGBrN	$\text{Br} + \text{BrNO}_3 \rightarrow \text{Br}_2 + \text{NO}_3$	$4.9\text{E}-11$	Orlando and Tyndall (1996)
G7301	StTGBrN	$\text{BrO} + \text{NO} \rightarrow \text{Br} + \text{NO}_2$	$8.7\text{E}-12 * \text{EXP}(260./\text{temp})$	Atkinson et al. (2007)
G7302	StTGBrN	$\text{BrO} + \text{NO}_2 \rightarrow \text{BrNO}_3$	$k_{\text{BrO_NO2}}$	Atkinson et al. (2007)*
G7303	TtGBrN	$\text{BrNO}_3 \rightarrow \text{BrO} + \text{NO}_2$	$k_{\text{BrO_NO2}} / (5.44\text{E}-9 * \text{EXP}(14192./\text{temp}) * 1. \text{E6} * \text{R}_{\text{gas}} * \text{temp} / (\text{atm}2\text{Pa} * \text{N}_A))$	Orlando and Tyndall (1996), Atkinson et al. (2007)*
G7400	StTGBr	$\text{Br} + \text{HCHO} \rightarrow \text{HBr} + \text{CO} + \text{HO}_2$	$7.7\text{E}-12 * \text{EXP}(-580./\text{temp})$	Atkinson et al. (2006)
G7401	TtGBr	$\text{Br} + \text{CH}_3\text{OOH} \rightarrow \text{CH}_3\text{O}_2 + \text{HBr}$	$2.6\text{E}-12 * \text{EXP}(-1600./\text{temp})$	Kondo and Benson (1984)
G7402a	TtGBr	$\text{BrO} + \text{CH}_3\text{O}_2 \rightarrow \text{HOBBr} + \text{HCHO}$	$f_{\text{BrO_CH3O2}} * 5.7\text{E}-12$	Aranda et al. (1997)
G7402b	TtGBr	$\text{BrO} + \text{CH}_3\text{O}_2 \rightarrow 1.0 \text{ } \alpha 3 \text{ lossxo} + 1.0 \text{ LossO3Br} + 1.0 \text{ LossO3}$ $+ \text{Br} + \text{HCHO} + \text{HO}_2$	$(1.-f_{\text{BrO_CH3O2}}) * 5.7\text{E}-12$	Aranda et al. (1997)
G7403	StTGBr	$\text{CH}_3\text{Br} + \text{OH} \rightarrow \text{ProdH2O} + 1.0 \text{ ProdLBr} + \text{LCARBON}$	$1.42\text{E}-12 * \text{EXP}(-1150./\text{temp})$	Burkholder et al. (2015)
G7404	TtGBrC	$\text{Br} + \text{C}_2\text{H}_4 \rightarrow .6666667 \text{ CH}_3\text{CH}(\text{O}_2)\text{CH}_2\text{OH} + \text{HBr}$	$2.8\text{E}-13 * \text{EXP}(224./\text{temp}) / (1. + 1.13\text{E}24 * \text{EXP}(-3200./\text{temp}) / C(\text{ind_O2}))$	Atkinson et al. (2006)
G7405	TtGBrC	$\text{Br} + \text{CH}_3\text{CHO} \rightarrow \text{HBr} + \text{CH}_3\text{C}(\text{O})\text{OO}$	$1.8\text{e}-11 * \text{EXP}(-460./\text{temp})$	Atkinson et al. (2006)
G7406	TtGBrC	$\text{Br} + \text{C}_2\text{H}_2 \rightarrow \text{LCARBON} + \text{CH}_3\text{O}_2 + \text{HBr}$	$6.35\text{e}-15 * \text{EXP}(440./\text{temp})$	Atkinson et al. (2006)
G7407	TtGBr	$\text{CHBr}_3 + \text{OH} \rightarrow \text{ProdH2O} + 3.0 \text{ ProdSBr} + \text{LCARBON}$ $+ \text{H}_2\text{O} + 3 \text{ Br}$	$9.0\text{E}-13 * \text{EXP}(-360./\text{temp})$	Burkholder et al. (2015)*
G7408	TtGBr	$\text{CH}_2\text{Br}_2 + \text{OH} \rightarrow \text{ProdH2O} + 2.0 \text{ ProdSBr} + \text{LCARBON}$ $+ \text{H}_2\text{O} + 2 \text{ Br}$	$2.0\text{E}-12 * \text{EXP}(-840./\text{temp})$	Burkholder et al. (2015)*
G7600	TtGBrCl	$\text{Br} + \text{BrCl} \rightarrow \text{Br}_2 + \text{Cl}$	$3.32\text{E}-15$	Manion et al. (2015)

Table 1: Gas phase reactions (... continued)

#	labels	reaction	rate coefficient	reference
G7601	TrGBrCl	Br + Cl ₂ → BrCl + Cl	1.10E-15	Dolson and Leone (1987)
G7602	TrGBrCl	Br ₂ + Cl → BrCl + Br	2.3E-10*EXP(135./temp)	Bedjanian et al. (1998)
G7603a	StTrGBrCl	BrO + ClO → 1.0 o3lossxo + 0.5 LossO3Br + 0.5 LossO3Cl + 1.0 LossO3 + Br + OClO	1.6E-12*EXP(430./temp)	Atkinson et al. (2007)
G7603b	StTrGBrCl	BrO + ClO → 2.0 o3lossxo + 1.0 LossO3Br + 1.0 LossO3Cl + 2.0 LossO3 + Br + Cl + O ₂	2.9E-12*EXP(220./temp)	Atkinson et al. (2007)
G7603c	StTrGBrCl	BrO + ClO → 2.0 o3lossxo + 1.0 LossO3Br + 1.0 LossO3Cl + 2.0 LossO3 + BrCl + O ₂	5.8E-13*EXP(170./temp)	Atkinson et al. (2007)
G7604	TrGBrCl	BrCl + Cl → Br + Cl ₂	1.45E-11	Clyne and Cruse (1972)
G7605	TrGBrCl	CHCl ₂ Br + OH → ProdH2O + 1.0 ProdSBr + 2.0 ProdSCL + LCARBON + 2 Cl + H ₂ O + Br	2.0E-12*EXP(-840./temp)	see note*
G7606	TrGBrCl	CHClBr ₂ + OH → ProdH2O + 2.0 ProdSBr + 1.0 ProdSCL + LCARBON + Cl + H ₂ O + 2 Br	2.0E-12*EXP(-840./temp)	see note*
G7607	TrGBrCl	CH ₂ ClBr + OH → ProdH2O + 1.0 ProdSBr + 1.0 ProdSCL + LCARBON + Cl + H ₂ O + Br	2.1E-12*EXP(-880./temp)	Burkholder et al. (2015)*
G9200a	StTrGS	SO ₂ + OH → 1.0 o3prodoh + 1.0 ProdO3 + SO ₃ + HO ₂	k_3rd(temp, cair, 3.3E-31, 4.3, 1.6E-12, 0., 0.6)	Sander et al. (2011)
G9400a	TrGCS	DMS + OH → 1. OHlossNMHC + 1.0 o3prodoh + 1.0	1.13E-11*EXP(-253./temp)	Atkinson et al. (2004)*
G9400b	TrGCS	ProdO3 + CH ₃ SO ₂ + HCHO DMS + OH → 1. OHlossNMHC + 1.0 o3prodoh + 1.0 ProdO3 + DMSO + HO ₂	k_DMS_OH	Atkinson et al. (2004)*
G9401	TrGCNS	DMS + NO ₃ → CH ₃ SO ₂ + HNO ₃ + HCHO	1.9E-13*EXP(520./temp)	Atkinson et al. (2004)
G9402	TrGCS	DMSO + OH → 1. OHlossNMHC + 0.40 o3prodoh + 0.40 ProdO3 + .6 SO ₂ + HCHO + .6 CH ₃ O ₂ + .4 HO ₂ + .4 CH ₃ SO ₃ H	1.E-10	Hynes and Wine (1996)
G9403	TrGS	CH ₃ SO ₂ → SO ₂ + CH ₃ O ₂	1.8E13*EXP(-8661./temp)	Barone et al. (1995)
G9404	TrGS	CH ₃ SO ₂ + O ₃ → CH ₃ SO ₃	3.E-13	Barone et al. (1995)
G9405	TrGS	CH ₃ SO ₃ + HO ₂ → CH ₃ SO ₃ H	5.E-11	Barone et al. (1995)
G9600	TrGCCIS	DMS + Cl → 1.0 o3produntagged + 1.0 ProdO3 + CH ₃ SO ₂ + HCl + HCHO	3.3E-10	Atkinson et al. (2004)
G9700	TrGBrCS	DMS + Br → 1.0 o3produntagged + 1.0 ProdO3 + CH ₃ SO ₂ + HBr + HCHO	9.E-11*EXP(-2386./temp)	Jefferson et al. (1994)
G9701	TrGBrCS	DMS + BrO → DMSO + Br	4.4E-13	Ingham et al. (1999)
G01Diag	StTrG	O ₃ (s) → LO ₃ (s)	k_03s	Roelofs and Lelieveld (1997)

Table 1: Gas phase reactions (... continued)

#	labels	reaction	rate coefficient	reference
G42085abs	TrGCN	$\text{CH}_3\text{CN} + \text{OH} \rightarrow \text{OH}$	$8.1\text{E}-13 \cdot \text{EXP}(-1080./\text{temp})$	Atkinson et al. (2006), Tyndall et al. (2001b)
G42086bcS	TrGCN	$\text{CH}_3\text{CN} + \text{O}(^1\text{D}) \rightarrow \text{O}(^1\text{D})$	$2.54\text{E}-10 \cdot \text{EXP}(-24./\text{temp})$ $\cdot (1.-0.0269 \cdot \text{EXP}(137./\text{temp}))$	Strekowski et al. (2010)
G6416S	TrGCCIN	$\text{Cl} + \text{CH}_3\text{CN} \rightarrow \text{Cl}$	$1.6\text{E}-11 \cdot \text{EXP}(-2104./\text{temp})$	Tyndall et al. (1996), Tyndall et al. (2001b), Sander et al. (2019)
G6500dc01	StGClF	$\text{CHF}_2\text{Cl} + \text{O}(^1\text{D}) \rightarrow 0.19 \text{ } \alpha 3\text{lossxo} + 0.75 \text{ ProdLCl} + 0.19 \text{ LossO}_3 + 0.19 \text{ LossO}_3 + 0.56 \text{ ClO} + 0.05 \text{ OH} + 0.25 \text{ O}(^3\text{P}) + 0.25 \text{ CHF}_2\text{Cl} + 0.75 \text{ LcARBON} + 0.19 \text{ Cl} + 1.5 \text{ LFLUORINE}$	$1.02\text{E}-10$	Burkholder et al. (2019)
G6500dc02	StG	$\text{CHF}_2\text{Cl} + \text{OH} \rightarrow \text{ProdH}_2\text{O} + 1.0 \text{ ProdLCl} + \text{LcARBON} + \text{H}_2\text{O} + 2 \text{ LFLUORINE} + \text{Cl}$	$9.2\text{e}-13 \cdot \text{EXP}(-1560./\text{temp})$	Burkholder et al. (2019)
G6500dc03	StG	$\text{CHF}_2\text{Cl} + \text{Cl} \rightarrow 1.0 \text{ ProdLCl} + \text{HCl} + \text{LcARBON} + 2 \text{ LFLUORINE} + \text{Cl}$	$5.9\text{e}-12 \cdot \text{EXP}(-2430./\text{temp})$	Burkholder et al. (2019)
G5300dc01	StGClF	$\text{CH}_2\text{FCF}_3 + \text{O}(^1\text{D}) \rightarrow 0.35 \text{ } \alpha 3\text{lossxo} + 0.35 \text{ LossO}_3 + 0.35 \text{ LossO}_3 + 0.65 \text{ O}(^3\text{P}) + 0.65 \text{ CH}_2\text{FCF}_3 + 0.24 \text{ OH} + 0.70 \text{ LcARBON} + 1.4 \text{ LFLUORINE}$	$4.9\text{E}-11$	Burkholder et al. (2019)*
G5300dc02	StG	$\text{CH}_2\text{FCF}_3 + \text{OH} \rightarrow \text{ProdH}_2\text{O} + 2 \text{ LcARBON} + \text{H}_2\text{O} + 4 \text{ LFLUORINE}$	$1.03\text{e}-12 \cdot \text{EXP}(-1620./\text{temp})$	Burkholder et al. (2019)
G5300dc03	StG	$\text{CH}_2\text{FCF}_3 + \text{Cl} \rightarrow \text{HCl} + 2 \text{ LcARBON} + 4 \text{ LFLUORINE}$	$2.1\text{e}-12 \cdot \text{EXP}(-2160./\text{temp})$	Burkholder et al. (2019)
G6500dc04	StG	$\text{CF}_2\text{ClCFCl}_2 + \text{O}(^1\text{D}) \rightarrow 0.10 \text{ } \alpha 3\text{lossxo} + 2.7 \text{ ProdLCl} + 0.10 \text{ LossO}_3 + 0.10 \text{ LossO}_3 + 0.1 \text{ O}(^3\text{P}) + 0.1 \text{ CF}_2\text{ClCFCl}_2 + 0.8 \text{ ClO} + 1.8 \text{ LcARBON} + 1.9 \text{ Cl} + 2.7 \text{ LFLUORINE}$	$2.32\text{e}-10$	Burkholder et al. (2019)
G6400dc01	StG	$\text{CH}_2\text{Cl}_2 + \text{OH} \rightarrow \text{ProdH}_2\text{O} + 2.0 \text{ ProdScl} + \text{LcARBON} + \text{H}_2\text{O} + 2 \text{ Cl}$	$1.92\text{e}-12 \cdot \text{EXP}(-880./\text{temp})$	Burkholder et al. (2019)
G6400dc02	StG	$\text{CH}_2\text{Cl}_2 + \text{Cl} \rightarrow 2.0 \text{ ProdScl} + \text{LcARBON} + \text{HCl} + 2 \text{ Cl}$	$7.4\text{e}-12 \cdot \text{EXP}(-910./\text{temp})$	Burkholder et al. (2019)
G5300dc04	StG	$\text{CHF}_3 + \text{O}(^1\text{D}) \rightarrow 0.25 \text{ } \alpha 3\text{lossxo} + 0.25 \text{ LossO}_3 + 0.25 \text{ LossO}_3 + 0.75 \text{ O}(^3\text{P}) + 0.75 \text{ CHF}_3 + 0.25 \text{ LcARBON} + 0.75 \text{ LFLUORINE}$	$8.7\text{e}-12 \cdot \text{EXP}(30./\text{temp})$	Burkholder et al. (2019)*
G5300dc05	StG	$\text{CHF}_3 + \text{OH} \rightarrow \text{ProdH}_2\text{O} + \text{LcARBON} + \text{H}_2\text{O} + 3 \text{ LFLUORINE}$	$6.1\text{e}-13 \cdot \text{EXP}(-2260./\text{temp})$	Burkholder et al. (2019)

Table 1: Gas phase reactions (... continued)

#	labels	reaction	rate coefficient	reference
G6500dc05	StG	$\text{CH}_3\text{CFCl}_2 + \text{O}(^1\text{D}) \rightarrow 0.69 \text{ o3lossxo} + 1.38 \text{ ProdLCI} + 0.69 \text{ LossO3O} + 0.69 \text{ LossO3} + 0.31 \text{ O}(^3\text{P}) + 0.31 \text{ CH}_3\text{CFCl}_2 + 1.38 \text{ LCARBON} + 1.38 \text{ Cl} + 1 \text{ LFLUORINE}$	2.6E-10	Burkholder et al. (2019)*
G6500dc06	StG	$\text{CH}_3\text{CFCl}_2 + \text{OH} \rightarrow \text{ProdH2O} + 2.0 \text{ ProdLCI} + \text{H}_2\text{O} + 2 \text{ LCARBON} + 1 \text{ LFLUORINE} + 2 \text{ Cl}$	1.25e-12*EXP(-1600./temp)	Burkholder et al. (2019)
G6500dc07	StG	$\text{CH}_3\text{CFCl}_2 + \text{Cl} \rightarrow 2.0 \text{ ProdLCI} + \text{HCl} + 2 \text{ LCARBON} + 1 \text{ LFLUORINE} + 2 \text{ Cl}$	3.5e-12*EXP(-2200./temp)	Burkholder et al. (2019)
G6500dc08	StG	$\text{CF}_2\text{ClCF}_2\text{Cl} + \text{O}(^1\text{D}) \rightarrow 0.90 \text{ o3lossxo} + 1.8 \text{ ProdLCI} + 0.90 \text{ LossO3O} + 0.90 \text{ LossO3} + 0.10 \text{ O}(^3\text{P}) + 0.10 \text{ CF}_2\text{ClCF}_2\text{Cl} + 1.80 \text{ LCARBON} + 1.80 \text{ Cl} + 3.6 \text{ LFLUORINE}$	1.3E-10 *EXP(25./temp)	Burkholder et al. (2019)
G5300dc06	StG	$\text{CHF}_2\text{CF}_3 + \text{O}(^1\text{D}) \rightarrow 0.75 \text{ o3lossxo} + 0.75 \text{ LossO3O} + 0.75 \text{ LossO3} + 0.25 \text{ CHF}_2\text{CF}_3 + 0.6 \text{ OH} + 1.50 \text{ LCARBON} + 3.5 \text{ LFLUORINE}$	9.5E-12 *EXP(25./temp)	Burkholder et al. (2019)*
G5300dc07	StG	$\text{CHF}_2\text{CF}_3 + \text{OH} \rightarrow \text{ProdH2O} + \text{H}_2\text{O} + 2 \text{ LCARBON} + 5 \text{ LFLUORINE}$	5.16e-13*EXP(-1670./temp)	Burkholder et al. (2019)
G6500dc09	StG	$\text{CHF}_2\text{CF}_3 + \text{Cl} \rightarrow \text{HCl} + 2 \text{ LCARBON} + 5 \text{ LFLUORINE}$	1.85e-12*EXP(-2600./temp)	Burkholder et al. (2019)
G5300dc08	StG	$\text{CH}_3\text{CF}_3 + \text{O}(^1\text{D}) \rightarrow 0.65 \text{ o3lossxo} + 0.65 \text{ LossO3O} + 0.65 \text{ LossO3} + 0.35 \text{ O}(^3\text{P}) + 0.35 \text{ CH}_3\text{CF}_3 + 0.38 \text{ OH} + 1.3 \text{ LCARBON} + 1.95 \text{ LFLUORINE}$	5.6e-11*EXP(20./temp)	Burkholder et al. (2019)*
G5300dc09	StG	$\text{CH}_3\text{CF}_3 + \text{OH} \rightarrow \text{ProdH2O} + \text{H}_2\text{O} + 2 \text{ LCARBON} + 3 \text{ LFLUORINE}$	1.07e-12*EXP(-2000./temp)	Burkholder et al. (2019)
G6500dc10	StG	$\text{CH}_3\text{CF}_3 + \text{Cl} \rightarrow \text{HCl} + 2 \text{ LCARBON} + 3 \text{ LFLUORINE}$	1.64e-11*EXP(-3900./temp)	Burkholder et al. (2019)
G6400dc03	StG	$\text{CHCl}_3 + \text{OH} \rightarrow \text{ProdH2O} + 3.0 \text{ ProdSCl} + \text{H}_2\text{O} + \text{LCARBON} + 3 \text{ Cl}$	2.2e-12*EXP(-920./temp)	Burkholder et al. (2019)
G6400dc04	StG	$\text{CHCl}_3 + \text{Cl} \rightarrow 3.0 \text{ ProdSCl} + \text{HCl} + \text{LCARBON} + 3 \text{ Cl}$	3.3e-12*EXP(-990./temp)	Burkholder et al. (2019)
G6500dc11	StG	$\text{CF}_3\text{CF}_2\text{Cl} + \text{O}(^1\text{D}) \rightarrow 0.86 \text{ o3lossxo} + 0.86 \text{ ProdLCI} + 0.86 \text{ LossO3O} + 0.86 \text{ LossO3} + 0.14 \text{ O}(^3\text{P}) + 0.14 \text{ CF}_3\text{CF}_2\text{Cl} + 1.72 \text{ LCARBON} + 4.3 \text{ LFLUORINE} + 0.86 \text{ Cl}$	5.4e-11*EXP(30./temp)	Burkholder et al. (2019)
G5300dc10	StG	$\text{CH}_2\text{F}_2 + \text{O}(^1\text{D}) \rightarrow 0.30 \text{ o3lossxo} + 0.30 \text{ LossO3O} + 0.30 \text{ LossO3} + 0.7 \text{ O}(^3\text{P}) + 0.7 \text{ CH}_2\text{F}_2 + 0.3 \text{ LCARBON} + 0.6 \text{ LFLUORINE}$	5.1e-11	Burkholder et al. (2019)
G5300dc11	StG	$\text{CH}_2\text{F}_2 + \text{OH} \rightarrow \text{ProdH2O} + \text{H}_2\text{O} + \text{LCARBON} + 2 \text{ LFLUORINE}$	1.7e-12*EXP(-1500./temp)	Burkholder et al. (2019)

Table 1: Gas phase reactions (... continued)

#	labels	reaction	rate coefficient	reference
G5300dc12	StG	$\text{CH}_3\text{CHF}_2 + \text{O}(^1\text{D}) \rightarrow 0.55 \text{ o3lossxo} + 0.55 \text{ LossO3O} + 0.55 \text{ LossO3} + 0.45 \text{ O}(^3\text{P}) + 0.45 \text{ CH}_3\text{CHF}_2 + 0.15 \text{ OH} + 1.1 \text{ LFCARBON} + 1.1 \text{ LFLUORINE}$	$1.75\text{e-}10$	Burkholder et al. (2019)
G5300dc13	StG	$\text{CH}_3\text{CHF}_2 + \text{OH} \rightarrow 2 \text{ LFCARBON} + 2 \text{ LFLUORINE}$	$8.7\text{e-}13*\text{EXP}(-975./\text{temp})$	Burkholder et al. (2019)
G6500dc12	StG	$\text{CH}_3\text{CHF}_2 + \text{Cl} \rightarrow \text{HCl} + 2 \text{ LFCARBON} + 2 \text{ LFLUORINE}$	$6.5\text{e-}12*\text{EXP}(-970./\text{temp})$	Burkholder et al. (2019)
G6500pg01	StG	$\text{CH}_3\text{CF}_2\text{Cl} + \text{O}(^1\text{D}) \rightarrow 0.65 \text{ o3lossxo} + 0.65 \text{ ProdLCI} + 0.65 \text{ LossO3O} + 0.65 \text{ LossO3} + 0.35 \text{ O}(^3\text{P}) + 0.35 \text{ CH}_3\text{CF}_2\text{Cl} + 1.3 \text{ LFCARBON} + 0.65 \text{ Cl} + 1.3 \text{ LFLUORINE}$	$2.0\text{e-}10$	Burkholder et al. (2019)
G6500pg02	StG	$\text{CH}_3\text{CF}_2\text{Cl} + \text{OH} \rightarrow \text{ProdH2O} + 1.0 \text{ ProdLCI} + \text{H}_2\text{O} + 2 \text{ LFCARBON} + 2 \text{ LFLUORINE} + \text{Cl}$	$1.3\text{e-}12*\text{EXP}(-1770./\text{temp})$	Burkholder et al. (2019)
G6500pg03	StG	$\text{CH}_3\text{CF}_2\text{Cl} + \text{Cl} \rightarrow 1.0 \text{ ProdLCI} + \text{HCl} + 2 \text{ LFCARBON} + 2 \text{ LFLUORINE} + \text{Cl}$	$1.35\text{e-}12*\text{EXP}(2400./\text{temp})$	Burkholder et al. (2019)
G7600pg01	StG	$\text{CBrF}_2\text{CBrF}_2 + \text{O}(^1\text{D}) \rightarrow 0.75 \text{ o3lossxo} + 1.5 \text{ ProdLBr} + 0.75 \text{ LossO3O} + 0.75 \text{ LossO3} + 0.25 \text{ O}(^3\text{P}) + 0.25 \text{ CBrF}_2\text{CBrF}_2 + 1.5 \text{ LFCARBON} + 1.5 \text{ Br} + 3.0 \text{ LFLUORINE}$	$1.6\text{e-}10$	Burkholder et al. (2019)
G9100	TrStGS	$\text{SO} + \text{O}_2 \rightarrow 2.0 \text{ o3produntagged} + 2.0 \text{ ProdO3} + \text{SO}_2 + \text{O}(^3\text{P})$	$1.25\text{e-}13*\text{exp}(-2190./\text{temp})$	Sander et al. (2011)
G9101	TrStGS	$\text{SO} + \text{O}_3 \rightarrow \text{SO}_2 + \text{O}_2$	$3.4\text{e-}12*\text{exp}(-1100./\text{temp})$	Sander et al. (2011)
G9102	TrStGS	$\text{S} + \text{O}_2 \rightarrow 1.0 \text{ o3produntagged} + 1.0 \text{ ProdO3} + \text{SO} + \text{O}(^3\text{P})$	$2.3\text{e-}12$	Sander et al. (2011)
G9201	TrStGS	$\text{SH} + \text{O}_2 \rightarrow \text{OH} + \text{SO}$	$4 \text{ e-}19$	Sander et al. (2011)
G9202	TrStGS	$\text{SO}_3 + \text{H}_2\text{O} \rightarrow \text{LossH2O} + \text{H}_2\text{SO}_4$	$8.5\text{e-}41*\text{exp}(6540./\text{temp})*\text{C}(\text{ind_H2O})$	Sander et al. (2003)
G9406	TrStGS	$\text{OCS} + \text{OH} \rightarrow \text{SH} + \text{CO}_2$	$1.1\text{e-}13*\text{exp}(-1200./\text{temp})$	Sander et al. (2011)
G9407	TrStGS	$\text{OCS} + \text{O}(^3\text{P}) \rightarrow 1.0 \text{ o3lossxo} + 1.0 \text{ LossO3Su} + 1.0 \text{ LossO3} + \text{CO} + \text{SO}$	$2.1\text{e-}11*\text{exp}(-2200./\text{temp})$	Sander et al. (2011)

General notes

Three-body reactions

Rate coefficients for three-body reactions are defined via the function **k_3rd**(T , M , k_0^{300} , n , k_{inf}^{300} , m , f_c). In the code, the temperature T is called **temp** and the concentration of “air molecules” M is called **cair**. Using the auxiliary variables $k_0(T)$, $k_{\text{inf}}(T)$, and k_{ratio} , **k_3rd** is defined as:

$$k_0(T) = k_0^{300} \times \left(\frac{300\text{K}}{T} \right)^n \quad (1)$$

$$k_{\text{inf}}(T) = k_{\text{inf}}^{300} \times \left(\frac{300\text{K}}{T} \right)^m \quad (2)$$

$$k_{\text{ratio}} = \frac{k_0(T)M}{k_{\text{inf}}(T)} \quad (3)$$

$$\mathbf{k_3rd} = \frac{k_0(T)M}{1 + k_{\text{ratio}}} \times f_c^{\left(\frac{1}{1 + (\log_{10}(k_{\text{ratio}}))^2} \right)} \quad (4)$$

A similar function, called **k_3rd_iupac** here, is used by Wallington et al. (2018) for three-body reactions. It has the same function parameters as **k_3rd** and it is defined as:

$$k_0(T) = k_0^{300} \times \left(\frac{300\text{K}}{T} \right)^n \quad (5)$$

$$k_{\text{inf}}(T) = k_{\text{inf}}^{300} \times \left(\frac{300\text{K}}{T} \right)^m \quad (6)$$

$$k_{\text{ratio}} = \frac{k_0(T)M}{k_{\text{inf}}(T)} \quad (7)$$

$$N = 0.75 - 1.27 \times \log_{10}(f_c) \quad (8)$$

$$\mathbf{k_3rd_iupac} = \frac{k_0(T)M}{1 + k_{\text{ratio}}} \times f_c^{\left(\frac{1}{1 + (\log_{10}(k_{\text{ratio}})/N)^2} \right)} \quad (9)$$

Structure-Activity Relationships (SAR)

Some unmeasured rate coefficients are estimated with structure-activity relationships, using the following parameters and substituent factors:

k for H-abstraction by OH in $\text{cm}^3 \text{s}^{-1}$	
k_p	$4.49 \times 10^{-18} \times (T/\text{K})^2 \exp(-320 \text{ K}/T)$
k_s	$4.50 \times 10^{-18} \times (T/\text{K})^2 \exp(253 \text{ K}/T)$
k_t	$2.12 \times 10^{-18} \times (T/\text{K})^2 \exp(696 \text{ K}/T)$
k_ROHRO	$2.1 \times 10^{-18} \times (T/\text{K})^2 \exp(-85 \text{ K}/T)$
k_CO2H	$0.7 \times k_{\text{CH}_3\text{CO}_2\text{H}+\text{OH}}$
k_ROOHHRO	$0.6 \times k_{\text{CH}_3\text{OOH}+\text{OH}}$
f_alk	1.23
f_sOH	3.44
f_tOH	2.68
f_sOOH	8.
f_tOOH	8.
f_ONO2	0.04
f_CH2ONO2	0.20
f_cpan	0.25
f_allyl	3.6
f_CHO	0.55
f_CO2H	1.67
f_CO	0.73
f_O	8.15
f_pCH2OH	1.29
f_tCH2OH	0.53

16

k for OH-addition to double bonds in $\text{cm}^3 \text{s}^{-1}$	
k_adp	$4.5 \times 10^{-12} \times (T/300 \text{ K})^{-0.85}$
k_ads	$1/4 \times (1.1 \times 10^{-11} \times \exp(485 \text{ K}/T) + 1.0 \times 10^{-11} \times \exp(553 \text{ K}/T))$
k_adt	$1.922 \times 10^{-11} \times \exp(450 \text{ K}/T) - k_{\text{ads}}$
k_adsecprim	3.0×10^{-11}
k_adtertprim	5.7×10^{-11}
a_PAN	0.56
a_CHO	0.31
a_COCH3	0.76
a_CH2OH	1.7
a_CH2OOH	1.7
a_COH	2.2
a_COOH	2.2
a_CO2H	0.25
a_CH2ONO2	0.64

RO₂ self and cross reactions

The self and cross reactions of organic peroxy radicals are treated according to the permutation reaction formalism as implemented in the MCM (Rickard and Pascoe, 2009), as described by Jenkin et al. (1997). Every organic peroxy radical reacts in a pseudo-first-order reaction with a rate constant that is expressed as $k^{\text{1st}} = 2 \times \sqrt{k_{\text{self}} \times k_{\text{CH3O2}} \times [\text{RO}_2]}$ where $k_{\text{self}} = \text{second-order rate coefficient of the self reaction of the organic peroxy radical}$, **k_CH3O2** = second-order rate coefficient of the self reaction of CH_3O_2 , and $[\text{RO}_2]$ = sum of the concentrations of all organic peroxy radicals.

Table 2: Photolysis reactions

#	labels	reaction	rate coefficient	reference
J (gas)				
J1000a	UpStTrGJ	$O_2 + h\nu \rightarrow 1.0 \text{ } \alpha^3\text{prodO}_2 + 2.0 \text{ ProdO}_3 + O(^3P) + O(^3P)$	jx(ip_02)	Sander et al. (2014)
J1001a	UpStTrGJ	$O_3 + h\nu \rightarrow O(^1D) + O_2$	jx(ip_01D)	Sander et al. (2014)
J1001b	UpStTrGJ	$O_3 + h\nu \rightarrow O(^3P) + O_2$	jx(ip_03P)	Sander et al. (2014)
J2100a	UpStGJ	$H_2O + h\nu \rightarrow \text{LossH}_2O + H + OH$	jx(ip_H2O)	Sander et al. (2014)
J2101	UpStTrGJ	$H_2O_2 + h\nu \rightarrow 2 \text{ OH}$	jx(ip_H2O2)	Sander et al. (2014)
J3100	UpStGJN	$N_2O + h\nu \rightarrow 1.0 \text{ } \alpha^3\text{prodnoy} + 1.0 \text{ ProdO}_3 + O(^1D) + N_2$	jx(ip_N2O)	Sander et al. (2014)
J3101	UpStTrGJN	$NO_2 + h\nu \rightarrow NO + O(^3P)$	jx(ip_N02)	Sander et al. (2014)
J3102a	UpStGJN	$NO + h\nu \rightarrow 1.0 \text{ } \alpha^3\text{prodnoy} + 1.0 \text{ ProdO}_3 + N + O(^3P)$	jx(ip_N0)	Sander et al. (2014)
J3103a	UpStTrGJN	$NO_3 + h\nu \rightarrow NO_2 + O(^3P)$	jx(ip_N020)	Sander et al. (2014)
J3103b	UpStTrGJN	$NO_3 + h\nu \rightarrow 2.0 \text{ } \alpha^3\text{lossno} + 2.0 \text{ LossO}_3N + NO + O_2$	jx(ip_N002)	Sander et al. (2014)
J3104	StTrGJN	$N_2O_5 + h\nu \rightarrow NO_2 + NO_3$	jx(ip_N205)	Sander et al. (2014)
J3200	TrGJN	$HONO + h\nu \rightarrow 1. \text{ LossJ3200} + NO + OH$	jx(ip_H0N0)	Sander et al. (2014)
J3201	StTrGJN	$HNO_3 + h\nu \rightarrow 1. \text{ LossJ3201} + NO_2 + OH$	jx(ip_HN03)	Sander et al. (2014)
J3202	StTrGJN	$HNO_4 + h\nu \rightarrow 0.333 \text{ } \alpha^3\text{prodnoy} + 0.333 \text{ ProdO}_3 + .667 \text{ NO}_2 + .667 \text{ HO}_2 + .333 \text{ NO}_3 + .333 \text{ OH}$	jx(ip_HN04)	Sander et al. (2014)
J4100	StTrGJ	$CH_3OOH + h\nu \rightarrow HCHO + OH + HO_2$	jx(ip_CH300H)	Sander et al. (2014)
J4101a	StTrGJ	$HCHO + h\nu \rightarrow H_2 + CO$	jx(ip_COH2)	Sander et al. (2014)
J4101b	StTrGJ	$HCHO + h\nu \rightarrow 1. \text{ HO2prodNMHCphoto} + 1. \text{ LossJ4101b} + H + CO + HO_2$	jx(ip_CH0H)	Sander et al. (2014)
J4102	StGJ	$CO_2 + h\nu \rightarrow 1.0 \text{ } \alpha^3\text{produntagged} + 1.0 \text{ ProdO}_3 + CO + O(^3P)$	jx(ip_CO2)	Sander et al. (2014)
J4103	StGJ	$CH_4 + h\nu \rightarrow 1.155 \text{ ProdH}_2O + CO + 0.31 \text{ H} + 0.69 \text{ H}_2 + 1.155 \text{ H}_2O$	jx(ip_CH4)	Sander et al. (2014)
J4200	TrGJC	$C_2H_5OOH + h\nu \rightarrow CH_3CHO + HO_2 + OH$	jx(ip_CH300H)	von Kuhlmann (2001)
J4201	TrGJC	$CH_3CHO + h\nu \rightarrow 1. \text{ HO2prodNMHCphoto} + CH_3O_2 + HO_2 + CO$	jx(ip_CH3CH0)	Sander et al. (2014)
J4202	TrGJC	$CH_3C(O)OOH + h\nu \rightarrow CH_3O_2 + OH + CO_2$	jx(ip_CH3C003H)	Sander et al. (2014)
J4203	TrGJCN	$NACA + h\nu \rightarrow NO_2 + HCHO + CO$	0.19*jx(ip_CH0H)	von Kuhlmann (2001)
J4204	TrGJCN	$PAN + h\nu \rightarrow CH_3C(O)OO + NO_2$	jx(ip_PAN)	Sander et al. (2014)
J4300	TrGJC	$iC_3H_7OOH + h\nu \rightarrow CH_3COCH_3 + HO_2 + OH$	jx(ip_CH300H)	von Kuhlmann (2001)
J4301	TrGJC	$CH_3COCH_3 + h\nu \rightarrow CH_3C(O)OO + CH_3O_2$	jx(ip_CH3C0CH3)	Sander et al. (2014)
J4302	TrGJC	$CH_3COCH_2OH + h\nu \rightarrow 1. \text{ HO2prodNMHCphoto} + 0.074*jx(ip_CH0H) + CH_3C(O)OO + HCHO + HO_2$	0.074*jx(ip_CH0H)	see note*

Table 2: Photolysis reactions (... continued)

#	labels	reaction	rate coefficient	reference
J4303	Tr-GJC	MGLYOX + $h\nu \rightarrow$ 1. HO2prodNMHCphoto + CH ₃ C(O)OO + CO + HO ₂	jx(ip_MGLYOX)	Sander et al. (2014)
J4304	Tr-GJC	CH ₃ COCH ₂ O ₂ H + $h\nu \rightarrow$ CH ₃ C(O)OO + HCHO + OH	jx(ip_CH300H)	see note*
J4306	Tr-GJCN	iC ₃ H ₇ ONO ₂ + $h\nu \rightarrow$ 1. HO2prodNMHCphoto + CH ₃ COCH ₃ + NO ₂ + HO ₂	3.7*jx(ip_PAN)	von Kuhlmann et al. (2003)*
J4400	Tr-GJC	LC ₄ H ₉ OOH + $h\nu \rightarrow$ OH + .67 MEK + .67 HO ₂ + .33 C ₂ H ₅ O ₂	jx(ip_CH300H)	Rickard and Pascoe (2009)
J4401	Tr-GJC	LC ₄ H ₉ OOH + $h\nu \rightarrow$.33 CH ₃ CHO + CO + HO ₂	0.019*jx(ip_COH2) + 0.015*jx(ip_MGLYOX)	Sander et al. (2014)
J4402	Tr-GJC	MVKOOH + $h\nu \rightarrow$ OH + .5 MGLYOX + .25 CH ₃ COCH ₂ OH + .75 HCHO + .75 HO ₂ + .25 CH ₃ C(O)OO + .25 CO	jx(ip_CH300H)	see note*
J4403	Tr-GJC	MEK + $h\nu \rightarrow$ CH ₃ C(O)OO + C ₂ H ₅ O ₂	0.42*jx(ip_CHOH)	von Kuhlmann et al. (2003)
J4404	Tr-GJC	LMEKOOH + $h\nu \rightarrow$ CH ₃ C(O)OO + CH ₃ CHO + OH	jx(ip_CH300H)	Rickard and Pascoe (2009)
J4405	Tr-GJC	BIACET + $h\nu \rightarrow$ 2 CH ₃ C(O)OO	2.15*jx(ip_MGLYOX)	see note*
J4406	Tr-GJCN	LC ₄ H ₉ NO ₃ + $h\nu \rightarrow$ 0.67 HO2prodNMHCphoto + NO ₂ + .67 MEK + .67 HO ₂ + .33 C ₂ H ₅ O ₂ + .33 CH ₃ CHO	3.7*jx(ip_PAN)	von Kuhlmann (2001)
J4407	Tr-GJCN	MPAN + $h\nu \rightarrow$ CH ₃ COCH ₂ OH + NO ₂	jx(ip_PAN)	see note*
J4500	Tr-GJC	ISOOH + $h\nu \rightarrow$ MVK + HCHO + HO ₂ + OH	jx(ip_CH300H)	see note*
J4501	Tr-GJCN	ISON + $h\nu \rightarrow$ 1. HO2prodNMHCphoto + MVK + HCHO + NO ₂ + HO ₂	3.7*jx(ip_PAN)	von Kuhlmann (2001)
J6000	St-Tr-GJCI	Cl ₂ + $h\nu \rightarrow$ Cl + Cl	jx(ip_Cl12)	Sander et al. (2014)
J6100	St-Tr-GJCI	Cl ₂ O ₂ + $h\nu \rightarrow$ 2.0 o3lossxo + 2.0 LossO3Cl + 2.0 LossO3 + 2 Cl	jx(ip_Cl1202)	Sander et al. (2014)
J6101	St-Tr-GJCI	OCIO + $h\nu \rightarrow$ 1.0 o3produntagged + 1.0 ProdO3 + ClO + O(³ P)	jx(ip_OC10)	Sander et al. (2014)
J6200	St-GJCI	HCl + $h\nu \rightarrow$ Cl + H	jx(ip_HCl1)	Sander et al. (2014)
J6201	St-Tr-GJCI	HOCl + $h\nu \rightarrow$ 1.0 o3lossxo + 1.0 LossO3Cl + 1.0 LossO3 + OH + Cl	jx(ip_HOCl1)	Sander et al. (2014)
J6300	Tr-GJCN	CINO ₂ + $h\nu \rightarrow$ 1.0 o3produntagged + 1.0 ProdO3 + Cl + NO ₂	jx(ip_Cl1N02)	Sander et al. (2014)
J6301a	St-Tr-GJCN	CINO ₃ + $h\nu \rightarrow$ Cl + NO ₃	jx(ip_Cl1N03)	Sander et al. (2014)
J6301b	St-Tr-GJCN	CINO ₃ + $h\nu \rightarrow$ ClO + NO ₂	jx(ip_Cl1N002)	Sander et al. (2014)
J6400	St-GJCI	CH ₃ Cl + $h\nu \rightarrow$ 1.0 ProdLCl + Cl + CH ₃ O ₂	jx(ip_CH3Cl1)	Sander et al. (2014)
J6401	St-GJCI	CCl ₄ + $h\nu \rightarrow$ 4.0 ProdLCl + LCCARBON + 4 Cl	jx(ip_CCl14)	Sander et al. (2014)
J6402	St-GJCI	CH ₃ CCl ₃ + $h\nu \rightarrow$ 3.0 ProdLCl + 2 LCCARBON + 3 Cl	jx(ip_CH3CCl3)	Sander et al. (2014)
J6500	St-GJCI	CFCl ₃ + $h\nu \rightarrow$ 3.0 ProdLCl + 3 Cl + LCCARBON + LFLUORINE	jx(ip_CFC13)	Sander et al. (2014)

Table 2: Photolysis reactions (... continued)

#	labels	reaction	rate coefficient	reference
J6501	StGJClF	$\text{CF}_2\text{Cl}_2 + h\nu \rightarrow 2.0 \text{ ProdLCl} + 2 \text{ Cl} + \text{LCARBON} + 2$ LFLUORINE	jx(ip_CF2Cl2)	Sander et al. (2014)
J7000	StTrGJBr	$\text{Br}_2 + h\nu \rightarrow \text{Br} + \text{Br}$	jx(ip_Br2)	Sander et al. (2014)
J7400	StTrGJBr	$\text{BrO} + h\nu \rightarrow \text{Br} + \text{O}(^3\text{P})$	jx(ip_BrO)	Sander et al. (2014)
J7200	StTrGJBr	$\text{HOBr} + h\nu \rightarrow 1.0 \text{ o3lossxo} + 1.0 \text{ LossO3Br} + 1.0 \text{ LossO3} + \text{Br}$ + OH	jx(ip_HOBr)	Sander et al. (2014)
J7300	TrGJBrN	$\text{BrNO}_2 + h\nu \rightarrow 1.0 \text{ o3produntagged} + 1.0 \text{ ProdO3} + \text{Br} + \text{NO}_2$	jx(ip_BrNO2)	Sander et al. (2014)
J7301	StTrGJBrN	$\text{BrNO}_3 + h\nu \rightarrow .85 \text{ Br} + .85 \text{ NO}_3 + .15 \text{ BrO} + .15 \text{ NO}_2$	jx(ip_BrNO3)	Sander et al. (2014)*
J7400	StGJBr	$\text{CH}_3\text{Br} + h\nu \rightarrow 1.0 \text{ ProdLBr} + \text{Br} + \text{CH}_3\text{O}_2$	jx(ip_CH3Br)	Sander et al. (2014)
J7401	TrGJBr	$\text{CH}_2\text{Br}_2 + h\nu \rightarrow 2.0 \text{ ProdSBr} + \text{LCARBON} + 2 \text{ Br}$	jx(ip_CH2Br2)	Sander et al. (2014)
J7402	TrGJBr	$\text{CHBr}_3 + h\nu \rightarrow 3.0 \text{ ProdSBr} + \text{LCARBON} + 3 \text{ Br}$	jx(ip_CHBr3)	Sander et al. (2014)
J7500	StGJBrF	$\text{CF}_3\text{Br} + h\nu \rightarrow 1.0 \text{ ProdLBr} + \text{LCARBON} + 3 \text{ LFLUORINE} +$ Br	jx(ip_CF3Br)	Sander et al. (2014)
J7600	StTrGJBrCl	$\text{BrCl} + h\nu \rightarrow \text{Br} + \text{Cl}$	jx(ip_BrCl)	Sander et al. (2014)
J7601	StGJBrClF	$\text{CF}_2\text{ClBr} + h\nu \rightarrow 1.0 \text{ ProdLBr} + 1.0 \text{ ProdLCl} + \text{LCARBON} +$ 2 LFLUORINE + Br + Cl	jx(ip_CF2ClBr)	Sander et al. (2014)
J7602	TrGJBrCl	$\text{CH}_2\text{ClBr} + h\nu \rightarrow 1.0 \text{ ProdSBr} + 1.0 \text{ ProdSCL} + \text{LCARBON} +$ Br + Cl	jx(ip_CH2ClBr)	Sander et al. (2014)
J7603	TrGJBrCl	$\text{CHCl}_2\text{Br} + h\nu \rightarrow 1.0 \text{ ProdSBr} + 2.0 \text{ ProdSCL} + \text{LCARBON} +$ Br + 2 Cl	jx(ip_CHCl2Br)	Sander et al. (2014)
J7604	TrGJBrCl	$\text{CHClBr}_2 + h\nu \rightarrow 2.0 \text{ ProdSBr} + 1.0 \text{ ProdSCL} + \text{LCARBON} +$ 2 Br + Cl	jx(ip_CHClBr2)	Sander et al. (2014)
J8401	StTrGJJI	$\text{CH}_3\text{I} + h\nu \rightarrow \text{CH}_3\text{O}_2$	JX(ip_CH3I)	Sander et al. (2014)
J6500dc01	StGJClF	$\text{CHF}_2\text{Cl} + h\nu \rightarrow 1.0 \text{ ProdLCl} + \text{Cl} + \text{LCARBON} + 2$ LFLUORINE	jx(ip_CHF2Cl)	Burkholder et al. (2019)*
J6500dc02	StGJCClF	$\text{CF}_2\text{ClCFCl}_2 + h\nu \rightarrow 3.0 \text{ ProdLCl} + 3 \text{ Cl} + 2 \text{ LCARBON} + 3$ LFLUORINE	jx(ip_CF2ClCFCl2)	Burkholder et al. (2019)
J6400dc01	StGJCl	$\text{CH}_2\text{Cl}_2 + h\nu \rightarrow 2.0 \text{ ProdLCl} + 2 \text{ Cl} + \text{LCARBON}$	jx(ip_CH2Cl2)	Burkholder et al. (2019)
J6500dc03	StGJCClF	$\text{CH}_3\text{CFCl}_2 + h\nu \rightarrow 2.0 \text{ ProdLCl} + 2 \text{ Cl} + 2 \text{ LCARBON} + 1$ LFLUORINE	jx(ip_CH3CFCl2)	Burkholder et al. (2019)
J6500dc04	StGJCClF	$\text{CF}_2\text{ClCF}_2\text{Cl} + h\nu \rightarrow 2.0 \text{ ProdLCl} + 2 \text{ Cl} + 2 \text{ LCARBON} + 4$ LFLUORINE	jx(ip_CF2ClCF2Cl)	Burkholder et al. (2019)
J6400dc02	StGJCl	$\text{CHCl}_3 + h\nu \rightarrow 3.0 \text{ ProdSCL} + 3 \text{ Cl} + \text{LCARBON}$	jx(ip_CHCl3)	Burkholder et al. (2019)
J6500dc05	StGJCClF	$\text{CF}_3\text{CF}_2\text{Cl} + h\nu \rightarrow 1.0 \text{ ProdLCl} + \text{Cl} + 2 \text{ LCARBON} + 5$ LFLUORINE	jx(ip_CF3CF2Cl)	Burkholder et al. (2019)

Table 2: Photolysis reactions (... continued)

#	labels	reaction	rate coefficient	reference
J6500dc06	StG	$\text{CH}_2\text{F}_2 + \text{Cl} \rightarrow \text{HCl} + \text{LCARBON} + 2 \text{ LFLUORINE}$	$7.6\text{e-}12 * \text{EXP}(-1630./\text{temp})$	Burkholder et al. (2019)
J6500pg01	StGJ	$\text{CH}_3\text{CF}_2\text{Cl} + \text{h}\nu \rightarrow 1.0 \text{ ProdLCI} + \text{Cl} + 2 \text{ LCARBON} + 2 \text{ jx(ip_CH3CF2Cl)}$		Burkholder et al. (2019)
J7600pg01	StGJ	LFLUORINE		
	StGJ	$\text{CBrF}_2\text{CBBrF}_2 + \text{h}\nu \rightarrow 2.0 \text{ ProdLBr} + 2 \text{ Br} + 2 \text{ LCARBON} + 4 \text{ jx(ip_CBBrF2CBBrF2)}$		Burkholder et al. (2019)
J9000	TrStGJS	LFLUORINE		
	TrStGJS	$\text{OCS} + \text{h}\nu \rightarrow \text{CO} + \text{S}$	JX(ip_OCS)	
J9001	TrStGJS	$\text{SO}_2 + \text{h}\nu \rightarrow \text{SO} + \text{O}(^3\text{P})$	$60.*\text{JX(ip_OCS)}$	
J9002	TrStGJS	$\text{SO}_3 + \text{h}\nu \rightarrow \text{SO}_2 + \text{O}(^3\text{P})$	JX(ip_S03)	
J9003	TrStGJS	$\text{H}_2\text{SO}_4 + \text{h}\nu \rightarrow \text{ProdH2O} + \text{SO}_3 + \text{H}_2\text{O}$	JX(ip_H2SO4)	
PH (aqueous)				

General notes

j-values are calculated with an external module (e.g., JVAL) and then supplied to the MECCA chemistry.

Values that originate from the Master Chemical Mechanism (MCM) by Rickard and Pascoe (2009) are translated according in the following way:

$\text{j}(11) \rightarrow \text{jx(ip_COH2)}$
 $\text{j}(12) \rightarrow \text{jx(ip_CHOH)}$
 $\text{j}(15) \rightarrow \text{jx(ip_HOCH2CHO)}$
 $\text{j}(18) \rightarrow \text{jx(ip_MACR)}$
 $\text{j}(22) \rightarrow \text{jx(ip_ACETOL)}$
 $\text{j}(23) + \text{j}(24) \rightarrow \text{jx(ip_MVK)}$
 $\text{j}(31) + \text{j}(32) + \text{j}(33) \rightarrow \text{jx(ip_GLYOX)}$
 $\text{j}(34) \rightarrow \text{jx(ip_MGLYOX)}$

$\text{j}(41) \rightarrow \text{jx(ip_CH3OOH)}$

$\text{j}(53) \rightarrow \text{j(isopropyl nitrate)}$

$\text{j}(54) \rightarrow \text{j(isopropyl nitrate)}$

$\text{j}(55) \rightarrow \text{j(isopropyl nitrate)}$

$\text{j}(56) + \text{j}(57) \rightarrow \text{jx(ip_NOA)}$

Specific notes

J4302: It is assumed that $\text{J}(\text{CH}_3\text{COCH}_2\text{OH})$ is 0.074 times that of J4101b.

J4304: It is assumed that $\text{J}(\text{CH}_3\text{COCH}_2\text{O}_2\text{H})$ is the same as $\text{J}(\text{CH}_3\text{OOH})$.

J4306: Following von Kuhlmann et al. (2003), we use $\text{J}(\text{C}_3\text{H}_7\text{ONO}_2) = 3.7 * \text{jx(ip_PAN)}$.

J4402: It is assumed that $\text{J}(\text{MVKOOH})$ is the same as $\text{J}(\text{CH}_3\text{OOH})$.

J4405: It is assumed that $\text{J}(\text{BIACET})$ is 2.15 times larger than $\text{J}(\text{MGLYOX})$, consistent with the photolysis rate coefficients used in the MCM (Rickard and Pascoe, 2009).

J4407: It is assumed that $\text{J}(\text{MPAN})$ is the same as $\text{J}(\text{PAN})$.

J4500: It is assumed that $\text{J}(\text{ISOOH})$ is the same as $\text{J}(\text{CH}_3\text{OOH})$.

J7301: The quantum yields are recommended by Burkholder et al. (2015) for $\lambda > 300\text{nm}$ and used here for the entire spectrum.

J6500dc01: OKAY!

Table 3: Reversible (Henry's law) equilibria and irreversible ("heterogenous") uptake

#	labels	reaction	rate coefficient	reference
---	--------	----------	------------------	-----------

General notes

The forward (`k_exf`) and backward (`k_exb`) rate coefficients are calculated in subroutine `mecca_aero_calc_k_ex` in the file `messy_mecca_aero.f90` using accommodation coefficients and Henry's law constants from `chemprop` (see `chemprop.pdf`).

For uptake of X ($X = \text{N}_2\text{O}_5$, ClNO_3 , or BrNO_3) and

subsequent reaction with H_2O , Cl^- , and Br^- in H3201, H6300, H6301, H6302, H7300, H7301, H7302, H7601, and H7602, we define:

$$k_{\text{ext}}(\text{X}) = \frac{k_{\text{mt}}(\text{X}) \times \text{LWC}}{[\text{H}_2\text{O}] + 5 \times 10^2 [\text{Cl}^-] + 3 \times 10^5 [\text{Br}^-]}$$

Here, k_{mt} = mass transfer coefficient, and LWC = liquid water content of the aerosol. The total uptake rate of X is only determined by k_{mt} . The factors only affect

the branching between hydrolysis and the halide reactions. The factor 5×10^2 was chosen such that the chloride reaction dominates over hydrolysis at about $[\text{Cl}^-] > 0.1 \text{ M}$ (see Fig. 3 in Behnke et al. (1997)), i.e. when the ratio $[\text{H}_2\text{O}]/[\text{Cl}^-]$ is less than 5×10^2 . The ratio $5 \times 10^2 / 3 \times 10^5$ was chosen such that the reactions with chloride and bromide are roughly equal for sea water composition (Behnke et al., 1994). These ratios were measured for uptake of N_2O_5 . Here, they are also used for ClNO_3 and BrNO_3 .

Table 4: Heterogeneous reactions

#	labels	reaction	rate coefficient	reference
HET200	StHetN	$\text{N}_2\text{O}_5 + \text{H}_2\text{O} \rightarrow 1.0 \text{ o3lossno} + \text{LossH}_2\text{O} + 1.0 \text{ LossO}_3\text{N}$	$\text{khet_St}(\text{ihs_N205_H2O})$	see general notes*
		+ 1.0 LossO_3 + 2 HNO_3		
HET201	TrHetN	$\text{N}_2\text{O}_5 \rightarrow 3.0 \text{ o3lossno} + 3.0 \text{ LossO}_3\text{N} + 3.0 \text{ LossO}_3 + 2 \text{ NO}_3^- (\text{cs}) + 2 \text{ H}^+ (\text{cs})$	$\text{khet_Tr}(\text{iht_N205})$	see general notes*
HET410	StHetCl	$\text{HOCl} + \text{HCl} \rightarrow 1.0 \text{ o3lossxo} + \text{ProdH}_2\text{O} + 1.0 \text{ LossO}_3\text{Cl}$	$\text{khet_St}(\text{ihs_HOCl_HCl})$	see general notes*
		+ 1.0 LossO_3 + Cl_2 + H_2O		
HET420	StHetClN	$\text{ClNO}_3 + \text{HCl} \rightarrow 1.0 \text{ o3lossno} + 0.5 \text{ LossO}_3\text{Cl} + 0.5 \text{ LossO}_3\text{N} + 1.0 \text{ LossO}_3 + \text{Cl}_2 + \text{HNO}_3$	$\text{khet_St}(\text{ihs_ClN03_HCl})$	see general notes*
HET421	StHetClN	$\text{ClNO}_3 + \text{H}_2\text{O} \rightarrow \text{LossH}_2\text{O} + \text{HOCl} + \text{HNO}_3$	$\text{khet_St}(\text{ihs_ClN03_H2O})$	see general notes*
HET422	StHetClN	$\text{N}_2\text{O}_5 + \text{HCl} \rightarrow 2.0 \text{ o3lossno} + 1.0 \text{ LossO}_3\text{Cl} + 1.0 \text{ LossO}_3\text{N} + 2.0 \text{ LossO}_3 + \text{ClNO}_2 + \text{HNO}_3$	$\text{khet_St}(\text{ihs_N205_HCl})$	see general notes*
HET510	StHetBr	$\text{HOBr} + \text{HBr} \rightarrow 1.0 \text{ o3lossxo} + \text{ProdH}_2\text{O} + 1.0 \text{ LossO}_3\text{Br}$	$\text{khet_St}(\text{ihs_HOBr_HBr})$	see general notes*
		+ 1.0 LossO_3 + Br_2 + H_2O		
HET520	StHetBrN	$\text{BrNO}_3 + \text{H}_2\text{O} \rightarrow \text{LossH}_2\text{O} + \text{HOBr} + \text{HNO}_3$	$\text{khet_St}(\text{ihs_BrN03_H2O})$	see general notes*
HET540	StHetBrClN	$\text{ClNO}_3 + \text{HBr} \rightarrow 1.0 \text{ o3lossno} + 0.333333 \text{ LossO}_3\text{Br} + 0.333333 \text{ LossO}_3\text{Cl} + 0.333333 \text{ LossO}_3\text{N} + 1.0 \text{ LossO}_3 + \text{BrCl} + \text{HNO}_3$	$\text{khet_St}(\text{ihs_ClN03_HBr})$	see general notes*
HET541	StHetBrClN	$\text{BrNO}_3 + \text{HCl} \rightarrow 1.0 \text{ o3lossno} + 0.333333 \text{ LossO}_3\text{Br} + 0.333333 \text{ LossO}_3\text{Cl} + 0.333333 \text{ LossO}_3\text{N} + 1.0 \text{ LossO}_3 + \text{BrCl} + \text{HNO}_3$	$\text{khet_St}(\text{ihs_BrN03_HCl})$	see general notes*
HET542	StHetBrCl	$\text{HOCl} + \text{HBr} \rightarrow 1.0 \text{ o3lossxo} + \text{ProdH}_2\text{O} + 0.5 \text{ LossO}_3\text{Br} + 0.5 \text{ LossO}_3\text{Cl} + 1.0 \text{ LossO}_3 + \text{BrCl} + \text{H}_2\text{O}$	$\text{khet_St}(\text{ihs_HOCl_HBr})$	see general notes*
HET543	StHetBrCl	$\text{HOBr} + \text{HCl} \rightarrow 1.0 \text{ o3lossxo} + \text{ProdH}_2\text{O} + 0.5 \text{ LossO}_3\text{Br} + 0.5 \text{ LossO}_3\text{Cl} + 1.0 \text{ LossO}_3 + \text{BrCl} + \text{H}_2\text{O}$	$\text{khet_St}(\text{ihs_HOBr_HCl})$	see general notes*

General notes

Heterogeneous reaction rates are calculated with an external module (e.g., MECCA KHET) and then supplied to the MECCA chemistry (see www.messy-interface.org for details)

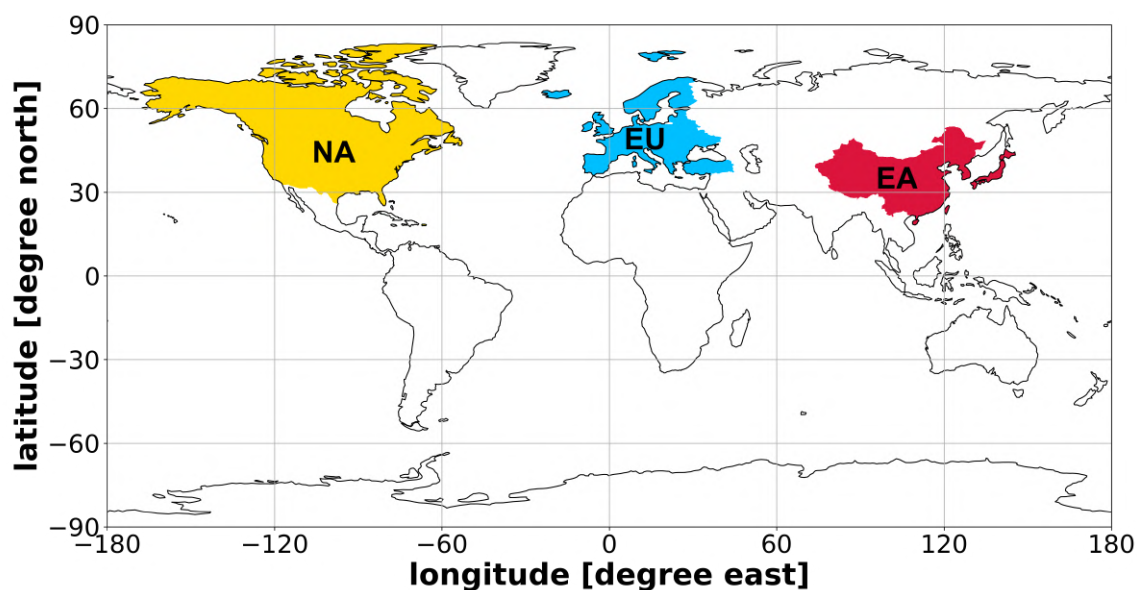


Figure A.2: Source regions (marked by colour) for tagging in the MECO(2) model setup are defined as North America (NA), Europe (EU) and East Asia (EA). All other countries and the ocean (white space) are considered as Rest of the World (ROW).

A.1.6 Extensions of the MEGAN namelist

To ensure the correct tagging of NMHCs from biogenic sources in EUMEGAN, I have included individual NMHC^{tag} tracers from the NMHC family in the MEGAN namelist. For accurate results, each NMHC tagging tracer must be scaled based on the number of carbon atoms, as explained in section 3.3.8.

B.2 Appendix Additional Results and Figures Chapter 4

B.2.1 Further detailed evaluation of EMeRGe Europe

For the flight across the Po Valley, taking place at July 20th, 2017, the simulated geographical distributions of the NO_y plumes at 925 hPa agree with the observations (Figs. B.3 and B.5). In this case, however, NO_y is mainly underestimated by the model near city centres (Milano plume, Figs. B.3 and B.5). At the same time, O_3 is mainly underestimated by the model near these city plumes, while it agrees well with the observations outside the plumes (Figs. B.4 and B.6).

Figure B.7 displays the measurements from the flight in the Benelux region at July 26th, 2017 in a composite with CM12 data. The NO_y plume of Antwerp is shifted northward in the CM12 simulation results. NO_y is mostly underestimated in the neighborhood of city centres (Fig. B.9). In between the city plumes, NO_y is well represented by CM12. At the same time O_3 is underestimated within plumes, especially between Bruges and Antwerp large O_3 mixing ratios are placed too far to the East by CM12 (Fig. B.8). Outside the city plume, starting at 12:50 UTC, O_3 is very well represented by CM12, which is confirmed by the vertical profiles (Fig. B.6). Overall, CM12 is able to capture the variability of NO_y and O_3 mixing ratios measured during the aircraft in-situ measurements. Specific patterns, however, are shifted. There is a tendency that in the neighborhood of city centres and in their downwind plumes, the model results partly underestimate NO_y and under-/overestimate O_3 .

B.2.2 Further detailed evaluation of EMeRGe Asia

Figure B.11 compares the in situ data with the CM12 output at 950 hPa along the western coast of Taiwan on March 24th, 2018, for NO_y . The NO_y plume southwest of Taipei is represented well by CM12, but it is slightly overestimated. The measured background NO_y along the flight route towards Tainan City in the Southwest of Taiwan shows local maxima, which are partially represented by CM12. Generally, CM12 overestimates the NO_y mixing ratio, with the largest difference within the massive outflow at 9:40 UTC, which was not measured by the HALO instrumentation. The vertical representation of NO_y in Figure B.14 confirms both, agreements and differences between the CM12 model output and in situ data. It indicates two NO_y plumes between 9:08 and 9:15, and between 9:35 and 9:45 UTC, respectively, which were not measured by HALO.

The comparison of the in situ data with the output of CM12 at 950 hPa along the western coast of Taiwan on the 24th of March 2018 for O_3 is presented in Figure B.12. It shows that CM12 represents the background O_3 well until 9:20 UTC. However, the vertical representation in Figure B.15 indicates that there is an underestimation of up to 20-25 nmol mol^{-1} of O_3 between 9:20 UTC and 9:35 UTC. The NO_y plume in the Southwest of Kaohsiung causes an O_3 plume between 9:35-9:45 UTC, which is well represented by CM12, both spatially and in terms of magnitude.

The focus of Figure B.16 is the outbound flight on March 24, 2018, towards Jejudo Island, which aimed to measure the outflows of the Shanghai River Delta and other metropolitan regions west of the flight track. However, the massive NO_y outflows simulated between 4:30 and 5:00 UTC between $29\text{--}31^\circ$ N in CM12 are not supported by the in situ data, as shown in Figure B.18, which depicts the massive plume in the vertical representation in CM12. The plume is passed by HALO at nearly 1000 hPa between 4:45–5:10 UTC, but in the in situ data, this plume is completely missing. The wind direction in CM12 during this time is Northwest, which agrees with the in situ data very well (Figure B.13). This confirms, that the source of the massive plume originates from the Shanghai delta.

The comparison of the in situ data with the output of CM12 for the O_3 mixing ratio above the East Chinese Sea is shown in Figures B.17 and . The Figures reveal a significant underestimation of O_3 within the emission plume between 4:45–5:10 UTC. Additionally, the O_3 mixing ratio is underestimated by CM12 up to 30 nmol mol^{-1} further Northeast.

On March 28, 2018, another flight was conducted along the West coast of Taiwan. The in situ data between 6:00 and 7:20 UTC is compared with the CM12 model output of 6 UTC in Figure B.20. It shows that CM12 overestimates NO_y above the ocean, but from 7:00 to 7:20 UTC, NO_y is well represented by CM12. Another part of the flight route from 7:40 to 8:30 UTC is shown in Figure B.22. The plumes between 7:40–8:00 UTC are well resolved by CM12. The vertical representation in Figure B.24 confirms the agreements and differences, indicating that two local plumes from 8:10 until 8:30 UTC are not represented in CM12, but the background NO_y is well represented.

The same analysis is conducted for O_3 for two different time periods of the flight on March 28, 2018, as shown in Figures B.21 and B.23. The vertical representation of O_3 in Figure B.25 shows the differences in ozone mixing ratios between CM12 and the in situ data. Only the local maxima of the O_3 mixing ratios at 6:45, 7:35, and 8:15–8:30 UTC are represented precisely by CM12. Apart from this, O_3 is mostly overestimated by CM12, locally up to 40 nmol mol^{-1} .

In general, CM12 is able to capture the variability of NO_y and O_3 mixing ratios in East Asia based on the aircraft in-situ measurements on these three flight days. However, in regions with strong gradients of mixing ratios, CM12 exhibits shifted or locally inaccurate patterns. These findings align with the EMeRGe Europe evaluation, which showed that CM12 accurately represents NO_y in rural areas, but underestimates it in urban areas and their downwind plumes. The complex topography of Taiwan further complicates the comparison with real-life data due to large NO_y gradients. Additionally, CM12 systematically overestimates O_3 levels above the ocean and coastal locations.

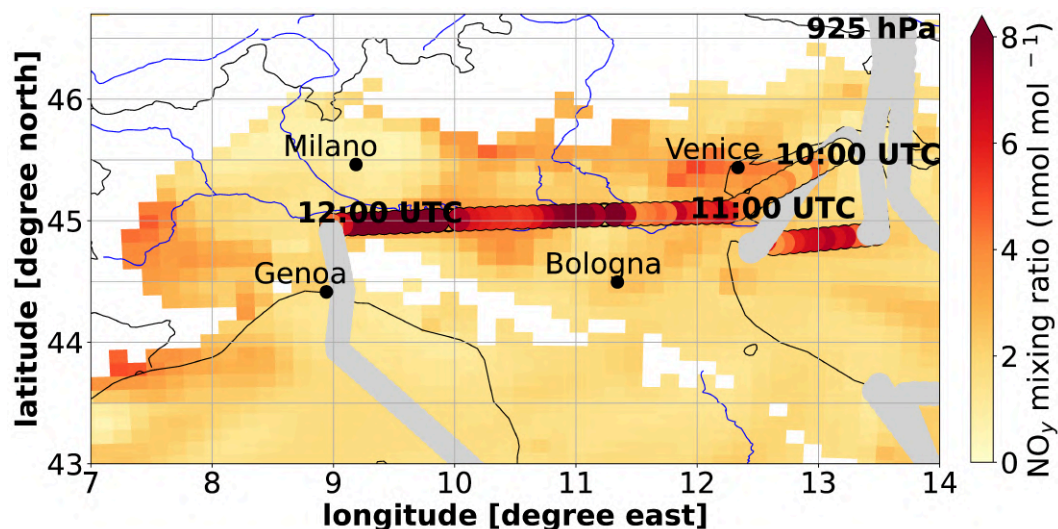


Figure B.3: CM12 simulated NO_y mixing ratios in nmol mol^{-1} at 12 UTC (background colour) at 925 hPa and the HALO in situ measurements (filled circles) for the flight date 20.07.2017 in Po Valley. The grey filled circles mask the measurement data, when HALO left the shown pressure level.

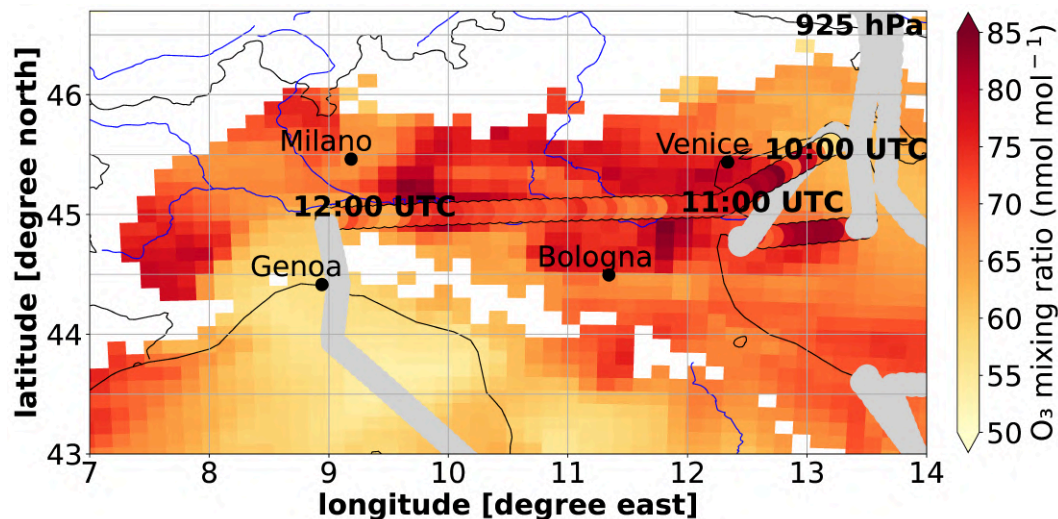


Figure B.4: CM12 simulated O_3 mixing ratios in nmol mol^{-1} at 12 UTC (background colour) at 925 hPa and the HALO in situ measurements (filled circles) for the flight date 20.07.2017 in Po Valley. The grey filled circles mask the measurement data, when HALO left the shown pressure level.

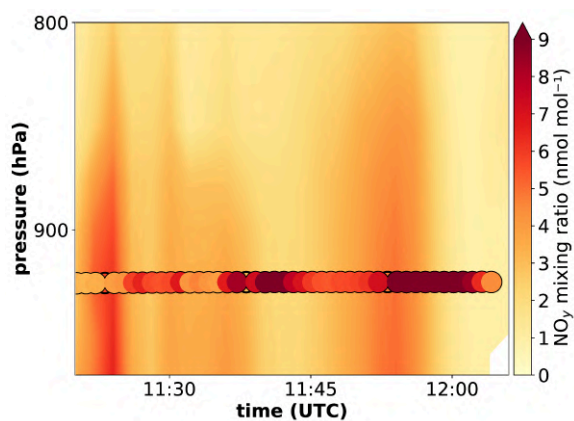


Figure B.5: Comparison between simulated (CM12) NO_y mixing ratios in nmol mol^{-1} sampled along the flight path of HALO (background colour) with the on board in situ measurements (filled circles) for the flight date 20.07.2017 in the Po Valley.

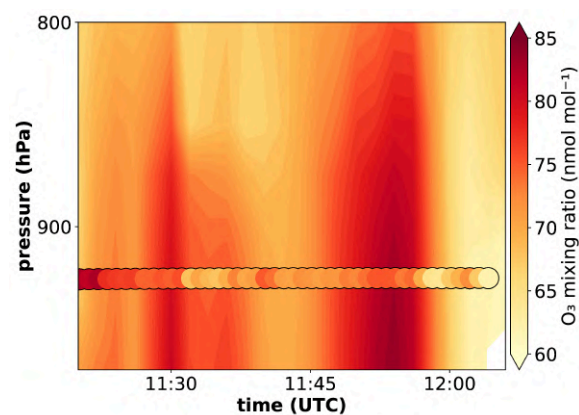


Figure B.6: Comparison between simulated (CM12) O_3 mixing ratios in nmol mol^{-1} sampled along the flight path of HALO (background colour) with the on board in situ measurements (filled circles) for the flight date 20.07.2017 in the Po Valley.

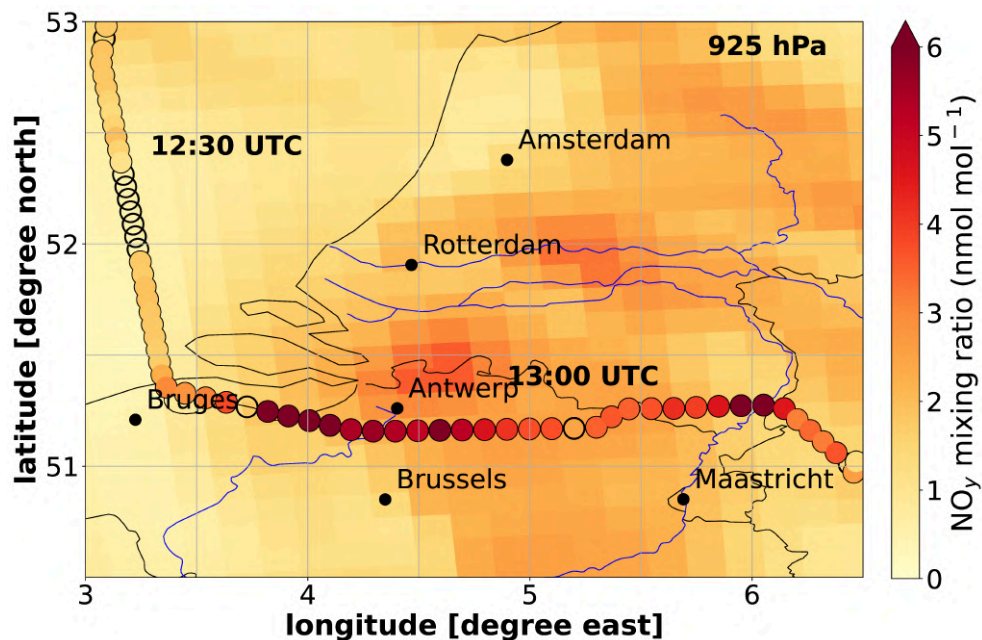


Figure B.7: CM12 simulated NO_y mixing ratios in nmol mol^{-1} at 12 UTC (background colour) at 925 hPa and the HALO in situ measurements (filled circles) for the flight date 26.07.2017 in the Benelux region. Unfilled circles mark the missing data.

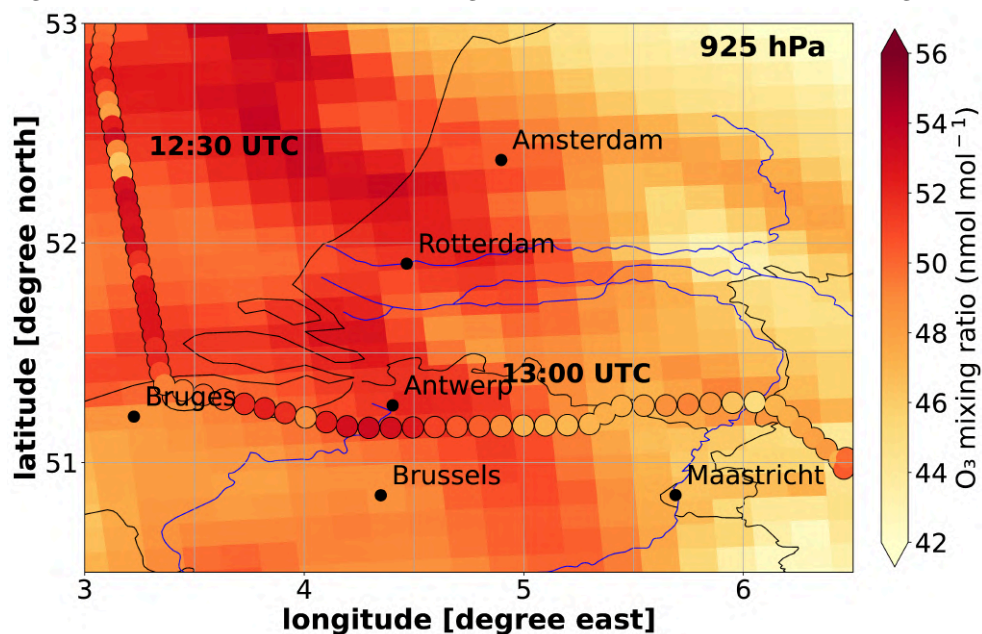


Figure B.8: CM12 simulated O_3 mixing ratios in nmol mol^{-1} at 13 UTC (background colour) at 925 hPa and the HALO in situ measurements (filled circles) for the flight date 26.07.2017 in the Benelux region.

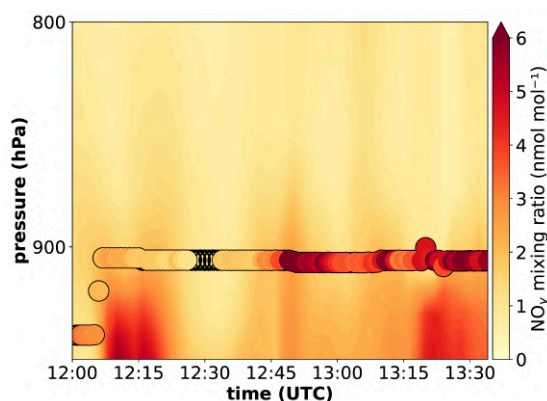


Figure B.9: Comparison between simulated (CM12) NO_y mixing ratios in nmol mol^{-1} sampled along the flight path of HALO (background colour) with the on board in situ measurements (filled circles) for the flight date 26.07.2017 in the Benelux region. Unfilled circles mark the missing data.

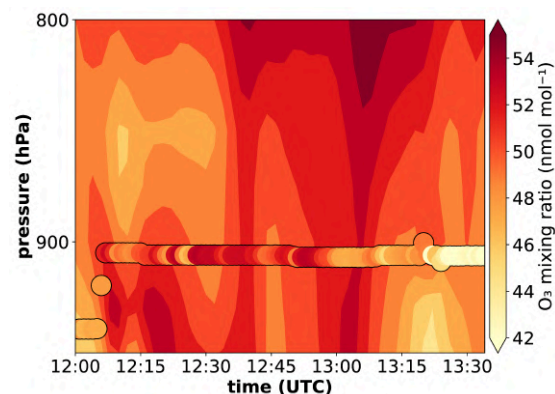


Figure B.10: Comparison between simulated (CM12) O_3 mixing ratios in nmol mol^{-1} sampled along the flight path of HALO (background colour) with the on board in situ measurements (filled circles) for the flight date 26.07.2017 in the Benelux region.

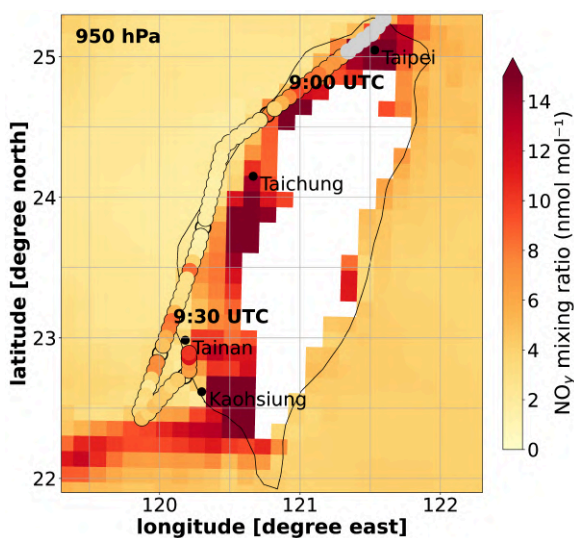


Figure B.11: CM12 simulated NO_y mixing ratios in nmol mol^{-1} at 6 UTC (background colour) and at 950 hPa, and the HALO in situ measurements (filled circles) for the flight date 24.03.2018 in Taiwan. Unfilled circles mark the missing data. The white spots mark the grid points in which the surface pressure is lower than 975 hPa. The grey filled circles mask the measurement data, when HALO left the shown pressure level.

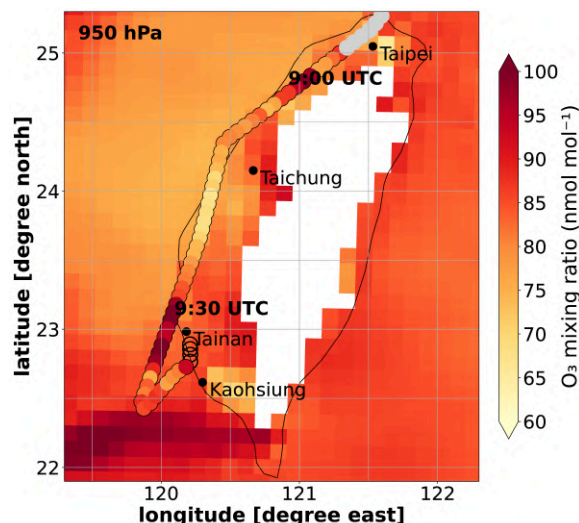


Figure B.12: CM12 simulated O_3 mixing ratios in nmol mol^{-1} at 6 UTC (background colour) and at 950 hPa, and the HALO in situ measurements (filled circles) for the flight date 24.03.2018 in Taiwan. The white spots mark the grid points in which the surface pressure is lower than 975 hPa. The grey filled circles mask the measurement data, when HALO left the shown pressure level.

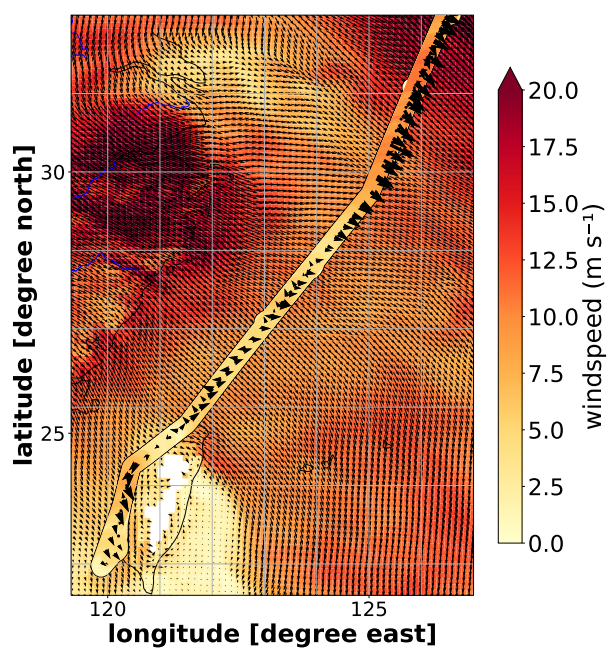


Figure B.13: Windspeed in m s^{-1} of the model output of CM12 (background colour) at 1000 hPa and the wind direction as quivers (black) in comparison with the measurements (dots) and large quivers (black) for the HALO flight at the 24th of March 2018 during EMeRGe Asia.

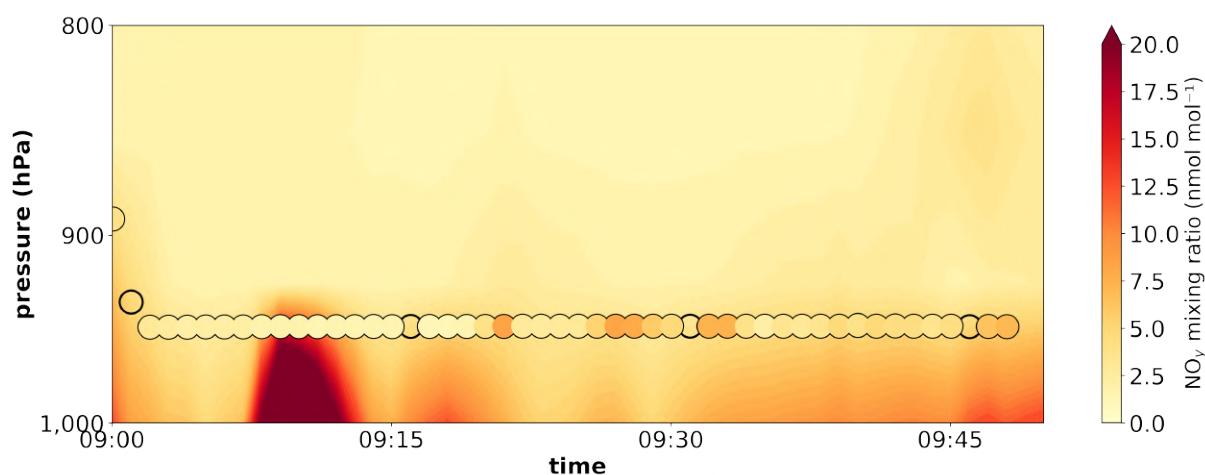


Figure B.14: Comparison between simulated (CM12) NO_y mixing ratios in nmol mol^{-1} sampled along the flight path of HALO (background colour) with the on board in situ measurements (filled circles) for the flight date 24.03.2018. Unfilled circles mark the missing data.

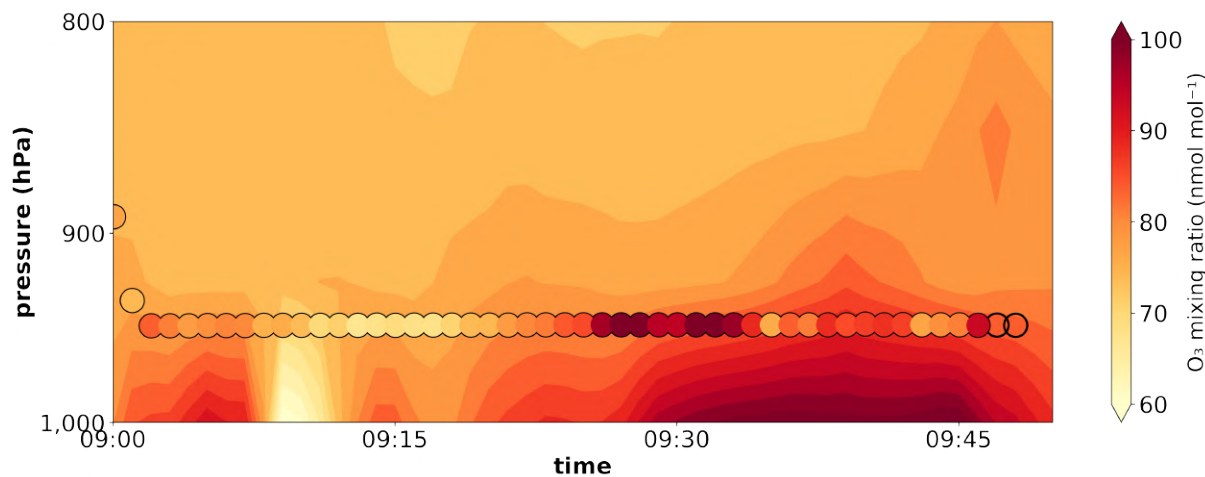


Figure B.15: Comparison between simulated (CM12) O_3 mixing ratios in nmol mol^{-1} sampled along the flight path of HALO (background colour) with the on board in situ measurements (filled circles) for the flight date 24.03.2018. Unfilled circles mark the missing data.

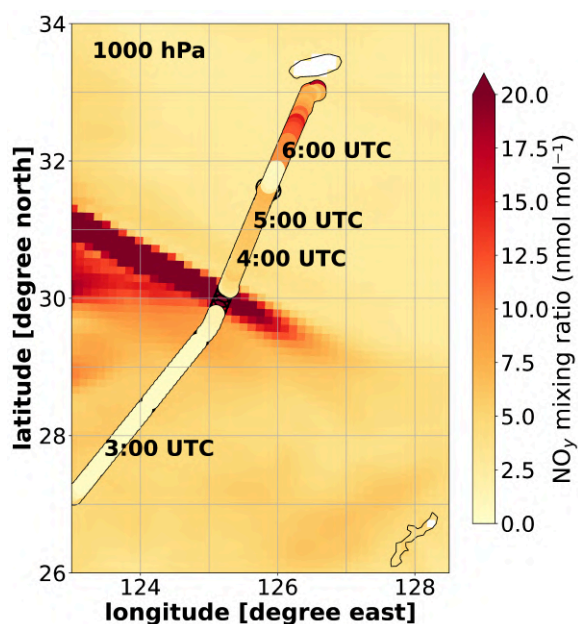


Figure B.16: CM12 simulated NO_y mixing ratios in nmol mol^{-1} at 6 UTC (background colour) and at 1000 hPa, and the HALO in situ measurements (filled circles) for the flight date 24.03.2018 in Taiwan. Unfilled circles mark the missing data. The white spots mark the grid points in which the surface pressure is lower than 1000 hPa.

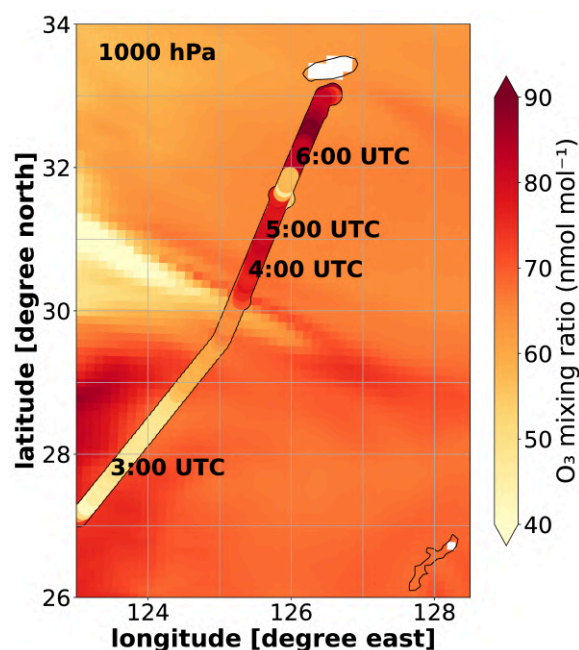


Figure B.17: CM12 simulated O_3 mixing ratios in nmol mol^{-1} at 6 UTC (background colour) and at 1000 hPa, and the HALO in situ measurements (filled circles) for the flight date 24.03.2018 in Taiwan. The white spots mark the grid points in which the surface pressure is lower than 1000 hPa.

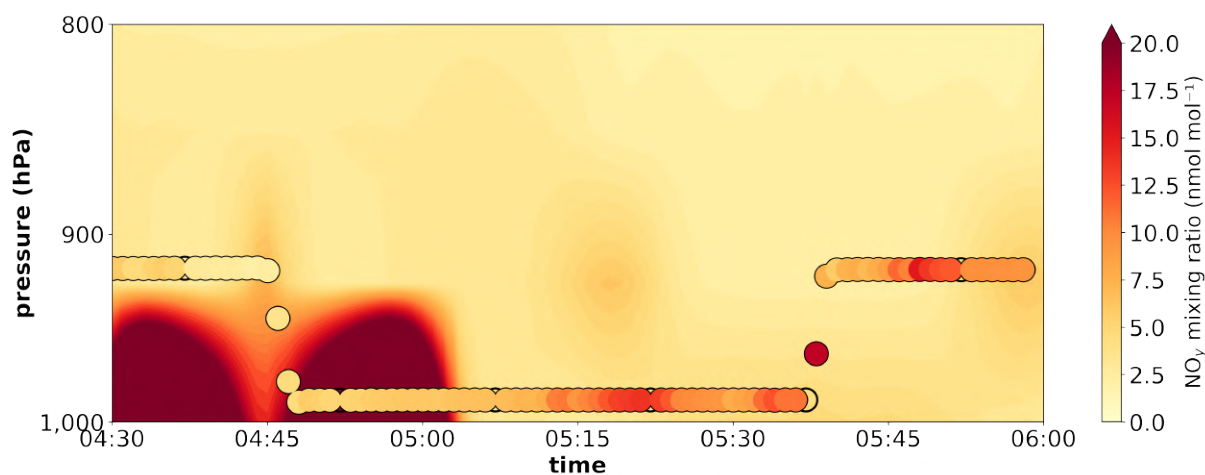


Figure B.18: Comparison between simulated (CM12) NO_y mixing ratios in nmol mol^{-1} sampled along the flight path of HALO (background colour) with the on board in situ measurements (filled circles) for the flight date 24.03.2018. Unfilled circles mark the missing data.

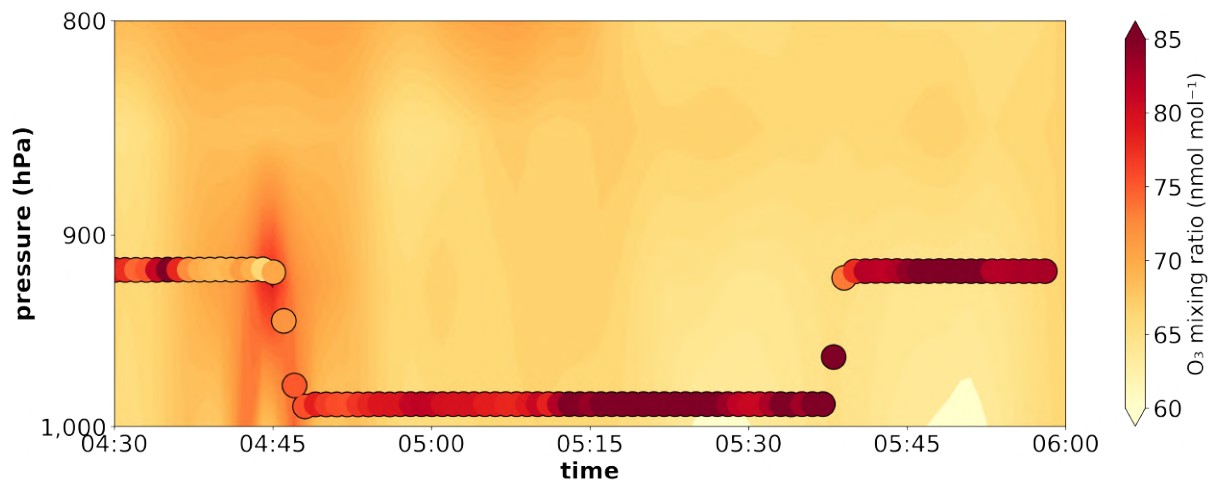


Figure B.19: Comparison between simulated (CM12) O_3 mixing ratios in nmol mol^{-1} sampled along the flight path of HALO (background colour) with the on board in situ measurements (filled circles) for the flight date 24.03.2018.

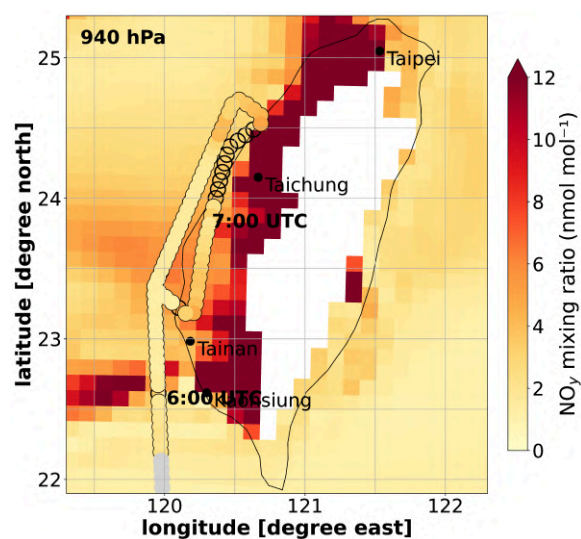


Figure B.20: CM12 simulated NO_y mixing ratios in nmol mol^{-1} at 6 UTC (background colour) and at 940 hPa, and the HALO in situ measurements (filled circles) for the flight date 28.03.2018 in Taiwan. The white spots mark the grid points in which the surface pressure is lower than 925 hPa. The grey filled circles mask the measurement data, when HALO left the shown pressure level. Unfilled circles mark the missing data.

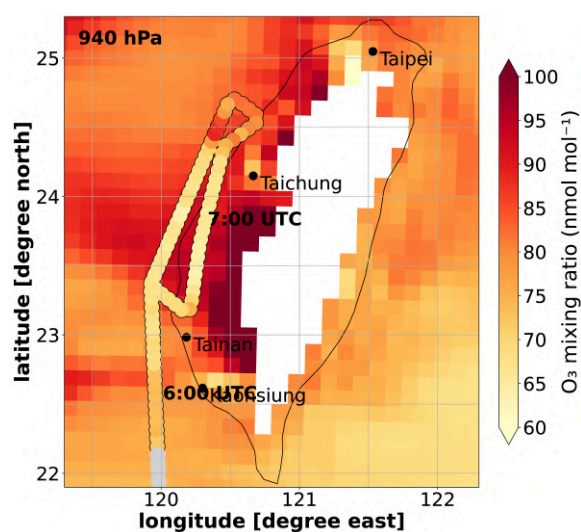


Figure B.21: CM12 simulated O_3 mixing ratios in nmol mol^{-1} at 6 UTC (background colour) and at 940 hPa, and the HALO in situ measurements (filled circles) for the flight date 28.03.2018 in Taiwan. The white spots mark the grid points in which the surface pressure is lower than 925 hPa. The grey filled circles mask the measurement data, when HALO left the shown pressure level. Unfilled circles mark the missing data.

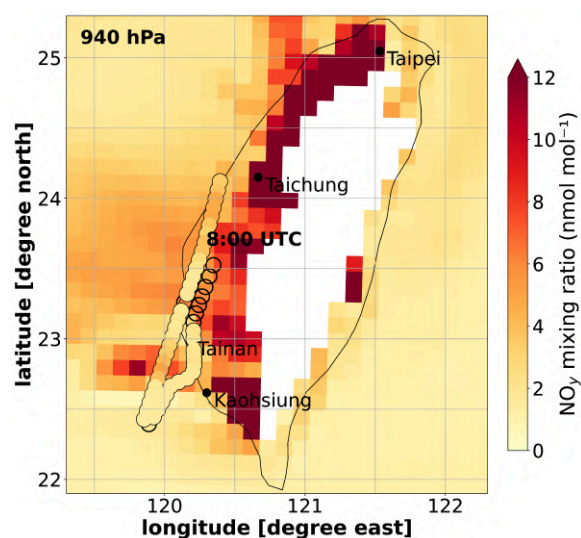


Figure B.22: CM12 simulated NO_y mixing ratios in nmol mol^{-1} at 9 UTC (background colour) and at 940 hPa, and the HALO in situ measurements (filled circles) for the flight date 28.03.2018 in Taiwan. Unfilled circles mark the missing data. The white spots mark the grid points in which the surface pressure is lower than 925 hPa.

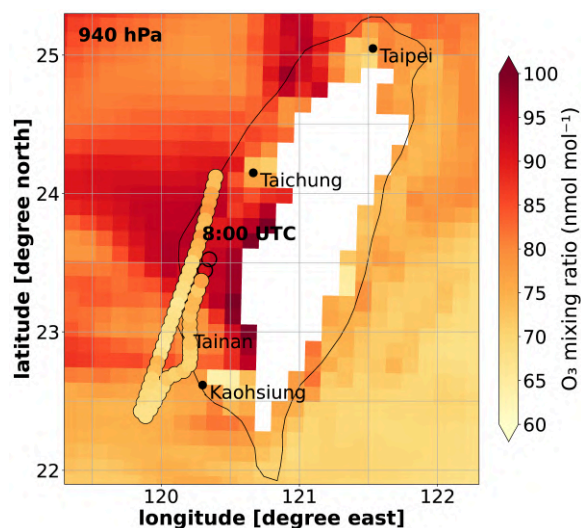


Figure B.23: CM12 simulated O_3 mixing ratios in nmol mol^{-1} at 9 UTC (background colour) and at 940 hPa, and the HALO in situ measurements (filled circles) for the flight date 28.03.2018 in Taiwan. Unfilled circles mark the missing data. The white spots mark the grid points in which the surface pressure is lower than 925 hPa.

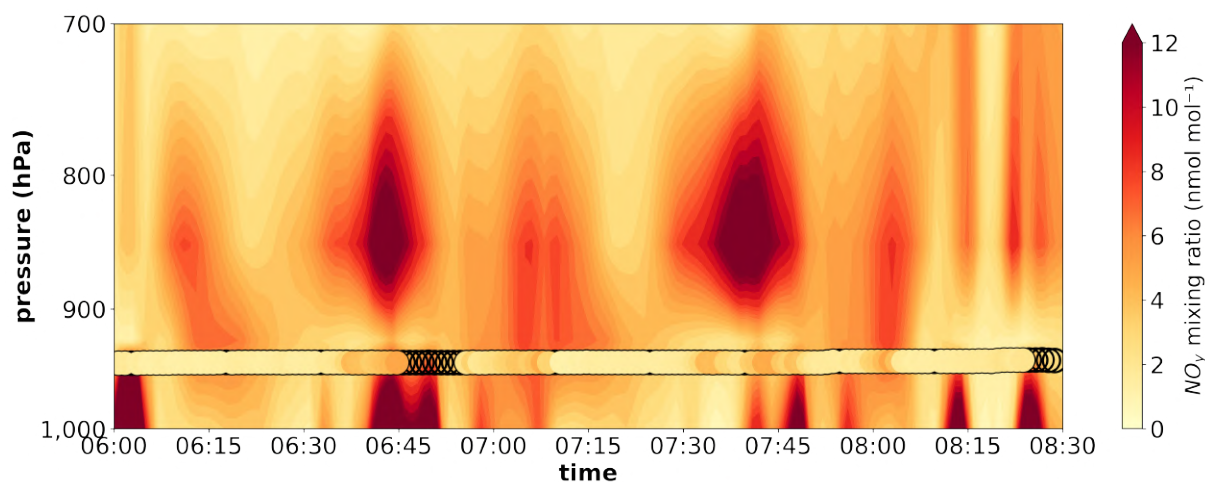


Figure B.24: Comparison between simulated (CM12) NO_y mixing ratios in nmol mol^{-1} sampled along the flight path of HALO (background colour) with the on board in situ measurements (filled circles) for the flight date 28.03.2018.

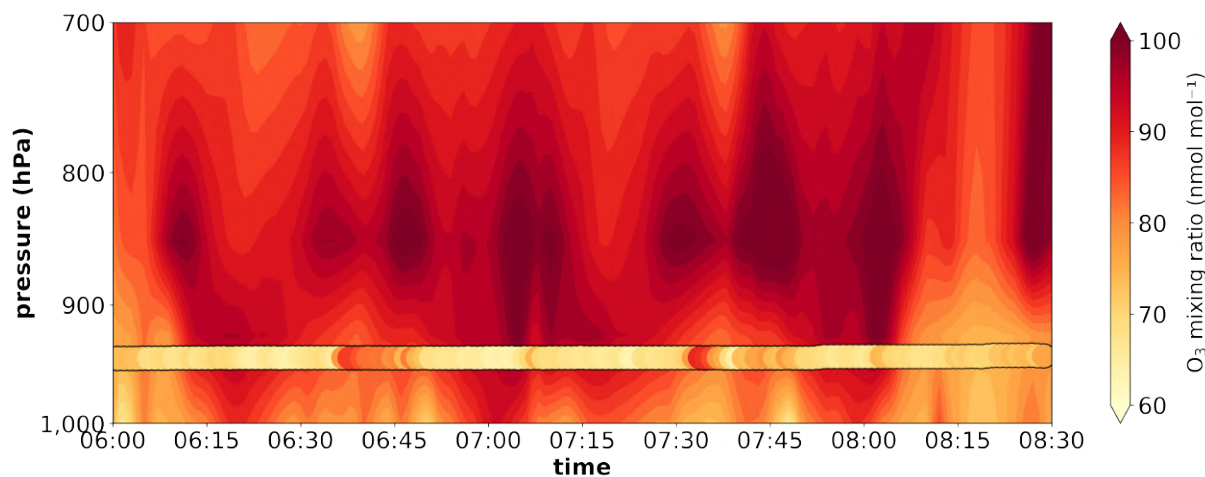


Figure B.25: Comparison between simulated (CM12) O_3 mixing ratios in nmol mol^{-1} sampled along the flight path of HALO (background colour) with the on board in situ measurements (filled circles) for the flight date 28.03.2018. Unfilled circles mark the missing data.

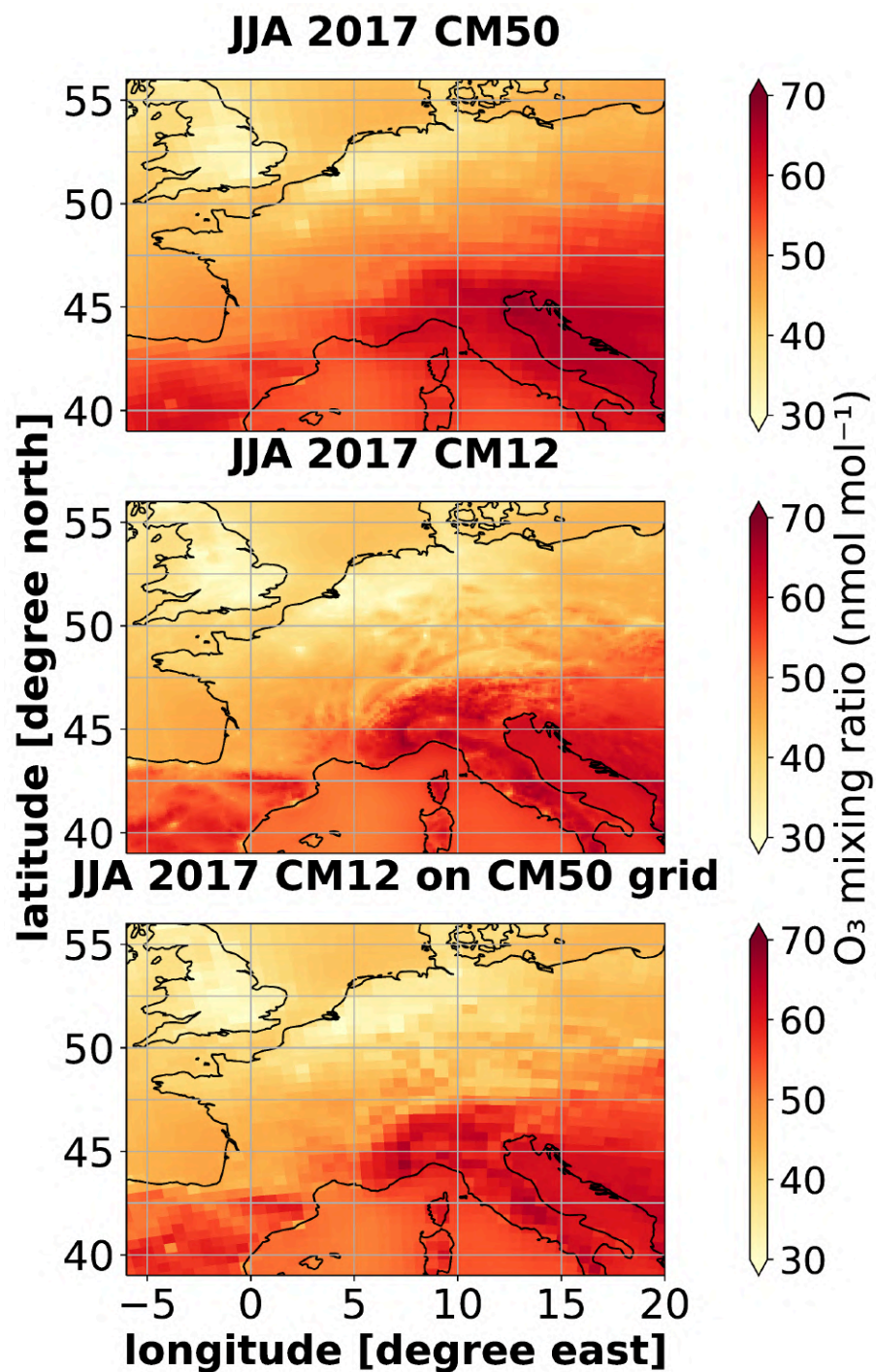


Figure B.26: Comparison of ground-level ozone between CM50 (50 km) and CM12 (12 km).

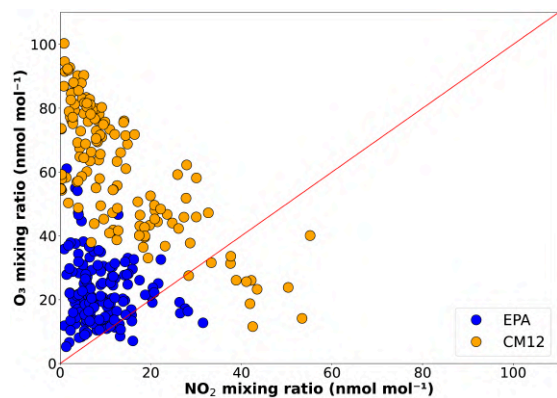


Figure B.27: Observed (EPA, blue) and simulated (CM12, orange) NO_2 versus O_3 mixing ratios (in nmol mol^{-1}) at 6 h local time in JJA 2018 at 153 rural EPA stations.

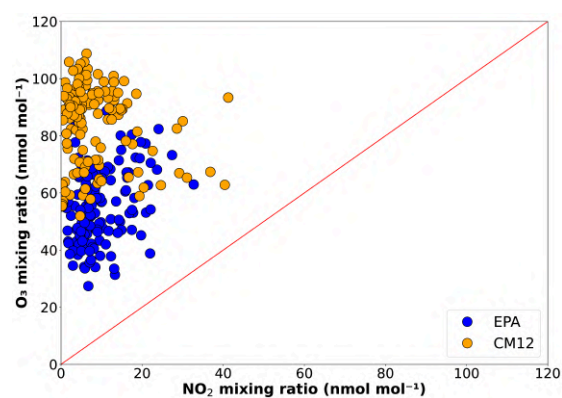


Figure B.28: Observed (EPA, blue) and simulated (CM12, orange) NO_2 versus MDA8 O_3 mixing ratios (in nmol mol^{-1}) at 6 h local time in JJA 2018 at 153 rural EPA stations.

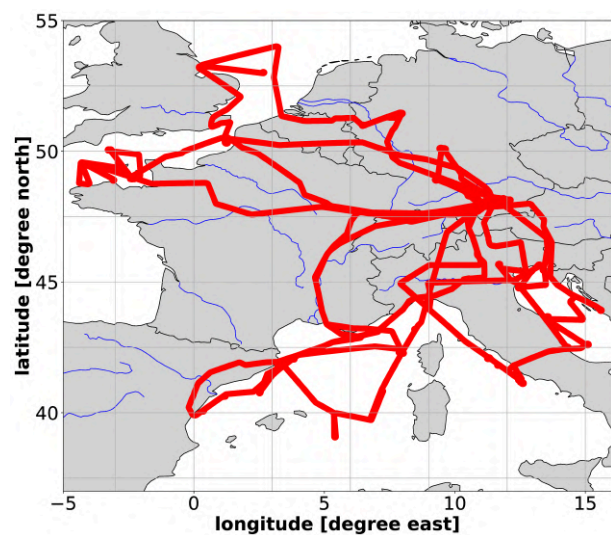


Figure B.29: Overview of all flights conducted during the EMeRGe Europe campaign.

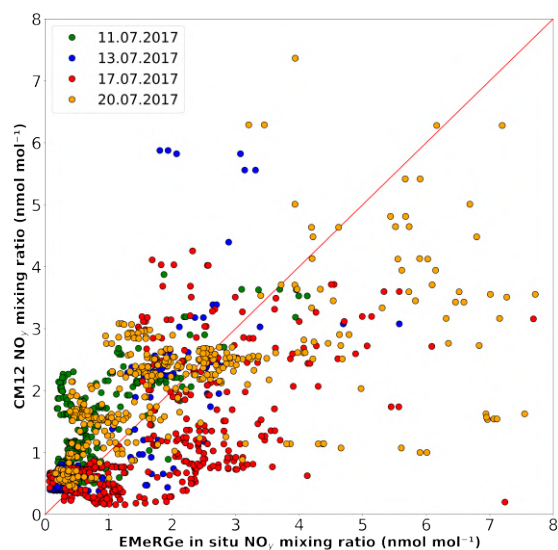


Figure B.30: NO_y mixing ratios in nmol mol^{-1} of the model output of CM12 on the vertical-axis versus the HALO in situ measurements on the horizontal-axis for all four flight dates 11.07.2017, 13.07.2017, 17.07.2017, 20.07.2017.

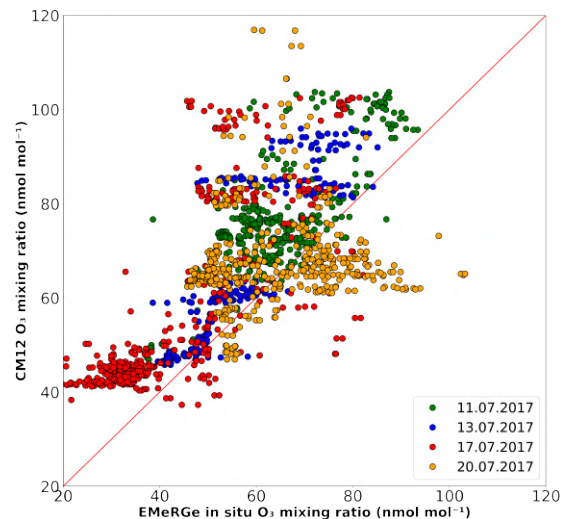


Figure B.31: O_3 mixing ratios in nmol mol^{-1} of the model output of CM12 on the vertical-axis versus the HALO in situ measurements on the horizontal-axis for all four flight dates 11.07.2017, 13.07.2017, 17.07.2017, 20.07.2017.

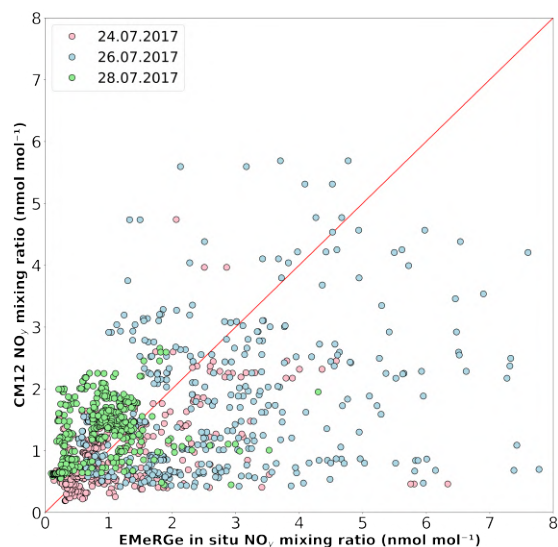


Figure B.32: NO_y mixing ratios in nmol mol^{-1} of the model output of CM12 on the vertical-axis versus the HALO in situ measurements on the horizontal-axis for all three flight dates 24.07.2017, 26.07.2017 and 28.07.2017.

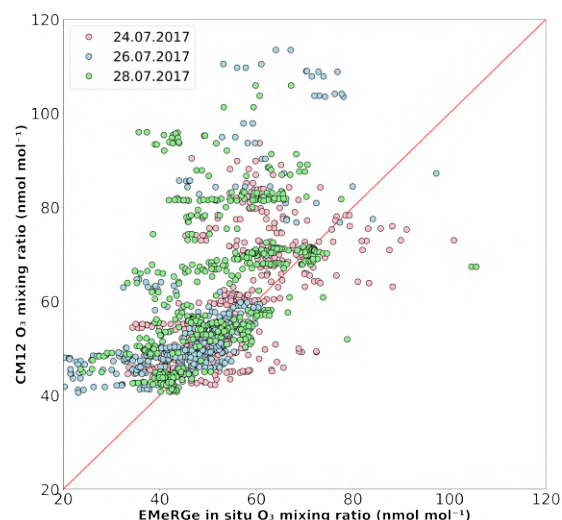


Figure B.33: O_3 mixing ratios in nmol mol^{-1} of the model output of CM12 on the vertical-axis versus the HALO in situ measurements on the horizontal-axis for all three flight dates 24.07.2017, 26.07.2017 and 28.07.2017.

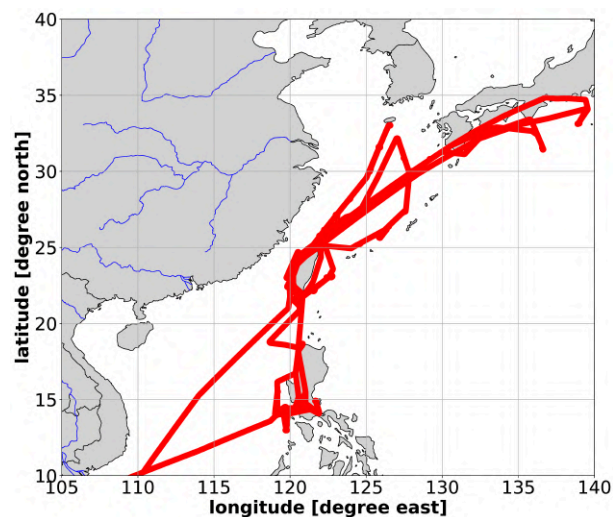


Figure B.34: Overview of all flights conducted during the EMeRGe Asia campaign.

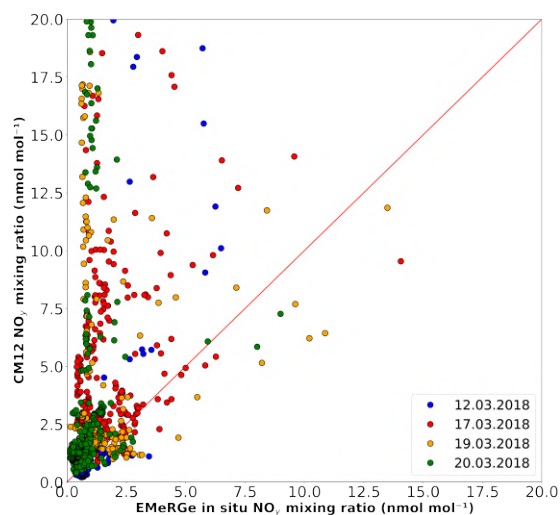


Figure B.35: NO_y mixing ratios in nmol mol⁻¹ of the model output of CM12 on the vertical-axis versus the HALO in situ measurements on the horizontal-axis for all three flight dates 12.03.2018, 17.03.2018, 19.03.2018, 20.03.2018.

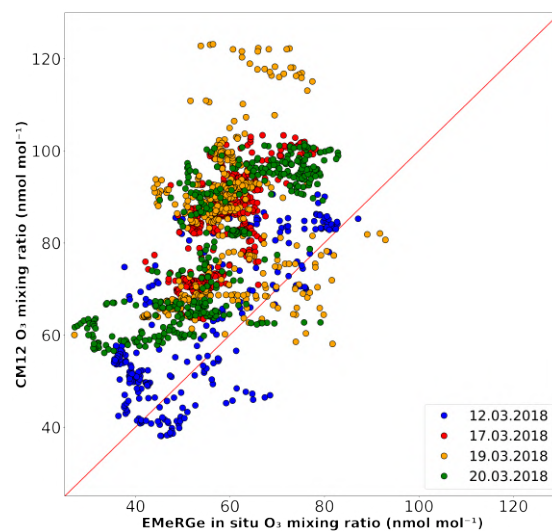


Figure B.36: O₃ mixing ratios in nmol mol⁻¹ of the model output of CM12 on the vertical-axis versus the HALO in situ measurements on the horizontal-axis for all three flight dates 12.03.2018, 17.03.2018, 19.03.2018, 20.03.2018.

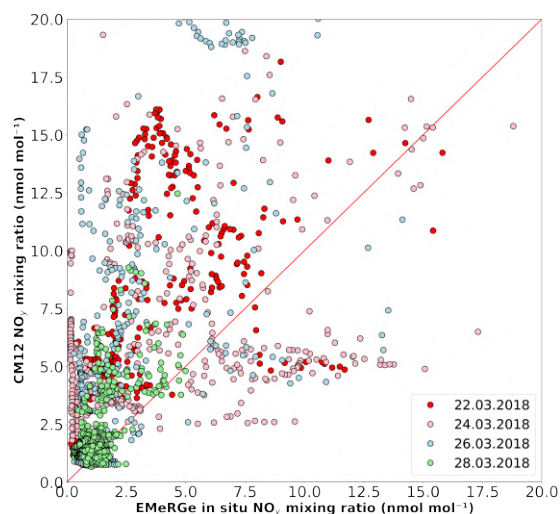


Figure B.37: NO_y mixing ratios in nmol mol⁻¹ of the model output of CM12 on the vertical-axis versus the HALO in situ measurements on the horizontal-axis for all three flight dates 22.03.2018, 24.03.2018, 26.03.2018 and 28.03.2018.

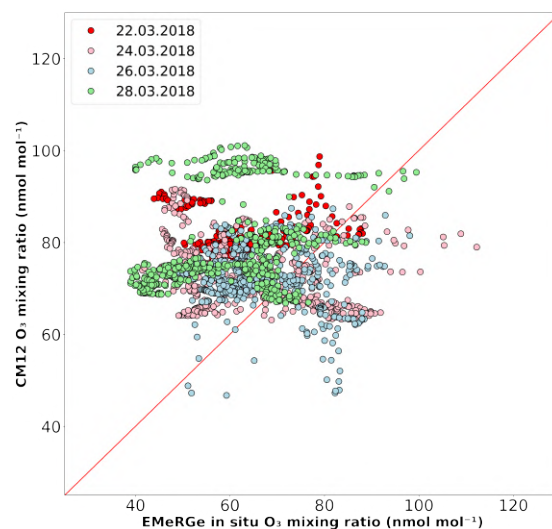


Figure B.38: O₃ mixing ratios in nmol mol⁻¹ of the model output of CM12 on the vertical-axis versus the HALO in situ measurements on the horizontal-axis for all three flight dates 22.03.2018, 24.03.2018, 26.03.2018 and 28.03.2018.

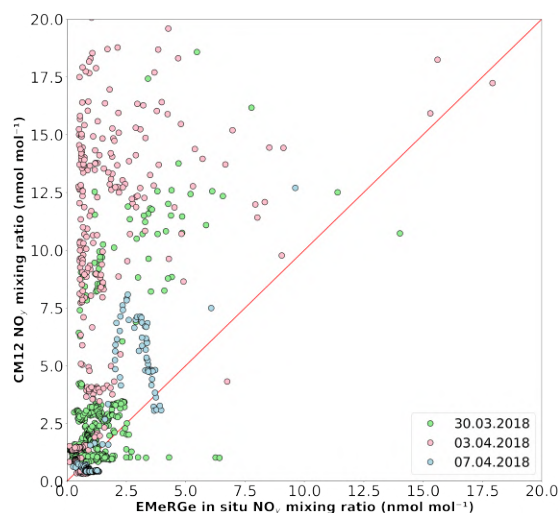


Figure B.39: NO_y mixing ratios in nmol mol⁻¹ of the model output of CM12 on the vertical-axis versus the HALO in situ measurements on the horizontal-axis for all three flight dates 30.03.2018, 04.07.2018 and 07.04.2018.

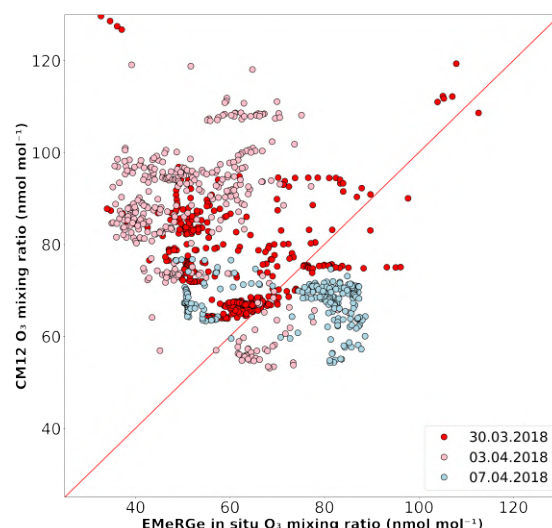


Figure B.40: O₃ mixing ratios in nmol mol⁻¹ of the model output of CM12 on the vertical-axis versus the HALO in situ measurements on the horizontal-axis for all three flight dates 30.03.2018, 04.07.2018 and 07.04.2018.

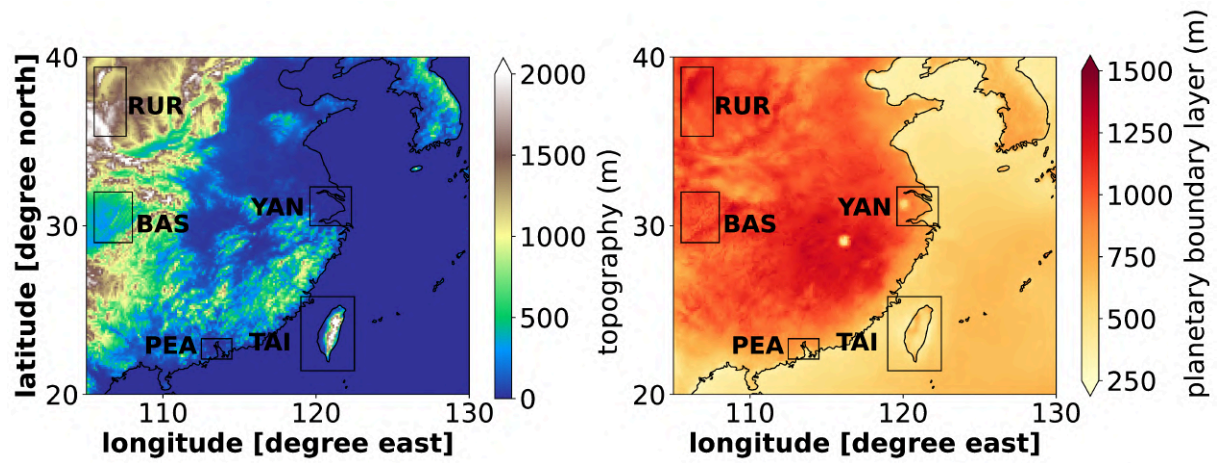


Figure B.41: Topography (left panel) and mean planetary boundary layer height (PBLH; right panel) in m for East Asia for JJA 2017–2018 in CM12. Study areas labelled after Table 5.2.

C.3 Appendix Tables and Figures Chapter 5 and 6

Table C.7: Annual totals of EDGAR v5.0 emissions (in Gg a⁻¹) in the European study areas for the year 2015 for the sectors land transport, anthropogenic non-traffic, shipping. The CO emissions are given in amount of CO, the NO_x emissions in amount of NO, the NMVOC emissions in amount of carbon [Crippa et al., 2020].

emission sector	species	BEN	PO	IRE	IBE
Land transport	CO	234	202	14	112
Non-traffic	CO	1338	662	38	188
Shipping	CO	15	6	1	0.1
Land transport	NO _x	202	151	13	87
Non-traffic	NO _x	344	152	18	62
Shipping	NO _x	46	35	6	0.6
Land transport	NMVOC	30	39	1	15
Non-traffic	NMVOC	618	364	29	101
Shipping	NMVOC	3	2	1	0.0

Table C.8: Annual totals of EDGAR v5.0 emissions (in Gg a⁻¹) in the East Asian study areas for the year 2015 for the sectors land transport, anthropogenic non-traffic, shipping. The CO emissions are given in amount of CO, the NO_x emissions in amount of NO, the NMVOC emissions in amount of carbon [Crippa et al., 2020].

emission sector	species	PEA	YAN	TAI	BAS	RUR
Land transport	CO	878	1392	2159	390	198
Non-traffic	CO	1716	16675	1115	1888	357
Shipping	CO	9	8	6	6	4
Land transport	NO _x	256	352	352	100	52
Non-traffic	NO _x	621	1661	508	401	225
Shipping	NO _x	40	33	77	24	17
Land transport	NMVOC	191	305	241	86	44
Non-traffic	NMVOC	689	1332	375	738	157
Shipping	NMVOC	1	1	3	1	1

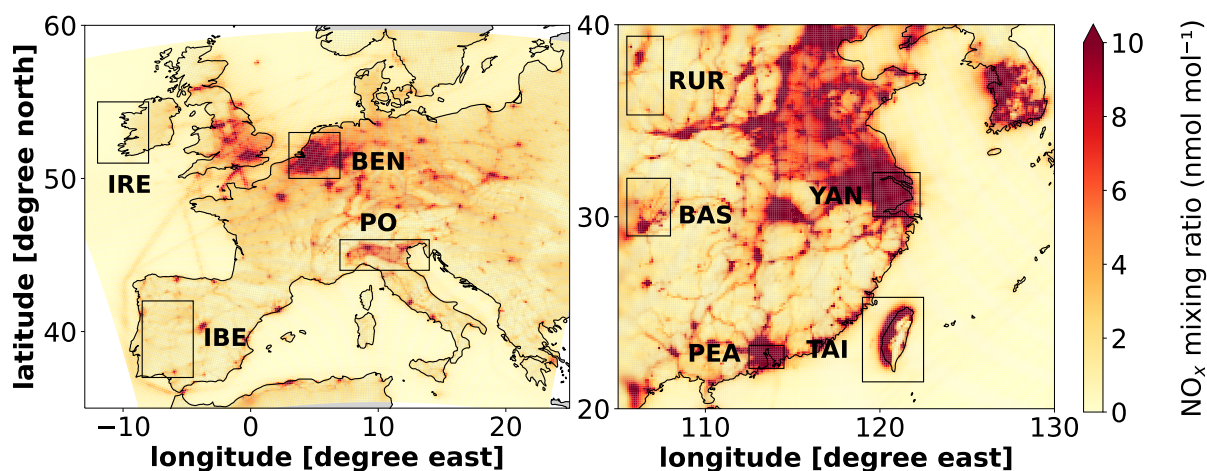


Figure C.42: Seasonal mean (JJA 2017–2018) of the ground-level NO_x mixing ratios in nmol mol^{-1} in CM12 for Europe (left) and East Asia (right). Rectangles mark the study areas labelled after Table 5.1. For East Asia the study areas are labelled after Table 5.2.

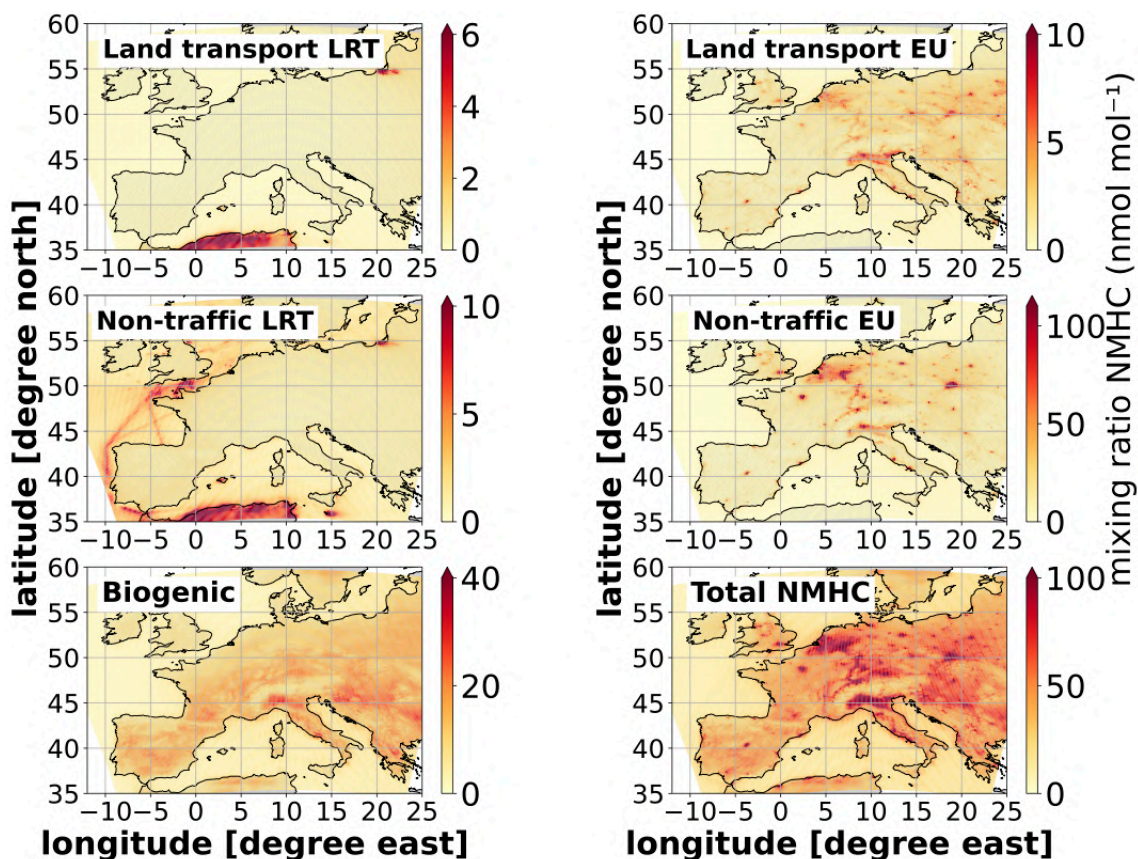


Figure C.43: Seasonal mean (JJA 2017–2018) absolute contributions of NMHC as mixing ratios in nmol mol^{-1} from long-range transported (LRT: ROW + NA + EA) NMHC and European NMHC emissions by sectors and total NMHC (lower right) as simulated with CM12.

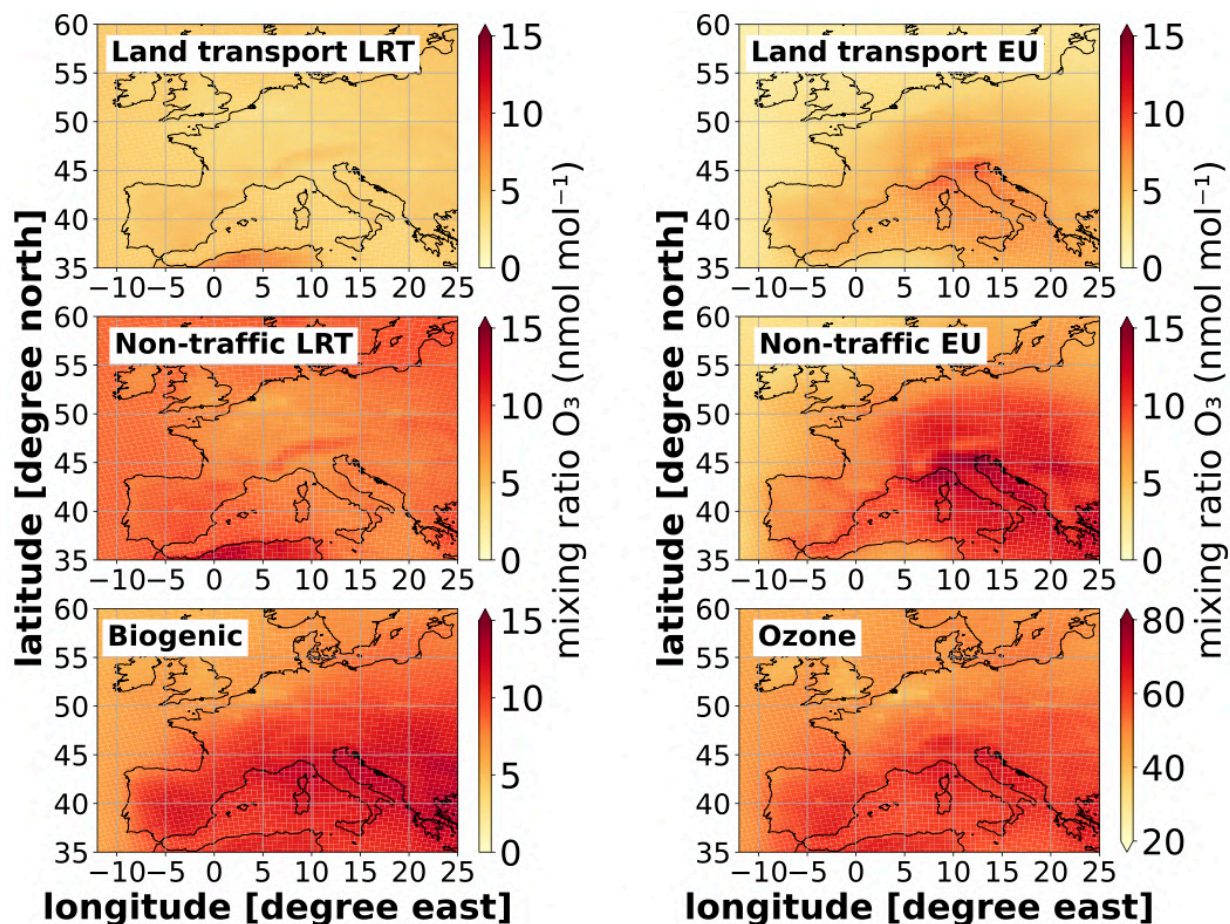


Figure C.44: Seasonal mean (JJA 2017–2018) absolute contribution as mixing ratios in nmol mol^{-1} of O_3 from long-range transported (LRT: ROW + NA + EA) and European emissions as simulated with CM50.

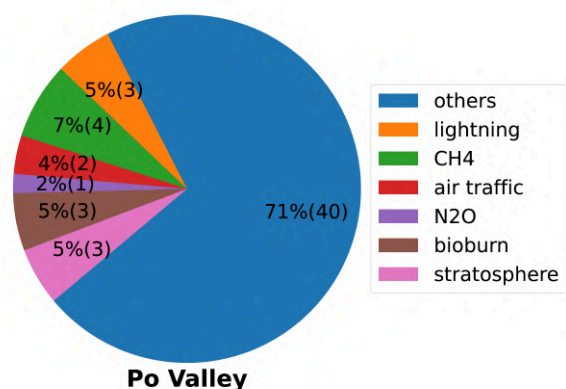


Figure C.45: Absolute (brackets) and relative contribution as mixing ratios in nmol mol^{-1} and %, respectively, of all sectors to ground-level O_3 as seasonal mean (JJA 2017–2018) in the Po Valley. "Others" here indicates the sum of the sectors land transport, anthropogenic non-traffic, shipping, and biogenic.

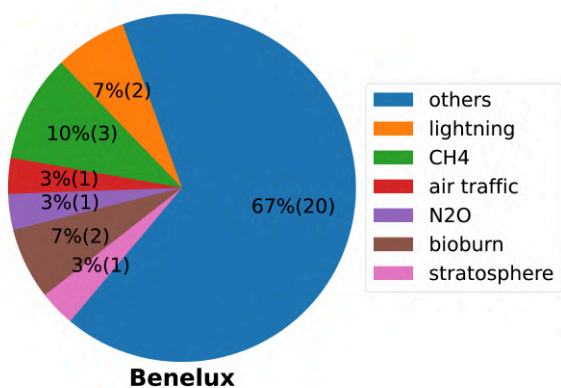


Figure C.46: Absolute (brackets) and relative contribution as mixing ratios in nmol mol⁻¹ and %, respectively, of all sectors to ground-level O₃ as seasonal mean (JJA 2017–2018) in the Benelux region. "Others" here indicates the sum of the sectors land transport, anthropogenic non-traffic, shipping, and biogenic.

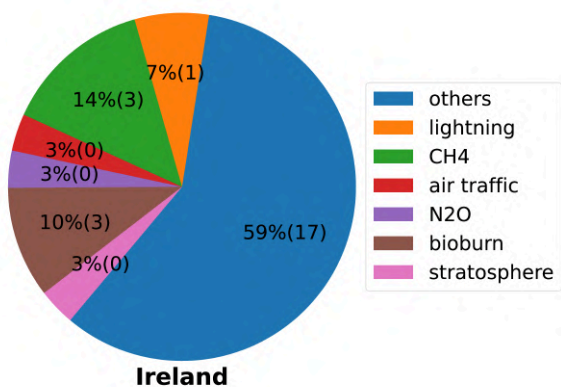


Figure C.47: Absolute (brackets) and relative contribution as mixing ratios in nmol mol⁻¹ and %, respectively, of all sectors to ground-level O₃ as seasonal mean (JJA 2017–2018) in Ireland. "Others" here indicates the sum of the sectors land transport, anthropogenic non-traffic, shipping, and biogenic.

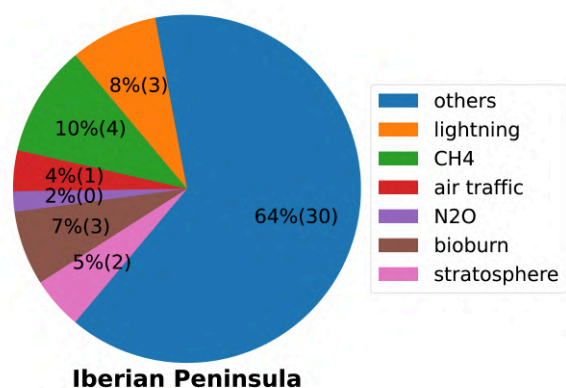


Figure C.48: Absolute (brackets) and relative contribution as mixing ratios in nmol mol⁻¹ and %, respectively, of all sectors to ground-level O₃ as seasonal mean (JJA 2017–2018) over the Iberian Peninsula. "Others" here indicates the sum of the sectors land transport, anthropogenic non-traffic, shipping, and biogenic.

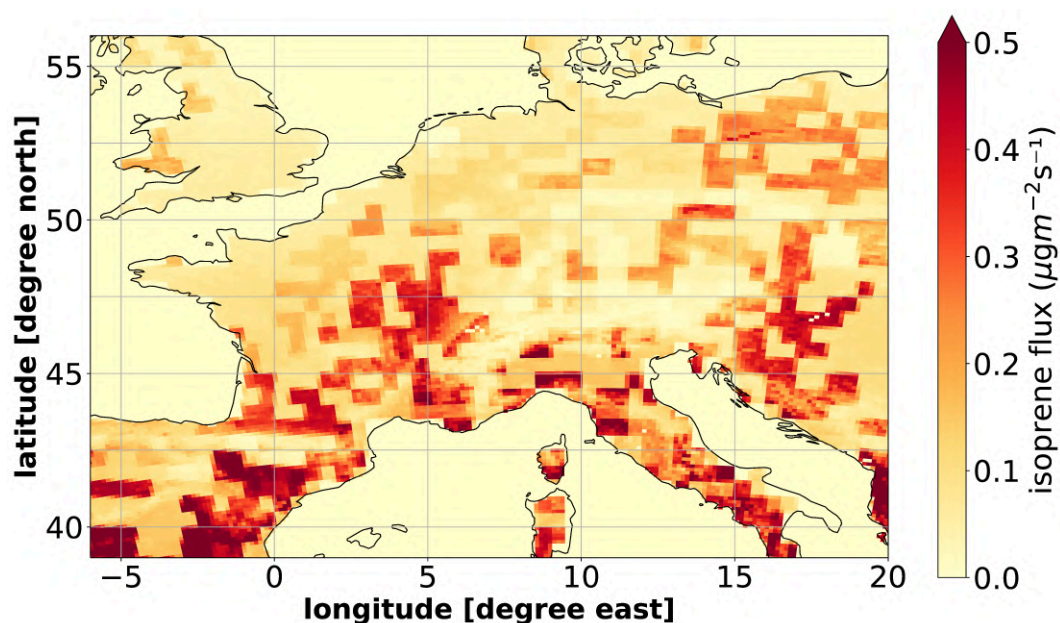


Figure C.49: Mean of the ground-level isoprene (C₅H₈) emission flux in $\mu\text{g m}^{-2}\text{s}^{-1}$ for JJA 2017–2018 in CM12 for Europe.

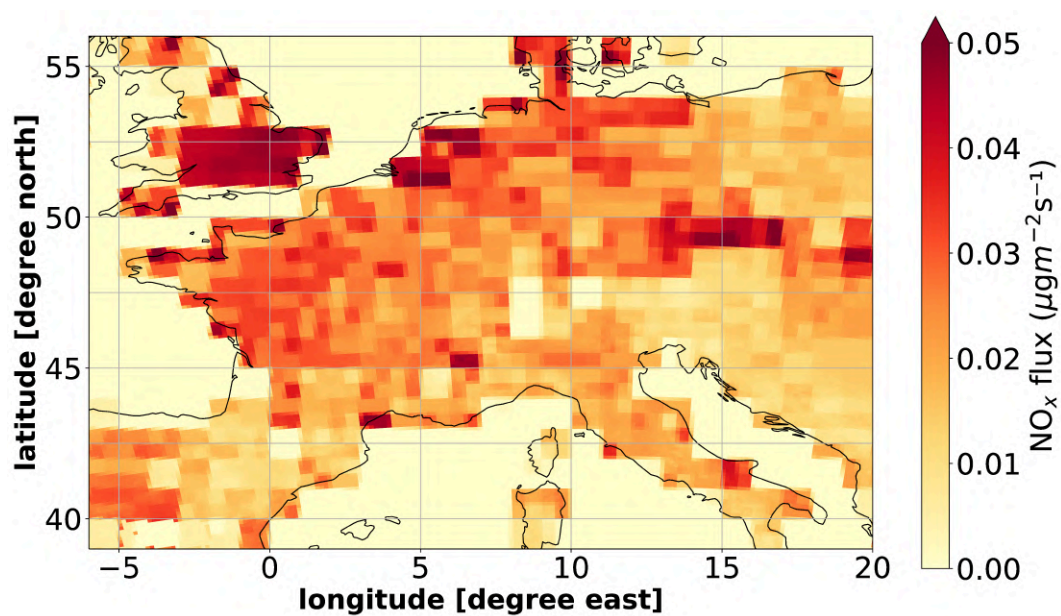


Figure C.50: Mean of the ground-level soil NO_x emission flux in $\mu\text{g m}^{-2}\text{s}^{-1}$ for JJA 2017–2018 in CM12 for Europe.

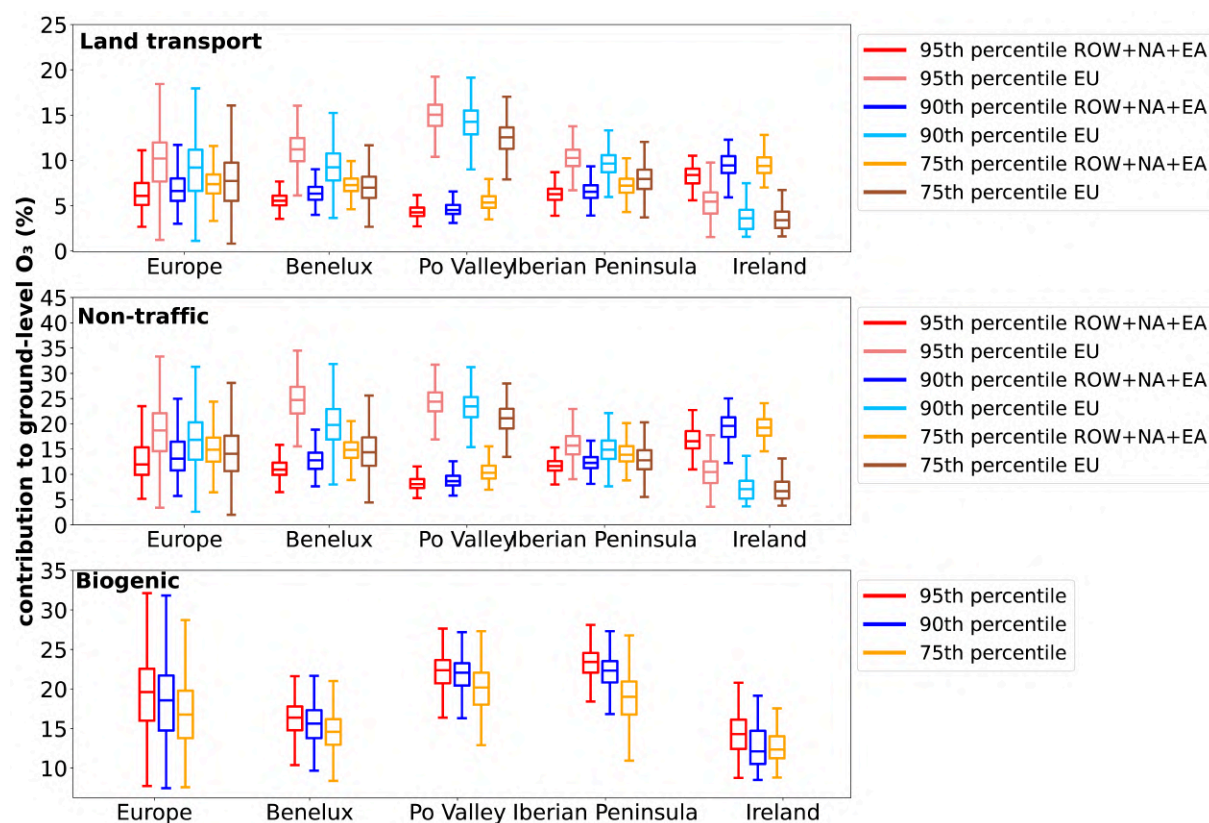


Figure C.51: Box-whisker plot showing the seasonal mean (JJA 2017–2018) contributions of the most important emission sectors at the 95th, 90th, and 75th percentiles of ozone as simulated by CM12 for JJA 2017–2018. The upper panel shows the relative regional contributions of O_3^{teu} and the sum of long-range transported relative contributions of O_3^{tra} , O_3^{tna} and O_3^{tea} . The middle panel shows the regional relative contributions of O_3^{ieu} and the sum of long-range transported relative contributions of O_3^{ind} , O_3^{ina} and O_3^{iea} . The lower panel shows the relative contributions of O_3^{soi} . The lower and upper ends of the boxes indicate the 25th and 75th percentile of the corresponding regional distribution, respectively, the bar the median, and the whiskers are defined as ± 1.5 the interquartile range of the contributions of all grid boxes within the indicated region.

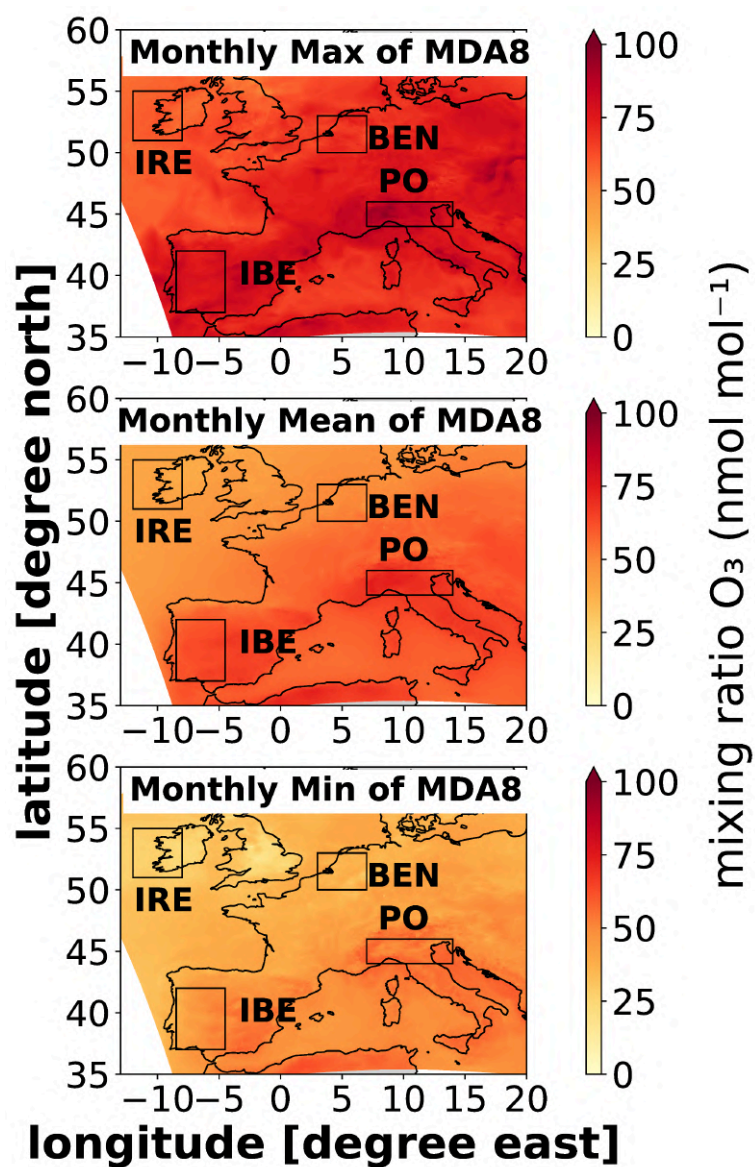


Figure C.52: Shown is ozone during the seasonal (JJA 2017–2018) maximum of the maximum daily 8-h average (MDA8) (upper panel), the seasonal mean of MDA8 (middle panel) and the seasonal minimum of MDA8 (lower panel) as mixing ratios in nmol mol⁻¹ based on 1-hourly model output from CM12 for Europe. The black rectangles mark the study areas labelled after Table 5.1.

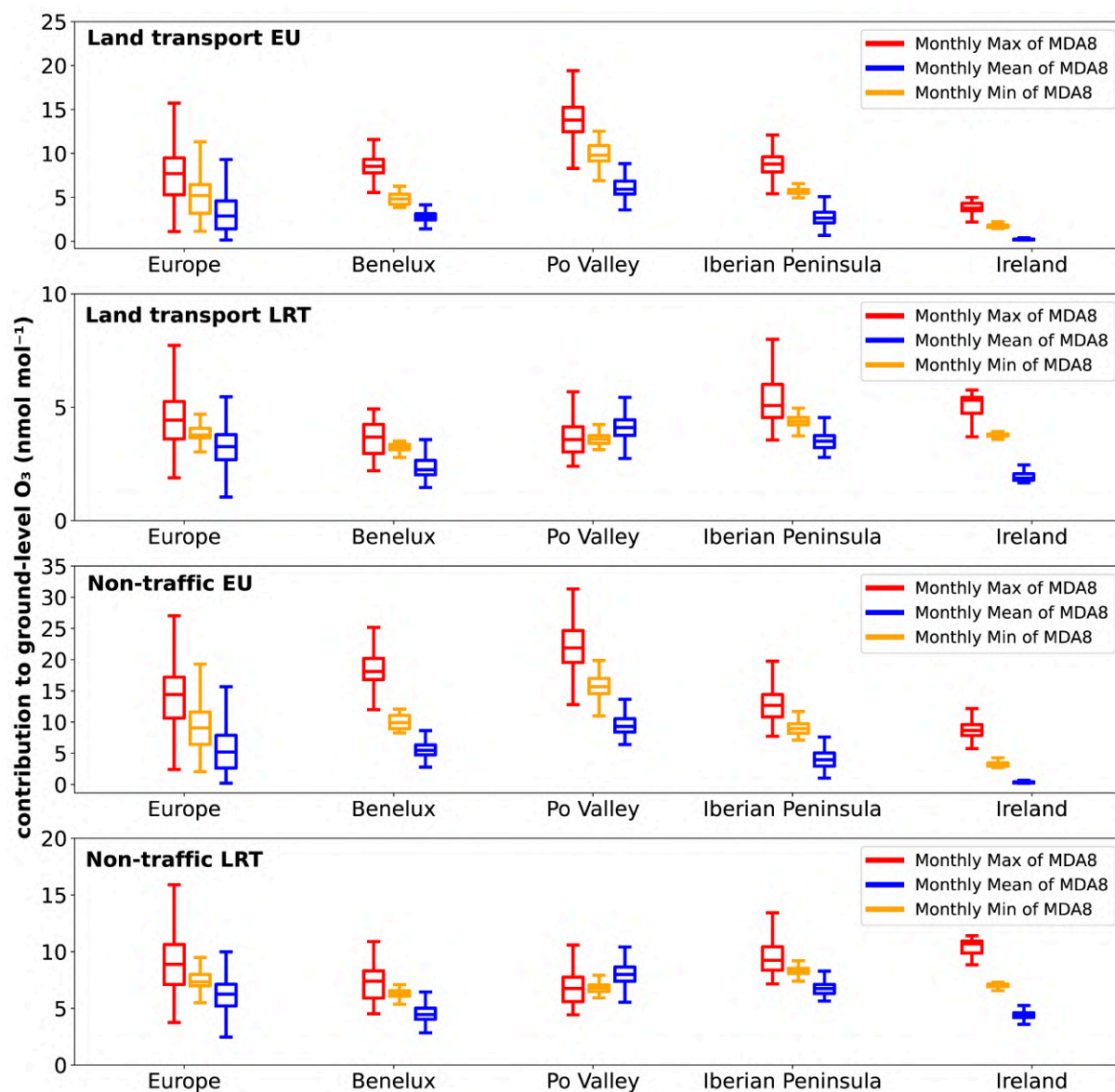


Figure C.53: Box-whisker plot showing the contributions of the most important European emission sectors of ozone as simulated by CM12 for JJA 2017–2018. Shown are ozone contributions for European (EU) and long range transported (LRT) land transport and anthropogenic non-traffic emissions to ground-level ozone during the seasonal maximum of the maximum daily 8-h average (MDA8), the seasonal mean of MDA8 and the seasonal minimum of MDA8 as ozone mixing ratio in nmol mol⁻¹ based on 1-hourly model output. The lower and upper ends of the boxes indicate the 25th and 75th percentile corresponding regional distribution, respectively, the bar the median, and the whiskers the minimum and maximum contributions of all grid boxes within the indicated region.

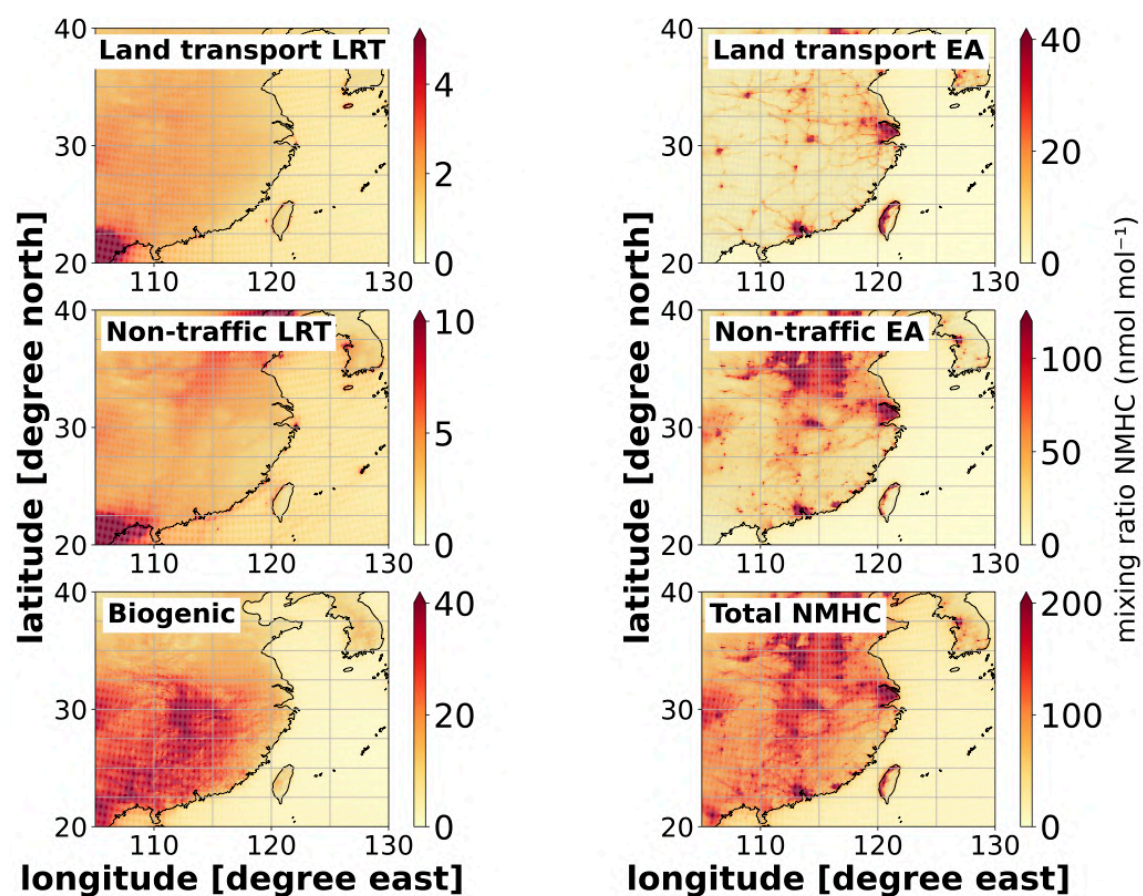


Figure C.54: Seasonal mean (JJA 2017–2018) absolute contributions of NMHC as mixing ratios in nmol mol^{-1} from long-range transported (LRT: ROW + NA + EU) NMHC and East Asian NMHC emissions by sectors and total NMHC (lower right) as simulated with CM12.

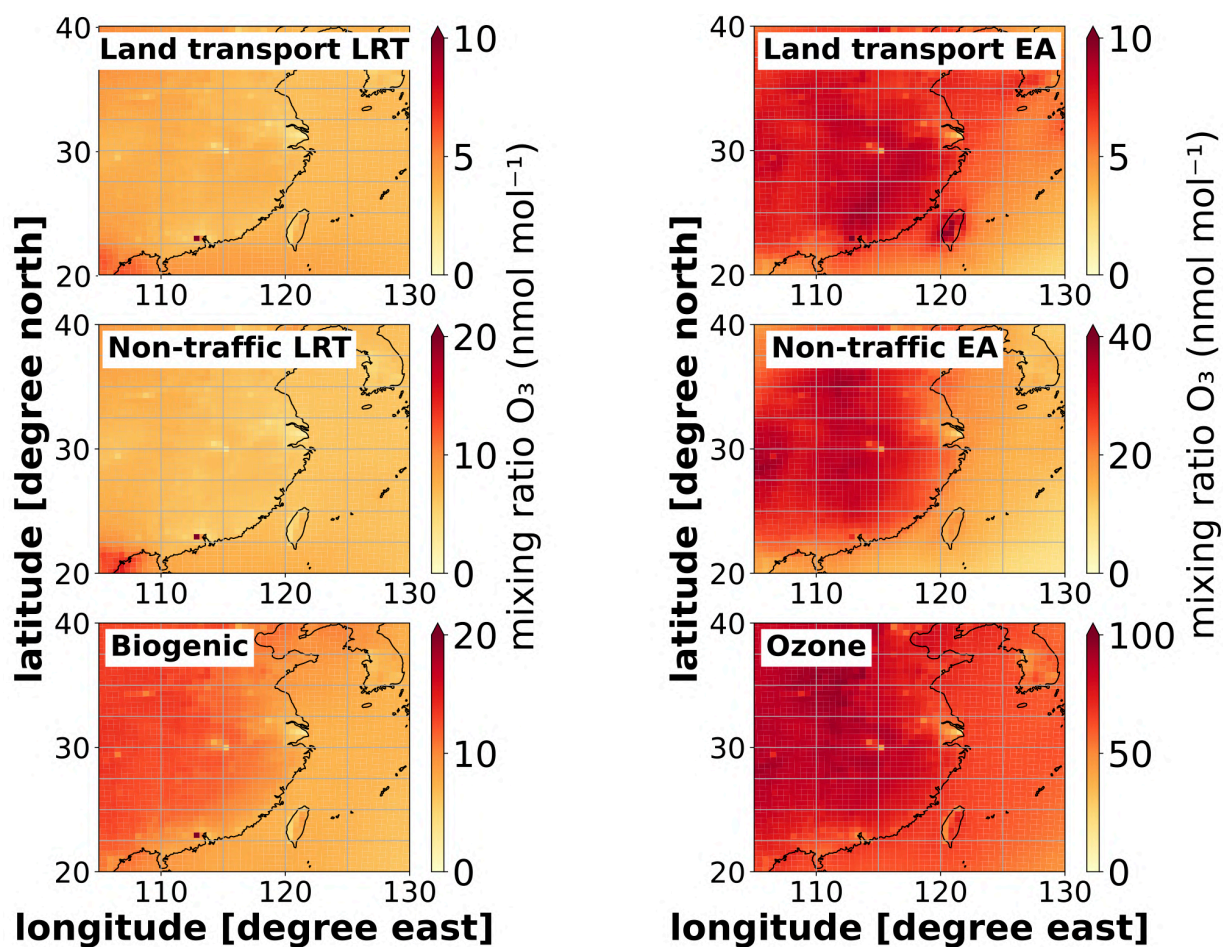


Figure C.55: Seasonal mean (JJA 2017–2018) absolute contribution as mixing ratios in nmol mol^{-1} to O_3 from long-range transported (LRT: ROW + NA + EA) and European emissions as simulated with CM50.

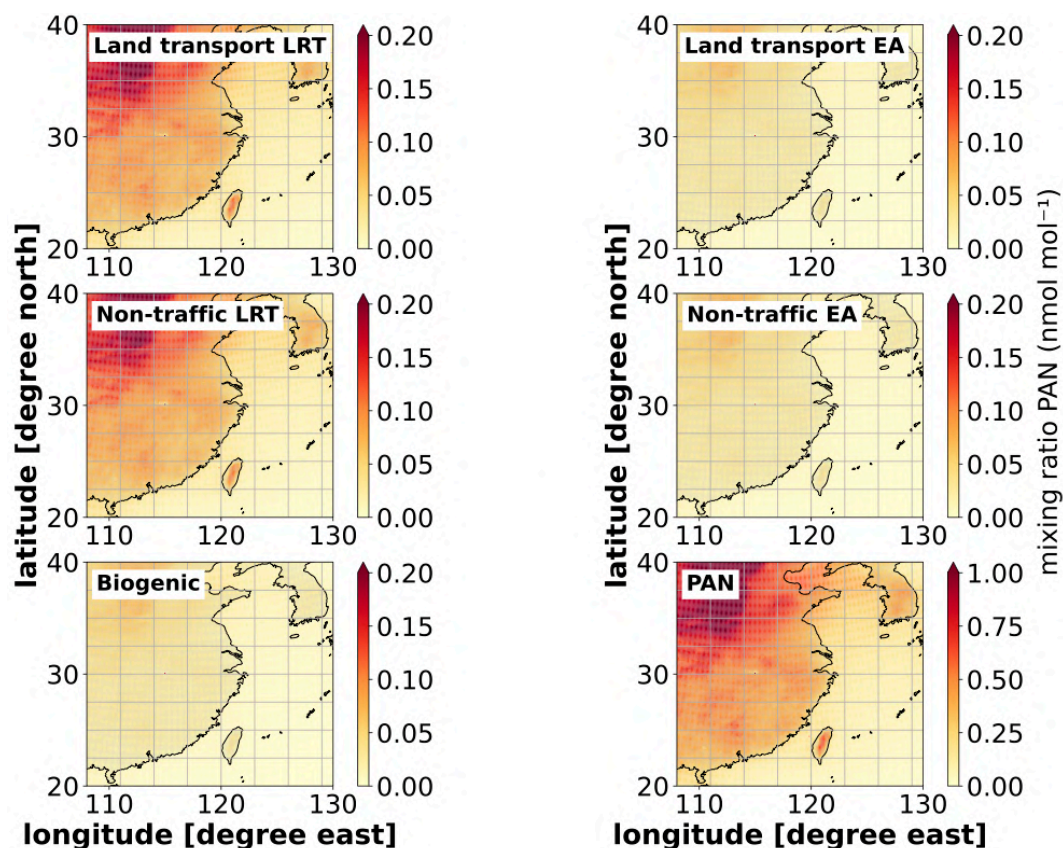


Figure C.56: Seasonal mean (JJA 2017–2018) absolute contributions of PAN as mixing ratios in nmol mol^{-1} from long-range transported (LRT: ROW + NA + EU) PAN and East Asian PAN formed from East Asian sources, and total PAN (lower right), as simulated with CM12.

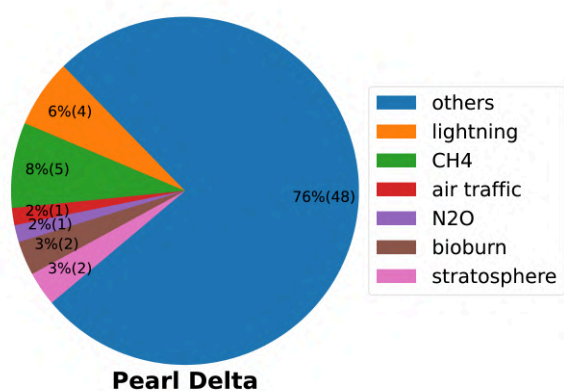


Figure C.57: Absolute (brackets) and relative contribution as mixing ratios in nmol mol^{-1} and %, respectively, of all sectors to ground-level O_3 as seasonal mean for JJA 2017–2018 in the Pearl Delta. "Others" here indicates the sum of the sectors land transport, anthropogenic non-traffic, shipping, and biogenic.

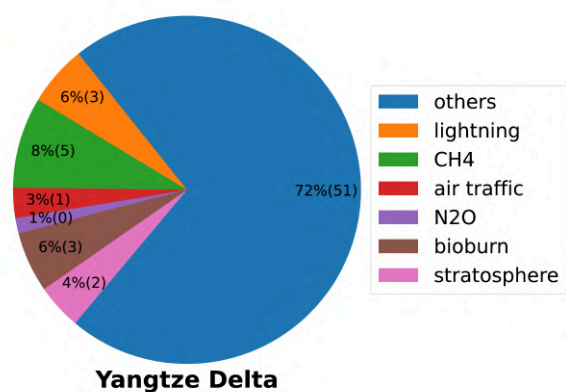


Figure C.58: Absolute (brackets) and relative contribution as mixing ratios in nmol mol⁻¹ and %, respectively, of all sectors to ground-level O₃ as seasonal mean for JJA 2017–2018 in the Yangtze Delta. "Others" here indicates the sum of the sectors land transport, anthropogenic non-traffic, shipping, and biogenic.

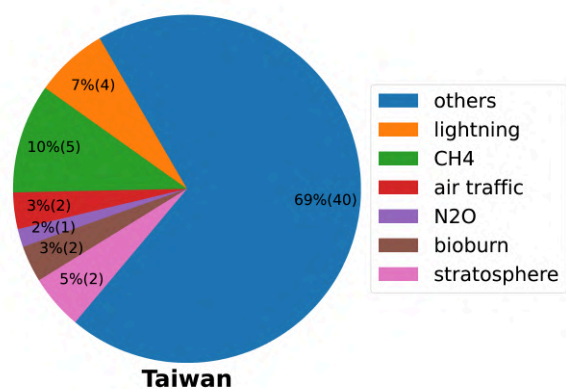


Figure C.59: Absolute (brackets) and relative contribution as mixing ratios in nmol mol⁻¹ and %, respectively, of all sectors to ground-level O₃ as seasonal mean for JJA 2017–2018 in Taiwan. "Others" here indicates the sum of the sectors land transport, anthropogenic non-traffic, shipping, and biogenic.

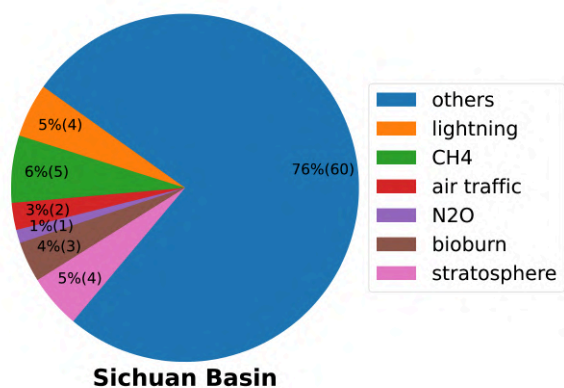


Figure C.60: Absolute (brackets) and relative contribution as mixing ratios in nmol mol⁻¹ and %, respectively, of all sectors to ground-level O₃ as seasonal mean for JJA 2017–2018 in the Sichuan Basin. "Others" here indicates the sum of the sectors land transport, anthropogenic non-traffic, shipping, and biogenic.

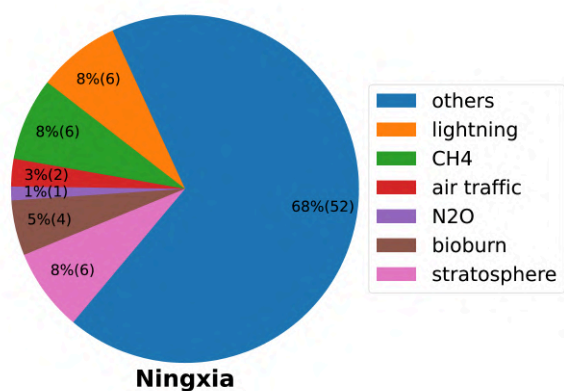


Figure C.61: Absolute (brackets) and relative contribution as mixing ratios in nmol mol⁻¹ and %, respectively, of all sectors to ground-level O₃ as seasonal mean for JJA 2017–2018 in Ningxia. "Others" here indicates the sum of the sectors land transport, anthropogenic non-traffic, shipping, and biogenic.

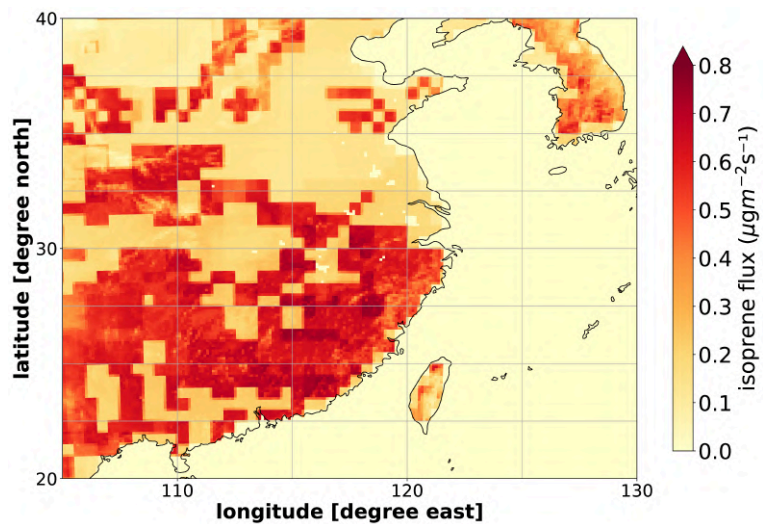


Figure C.62: Mean of the ground-level isoprene (C_5H_8) emission flux in $\mu\text{g m}^{-2}\text{s}^{-1}$ for JJA 2017–2018 in CM12 for East Asia.

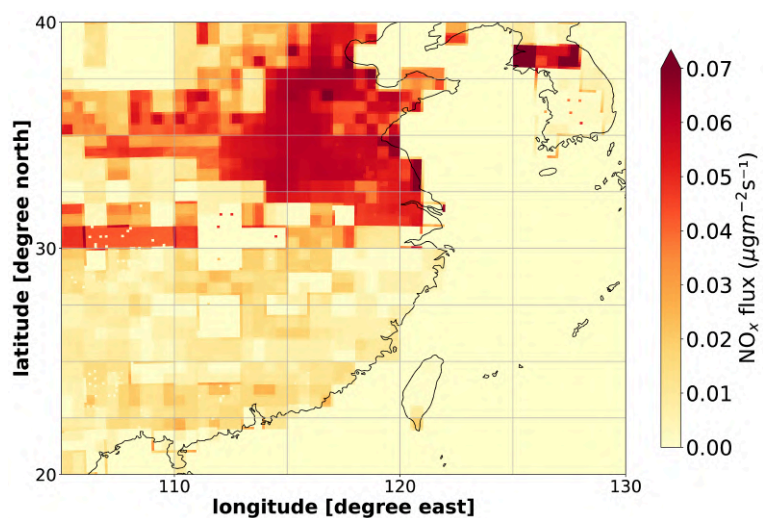


Figure C.63: Mean of the ground-level soil NO_x emission flux in $\mu\text{g m}^{-2}\text{s}^{-1}$ for JJA 2017–2018 in CM12 for East Asia.

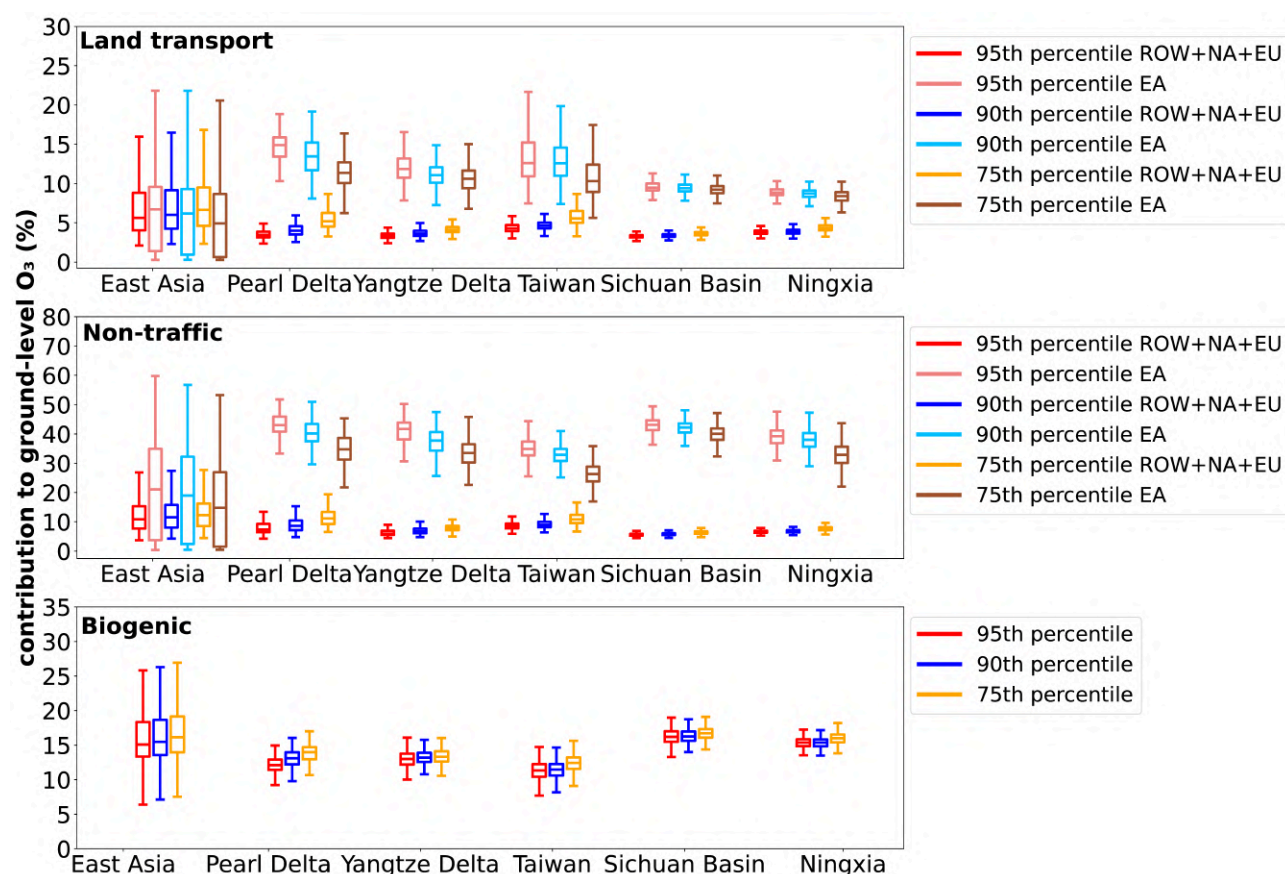


Figure C.64: Box-whisker plot showing the seasonal mean (JJA 2017–2018) contributions of the most important emission sectors at the 95th, 90th, and 75th percentiles of ozone as simulated by CM12 in East Asia. The upper panel shows the relative regional contributions of O_3^{tea} and the sum of long-range transported relative contributions of O_3^{tra} , O_3^{tna} and O_3^{teu} . The middle panel shows the regional relative contributions of O_3^{iea} and the sum of long-range transported relative contributions of O_3^{ind} , O_3^{ina} and O_3^{ieu} . The lower panel shows the relative contributions of O_3^{soi} . The lower and upper ends of the boxes indicate the 25th and 75th percentile of the corresponding regional distribution, respectively, the bar the median, and the whiskers are defined as ± 1.5 the interquartile range of the contributions of all grid boxes within the indicated region.

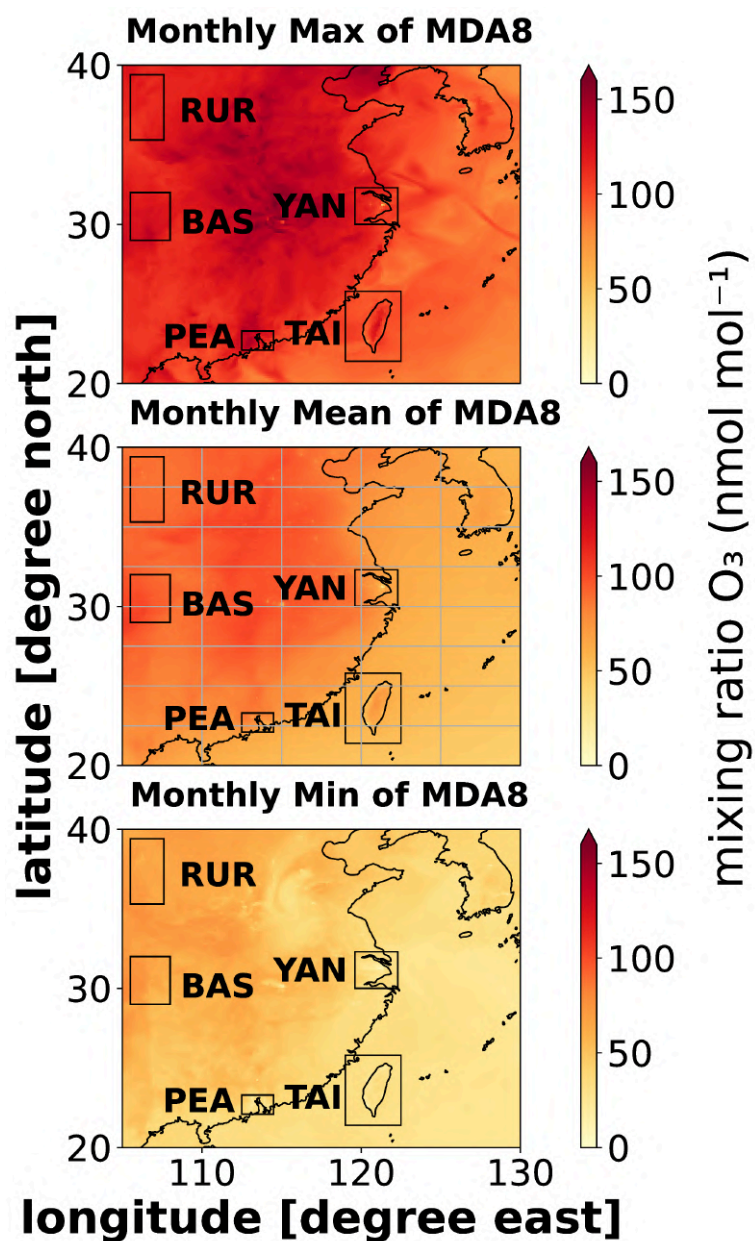


Figure C.65: Shown is ozone in JJA 2017–2018 during the seasonal maximum of the maximum daily 8-h average (MDA8) (upper panel), the seasonal mean of MDA8 (middle panel) and the seasonal minimum of MDA8 (lower panel) as mixing ratios in nmol mol⁻¹ based on 1-hourly model output from CM12 for East Asia. The black rectangles mark the study areas labelled after Table 5.2.

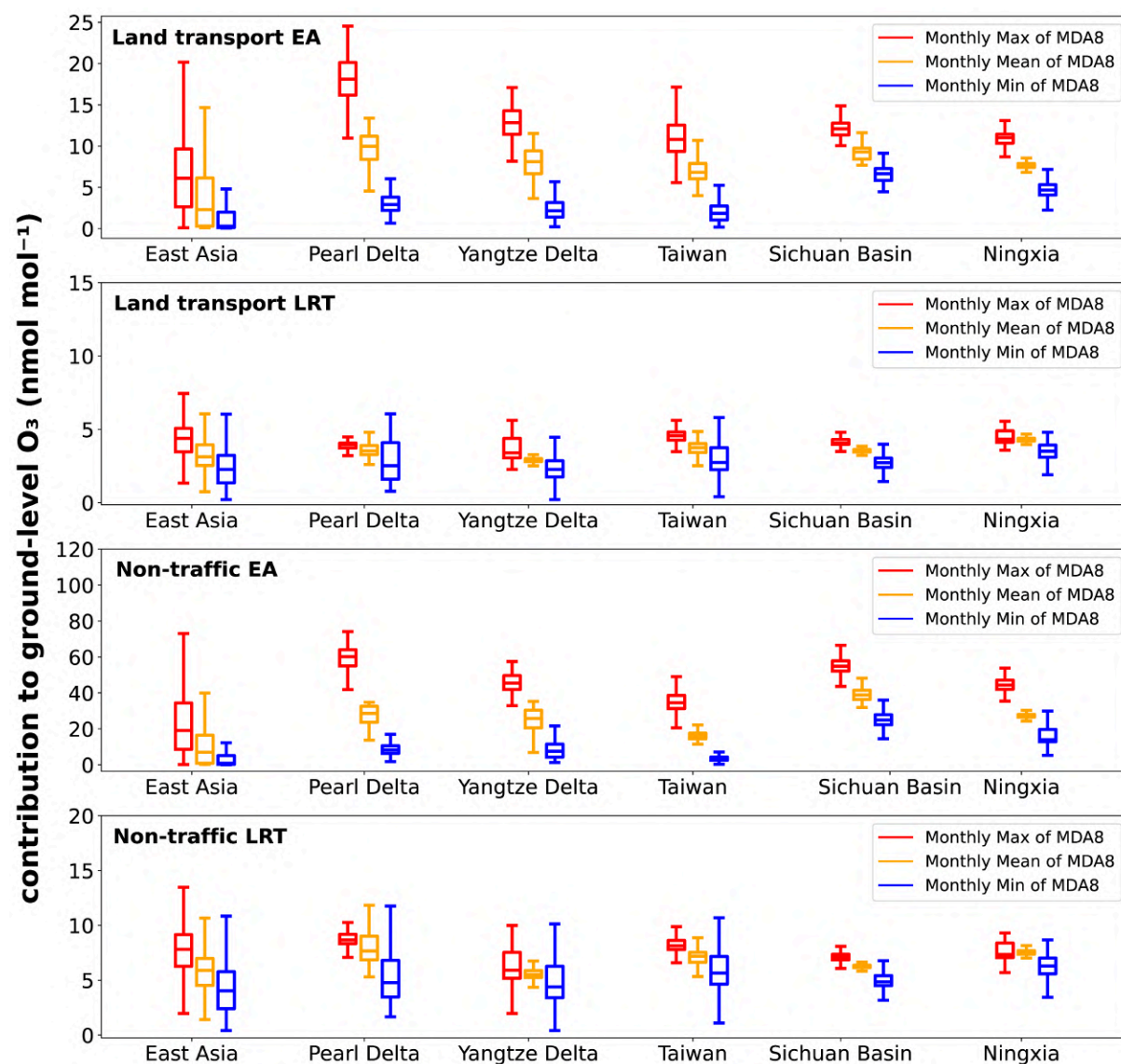


Figure C.66: Box-whisker plot showing the contributions of the most important East Asian emission sectors of ozone as simulated by CM12 for JJA 2017–2018. Shown are ozone contributions for East Asian (EA) and long range transported (LRT) land transport and anthropogenic non-traffic emissions to ground-level ozone during the seasonal maximum of the maximum daily 8-h average (MDA8), the seasonal mean of MDA8 and the seasonal minimum of MDA8 as ozone mixing ratio in nmol mol⁻¹ based on 1-hourly model output. The lower and upper ends of the boxes indicate the 25th and 75th percentile corresponding regional distribution, respectively, the bar the median, and the whiskers the minimum and maximum contributions of all grid boxes within the indicated region.

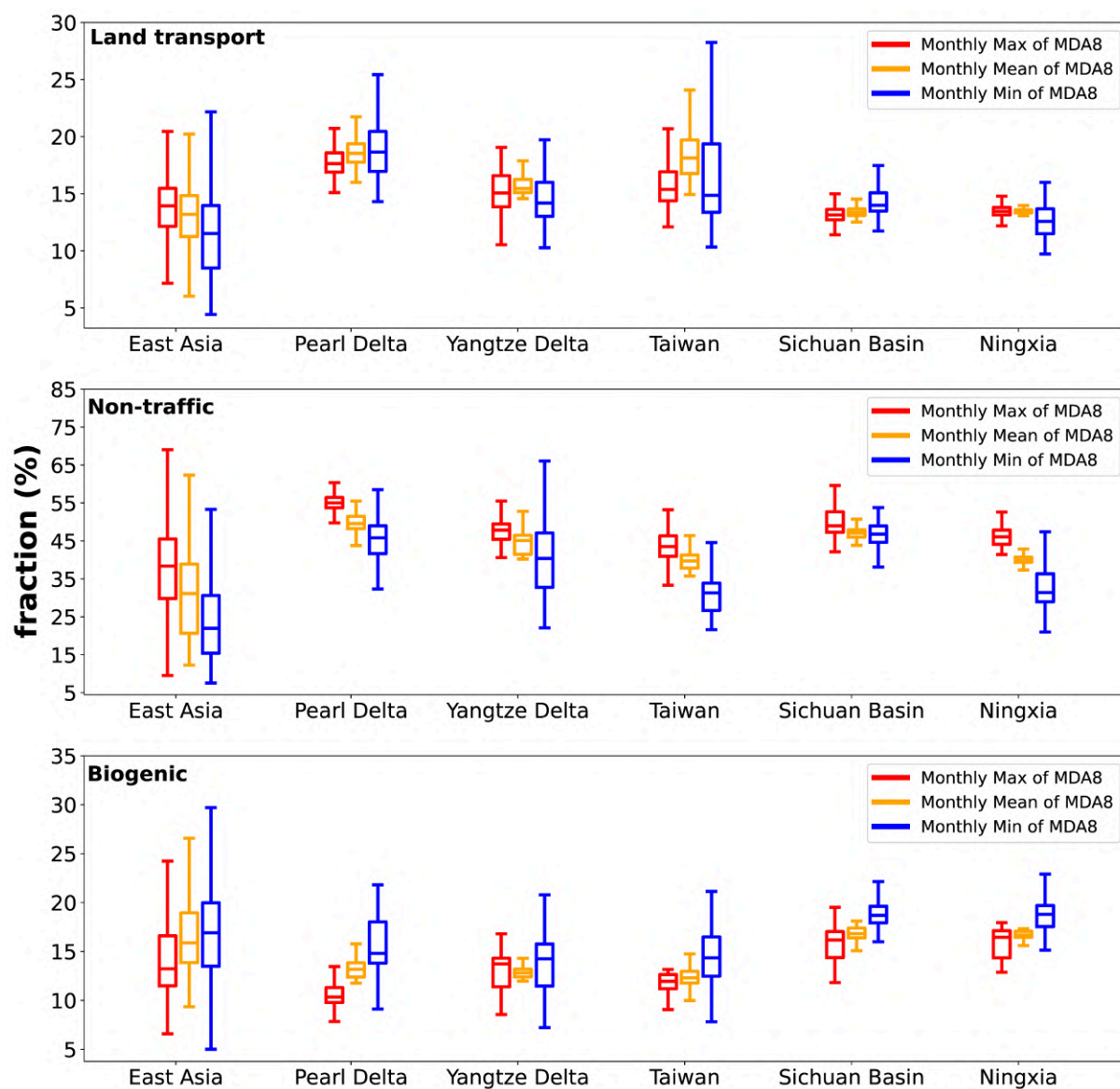


Figure C.67: Box-whisker plot showing the relative contributions (%) of the most important European emission sectors of ozone as simulated by CM12 for JJA 2017–2018. Shown are relative ozone contributions for land transport, anthropogenic non-traffic and biogenic emissions to ground-level ozone during the seasonal maximum of the maximum daily 8-h average (MDA8), the seasonal mean of MDA8 and the seasonal minimum of MDA8 based on 1-hourly model output. The lower and upper ends of the boxes indicate the 25th and 75th percentile corresponding regional distribution, respectively, the bar the median, and the whiskers the minimum and maximum contributions of all grid boxes within the indicated region.

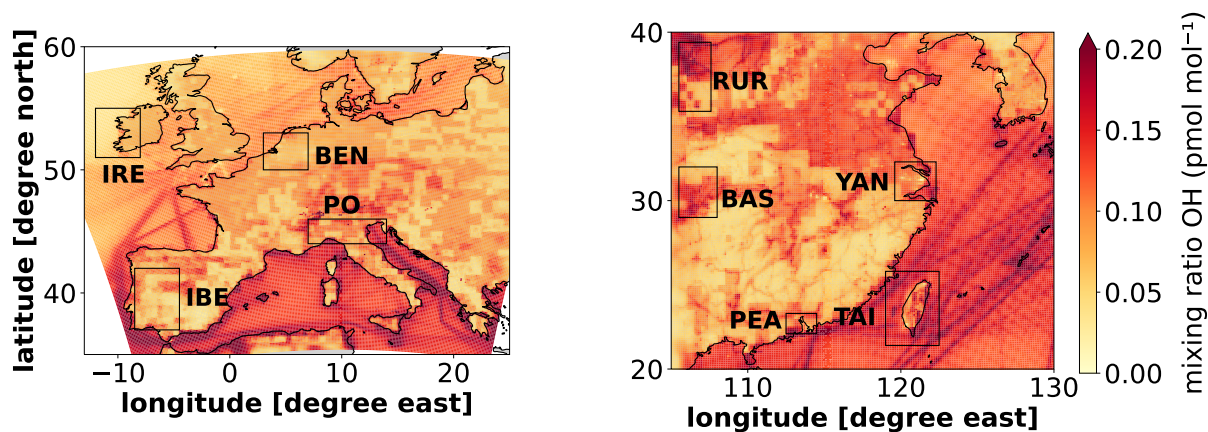


Figure C.68: Seasonal mean (JJA 2017–2018) of the ground-level OH mixing ratio pmol mol^{-1} for CM12 for Europe (left) and East Asia (right). Rectangles mark the study areas for Europe labelled after Table 5.1. East Asian study areas are labelled after Table 5.2.

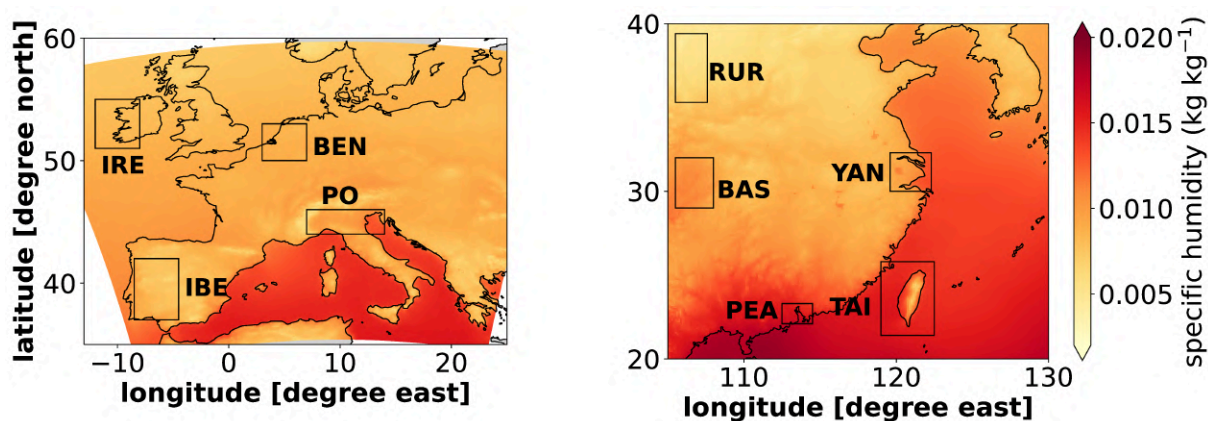


Figure C.69: Seasonal mean (JJA 2017–2018) of the specific humidity in kg kg^{-1} for CM12 for Europe (left) and East Asia (right). Rectangles mark the study areas for Europe labelled after Table 5.1. East Asian study areas are labelled after Table 5.2.

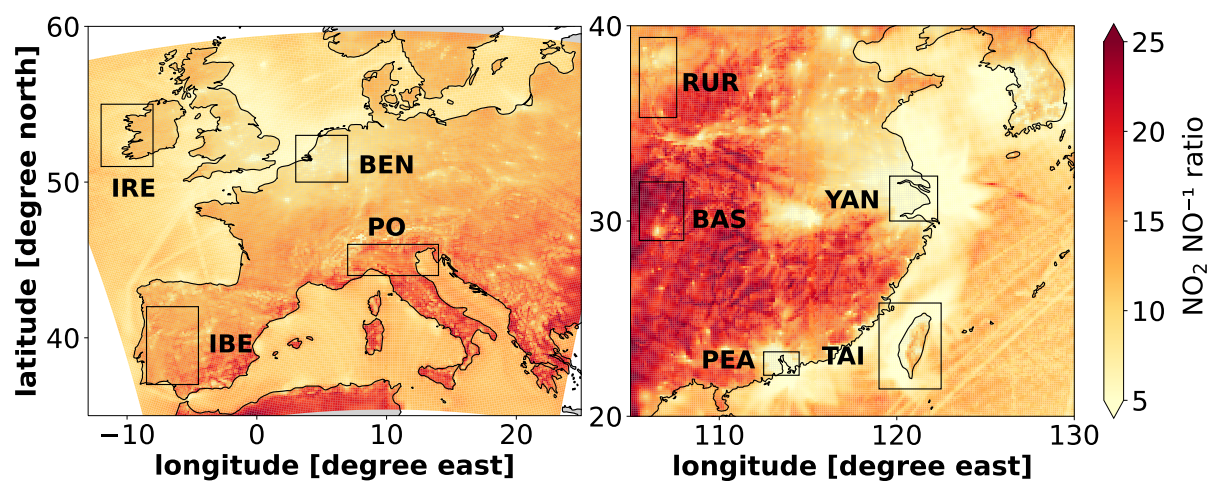


Figure C.70: Seasonal mean (JJA 2017–2018) of the $\text{NO}_2\text{-NO}^{-1}$ ratio for CM12 for Europe (left) and East Asia (right). Rectangles mark the study areas for Europe labelled after Table 5.1. East Asian study areas are labelled after Table 5.2.

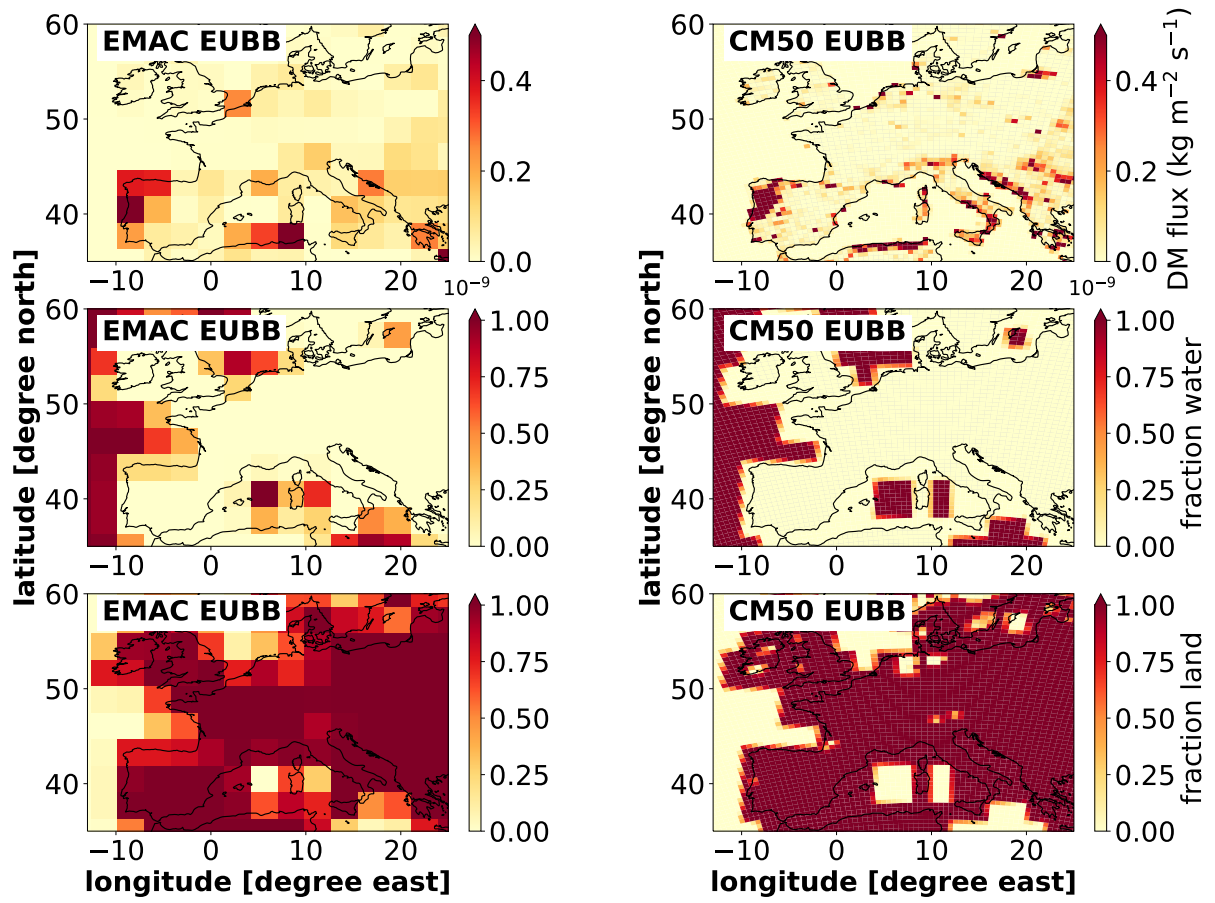


Figure C.71: Annual mean (2017–2018) of the dry particulate matter (DM) flux in $\text{kg m}^{-2} \text{s}^{-1}$ of the model results from EUBB for the instances EMAC (upper left) and CM50 (upper right) for Europe. Fraction of the firetype (FT) water middle left (EMAC) and middle right (CM50) panel. Sum of all land firetypes (FT) land lower left (EMAC) and lower right (CM50) panel.

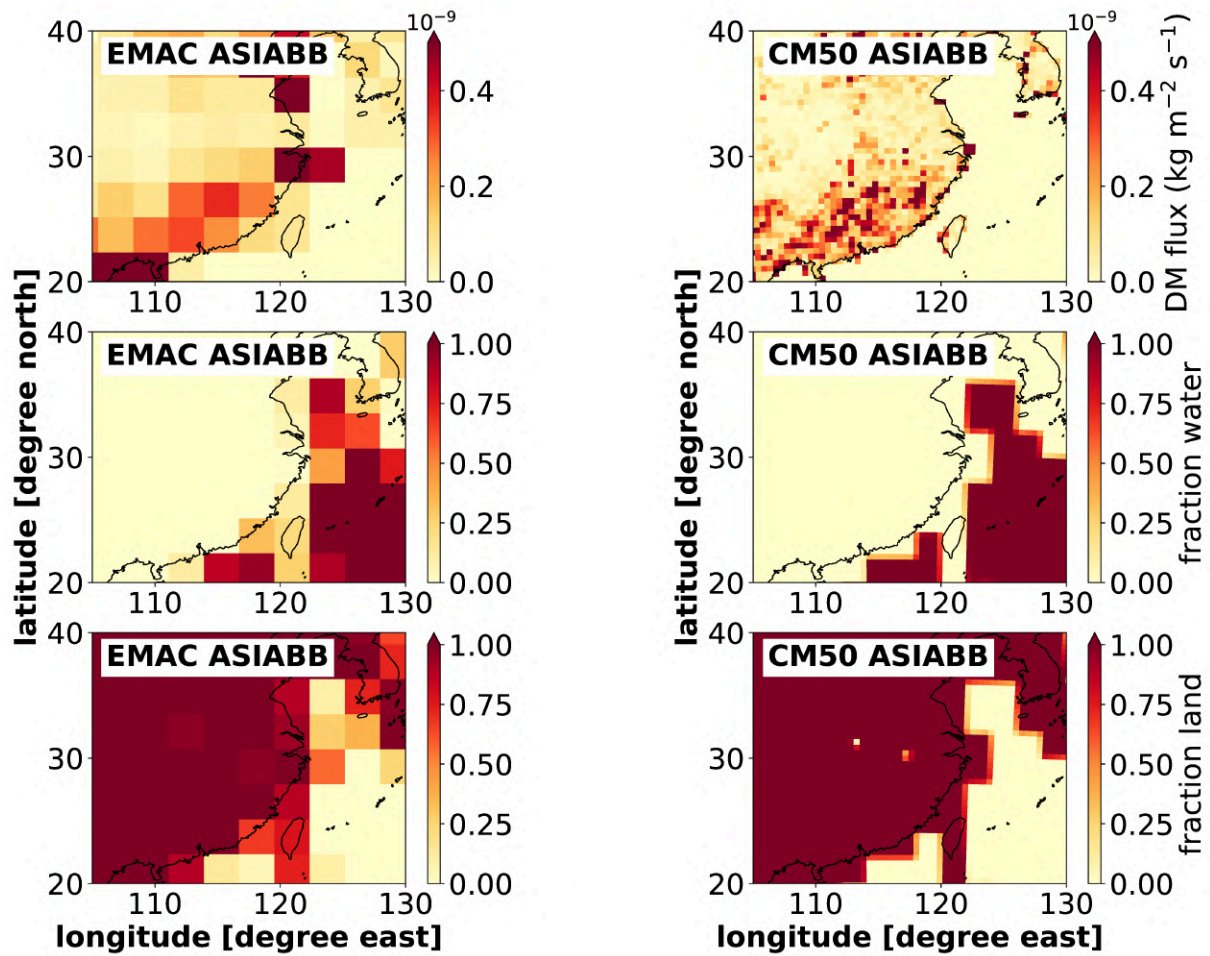


Figure C.72: Annual mean (2017–2018) of the dry particulate matter (DM) flux in $\text{kg m}^{-2} \text{s}^{-1}$ of the model results from ASIABB for the instances EMAC (upper left) and CM50 (upper right) for East Asia. Fraction of the firetype (FT) water middle left (EMAC) and middle right (CM50) panel. Sum of all land firetypes (FT) land lower left (EMAC) and lower right (CM50) panel.

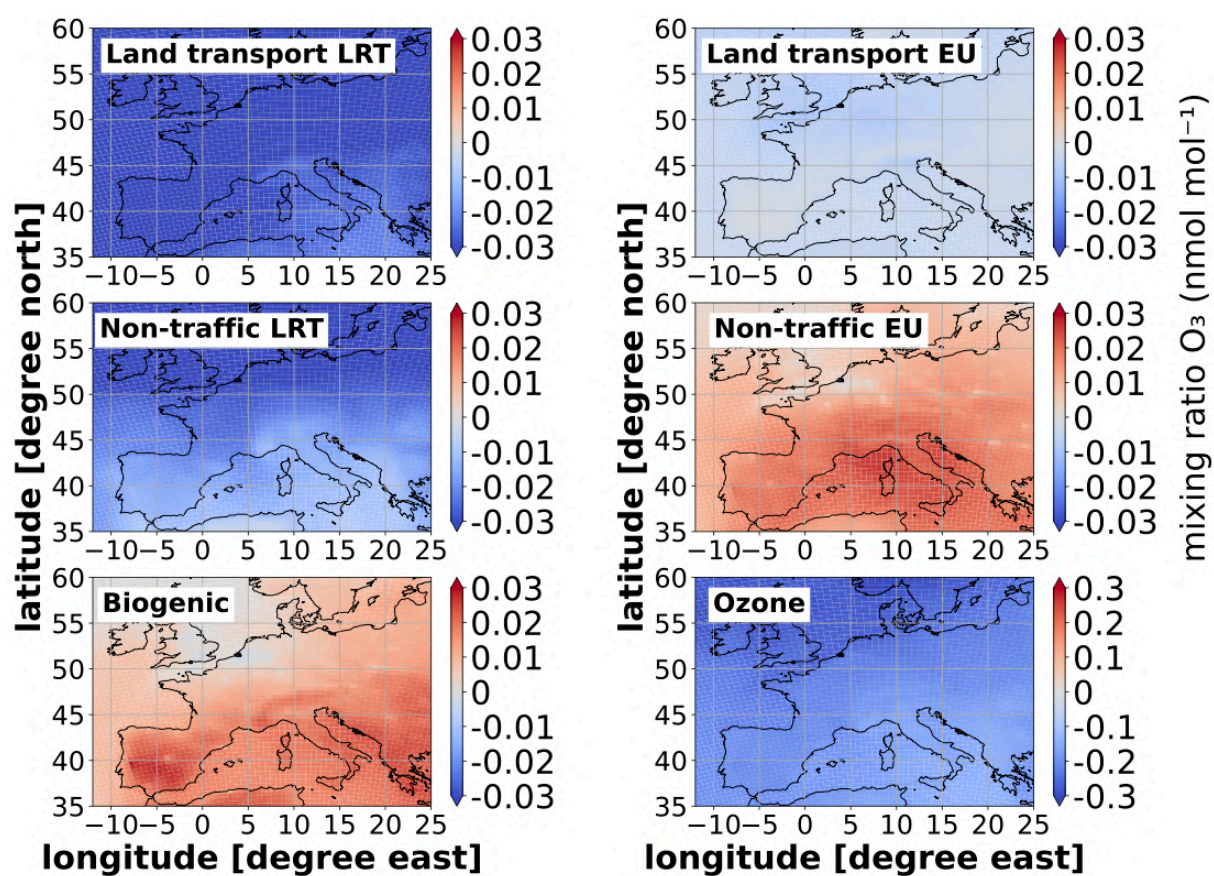


Figure C.73: Seasonal mean (2017–2018) of the ground-level O_3 contributions from long-range transported (LRT: ROW + NA + EU) and European emissions in nmol mol^{-1} as simulated by CM50. Shown are the differences between EUBB minus EUREF.

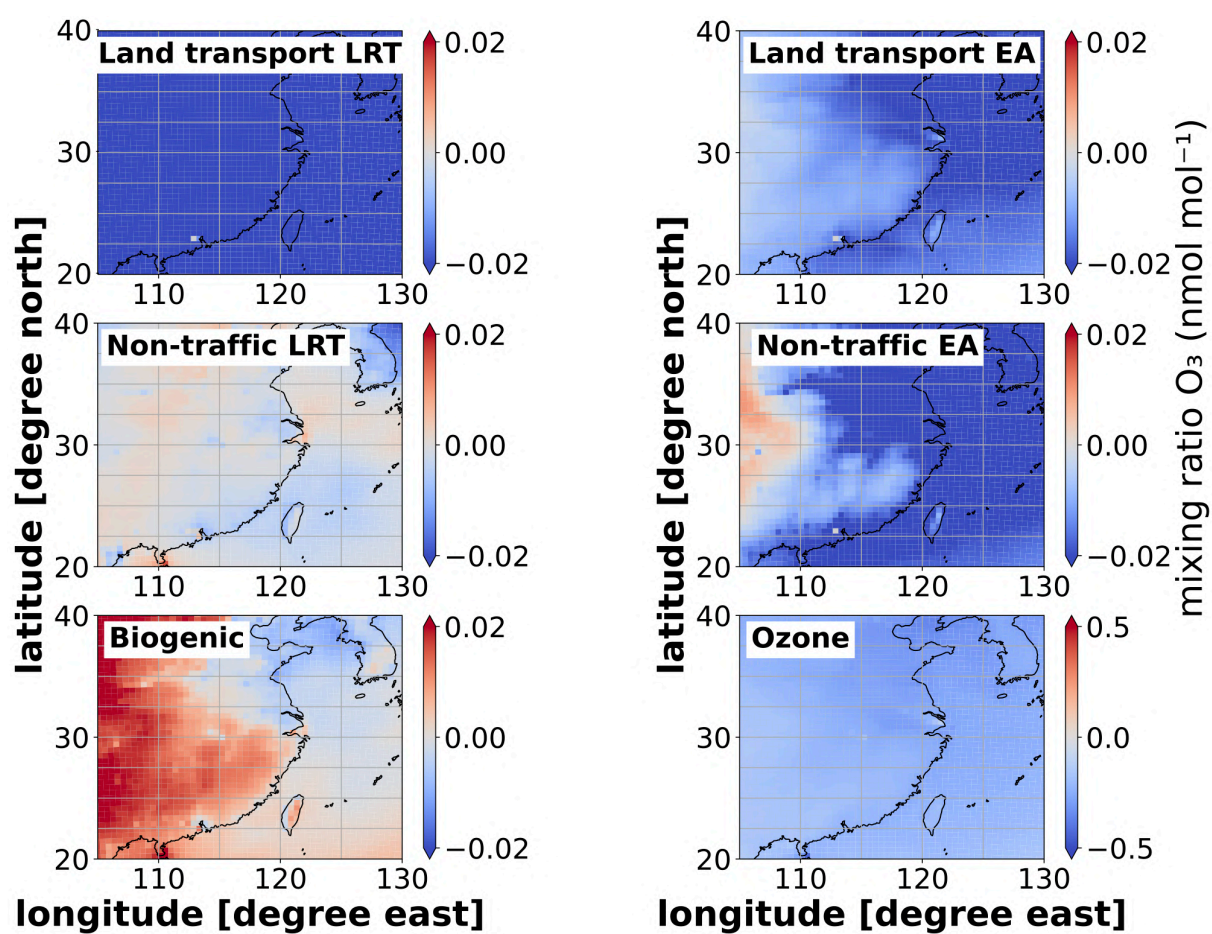


Figure C.74: Seasonal mean (2017–2018) of the ground-level O_3 contributions from long-range transported (LRT: ROW + NA + EA) and East Asian emissions in nmol mol^{-1} as simulated by CM50. Shown are the differences between EUBB minus EUREF.

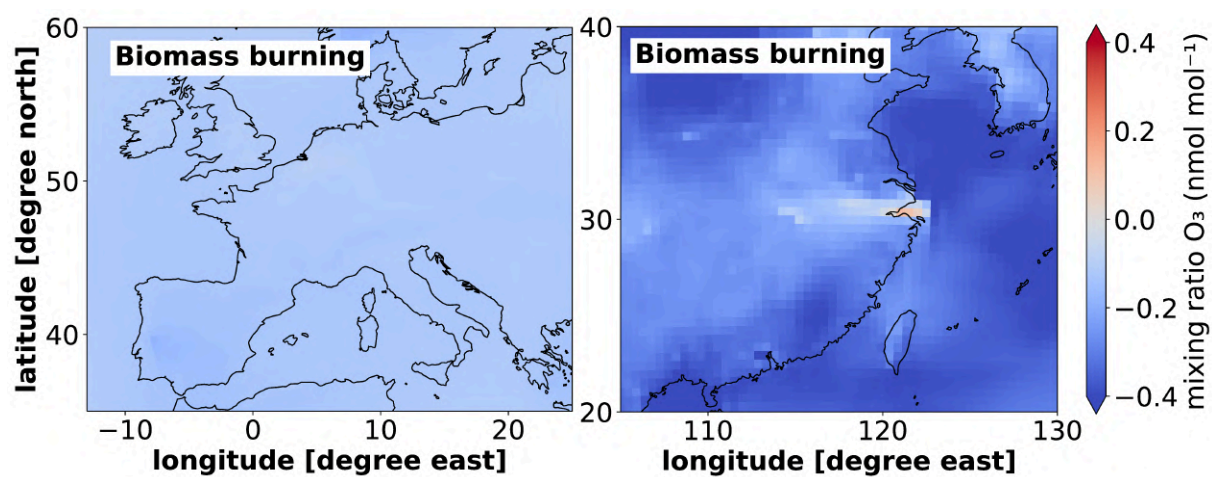


Figure C.75: Seasonal mean (JJA 2017–2018) of the ground-level O₃ contributions from biomass burning emissions in nmol mol⁻¹ as simulated by CM50. Shown are the differences between EUBB minus EUREF (left) and ASIABB minus ASIAREF (right).

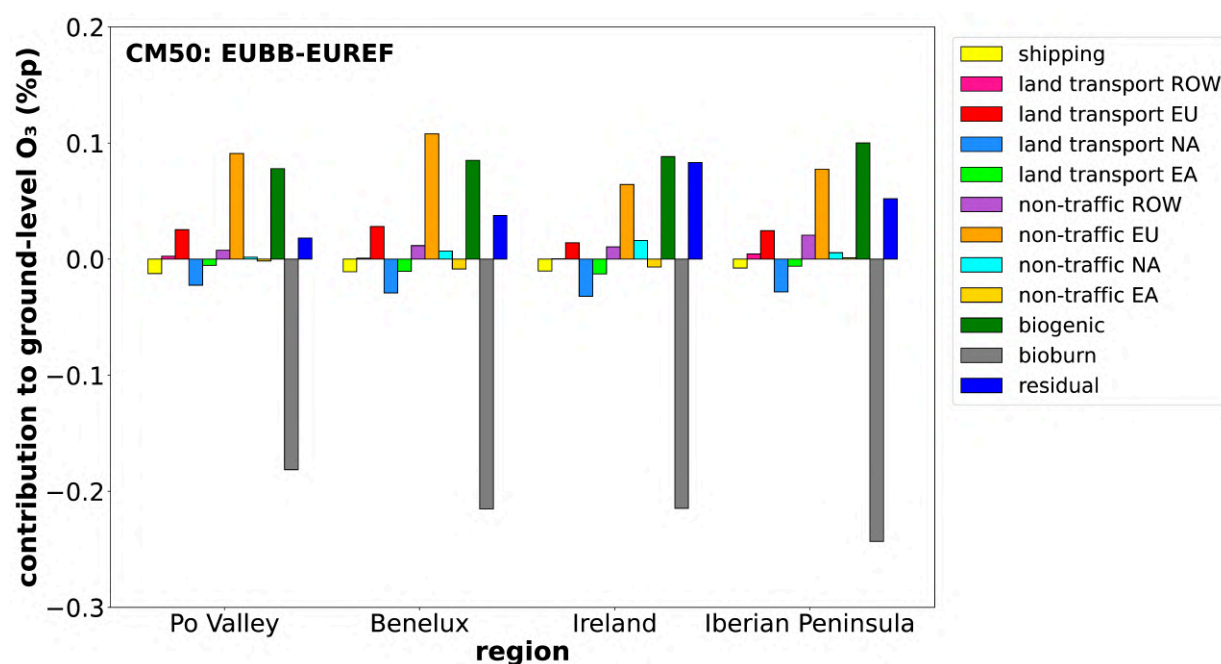


Figure C.76: Seasonal mean of the relative differences in percentage points (%p) between EUBB minus EUREF of the absolute contributions of different emissions sectors and regions to ground level ozone in four European study areas as simulated with CM50.

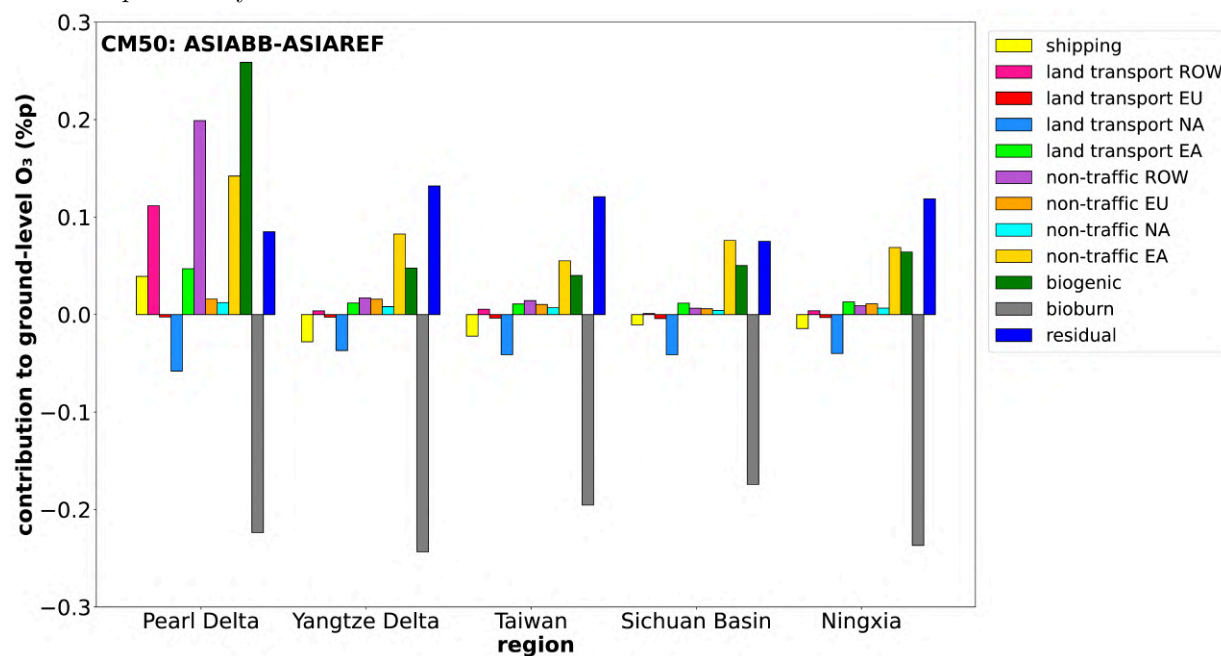


Figure C.77: Seasonal mean of the differences in percentage points (%p) between ASIABB minus ASIAREF of the absolute contributions of different emissions sectors and regions to ground level ozone in four European study areas as simulated with CM50.

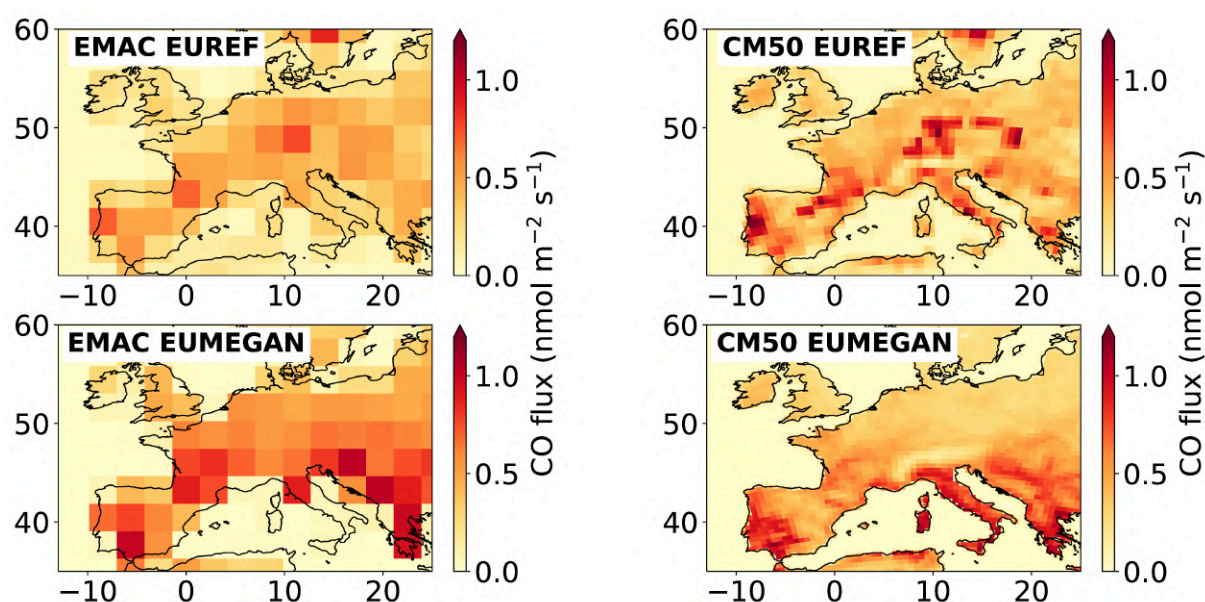


Figure C.78: Annual mean (2017–2018) of the biogenic CO flux in $\text{nmol m}^{-2} \text{s}^{-1}$ of the model results from EUREF (GEIA emission inventory for the year 2000) for the instances EMAC (upper left) and CM50 (upper right) for Europe. The same is shown for EUMEGAN (T42 climatology for the year 2000) in the lower left (EMAC) and lower right (CM50) panel.

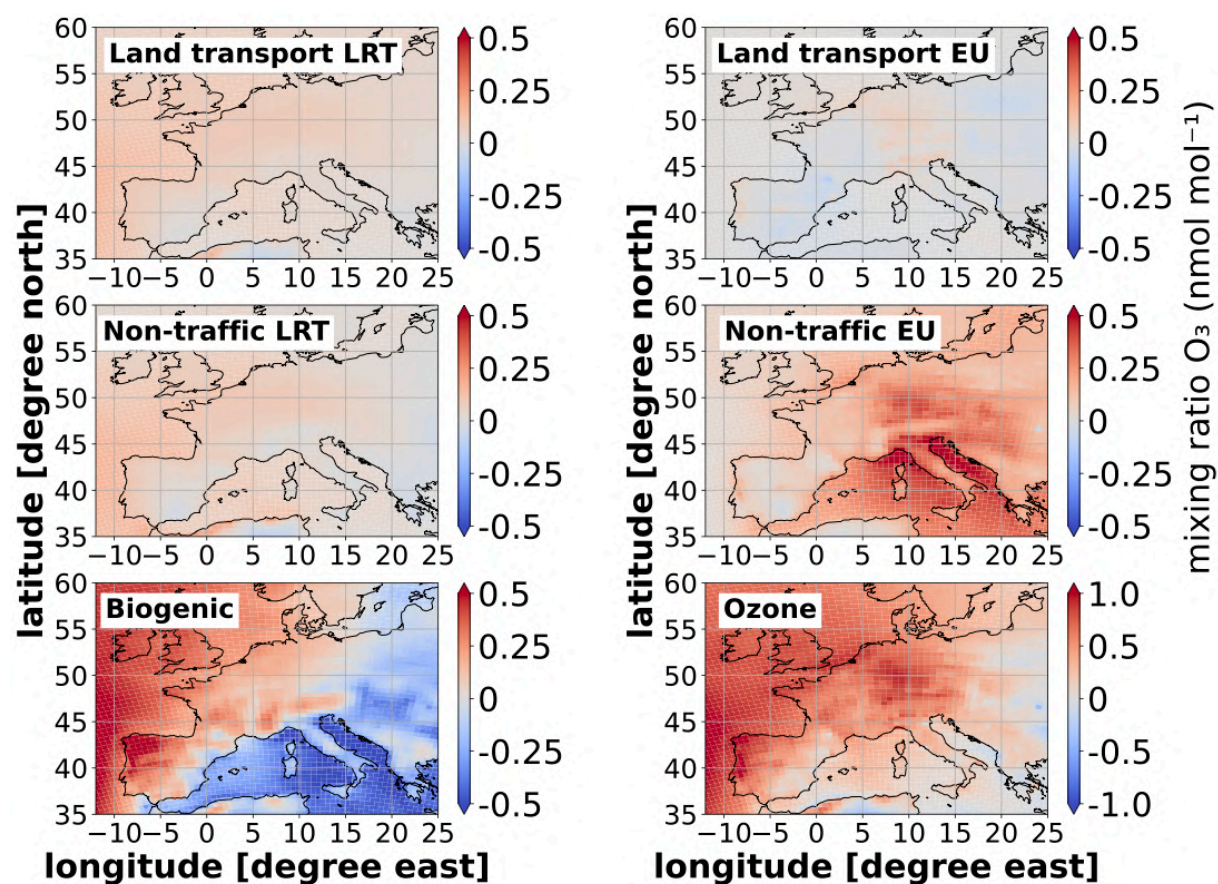


Figure C.79: Seasonal mean (2017) of the ground-level O_3 contributions from long-range transported (LRT: ROW + NA + EU) and European emissions in nmol mol^{-1} as simulated by CM50. Shown are the differences between EUMEGAN minus EUREF.

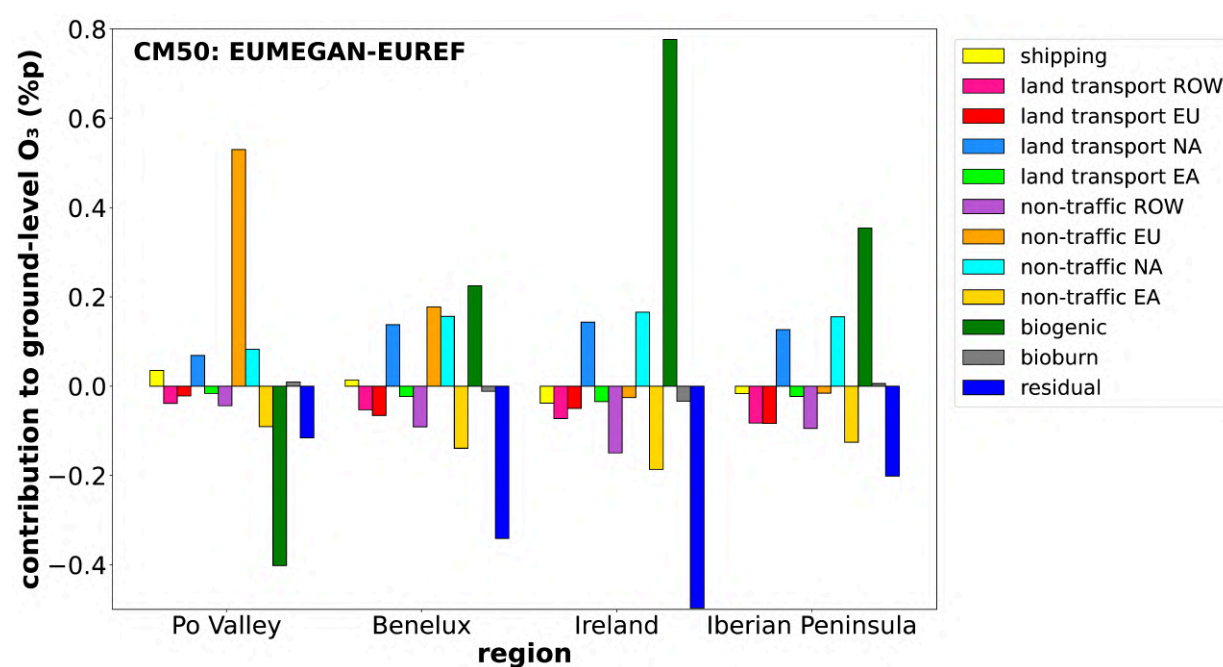


Figure C.80: Seasonal mean (JJA 2017) of the relative differences in percentage points (%p) between EUMEGAN minus EUREF of the absolute contributions of different emissions sectors and regions to ground level ozone in four European study areas as simulated with CM50.

Bibliography

- Altimir, N., Kolari, P., Tuovinen, J.-P., Vesala, T., Bäck, J., Suni, T., Kulmala, M., and Hari, P. Foliage surface ozone deposition: a role for surface moisture? *Biogeosciences*, 3(2):209–228, 2006. doi: 10.5194/bg-3-209-2006. URL <https://bg.copernicus.org/articles/3/209/2006/>.
- Andrés Hernández, M. D., Hilboll, A., Ziereis, H., Förster, E., Krüger, O. O., Kaiser, K., Schneider, J., Barnaba, F., Vrekoussis, M., Schmidt, J., Huntrieser, H., Blechschmidt, A.-M., George, M., Nenakhov, V., Harlass, T., Holanda, B. A., Wolf, J., Eirenschmalz, L., Krebsbach, M., Pöhlker, M. L., Kalisz Hedegaard, A. B., Mei, L., Pfeilsticker, K., Liu, Y., Koppmann, R., Schlager, H., Bohn, B., Schumann, U., Richter, A., Schreiner, B., Sauer, D., Baumann, R., Mertens, M., Jöckel, P., Kilian, M., Stratmann, G., Pöhlker, C., Campanelli, M., Pandolfi, M., Sicard, M., Gómez-Amo, J. L., Pujadas, M., Bigge, K., Kluge, F., Schwarz, A., Daskalakis, N., Walter, D., Zahn, A., Pöschl, U., Bönisch, H., Borrmann, S., Platt, U., and Burrows, J. P. Overview: On the transport and transformation of pollutants in the outflow of major population centres – observational data from the EMeRGe European intensive operational period in summer 2017. *Atmospheric Chemistry and Physics*, 22(9):5877–5924, 2022. doi: 10.5194/acp-22-5877-2022. URL <https://acp.copernicus.org/articles/22/5877/2022/>.
- Arakawa, A. and Lamb, V. Computational Design of the Basic Dynamical Process of the UCLA General Circulation Model. *Methods Computational Physics*, 1977. doi: <http://dx.doi.org/10.1016/B978-0-12-460817-7.50009-4>.
- Archibald, A., Neu, J., Elshorbany, Y., Cooper, O., Young, P., Akiyoshi, H., Cox, R., Coyle, M., Derwent, R., Deushi, M., Finco, A., Frost, G., Galbally, I., Gerosa, G., Granier, C., Griffiths, P., Hossaini, R., Hu, L., Jöckel, P., and Zeng, G. Tropospheric Ozone Assessment Report: A critical review of changes in the tropospheric ozone burden and budget from 1850 to 2100. 01 2021.
- Ashworth, K., Wild, O., and Hewitt, C. N. Sensitivity of isoprene emissions estimated using MEGAN to the time resolution of input climate data. *Atmospheric Chemistry and Physics*, 10(3):1193–1201, 2010. doi: 10.5194/acp-10-1193-2010. URL <https://acp.copernicus.org/articles/10/1193/2010/>.
- Bieser, J., Aulinger, A., Matthias, V., Quante, M., and Denier van der Gon, H. Vertical

- emission profiles for Europe based on plume rise calculations. *Environmental pollution (Barking, Essex : 1987)*, 159:2935–46, 05 2011. doi: 10.1016/j.envpol.2011.04.030.
- Butler, T., Lupascu, A., Coates, J., and Zhu, S. TOAST 1.0: Tropospheric Ozone Attribution of Sources with Tagging for CESM 1.2.2. *Geoscientific Model Development*, 11 (7):2825–2840, 2018. doi: 10.5194/gmd-11-2825-2018. URL <https://gmd.copernicus.org/articles/11/2825/2018/>.
- Cantrell, C. A., Shetter, R. E., Calvert, J. G., Eisele, F. L., Williams, E., Baumann, K., Brune, W. H., Stevens, P. S., and Mather, J. H. Peroxy radicals from photostationary state deviations and steady state calculations during the Tropospheric OH Photochemistry Experiment at Idaho Hill, Colorado, 1993. *Journal of Geophysical Research: Atmospheres*, 102(D5):6369–6378, 1997. doi: <https://doi.org/10.1029/96JD01703>. URL <https://agupubs.onlinelibrary.wiley.com/doi/abs/10.1029/96JD01703>.
- Chate, D. M., Ghude, S. D., Beig, G., Mahajan, A. S., Jena, C., Srinivas, R., Dahiya, A., and Kumar, N. Deviations from the O₃–NO–NO₂ photo-stationary state in Delhi, India. *Atmospheric Environment*, 96:353–358, 2014. ISSN 1352-2310. doi: <https://doi.org/10.1016/j.atmosenv.2014.07.054>. URL <https://www.sciencedirect.com/science/article/pii/S1352231014005846>.
- Chen, T.-F., Tsai, C.-Y., Chen, C.-H., and Chang, K.-H. Effect of Long-range Transport from Changing Emission on Ozone-NO_x-VOC Sensitivity: Implication of Control Effect of Long-range Transport from Changing Emission on Ozone-NO_x-VOC Sensitivity: Implication of Control Strategy to Improve Ozone. 06 2022. doi: 10.29424/JIT.202109_3(2).0005.
- Chou, C., Liu, S., Lin, C.-Y., Shiu, C.-J., and Chang, K.-H. The trend of surface ozone in Taipei, Taiwan, and its causes: Implications for ozone control strategies. *Atmospheric Environment*, 40:3898–3908, 07 2006. doi: 10.1016/j.atmosenv.2006.02.018.
- Clappier, A., Belis, C. A., Pernigotti, D., and Thunis, P. Source apportionment and sensitivity analysis: two methodologies with two different purposes. *Geoscientific Model Development*, 10(11):4245–4256, 2017. doi: 10.5194/gmd-10-4245-2017. URL <https://gmd.copernicus.org/articles/10/4245/2017/>.
- Clifton, O. E., Fiore, A. M., Massman, W. J., Baublitz, C. B., Coyle, M., Emberson, L., Fares, S., Farmer, D. K., Gentine, P., Gerosa, G., Guenther, A. B., Helmig, D., Lombardozzi, D. L., Munger, J. W., Patton, E. G., Pusede, S. E., Schwede, D. B., Silva, S. J., Sörgel, M., Steiner, A. L., and Tai, A. P. K. Dry Deposition of Ozone Over Land: Processes, Measurement, and Modeling. *Reviews of Geophysics*, 58(1):e2019RG000670, 2020. doi: <https://doi.org/10.1029/2019RG000670>. URL <https://agupubs.onlinelibrary.wiley.com/doi/abs/10.1029/2019RG000670>. e2019RG000670 2019RG000670.
- Copernicus, E. Copernicus Sentinel data, 2019. URL <https://sentinels.copernicus.eu/web/sentinel/missions/sentinel-5p/>.

- Crippa, M., Solazzo, E., Huang, G., Guizzardi, D., Koffi, E., Muntean, M., Schieberle, C., Friedrich, R., and Janssens-Maenhout, G. High resolution temporal profiles in the Emissions Database for Global Atmospheric Research. *Scientific Data*, 7, 04 2020. doi: 10.1038/s41597-020-0462-2.
- Crutzen, P. A. A discussion of the chemistry of some minor constituents in the stratosphere and troposphere. *Pure and Applied Geophysics*, 106:1385–139, 1973. doi: <https://doi.org/10.1007/BF00881092>.
- Crutzen, P. J. SST's: A Threat to the Earth's Ozone Shield. *Ambio*, 1(2):41–51, 1972. ISSN 00447447, 16547209. URL <http://www.jstor.org/stable/4311946>.
- Crutzen, P. J. Photochemical reactions initiated by and influencing ozone in unpolluted tropospheric air. *Tellus*, 26(1-2):47–57, 1974. doi: <https://doi.org/10.1111/j.2153-3490.1974.tb01951.x>. URL <https://onlinelibrary.wiley.com/doi/abs/10.1111/j.2153-3490.1974.tb01951.x>.
- Crutzen, P. J. and Schmailzl, U. Chemical budgets of the stratosphere. *Planetary and Space Science*, 31(9):1009–1032, 1983. ISSN 0032-0633. doi: [https://doi.org/10.1016/0032-0633\(83\)90092-2](https://doi.org/10.1016/0032-0633(83)90092-2). URL <https://www.sciencedirect.com/science/article/pii/0032063383900922>.
- Dahlmann, K., Grewe, V., Ponater, M., and Matthes, S. Quantifying the contributions of individual NO_x sources to the trend in ozone radiative forcing. *Atmospheric Environment*, 45(17):2860–2868, 2011. ISSN 1352-2310. doi: <https://doi.org/10.1016/j.atmosenv.2011.02.071>. URL <https://www.sciencedirect.com/science/article/pii/S1352231011002366>.
- Deckert, R., Jöckel, P., Grewe, V., Gottschaldt, K.-D., and Hoor, P. A quasi chemistry-transport model mode for EMAC. *Geoscientific Model Development*, 4(1):195–206, 2011. doi: 10.5194/gmd-4-195-2011. URL <https://gmd.copernicus.org/articles/4/195/2011/>.
- Delang, M., Becker, J. S., Chang, K., Serre, M. L., Cooper, O. R., Schultz, M. G., Schröder, S., Lu, X., Zhang, L., Deushi, M., Josse, B., Keller, C. A., Lamarque, J., Lin, M., Liu, J., Marécal, V., Strode, S. A., Sudo, K., Tilmes, S., Zhang, L., Cleland, S. E., Collins, E. L., Brauer, M., and West, J. J. Mapping Yearly Fine Resolution Global Surface Ozone through the Bayesian Maximum Entropy Data Fusion of Observations and Model Output for 1990-2017. *Environmental science & technology*, 2021.
- Dentener, F., Drevet, J., Lamarque, J. F., Bey, I., Eickhout, B., Fiore, A. M., Hauglustaine, D., Horowitz, L. W., Krol, M., Kulshrestha, U. C., Lawrence, M., Galy-Lacaux, C., Rast, S., Shindell, D., Stevenson, D., Noije, T. V., Atherton, C., Bell, N., Bergman, D., Butler, T., Cofala, J., Collins, B., Doherty, R., Ellingsen, K., Galloway, J., Gauss, M., Montanaro, V., Müller, J. F., Pitari, G., Rodriguez, J., Sanderson, M., Solomon,

- F., Strahan, S., Schultz, M., Sudo, K., Szopa, S., and Wild, O. Nitrogen and sulfur deposition on regional and global scales: A multimodel evaluation. *Global Biogeochemical Cycles*, 20(4):n/a–n/a, oct 2006. doi: 10.1029/2005gb002672.
- Di Carlo, P., Aruffo, E., Biancofiore, F., Busilacchio, M., Pitari, G., Dari-Salisburgo, C., Tuccella, P., and Kajii, Y. Wildfires impact on surface nitrogen oxides and ozone in Central Italy. *Atmospheric Pollution Research*, 6(1):29–35, 2015. ISSN 1309-1042. doi: <https://doi.org/10.5094/APR.2015.004>. URL <https://www.sciencedirect.com/science/article/pii/S1309104215302488>.
- Diehl, T., Heil, A., Chin, M., Pan, X., Streets, D., Schultz, M., and Kinne, S. Anthropogenic, biomass burning, and volcanic emissions of black carbon, organic carbon, and SO₂ from 1980 to 2010 for hindcast model experiments. *Atmospheric Chemistry and Physics Discussions*, 12:24895–24954, 2012. doi: 10.5194/acpd-12-24895-2012. URL <https://acp.copernicus.org/preprints/12/24895/2012/>.
- Dietmüller, S., Jöckel, P., Tost, H., Kunze, M., Gellhorn, C., Brinkop, S., Frömming, C., Ponater, M., Steil, B., Lauer, A., and Hendricks, J. A new radiation infrastructure for the Modular Earth Submodel System (MESSy, based on version 2.51). *Geoscientific Model Development*, 9(6):2209–2222, 2016. doi: 10.5194/gmd-9-2209-2016. URL <https://gmd.copernicus.org/articles/9/2209/2016/>.
- Doms, G. and Schättler, U. The Nonhydrostatic Limited-Area Model LM (Lokal-Modell) of DWD: Part I: Scientific Documentation, Deutscher Wetterdienst, Offenbach. 1999.
- Duran, S., G. J. G. R. S. T. J. *Dost-Pagasa Annual Report On Philippine Tropical Cyclones*. Weather Division Philippine Atmospheric, Geophysical and Astronomical Services Administration (PAGASA) Department of Science and Technology, 2018. URL <https://pubfiles.pagasa.dost.gov.ph/pagasaweb/files/tamss/weather/tcsummary/ARTC2018.pdf>.
- Eckhardt, S., Stohl, A., Wernli, H., James, P., Forster, C., and Spichtinger, N. A 15-Year Climatology of Warm Conveyor Belts. *Journal of Climate*, 17(1):218 – 237, 2004. doi: 10.1175/1520-0442(2004)017<0218:AYCOWC>2.0.CO;2. URL https://journals.ametsoc.org/view/journals/clim/17/1/1520-0442_2004_017_0218_aycowc_2.0.co_2.xml.
- Elliott, M. A. *Diesel Fuel Combustion*, chapter 20, pages 280–293. 1958. doi: 10.1021/ba-1958-0020.ch020. URL <https://pubs.acs.org/doi/abs/10.1021/ba-1958-0020.ch020>.
- Environmental Protection Agency. Environmental Protection Agency Air Quality Stations China, 2018. URL <https://aqicn.org/map/china/>. Accessed on 11. November 2022.

- European Environment Agency. Air Quality e-Reporting products on EEA data service, 2018. URL <https://www.eea.europa.eu/data-and-maps/data/aqereporting-8>. Accessed on 11. November 2022.
- Finkelstein, P. L., Ellestad, T. G., Clarke, J. F., Meyers, T. P., Schwede, D. B., Hebert, E. O., and Neal, J. A. Ozone and sulfur dioxide dry deposition to forests: Observations and model evaluation. *Journal of Geophysical Research: Atmospheres*, 105(D12):15365–15377, 2000. doi: <https://doi.org/10.1029/2000JD900185>. URL <https://agupubs.onlinelibrary.wiley.com/doi/abs/10.1029/2000JD900185>.
- Fowler, D., Amann, M., Anderson, R., Ashmore, M., Cox, P.; Depledge, M., Derwent, D., Grennfelt, P., Hewitt, N., Hov, O., Jenkin, M., Kelly, F., Liss, P., Pilling, M., Pyle, J., Slingo, J., and Stevenson, D. *Ground-level ozone in the 21st century: future trends, impacts and policy implications*, volume (Royal Society Policy Document 15/08). The Royal Society, 2008.
- Garland, J. and Penkett, S. Absorption of peroxy acetyl nitrate and ozone by natural surfaces. *Atmospheric Environment (1967)*, 10(12):1127–1131, 1976. ISSN 0004-6981. doi: [https://doi.org/10.1016/0004-6981\(76\)90122-0](https://doi.org/10.1016/0004-6981(76)90122-0). URL <https://www.sciencedirect.com/science/article/pii/0004698176901220>.
- Global Burden of Disease Collaborative Network. Global Burden of Disease Study 2019 (GBD 2019). 2021. doi: <https://doi.org/10.6069/1D4Y-YQ37>. URL <https://vizhub.healthdata.org/gbd-results/>.
- Granier, C. and Brasseur, G. P. The impact of road traffic on global tropospheric ozone. *Geophysical Research Letters*, 30(2), 2003. doi: <https://doi.org/10.1029/2002GL015972>. URL <https://agupubs.onlinelibrary.wiley.com/doi/abs/10.1029/2002GL015972>.
- Grewe, V. Technical Note: A diagnostic for ozone contributions of various NO_x emissions in multi-decadal chemistry-climate model simulations. *Atmospheric Chemistry and Physics*, 4(3):729–736, 2004. doi: 10.5194/acp-4-729-2004. URL <https://acp.copernicus.org/articles/4/729/2004/>.
- Grewe, V. Impact of Lightning on Air Chemistry and Climate. In Betz, H. D., Schumann, U., and Laroche, P., editors, *Lightning: Principles, Instruments and Applications: Review of Modern Lightning Research*, pages 537–550. Springer Verlag, Dezember 2008. URL <https://elib.dlr.de/56813/>.
- Grewe, V., Tsati, E., and Hoor, P. On the attribution of contributions of atmospheric trace gases to emissions in atmospheric model applications. *Geoscientific Model Development*, 3(2):487–499, 2010. doi: 10.5194/gmd-3-487-2010. URL <https://gmd.copernicus.org/articles/3/487/2010/>.

- Grewe, V., Tsati, E., Mertens, M., Frömming, C., and Jöckel, P. Contribution of emissions to concentrations: the TAGGING 1.0 submodel based on the Modular Earth Submodel System (MESSy 2.52). *Geoscientific Model Development*, 10(7):2615–2633, 2017. doi: 10.5194/gmd-10-2615-2017. URL <https://gmd.copernicus.org/articles/10/2615/2017/>.
- Gschwandtner, G. Trends and uncertainties in anthropogenic VOC and NO_x emissions. *Water, Air, and Soil Pollution*, 67:39–46, 1993.
- Guenther, A., Hewitt, C. N., Erickson, D., Fall, R., Geron, C., Graedel, T., Harley, P., Klinger, L., Lerdau, M., McKay, W., Pierce, T., Scholes, B., Steinbrecher, R., Tallamraju, R., Taylor, J., and Zimmerman, P. A global model of natural volatile organic compound emissions. *Journal of geophysical research*, 100:8873–8892, 05 1995. doi: 10.1029/94JD02950.
- Guenther, A., Karl, T., Harley, P., Wiedinmyer, C., Palmer, P. I., and Geron, C. Estimates of global terrestrial isoprene emissions using MEGAN (Model of Emissions of Gases and Aerosols from Nature). *Atmospheric Chemistry and Physics*, 6(11):3181–3210, 2006. doi: 10.5194/acp-6-3181-2006. URL <https://acp.copernicus.org/articles/6/3181/2006/>.
- Guenther, A. B., Zimmerman, P. R., Harley, P. C., Monson, R. K., and Fall, R. Isoprene and monoterpene emission rate variability: Model evaluations and sensitivity analyses. *Journal of Geophysical Research: Atmospheres*, 98(D7):12609–12617, 1993. doi: <https://doi.org/10.1029/93JD00527>. URL <https://agupubs.onlinelibrary.wiley.com/doi/abs/10.1029/93JD00527>.
- Haagen-Smith, A. J. Chemistry and physiology of Los Angeles smog. *Ind. Eng. Chem*, 44: 1342–1346, 1952. doi: <https://doi.org/10.1021/ie50510a045>.
- Han, H., Liu, J., Yuan, H., Wang, T., Zhuang, B., and Zhang, X. Foreign influences on tropospheric ozone over East Asia through global atmospheric transport. *Atmospheric Chemistry and Physics*, 19(19):12495–12514, 2019. doi: 10.5194/acp-19-12495-2019. URL <https://acp.copernicus.org/articles/19/12495/2019/>.
- Hauglustaine, D., Emmons, L., and Newchurch, M. e. a. On the Role of Lightning NO_x in the Formation of Tropospheric Ozone Plumes: A Global Model Perspective. *Journal of Atmospheric Chemistry*, 38:3277–3294, 2001. doi: <https://doi.org/10.1023/A:1006452309388>.
- Hayyan, M., Hashim, M. A., and AlNashef, I. M. Superoxide ion: Generation and chemical implications. *Chemical Reviews*, 116(5):3029–3085, 2016. doi: 10.1021/acs.chemrev.5b00407. URL <https://doi.org/10.1021/acs.chemrev.5b00407>. PMID: 26875845.

- Heil, A., Kaiser, J., van der Werf, G., Wooster, M., Schultz, M., and van der Gon, H. Assessment of the real-time fire emissions (GFASv0) by MACC. (628):43, 07 2010. doi: 10.21957/2m000mza9. URL <https://www.ecmwf.int/node/9842>.
- Helmig, D., Ganzeveld, L., Butler, T., and Oltmans, S. J. The role of ozone atmosphere-snow gas exchange on polar, boundary-layer tropospheric ozone - a review and sensitivity analysis. *Atmospheric Chemistry and Physics*, 7(1):15–30, 2007. doi: 10.5194/acp-7-15-2007. URL <https://acp.copernicus.org/articles/7/15/2007/>.
- Hersbach, H., Bell, B., Berrisford, P., Hirahara, S., Horányi, A., Muñoz-Sabater, J., Nicolas, J., Peubey, C., Radu, R., Schepers, D., Simmons, A., Soci, C., Abdalla, S., Abellan, X., Balsamo, G., Bechtold, P., Biavati, G., Bidlot, J., Bonavita, M., De Chiara, G., Dahlgren, P., Dee, D., Diamantakis, M., Dragani, R., Flemming, J., Forbes, R., Fuentes, M., Geer, A., Haimberger, L., Healy, S., Hogan, R. J., Hólm, E., Janisková, M., Keeley, S., Laloyaux, P., Lopez, P., Lupu, C., Radnoti, G., de Rosnay, P., Rozum, I., Vamborg, F., Villaume, S., and Thépaut, J.-N. The ERA5 global re-analysis. *Quarterly Journal of the Royal Meteorological Society*, 146(730):1999–2049, 2020. doi: <https://doi.org/10.1002/qj.3803>. URL <https://rmets.onlinelibrary.wiley.com/doi/abs/10.1002/qj.3803>.
- Hofmann, C., Kerkweg, A., Wernli, H., and Jöckel, P. The 1-way on-line coupled atmospheric chemistry model system MECO(n) – Part 3: Meteorological evaluation of the on-line coupled system. *Geoscientific Model Development*, 5, 01 2012. doi: 10.5194/gmd-5-129-2012.
- Hornbrook, R. S., Crawford, J. H., Edwards, G. D., Goyea, O., Mauldin III, R. L., Olson, J. S., and Cantrell, C. A. Measurements of tropospheric HO₂ and RO₂ by oxygen dilution modulation and chemical ionization mass spectrometry. *Atmospheric Measurement Techniques*, 4(4):735–756, 2011. doi: 10.5194/amt-4-735-2011. URL <https://amt.copernicus.org/articles/4/735/2011/>.
- Hosaynali Beygi, Z., Fischer, H., Harder, H. D., Martinez, M., Sander, R., Williams, J., Brookes, D. M., Monks, P. S., and Lelieveld, J. Oxidation photochemistry in the Southern Atlantic boundary layer: unexpected deviations of photochemical steady state. *Atmospheric Chemistry and Physics*, 11(16):8497–8513, 2011. doi: 10.5194/acp-11-8497-2011. URL <https://acp.copernicus.org/articles/11/8497/2011/>.
- Hu, L., Jacob, D. J., Liu, X., Zhang, Y., Zhang, L., Kim, P. S., Sulprizio, M. P., and Yantosca, R. M. Global budget of tropospheric ozone: Evaluating recent model advances with satellite (OMI), aircraft (IAGOS), and ozonesonde observations. *Atmospheric Environment*, 167:323–334, 2017.
- Hudman, R. C., Moore, N. E., Mebust, A. K., Martin, R. V., Russell, A. R., Valin, L. C., and Cohen, R. C. Steps towards a mechanistic model of global soil nitric oxide emissions:

- implementation and space based-constraints. *Atmospheric Chemistry and Physics*, 12 (16):7779–7795, aug 2012. doi: 10.5194/acp-12-7779-2012.
- Hui, K., Yuan, Y., Xi, B., and Tan, W. A review of the factors affecting the emission of the ozone chemical precursors VOCs and NO_x from the soil. *Environment International*, 172:107799, 02 2023. doi: 10.1016/j.envint.2023.107799.
- Huijnen, V., Williams, J., van Weele, M., van Noije, T., Krol, M., Dentener, F., Segers, A., Houweling, S., Peters, W., de Laat, J., Boersma, F., Bergamaschi, P., van Velthoven, P., Le Sager, P., Eskes, H., Alkemade, F., Scheele, R., Nédélec, P., and Pätz, H.-W. The global chemistry transport model TM5: description and evaluation of the tropospheric chemistry version 3.0. *Geoscientific Model Development*, 3(2):445–473, 2010. doi: 10.5194/gmd-3-445-2010. URL <https://gmd.copernicus.org/articles/3/445/2010/>.
- IPCC. *Fourth Assessment Report: Climate Change 2007: The AR4 Synthesis Report*. Geneva: IPCC, 2007. URL <http://www.ipcc.ch/ipccreports/ar4-wg1.htm>.
- IPCC. *Climate Change 2014: Synthesis Report. Contribution of Working Groups I, II and III to the Fifth Assessment Report of the Intergovernmental Panel on Climate Change*. IPCC, Geneva, Switzerland, 2014.
- IPCC. *Climate Change 2022: Mitigation of Climate Change. Contribution of Working Group III to the Sixth Assessment Report of the Intergovernmental Panel on Climate Change*. Cambridge University Press, Cambridge, UK and New York, NY, USA, 2022. doi: 10.1017/9781009157926.
- Irie, H., Kanaya, Y., Akimoto, H., Iwabuchi, H., Shimizu, A., and Aoki, K. First retrieval of tropospheric aerosol profiles using MAX-DOAS and comparison with lidar and sky radiometer measurements. *Atmospheric Chemistry and Physics*, 8(2):341–350, 2008. doi: 10.5194/acp-8-341-2008. URL <https://acp.copernicus.org/articles/8/341/2008/>.
- Jain, A., Tao, Z., Yang, X., and Gillespie, C. Estimates of global biomass burning emissions for reactive greenhouse gases (CO, NMHCs, and NO_x) and CO₂. *J. Geophys. Res.*, 111, 03 2006. doi: 10.1029/2005JD006237.
- Jimenez-Montenegro, L., López-Fernández, M., and Gimenez, E. Worldwide Research on the Ozone Influence in Plants. *Agronomy*, 11:1504, 07 2021. doi: 10.3390/agronomy11081504.
- Jöckel, P., Kerkweg, A., Buchholz-Dietsch, J., Tost, H., Sander, R., and Pozzer, A. Technical Note: Coupling of chemical processes with the Modular Earth Submodel System (MESSy) submodel TRACER. *Atmospheric Chemistry and Physics*, 8(6):1677–1687, 2008. doi: 10.5194/acp-8-1677-2008. URL <https://acp.copernicus.org/articles/8/1677/2008/>.

- Jöckel, P., Tost, H., Pozzer, A., Kunze, M., Kirner, O., Brenninkmeijer, C., Brinkop, S., Cai, D., Dyroff, C., Eckstein, J., Frank, F., Garny, H., Gottschaldt, K., Graf, P., Volker, G., Kerkweg, A., Kern, B., Matthes, S., Mertens, M., and Zahn, A. Earth System Chemistry integrated Modelling (ESCiMo) with the Modular Earth Submodel System (MESSy) version 2.51. *Geoscientific Model Development*, 9:1153–1200, 03 2016. doi: 10.5194/gmd-9-1153-2016.
- Jonson, J. E., Gauss, M., Schulz, M., Jalkanen, J.-P., and Fagerli, H. Effects of global ship emissions on European air pollution levels. *Atmospheric Chemistry and Physics*, 20(19): 11399–11422, 2020. doi: 10.5194/acp-20-11399-2020. URL <https://acp.copernicus.org/articles/20/11399/2020/>.
- Jöckel, P., Sander, R., Kerkweg, A., Tost, H., and Lelieveld, J. Technical Note: The Modular Earth Submodel System (MESSy) - a new approach towards Earth System Modeling. *Atmospheric Chemistry and Physics*, 5(2):433–444, 2005. doi: 10.5194/acp-5-433-2005. URL <https://acp.copernicus.org/articles/5/433/2005/>.
- Jöckel, P., Tost, H., Pozzer, A., Brühl, C., Buchholz, J., Ganzeveld, L., Hoor, P., Kerkweg, A., Lawrence, M., Sander, R., Steil, B., Stiller, G., Tanarhte, M., Taraborrelli, D., van Aardenne, J., and Lelieveld, J. The atmospheric chemistry general circulation model ECHAM5/MESSy1: consistent simulation of ozone from the surface to the mesosphere. *Atmospheric Chemistry and Physics*, 6(12):5067–5104, nov 2006. doi: 10.5194/acp-6-5067-2006.
- Jöckel, P., Kerkweg, A., Pozzer, A., Sander, R., Tost, H., Riede, H., Baumgaertner, A., Gromov, S., and Kern, B. Development cycle 2 of the Modular Earth Submodel System (MESSy2). *Geoscientific Model Development*, 3(2):717–752, dec 2010. doi: 10.5194/gmd-3-717-2010.
- Jöckel, P., Tost, H., Pozzer, A., Kunze, M., Kirner, O., Brenninkmeijer, C. A. M., Brinkop, S., Cai, D. S., Dyroff, C., Eckstein, J., Frank, F., Garny, H., Gottschaldt, K.-D., Graf, P., Grewe, V., Kerkweg, A., Kern, B., Matthes, S., Mertens, M., Meul, S., Neumaier, M., Nützel, M., Oberländer-Hayn, S., Ruhnke, R., Runde, T., Sander, R., Scharffe, D., and Zahn, A. Earth System Chemistry integrated Modelling (ESCiMo) with the Modular Earth Submodel System (MESSy) version 2.51. *Geoscientific Model Development*, 9(3): 1153–1200, 3 2016. doi: 10.5194/gmd-9-1153-2016.
- Kaiser, J. W., Heil, A., Andreae, M. O., Benedetti, A., Chubarova, N., Jones, L., Morcrette, J.-J., Razinger, M., Schultz, M. G., Suttie, M., and van der Werf, G. R. Biomass burning emissions estimated with a global fire assimilation system based on observed fire radiative power. *Biogeosciences*, 9(1):527–554, 2012. doi: 10.5194/bg-9-527-2012. URL <https://bg.copernicus.org/articles/9/527/2012/>.
- Karamchandani, P., Long, Y., Pirovano, G., Balzarini, A., and Yarwood, G. Source-sector contributions to European ozone and fine PM in 2010 using AQMEII model-

- ing data. *Atmospheric Chemistry and Physics*, 17(9):5643–5664, 2017. doi: 10.5194/acp-17-5643-2017. URL <https://acp.copernicus.org/articles/17/5643/2017/>.
- Kerkweg, A. and Jöckel, P. The infrastructure MESSy submodels GRID (v1.0) and IMPORT (v1.0). *Geoscientific Model Development Discussions*, 8:8607–8633, 2015. doi: 10.5194/gmdd-8-8607-2015. URL <https://gmd.copernicus.org/preprints/8/8607/2015/>.
- Kerkweg, A. and Jöckel, P. The 1-way on-line coupled atmospheric chemistry model system MECO(n) - Part 1: Description of the limited-area atmospheric chemistry model COSMO/MESSy. *Geoscientific Model Development*, 5(1):87–110, jan 2012. doi: 10.5194/gmd-5-87-2012.
- Kerkweg, A., Buchholz, J., Ganzeveld, L., Pozzer, A., Tost, H., and Jöckel, P. Technical Note: An implementation of the dry removal processes DRY DEPosition and SEDimentation in the Modular Earth Submodel System (MESSy). *Atmospheric Chemistry and Physics*, 6(12):4617–4632, 2006a. doi: 10.5194/acp-6-4617-2006. URL <https://acp.copernicus.org/articles/6/4617/2006/>.
- Kerkweg, A., Sander, R., Tost, H., and Jöckel, P. Technical note: Implementation of prescribed (OFFLEM), calculated (ONLEM), and pseudo-emissions (TNUDGE) of chemical species in the Modular Earth Submodel System (MESSy). *Atmospheric Chemistry and Physics*, 6(11):3603–3609, 2006b. doi: 10.5194/acp-6-3603-2006. URL <https://acp.copernicus.org/articles/6/3603/2006/>.
- Kerkweg, A., Hofmann, C., Jöckel, P., Mertens, M., and Pante, G. The on-line coupled atmospheric chemistry model system MECO(n) – Part 5: Expanding the Multi-Model-Driver (MMD v2.0) for 2-way data exchange including data interpolation via GRID (v1.0). *Geoscientific Model Development*, 11(3):1059–1076, 2018. doi: 10.5194/gmd-11-1059-2018. URL <https://gmd.copernicus.org/articles/11/1059/2018/>.
- Kern, B. *Chemical interaction between ocean and atmosphere*. PhD thesis, 11 2013.
- Kilian, M., Volker, G., Joeckel, P., Kerkweg, A., Mertens, M., Ziereis, H., and Zahn, A. Ozone source attribution in polluted European areas during summer as simulated with MECO(n). *Submitted to Atmospheric Chemistry and Physics Discussion*, 2023.
- Kleinman, L. I., e. a. Ozone formation at a rural site in the southeastern United States. *J. Geophys. Res.*, 99:3469–3482, 1994.
- Kondo, Y., Nakamura, K., Chen, G., Takegawa, N., Koike, M., Miyazaki, Y., Kita, K., Crawford, J., Ko, M., Blake, D., Kawakami, S., Shirai, T., Liley, B., Wang, Y., and Ogawa, T. Photochemistry of ozone over the western Pacific from winter to spring. *Journal of Geophysical Research-Atmospheres*, 109, 12 2004. doi: 10.1029/2004jd004871.

- Lamarque, J.-F., Bond, T. C., Eyring, V., Granier, C., Heil, A., Klimont, Z., Lee, D., Liousse, C., Mieville, A., Owen, B., Schultz, M. G., Shindell, D., Smith, S. J., Stehfest, E., Van Aardenne, J., Cooper, O. R., Kainuma, M., Mahowald, N., McConnell, J. R., Naik, V., Riahi, K., and van Vuuren, D. P. Historical (1850–2000) gridded anthropogenic and biomass burning emissions of reactive gases and aerosols: methodology and application. *Atmospheric Chemistry and Physics*, 10(15):7017–7039, 2010. doi: 10.5194/acp-10-7017-2010. URL <https://acp.copernicus.org/articles/10/7017/2010/>.
- Lavoie, G. A., Heywood, J. B., and Keck, J. C. Experimental and Theoretical Study of Nitric Oxide Formation in Internal Combustion Engines. *Combustion Science and Technology*, 1(4):313–326, 1970. doi: 10.1080/00102206908952211.
- Leighton, P. *Photochemistry of Air Pollution*. Eric Hutchinson and P. Van Rysselberghe. Academic Press, 1961. URL <https://books.google.at/books?id=DEtRAAAAMAAJ>.
- Li, L., An, J., Shi, Y., Zhou, M., Yan, R., Huang, C., Wang, H., Lou, S., Wang, Q., Lu, Q., and Wu, J. Source apportionment of surface ozone in the Yangtze River Delta, China in the summer of 2013. *Atmospheric Environment*, 144:194–207, 2016. ISSN 1352-2310. doi: <https://doi.org/10.1016/j.atmosenv.2016.08.076>. URL <https://www.sciencedirect.com/science/article/pii/S1352231016306823>.
- Li, L., An, J., Huang, L., Yan, R., Huang, C., and Yarwood, G. Ozone source apportionment over the Yangtze River Delta region, China: Investigation of regional transport, sectoral contributions and seasonal differences. *Atmospheric Environment*, 202, 04 2019. doi: 10.1016/j.atmosenv.2019.01.028.
- Li, L., Yang, W., Xie, S., and Wu, Y. Estimations and uncertainty of biogenic volatile organic compound emission inventory in China for 2008–2018. *Science of The Total Environment*, 733:139301, 2020a. ISSN 0048-9697. doi: <https://doi.org/10.1016/j.scitotenv.2020.139301>. URL <https://www.sciencedirect.com/science/article/pii/S0048969720328187>.
- Li, X., Wang, Z., Du, L., Liu, X., Wang, X., Chen, C., Meng, X., Li, H., Zhuang, Q., Deng, W., Pan, X., and Chu, X. Shipborne MAX-DOAS Observations of Tropospheric Trace Gases over a Coastal City and the Yellow Sea near Qingdao, China. *Journal of Atmospheric and Oceanic Technology*, 37, 01 2020b. doi: 10.1175/JTECH-D-18-0179.1.
- Li, Y., Lau, A. K.-H., Fung, J. C.-H., Zheng, J. Y., Zhong, L. J., and Louie, P. K. K. Ozone source apportionment (OSAT) to differentiate local regional and super-regional source contributions in the Pearl River Delta region, China. *Journal of Geophysical Research: Atmospheres*, 117(D15), 2012. doi: <https://doi.org/10.1029/2011JD017340>. URL <https://agupubs.onlinelibrary.wiley.com/doi/abs/10.1029/2011JD017340>.
- Liu, H., Zhang, M., and Han, X. A review of surface ozone source apportionment in China. *Atmospheric and Oceanic Science Letters*, 13(5):470–484, 2020. doi: 10.1080/16742834.2020.1768025. URL <https://doi.org/10.1080/16742834.2020.1768025>.

- Liu, Y. and Wang, T. Worsening urban ozone pollution in China from 2013 to 2017 – Part 1: The complex and varying roles of meteorology. *Atmospheric Chemistry and Physics*, 20(11):6305–6321, 2020. doi: 10.5194/acp-20-6305-2020. URL <https://acp.copernicus.org/articles/20/6305/2020/>.
- Logan, J. A. Nitrogen oxides in the troposphere: Global and regional budgets. *J. Geophys. Res.; (United States)*, 88, 12 1983. doi: 10.1029/JC088iC15p10785. URL <https://www.osti.gov/biblio/6984222>.
- Loreto, F. and Sharkey, T. D. On the relationship between isoprene emission and photo-synthetic metabolites under different environmental conditions. *Planta*, 189(3):420–424, 1993. ISSN 00320935, 14322048. URL <http://www.jstor.org/stable/23382262>.
- Lupaşcu, A. and Butler, T. Source attribution of European surface O₃ using a tagged O₃ mechanism. *Atmospheric Chemistry and Physics*, 19(23):14535–14558, 2019. doi: 10.5194/acp-19-14535-2019. URL <https://acp.copernicus.org/articles/19/14535/2019/>.
- Lupaşcu, A., Otero, N., Minkos, A., and Butler, T. Attribution of surface ozone to NO_x and VOC sources during two different high ozone events. *Atmospheric Chemistry and Physics Discussions*, 2022:1–36, 2022. doi: 10.5194/acp-2022-189. URL <https://acp.copernicus.org/preprints/acp-2022-189/>.
- Mailler, S., Khvorostyanov, D., and Menut, L. Impact of the vertical emission profiles on background gas-phase pollution simulated from the EMEP emissions over Europe. *Atmospheric Chemistry and Physics*, 13(12):5987–5998, 2013. doi: 10.5194/acp-13-5987-2013. URL <https://acp.copernicus.org/articles/13/5987/2013/>.
- McDuffie, E. E., Smith, S. J., O’Rourke, P., Tibrewal, K., Venkataraman, C., Marais, E. A., Zheng, B., Crippa, M., Brauer, M., and Martin, R. V. A global anthropogenic emission inventory of atmospheric pollutants from sector- and fuel-specific sources (1970–2017): an application of the Community Emissions Data System (CEDS). *Earth System Science Data*, 12(4):3413–3442, 2020. doi: 10.5194/essd-12-3413-2020. URL <https://essd.copernicus.org/articles/12/3413/2020/>.
- McElroy, M. B., Salawitch, R. J., and Minschwaner, K. The changing stratosphere. , 40 (2-3):373–401, Feb. 1992. doi: 10.1016/0032-0633(92)90070-5.
- Mebust, A. K., Russell, A. R., Hudman, R. C., Valin, L. C., and Cohen, R. C. Characterization of wildfire NO_x emissions using MODIS fire radiative power and OMI tropospheric NO₂ columns. *Atmospheric Chemistry and Physics*, 11(12):5839–5851, 2011. doi: 10.5194/acp-11-5839-2011. URL <https://acp.copernicus.org/articles/11/5839/2011/>.
- Meloan, J., Siegmund, P., van Velthoven, P., Kelder, H., Sprenger, M., Wernli, H., Kentarchos, A., Roelofs, G., Feichter, J., Land, C., Forster, C., James, P., Stohl,

- A., Collins, W., and Cristofanelli, P. Stratosphere-troposphere exchange: A model and method intercomparison. *Journal of Geophysical Research: Atmospheres*, 108 (D12), 2003. doi: <https://doi.org/10.1029/2002JD002274>. URL <https://agupubs.onlinelibrary.wiley.com/doi/abs/10.1029/2002JD002274>.
- Mertens, M. Contribution of road traffic emissions to tropospheric ozone in Europe and Germany. *Ph.D. thesis, Ludwig-Maximilians-Universität München*, 2017:1–210, 01 2017.
- Mertens, M., Kerkweg, A., Jöckel, P., Tost, H., and Hofmann, C. The 1-way on-line coupled model system MECO(n) – Part 4: Chemical evaluation (based on MESSy v2.52). *Geoscientific Model Development*, 9(10):3545–3567, 2016a. doi: 10.5194/gmd-9-3545-2016. URL <https://gmd.copernicus.org/articles/9/3545/2016/>.
- Mertens, M., Kerkweg, A., Jöckel, P., Tost, H., and Hofmann, C. The 1-way on-line coupled model system MECO(n) – Part 4: Chemical evaluation (based on MESSy v2.52). *Geoscientific Model Development*, 9:3545–3567, 10 2016b. doi: 10.5194/gmd-9-3545-2016.
- Mertens, M., Grewe, V., Rieger, V. S., and Jöckel, P. Revisiting the contribution of land transport and shipping emissions to tropospheric ozone. *Atmospheric Chemistry and Physics*, 18(8):5567–5588, 2018. doi: 10.5194/acp-18-5567-2018. URL <https://acp.copernicus.org/articles/18/5567/2018/>.
- Mertens, M., Kerkweg, A., Grewe, V., Jöckel, P., and Sausen, R. Are contributions of emissions to ozone a matter of scale? – a study using MECO(n) (MESSy v2.50). *Geoscientific Model Development*, 13(1):363–383, 2020a. doi: 10.5194/gmd-13-363-2020. URL <https://gmd.copernicus.org/articles/13/363/2020/>.
- Mertens, M., Kerkweg, A., Grewe, V., Jöckel, P., and Sausen, R. Attributing ozone and its precursors to land transport emissions in Europe and Germany. *Atmospheric Chemistry and Physics*, 20(13):7843–7873, 2020b. doi: 10.5194/acp-20-7843-2020. URL <https://acp.copernicus.org/articles/20/7843/2020/>.
- Mertens, M., Jöckel, P., Matthes, S., Nützel, M., Grewe, V., and Sausen, R. Covid-19 induced lower-tropospheric ozone changes. *Environmental Research Letters*, 16(6): 064005, may 2021. doi: 10.1088/1748-9326/abf191. URL <https://dx.doi.org/10.1088/1748-9326/abf191>.
- Moiseenko, K. B., Shtabkin, Y. A., Berezina, E. V., and Skorokhod, A. I. Regional Photochemical Surface-Ozone Sources in Europe and Western Siberia. *Izvestiya, Atmospheric and Oceanic Physics*, 54(6):545–557, 2018. URL <https://eurekamag.com/research/067/651/067651057.php>.
- Molina, M. J. and Rowland, F. S. Stratospheric sink for chlorofluoromethanes: chlorine atom-catalysed destruction of ozone. , 249(5460):810–812, jun 1974. doi: 10.1038/249810a0.

- Monks, P. Gas-Phase Radical Chemistry in the Troposphere. *Chemical Society reviews*, 34:376–95, 06 2005. doi: 10.1039/b307982c.
- Monson, R. K., Trahan, N., Rosenstiel, T. N., Veres, P., Moore, D., Wilkinson, M., Norby, R. J., Volder, A., Tjoelker, M. G., Briske, D. D., Karnosky, D. F., and Fall, R. Isoprene emission from terrestrial ecosystems in response to global change: minding the gap between models and observations. *Philosophical Transactions of the Royal Society A: Mathematical, Physical and Engineering Sciences*, 365(1856):1677–1695, 2007. doi: 10.1098/rsta.2007.2038. URL <https://royalsocietypublishing.org/doi/abs/10.1098/rsta.2007.2038>.
- Myhre, G., Samset, B. H., Schulz, M., Balkanski, Y., Bauer, S., Bernsten, T. K., Bian, H., Bellouin, N., Chin, M., Diehl, T., Easter, R. C., Feichter, J., Ghan, S. J., Hauglustaine, D., Iversen, T., Kinne, S., Kirkevåg, A., Lamarque, J.-F., Lin, G., Liu, X., Lund, M. T., Luo, G., Ma, X., van Noije, T., Penner, J. E., Rasch, P. J., Ruiz, A., Seland, Ø., Skeie, R. B., Stier, P., Takemura, T., Tsigaridis, K., Wang, P., Wang, Z., Xu, L., Yu, H., Yu, F., Yoon, J.-H., Zhang, K., Zhang, H., and Zhou, C. Radiative forcing of the direct aerosol effect from AeroCom Phase II simulations. *Atmospheric Chemistry and Physics*, 13(4): 1853–1877, 2013. doi: 10.5194/acp-13-1853-2013. URL <https://acp.copernicus.org/articles/13/1853/2013/>.
- Niinemets, U., Tenhunen, J. D., Harley, P. C., and Steinbrecher, R. A model of isoprene emission based on energetic requirements for isoprene synthesis and leaf photosynthetic properties for Liquidambar and Quercus. *Plant, Cell & Environment*, 22 (11):1319–1335, 1999. doi: <https://doi.org/10.1046/j.1365-3040.1999.00505.x>. URL <https://onlinelibrary.wiley.com/doi/abs/10.1046/j.1365-3040.1999.00505.x>.
- Ninneman, M., Lu, S., Lee, P., McQueen, J., Huang, J., Demerjian, K., and Schwab, J. Observed and Model-Derived Ozone Production Efficiency over Urban and Rural New York State. *Atmosphere*, 8(7), 2017. ISSN 2073-4433. doi: 10.3390/atmos8070126. URL <https://www.mdpi.com/2073-4433/8/7/126>.
- Ninneman, M., Demerjian, K. L., and Schwab, J. J. Ozone Production Efficiencies at Rural New York State Locations: Relationship to Oxides of Nitrogen Concentrations. *Journal of Geophysical Research: Atmospheres*, 124 (4):2363–2376, 2019. doi: <https://doi.org/10.1029/2018JD029932>. URL <https://agupubs.onlinelibrary.wiley.com/doi/abs/10.1029\let\reserved@d=\def,{\@@par}}\def\reserved@b{\@tempskipa\lastskip\unskip\penalty-\@M}\futurelet\@let@token\let2018JD029932>.
- Norton, J. and Ouyang, Y. Controls and Adaptive Management of Nitrification in Agricultural Soils. *Frontiers in microbiology*, 10:1116–1123, 2019. doi: doi:10.3389/fmicb.2019.01931.

- Olszyna, K. J., Bailey, E. M., Simonaitis, R., and Meagher, J. F. O₃ and NO_y relationships at a rural site. *Journal of Geophysical Research: Atmospheres*, 99(D7): 14557–14563, 1994. doi: <https://doi.org/10.1029/94JD00739>. URL <https://agupubs.onlinelibrary.wiley.com/doi/abs/10.1029/94JD00739>.
- Ou, J., Huang, Z., Klimont, Z., Jia, G., Zhang, S., Li, C., Meng, J., Mi, Z., Zheng, H., Shan, Y., Louie, P., Zheng, J., and Guan, D. Role of export industries on ozone pollution and its precursors in China. *Nature Communications*, 11, 10 2020. doi: 10.1038/s41467-020-19035-x.
- Pacifico, F., Harrison, S., Jones, C., and Sitch, S. Isoprene emissions and climate. *Atmospheric Environment*, 43(39):6121–6135, 2009. ISSN 1352-2310. doi: <https://doi.org/10.1016/j.atmosenv.2009.09.002>. URL <https://www.sciencedirect.com/science/article/pii/S1352231009007663>.
- Pacifico, F., Folberth, G., Jones, C., Harrison, S., and Sitch, S. Biogenic isoprene emissions in a coupled climate-vegetation-chemistry model. 05 2010.
- Pan, X., Ichoku, C., Chin, M., Bian, H., Darmenov, A., Colarco, P., Ellison, L., Kucsera, T., da Silva, A., Wang, J., Oda, T., and Cui, G. Six global biomass burning emission datasets: intercomparison and application in one global aerosol model. *Atmospheric Chemistry and Physics*, 20(2):969–994, 2020. doi: 10.5194/acp-20-969-2020. URL <https://acp.copernicus.org/articles/20/969/2020/>.
- Pay, M. T., Gangoiti, G., Guevara, M., Napelenok, S., Querol, X., Jorba, O., and Pérez García-Pando, C. Ozone source apportionment during peak summer events over southwestern Europe. *Atmospheric Chemistry and Physics*, 19(8):5467–5494, 2019. doi: 10.5194/acp-19-5467-2019. URL <https://acp.copernicus.org/articles/19/5467/2019/>.
- Pei, J., Liu, P., Fang, H., Gao, X., Pan, B., Li, H., Guo, H., and Zhang, F. Estimating Yield and Economic Losses Induced by Ozone Exposure in South China Based on Full-Coverage Surface Ozone Reanalysis Data and High-Resolution Rice Maps. *Agriculture*, 13(2), 2023. ISSN 2077-0472. doi: 10.3390/agriculture13020506. URL <https://www.mdpi.com/2077-0472/13/2/506>.
- Pozzer, A., Jöckel, P., Sander, R., Williams, J., Ganzeveld, L., and Lelieveld, J. Technical Note: The MESSy-submodel AIRSEA calculating the air-sea exchange of chemical species. *Atmospheric Chemistry and Physics*, 6(12):5435–5444, 2006. doi: 10.5194/acp-6-5435-2006. URL <https://acp.copernicus.org/articles/6/5435/2006/>.
- Pozzer, A., Jöckel, P., Tost, H., Sander, R., Ganzeveld, L., Kerkweg, A., and Lelieveld, J. Simulating organic species with the global atmospheric chemistry general circulation model ECHAM5/MESSy1: a comparison of model results with observations. *Atmospheric Chemistry and Physics*, 7(10):2527–2550, 2007. doi: 10.5194/acp-7-2527-2007. URL <https://acp.copernicus.org/articles/7/2527/2007/>.

- Price, C. and Rind, D. A simple lightning parameterization for calculating global lightning distributions. *Journal of Geophysical Research: Atmospheres*, 97(D9):9919–9933, 1992. doi: <https://doi.org/10.1029/92JD00719>. URL <https://agupubs.onlinelibrary.wiley.com/doi/abs/10.1029/92JD00719>.
- Pöschl, U., von Kuhlmann, R., Poisson, N., and Crutzen, P. Development and Intercomparison of Condensed Isoprene Oxidation Mechanisms for Global Atmospheric Modeling. *Journal of Atmospheric Chemistry*, 37:29–152, 2000. doi: 10.1023/A:1006391009798.
- Rich, S., Waggoner, P. E., and Tomlinson, H. Ozone uptake by bean leaves. *Science (New York, N.Y.)*, 169(3940:79—80, 1970. doi: <https://doi.org/10.1126/science.169.3940.79>.
- Ridley, B., Madronich, S., Chatfield, R., Walega, J., Shetter, R., Carroll, M., and Montzka, D. Measurements and model simulations of the photostationary state during MLOPEX: Implications for radical concentrations and ozone production and loss rates. *Journal of Geophysical Research*, 97:10375–10388, 01 1992.
- Rieger, V. S., Mertens, M., and Grewe, V. An advanced method of contributing emissions to short-lived chemical species (OH and HO₂): the TAGGING 1.1 submodel based on the Modular Earth Submodel System (MESSy 2.53). *Geoscientific Model Development*, 11(6):2049–2066, 2018. doi: 10.5194/gmd-11-2049-2018. URL <https://gmd.copernicus.org/articles/11/2049/2018/>.
- Rockel, Burkhard and Will, Andreas and Hense, Andrea. The Regional Climate Model COSMO-CLM (CCLM). *Meteorologische Zeitschrift*, 17(4):347–348, 08 2008. doi: 10.1127/0941-2948/2008/0309. URL <http://dx.doi.org/10.1127/0941-2948/2008/0309>.
- Roeckner, E., Brokopf, R., Esch, M., Giorgetta, M., Hagemann, S., Kornblueh, L., Manzini, E., Schlese, U., and Schulzweida, U. Sensitivity of Simulated Climate to Horizontal and Vertical Resolution in the ECHAM5 Atmosphere Model. *Journal of Climate*, 19(16): 3771–3791, 2006a. doi: 10.1175/JCLI3824.1. URL <https://journals.ametsoc.org/view/journals/clim/19/16/jcli3824.1.xml>.
- Roeckner, E., Bäuml, G., Bonaventura, L., Brokopf, R. and Esch, M. G., and M., e. a. The atmospheric general circulation model ECHAM 5. PART I: Model description., 2006b.
- Rohrer, F., Brüning, D., and Grobler, E. e. a. State of NO and NO₂ Observed During the POPCORN Field Campaign at a Rural Site in Germany. *Journal of Atmospheric Chemistry*, 31:119–137, 1998. doi: <https://doi.org/10.1023/A:1006166116242>.
- Rondón, A., Johansson, C., and Granat, L. Dry deposition of nitrogen dioxide and ozone to coniferous forests. *Journal of Geophysical Research: Atmospheres*, 98(D3): 5159–5172, 1993. doi: <https://doi.org/10.1029/92JD02335>. URL <https://agupubs.onlinelibrary.wiley.com/doi/abs/10.1029/92JD02335>.

- Sander, R., Baumgaertner, A., Gromov, S., Harder, H., Jöckel, P., Kerkweg, A., Kubistin, D., Regelin, E., Riede, H., Sandu, A., Taraborrelli, D., Tost, H., and Xie, Z.-Q. The atmospheric chemistry box model CAABA/MECCA-3.0. *Geoscientific Model Development*, 4(2):373–380, 2011. doi: 10.5194/gmd-4-373-2011. URL <https://gmd.copernicus.org/articles/4/373/2011/>.
- Sander, R., Jöckel, P., Kirner, O., Kunert, A. T., Landgraf, J., and Pozzer, A. The photolysis module JVAL-14, compatible with the MESSy standard, and the JVal PreProcessor (JVPP). *Geoscientific Model Development*, 7(6):2653–2662, 2014. doi: 10.5194/gmd-7-2653-2014. URL <https://gmd.copernicus.org/articles/7/2653/2014/>.
- Sander, R., Baumgaertner, A., Cabrera-Perez, D., Frank, F., Gromov, S., Groöf, J.-U., Harder, H., Huijnen, V., Jöckel, P., Karydis, V. A., Niemeyer, K. E., Pozzer, A., Riede, H., Schultz, M. G., Taraborrelli, D., and Tauer, S. The community atmospheric chemistry box model CAABA/MECCA-4.0. *Geoscientific Model Development*, 12(4):1365–1385, 2019. doi: 10.5194/gmd-12-1365-2019. URL <https://gmd.copernicus.org/articles/12/1365/2019/>.
- Schumann, U. and Huntrieser, H. The global lightning-induced nitrogen oxides source. *Atmospheric Chemistry and Physics*, 7(14):3823–3907, 2007. doi: 10.5194/acp-7-3823-2007. URL <https://acp.copernicus.org/articles/7/3823/2007/>.
- Seinfeld, J. and Pandis, S. *Atmospheric Chemistry and Physics: From Air Pollution to Climate Change*. John Wiley and Sons, New York, 2006.
- Shen, J. and Gao, Z. Ozone removal on building material surface: A literature review. *Building and Environment*, 134:205–217, 04 2018. doi: 10.1016/j.buildenv.2018.02.046.
- Sillman, S. The use of NO_y, H₂O₂, and HNO₃ as indicators for ozone-no x -hydrocarbon sensitivity in urban locations. *Journal of Geophysical Research: Atmospheres*, 100(D7):14175–14188, 1995. doi: <https://doi.org/10.1029/94JD02953>. URL <https://agupubs.onlinelibrary.wiley.com/doi/abs/10.1029/94JD02953>.
- Sillman, S. The relation between ozone, NO_x and hydrocarbons in urban and polluted rural environments. *Atmospheric Environment*, 33(12):1821–1845, 1999. ISSN 1352-2310. doi: [https://doi.org/10.1016/S1352-2310\(98\)00345-8](https://doi.org/10.1016/S1352-2310(98)00345-8). URL <https://www.sciencedirect.com/science/article/pii/S1352231098003458>.
- Sillman, S. Ozone production efficiency and loss of NO_x in power plant plumes: Photochemical model and interpretation of measurements in Tennessee. *Journal of Geophysical Research: Atmospheres*, 105(D7):9189–9202, 2000. doi: <https://doi.org/10.1029/1999JD901014>. URL <https://agupubs.onlinelibrary.wiley.com/doi/abs/10.1029/1999JD901014>.
- Sillman, S., He, D., Pippin, M., Daum, P., Imre, D., Kleinman, L., Lee, J., and Weinstein-Lloyd, J. Model correlations for ozone, reactive nitrogen, and peroxides for Nashville

- in comparison with measurements: Implications for O_3 - NO_x -hydrocarbon chemistry. *Journal of Geophysical Research*, 1032:22629–22644, 09 1998. doi: 10.1029/98JD00349.
- Simpson, D., Guenther, A., Hewitt, C. N., and Steinbrecher, R. Biogenic emissions in Europe: 1. Estimates and uncertainties. *Journal of Geophysical Research: Atmospheres*, 100(D11):22875–22890, 1995. doi: <https://doi.org/10.1029/95JD02368>. URL <https://agupubs.onlinelibrary.wiley.com/doi/abs/10.1029/95JD02368>.
- Sindelarova, K., Granier, C., Bouarar, I., Guenther, A., Tilmes, S., Stavrou, T., Müller, J.-F., Kuhn, U., Stefani, P., and Knorr, W. Global data set of biogenic VOC emissions calculated by the MEGAN model over the last 30 years. *Atmospheric Chemistry and Physics*, 14(17):9317–9341, 2014. doi: 10.5194/acp-14-9317-2014. URL <https://acp.copernicus.org/articles/14/9317/2014/>.
- Skeie, R., Myhre, G., Hodnebrog, , Cameron-Smith, P., Deushi, M., Hegglin, M., Horowitz, L., Kramer, R., Michou, M., Mills, M., Olivie, D., Connor, F., Paynter, D., Samset, B. H., Sellar, A., Shindell, D., Takemura, T., Tilmes, S., and Wu, T. Historical total ozone radiative forcing derived from CMIP6 simulations. *npj Climate and Atmospheric Science*, 3, 12 2020. doi: 10.1038/s41612-020-00131-0.
- Steppeler, J., Doms, G., and Schättler, U. e. a. Meso-gamma scale forecasts using the nonhydrostatic model LM. *Meteorol Atmos Phys*, 82:75–96, 2003. doi: <https://doi.org/10.1007/s00703-001-0592-9>.
- Stohl, A., Eckhardt, S., Forster, C., James, P., and Spichtinger, N. On the pathways and timescales of intercontinental air pollution transport. *Journal of Geophysical Research: Atmospheres*, 107(D23):ACH 6–1–ACH 6–17, 2002. doi: <https://doi.org/10.1029/2001JD001396>. URL <https://agupubs.onlinelibrary.wiley.com/doi/abs/10.1029/2001JD001396>.
- Szintai, B. and Kaufmann, P. TKE as a Measure of Turbulence. 04 2014.
- Tai, A., Sadiq, M., Pang, J., and Yung, D. Impacts of Surface Ozone Pollution on Global Crop Yields: Comparing Different Ozone Exposure Metrics and Incorporating Co-effects of CO_2 . *Frontiers in Sustainable Food Systems*, 5:534616, 03 2021. doi: 10.3389/fsufs.2021.534616.
- Tan, W., Liu, C., Wang, S., Xing, C., Su, W., Zhang, C., Xia, C., Liu, H., Cai, Z., and Liu, J. Tropospheric NO_2 , SO_2 , and HCHO over the East China Sea, using ship-based MAX-DOAS observations and comparison with OMI and OMPS satellite data. *Atmospheric Chemistry and Physics*, 18(20):15387–15402, 2018. doi: 10.5194/acp-18-15387-2018. URL <https://acp.copernicus.org/articles/18/15387/2018/>.
- Terrenoire, E., Hauglustaine, D. A., Cohen, Y., Cozic, A., Valorso, R., Lefèvre, F., and Matthes, S. Impact of present and future aircraft NO_x and aerosol emissions on atmospheric composition and associated direct radiative forcing of climate. *Atmospheric*

- Chemistry and Physics*, 22(18):11987–12023, 2022. doi: 10.5194/acp-22-11987-2022. URL <https://acp.copernicus.org/articles/22/11987/2022/>.
- Thurston, G. D. Outdoor Air Pollution: Sources, Atmospheric Transport, and Human Health Effects. In *International Encyclopedia of Public Health*, pages 367–377. Elsevier, 2017. doi: 10.1016/b978-0-12-803678-5.00320-9.
- Tost, H., Jöckel, P., Kerkweg, A., Sander, R., and Lelieveld, J. Technical note: A new comprehensive SCAVenging submodel for global atmospheric chemistry modelling. *Atmospheric Chemistry and Physics*, 6(3):565–574, 2006a. doi: 10.5194/acp-6-565-2006. URL <https://acp.copernicus.org/articles/6/565/2006/>.
- Tost, H., Jöckel, P., and Lelieveld, J. Influence of different convection parameterisations in a GCM. *Atmospheric Chemistry and Physics*, 6(12):5475–5493, 2006b. doi: 10.5194/acp-6-5475-2006. URL <https://acp.copernicus.org/articles/6/5475/2006/>.
- Tost, H., Jöckel, P., and Lelieveld, J. Lightning and convection parameterisations; uncertainties in global modelling. *Atmospheric Chemistry and Physics*, 7(17):4553–4568, 2007. doi: 10.5194/acp-7-4553-2007. URL <https://acp.copernicus.org/articles/7/4553/2007/>.
- Tost, H., Lawrence, M. G., Brühl, C., Jöckel, P., Team, T. G., and Team, T. S.-O.-D. Uncertainties in atmospheric chemistry modelling due to convection parameterisations and subsequent scavenging. *Atmospheric Chemistry and Physics*, 10(4):1931–1951, 2010. doi: 10.5194/acp-10-1931-2010. URL <https://acp.copernicus.org/articles/10/1931/2010/>.
- Travis, K. R. and Jacob, D. J. Systematic bias in evaluating chemical transport models with maximum daily 8 h average (MDA8) surface ozone for air quality applications: a case study with GEOS-Chem v9.02. *Geoscientific Model Development*, 12(8):3641–3648, 2019. doi: 10.5194/gmd-12-3641-2019. URL <https://gmd.copernicus.org/articles/12/3641/2019/>.
- Tsati, E.-E. Investigation of the impacts of emissions on the trace gas budgets in the troposphere by using global climate chemistry model simulations, September 2014. URL <http://nbn-resolving.de/urn:nbn:de:bvb:19-175246>.
- Vinken, G. C. M., Boersma, K. F., Maasakkers, J. D., Adon, M., and Martin, R. V. World-wide biogenic soil NO_x emissions inferred from OMI NO₂ observations. *Atmospheric Chemistry and Physics*, 14(18):10363–10381, sep 2014. doi: 10.5194/acp-14-10363-2014.
- von Kuhlmann, R., Lawrence, M. G., Crutzen, P. J., and Rasch, P. J. A model for studies of tropospheric ozone and nonmethane hydrocarbons: Model description and ozone results. *Journal of Geophysical Research: Atmospheres*, 108(D9), 2003. doi: <https://doi.org/10.1029/2002JD002893>. URL <https://agupubs.onlinelibrary.wiley.com/doi/abs/10.1029/2002JD002893>.

- Wang, M., Yim, S. H., Wong, D., and Ho, K. Source contributions of surface ozone in China using an adjoint sensitivity analysis. *Science of The Total Environment*, 662: 385–392, 2019. ISSN 0048-9697. doi: <https://doi.org/10.1016/j.scitotenv.2019.01.116>. URL <https://www.sciencedirect.com/science/article/pii/S0048969719301329>.
- Wang, Y., Li, L., Feng, J., Huang, C., Huang, H., Chen, C., Wang, H., Sheng, G., and Fu, J. Source apportionment of ozone in the summer of 2010 in Shanghai using OSAT method. *Huanjing Kexue Xuebao/Acta Scientiae Circumstantiae*, 34:567–573, 03 2014. doi: 10.13671/j.hjkxxb.2014.0104.
- Wang, Y., Wild, O., Ashworth, K., Chen, X., Wu, Q., Qi, Y., and Wang, Z. Reductions in crop yields across China from elevated ozone. *Environmental Pollution*, 292:118218, 2022. ISSN 0269-7491. doi: <https://doi.org/10.1016/j.envpol.2021.118218>. URL <https://www.sciencedirect.com/science/article/pii/S0269749121018005>.
- Wang, Z. S., Chien, C.-J., and Tonnesen, G. S. Development of a tagged species source apportionment algorithm to characterize three-dimensional transport and transformation of precursors and secondary pollutants. *Journal of Geophysical Research: Atmospheres*, 114(D21), 2009. doi: <https://doi.org/10.1029/2008JD010846>. URL <https://agupubs.onlinelibrary.wiley.com/doi/abs/10.1029/2008JD010846>.
- WHO. The world health report 2006: working together for health, 2006.
- Wooster, M. J., Roberts, G., Perry, G. L. W., and Kaufman, Y. J. Retrieval of biomass combustion rates and totals from fire radiative power observations: FRP derivation and calibration relationships between biomass consumption and fire radiative energy release. *Journal of Geophysical Research: Atmospheres*, 110(D24), 2005. doi: <https://doi.org/10.1029/2005JD006318>. URL <https://agupubs.onlinelibrary.wiley.com/doi/abs/10.1029/2005JD006318>.
- World Health Organization. *WHO global air quality guidelines: particulate matter (PM_{2.5} and PM₁₀), ozone, nitrogen dioxide, sulfur dioxide and carbon monoxide*. World Health Organization, 2021.
- Wuest, R. *Mathematik für Physiker und Mathematiker, vol. 1: Reelle Analysis und Lineare Algebra 3. edn*. WILEY-VCH GmbH Co. KGaA, 2009. ISBN 9780691001852. URL <http://www.jstor.org/stable/j.ctt7t8hg>.
- Xu, R., Wang, D., Li, J., Wan, H., Shen, S., and Guo, X. A Hybrid Deep Learning Model for Air Quality Prediction Based on the Time–Frequency Domain Relationship. *Atmosphere*, 14(2), 2023. ISSN 2073-4433. doi: 10.3390/atmos14020405. URL <https://www.mdpi.com/2073-4433/14/2/405>.
- Yang, X., Wu, K., Wang, H., Liu, Y., Gu, S., Lu, Y., Zhang, X., Hu, Y., Ou, Y., Wang, S., and Wang, Z. Summertime ozone pollution in Sichuan Basin, China: Meteorological conditions, sources and process analysis. *Atmospheric Environment*, 226:117392, 2020.

- ISSN 1352-2310. doi: <https://doi.org/10.1016/j.atmosenv.2020.117392>. URL <https://www.sciencedirect.com/science/article/pii/S135223102030131X>.
- Ye, X., Wang, X., and Zhang, L. Diagnosing the Model Bias in Simulating Daily Surface Ozone Variability Using a Machine Learning Method: The Effects of Dry Deposition and Cloud Optical Depth. *Environmental Science & Technology*, 56(23):16665–16675, 2022. doi: 10.1021/acs.est.2c05712. URL <https://doi.org/10.1021/acs.est.2c05712>. PMID: 36437714.
- Yienger, J. J. and Levy, H. Empirical model of global soil-biogenic NO emissions. *Journal of Geophysical Research*, 100(D6):11447, 1995. doi: 10.1029/95jd00370.
- Young, P. J., Archibald, A. T., Bowman, K. W., Lamarque, J.-F., Naik, V., Stevenson, D. S., Tilmes, S., Voulgarakis, A., Wild, O., Bergmann, D., Cameron-Smith, P., Cionni, I., Collins, W. J., Dalsøren, S. B., Doherty, R. M., Eyring, V., Faluvegi, G., Horowitz, L. W., Josse, B., Lee, Y. H., MacKenzie, I. A., Nagashima, T., Plummer, D. A., Righi, M., Rumbold, S. T., Skeie, R. B., Shindell, D. T., Strode, S. A., Sudo, K., Szopa, S., and Zeng, G. Pre-industrial to end 21st century projections of tropospheric ozone from the Atmospheric Chemistry and Climate Model Intercomparison Project (ACCMIP). *Atmos. Chem. Phys.*, 13:2063–2090, 2013. doi: 10.5194/acp-13-2063-2013.
- Zeldovich, Y. and Raizer, Y. *Physics of Shock Waves and High-Temperature Hydrodynamic Phenomena*. Dover Books on Physics. Dover Publications, 2002. ISBN 9780486420028. URL <https://books.google.at/books?id=zVf27TMNdToC>.
- Zeldovich, Y. and Semenov, N. Kinetics of chemical reactions in flames. *Journal of Experimental and Theoretical Physics (USSR)*, 10(1084):1116–1123, 1946.
- Ziereis, H., Hoor, P., Groß, J.-U., Zahn, A., Stratmann, G., Stock, P., Lichtenstern, M., Krause, J., Bense, V., Afchine, A., Rolf, C., Woiwode, W., Braun, M., Ungermann, J., Marsing, A., Voigt, C., Engel, A., Sinnhuber, B.-M., and Oelhaf, H. Redistribution of total reactive nitrogen in the lowermost Arctic stratosphere during the cold winter 2015/2016. *Atmospheric Chemistry and Physics*, 22(5):3631–3654, 2022. doi: 10.5194/acp-22-3631-2022. URL <https://acp.copernicus.org/articles/22/3631/2022/>.

Acronyms

ACP	Atmospheric Chemistry and Physics
AIRBASE	The European air quality database
AR	Assessment Report
AQICN	World Air Quality Index
AWB	Agriculture Waste Burning
BAS	Sichuan Basin
BEN	Benelux region
BIOBURN	BIOBURN submodel
BL	Planetary Boundary Layer
BMIL	Base Model Interface Layer
BML	Base Model Layer
CCMI	Chemistry-Climate Model Initiative
CCMI-2	Chemistry-Climate Model Initiative phase 2)
CEDS	Community Emissions Data System
CLM	Climate Limited-area Modelling-community
COD	Cloud Optical Depth
CMAQ	Community Multiscale Air Quality
CTM	Chemical Transport Model
COSMO	Consortium for Small-scale Modeling-Climate Limited-area Modelling/Modular Earth Submodel System
D21	Delang et al. [2021] dataset

DM	Dry Particulate Matter
EA	East Asia
ECHAM5	5th generation European Centre Hamburg General Circulation Model
ECMWF	European Centre for Medium-Range Weather Forecasts
EDGAR	Emissions Database For Global Atmospheric Research
EEA	European Environment Agency
EF	Emission Factor
EMAC	ECHAM5/MESSy Atmospheric Chemistry
EMeRGe	Effect of Megacities on the Transport and Transformation of Pollutants on the Regional to Global Scales
EOC	Earth Observation Center
EPA	Environmental Protection Agency
ERA5	ECMWF Reanalysis v5
EU	Europe
ESA	European Space Agency
ESMs	Earth System Models
GCM	General Circulation Model
GEOS-CHEM	Global 3-D model of Atmospheric Composition driven by assimilated meteorological observations from the Goddard Earth Observing System (GEOS).
GEIA	Global Emissions Initiative
GFAS	Global Fire Assimilation System
GS	Global Scaling Factor
FRP	Fire Radiative Power
FT	Firetype
HALO	High Altitude and Long Range Aircraft
IBE	Iberian Peninsula

IPCC	Intergovernmental Panel on Climate Change
IRE	West Ireland
JJA	June, July and August
LAI	Leaf Area Index
LNO_x	Lightning-induced NO _x
LRT	Long Range Transport
M³Fusion method	A new statistical approach for combining observations and multiple model output.
MAX-DOAS	Multi-axis Differential Optical Absorption Spectroscopy
MB	Mean Bias
MDA8	Daily maximum of the 8-hour rolling mean of the O ₃ concentration
MECCA	Module Efficiently Calculating the Chemistry of the Atmosphere
MECO(n)	MESSy-fied ECHAM and COSMO models nested n-times
MEGAN	Model of Emissions of Gases and Aerosols from Nature
MIM	Mainz Isoprene Mechanism
MODIS	Moderate Resolution Imaging Spectroradiometer
NA	North America
NIR	Near-infrared
NMHCs	Non-methane Hydrocarbons
NWP	Numerical Weather Prediction Model
OFFEMIS	OFFline EMISsions
OPE	Ozone Production Efficiency
OSDMA8	seasonal daily maximum 8-hour mixing ratio of ground-level O ₃
PAN	Peroxyacetyl Nitrate
PBLH	Planetary Boundary Layer Height
PDF	Probability Density Function

PEA	Pearl River Delta
PFT	Plant Functional Types
PO	Po Valley
QCTM	Quasi chemistry-transport model
R²	Squared Pearson Correlation Coefficient
RCP	Representative Concentration Pathway
RF	Radiative Forcing
RMSE	Root Mean Squared Error
ROW	Rest of the World
RS	Regional Scaling Factor
RUR	Rural region Ningxia
SCDs	Slant Column Densities
SD	Specified Dynamics
S4D	Sampling in 4 Dimensions
S5P	Sentinel 5P
SCAV	Scavenging
SLP	Sea Level Pressure
SORBIT	Submodel to sample data along sun-synchronous satellite orbits.
SMCL	Submodel Core Layer
SMIL	Submodel Interface Layer
SNAP	Selected Nomenclature for sources of Air Pollution
SR	Sillman Ratio
SWIR	Shortwave-infrared
TAGGING	Submodel to calculate contribution to different emission categories to concentrations (e.g. NO _y or O ₃).
TAI	Taiwan

TOAR	Tropospheric Ozone Assessment Report
TROPOMI	Tropospheric Monitoring Instrument
Tg	Teragram
UV	Ultraviolet
VCDs	Vertical Column Densities
VIS	Visible
VF	Vertical Fraction
VOC	Volatile Organic Compounds
WHO	World Health Organization
YAN	Yangtze River Delta

Danksagung

An dieser Stelle möchte ich mich zuallererst bei meinem Hauptbetreuer Mariano Mertens und meinem Ko-Betreuer Patrick Jöckel bedanken. Vielen Dank, dass ihr mir bei jeder Frage tatkräftig zur Seite gestanden seid und immer ein offenes Ohr für mich hattet. Ich durfte unter eurer Anleitung viel lernen, und besonders hervorheben möchte ich eure Geduld und aufmunternden Worte bei Tiefpunkten. Bedanken möchte ich mich auch bei meinem Doktorvater Prof. Dr. Robert Sausen für seine Unterstützung und Korrektur.

Ein besonderer Dank geht an meine Eltern und meine drei Geschwister, die mich immer unterstützt, ermutigt und angefeuert haben. Außerdem möchte ich mich bei all meinen Freunden, meiner Kirchengemeinde und meinen vielen Bekannten bedanken, die in diesen vier Jahren immer für mich da waren.

Last but not least bin ich Gott von Herzen dankbar, dass er mir immer wieder die Kraft und das Durchhaltevermögen geschenkt hat, dieses Projekt erfolgreich zum Abschluss zu bringen.

*“The LORD is my rock, and my fortress, and my deliverer;
my God, my strength, in whom I will trust;
my buckler, and the horn of my salvation, and my high tower.”*
The Bible: Psalms 18,2